



EV TRAPPING

RAMAN CHARACTERIZATION
OF SINGLE TUMOR-DERIVED
EXTRACELLULAR VESICLES

AGUSTIN ENCISO MARTINEZ

EV TRAPPING

RAMAN CHARACTERIZATION
OF SINGLE TUMOR-DERIVED
EXTRACELLULAR VESICLES

Agustin Enciso Martinez

EV TRAPPING

RAMAN CHARACTERIZATION OF SINGLE TUMOR-DERIVED EXTRACELLULAR VESICLES

DISSERTATION

to obtain

the degree of doctor at the University of Twente,

on the authority of the rector magnificus,

prof. dr. T.T.M. Palstra,

on account of the decision of the Doctorate Board,

to be publicly defended

on Thursday 2 July 2020 at 14:45

by

Agustin Enciso Martinez

born on 25 December 1990

in Zacatecas, Mexico

This dissertation has been approved by:

Supervisors:

Prof. dr. L.W.M.M. Terstappen, MD

Dr. C. Otto

ISBN: 978-90-365-5019-2

DOI: 10.3990/1.9789036550192

URL: <https://doi.org/10.3990/1.9789036550192>

Cover artwork by Deyla Lerma (@deysign). Branding & Stationery Design Studio, deysign.myportfolio.com

Lay-out by Jules Verkade, persoonlijkproefschrift.nl

Printed by Ipskamp Printing, proefschriften.net

© 2020 Agustin Enciso Martinez, The Netherlands. All rights reserved. No parts of this thesis may be reproduced, stored in a retrieval system or transmitted in any form or by any means without permission of the author. Alle rechten voorbehouden. Niets uit deze uitgave mag worden vermenigvuldigd, in enige vorm of op enige wijze, zonder voorafgaande schriftelijke toestemming van de auteur.

Graduation Committee:

Chairman/Secretary:

Prof. dr. J.L. Herek University of Twente

Supervisors:

Prof. dr. L.W.M.M. Terstappen, MD University of Twente

dr. C. Otto University of Twente

Committee Members:

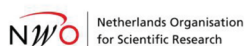
Prof. dr. S. Manohar University of Twente

Prof. dr. F.G. Mugele University of Twente

Prof. dr. W.H. Roos University of Groningen

Prof. dr. G.W. Jenster Erasmus University Rotterdam

Prof. dr. A.G.J.M. van Leeuwen AMC - University of Amsterdam



UNIVERSITY OF TWENTE.

The work described in this thesis was conducted at the Medical Cell BioPhysics department of the University of Twente, Enschede, The Netherlands. This work was supported by the Netherlands Organisation for Scientific Research – Domain Applied and Engineering Sciences (NWO-TTW), under the Perspectief research program Cancer-ID (project: 14193).

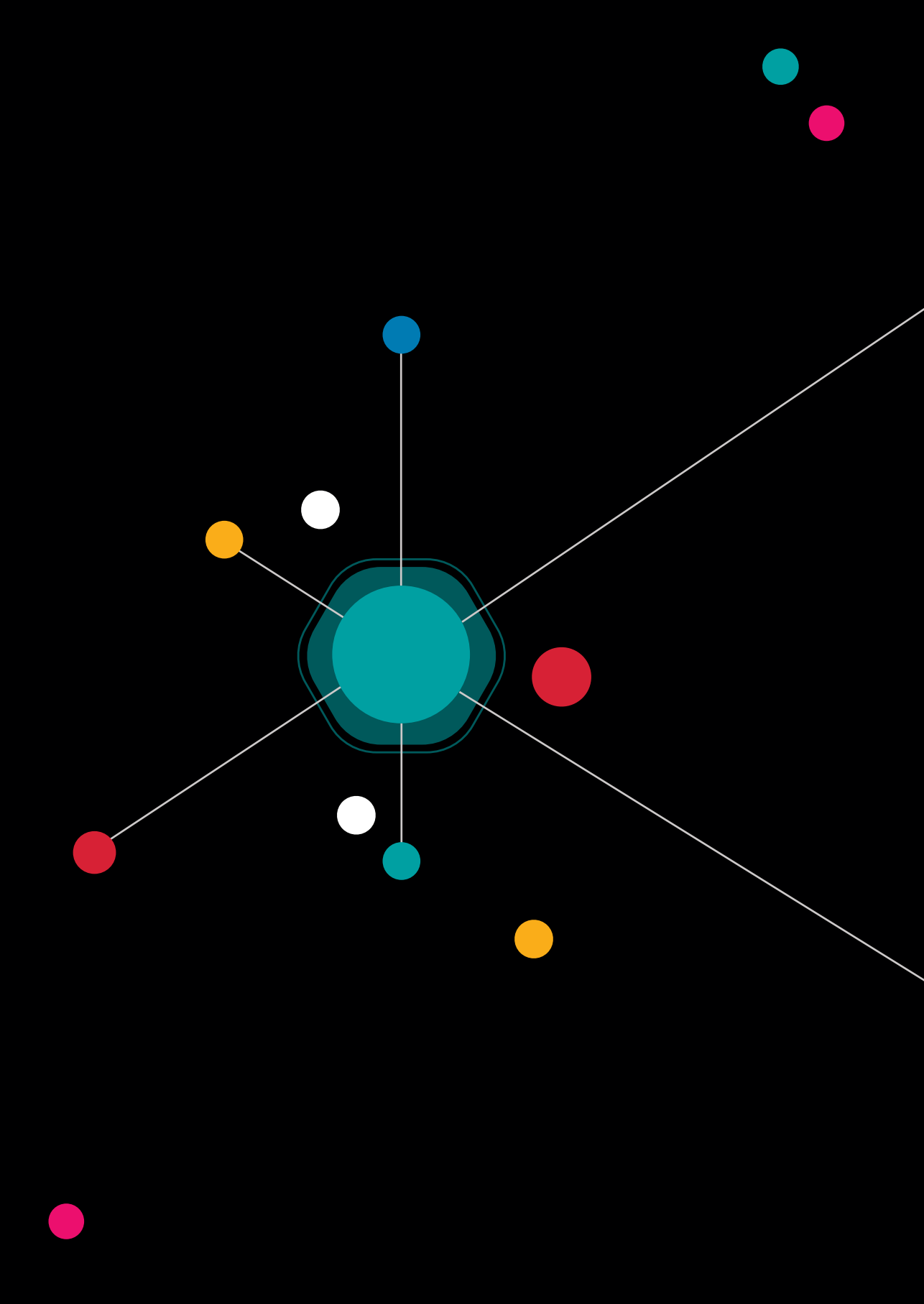
*Cancer begins and ends with people. In the midst of scientific abstraction,
it is sometimes possible to forget this one basic fact...*

- June Goodfield

To cancer patients

Contents

Chapter 1	Introduction	9
Chapter 2	Optical analytical techniques	27
Chapter 3	SEM-Raman image cytometry	43
Chapter 4	Immuno-capture of extracellular vesicles for individual multi-modal characterization using AFM, SEM and Raman spectroscopy	61
Chapter 5	Synchronized Rayleigh and Raman scattering for the characterization of single optically trapped extracellular vesicles	89
Chapter 6	Label-free identification and chemical characterization of single EVs and lipoproteins by synchronous Rayleigh and Raman scattering	105
Chapter 7	Label-free detection and characterization of single submicrometer particles in plasma of prostate cancer patients	137
Chapter 8	Organosilicon uptake by biological membranes	161
Chapter 9	Conclusions and outlook	181
Appendices	Summary	192
	Samenvatting	195
	Scientific output	198
	Acknowledgments	201
	Curriculum Vitae	205






Chapter 1

Introduction



Part of section 1.4 has been published as:

L. G. Rikkert et al., Cancer-ID: towards identification of cancer by tumor-derived extracellular vesicles in blood, *Front Oncol*, 2020, 10, 608.



1.1 Thesis motivation

Worldwide, 1 out of 6 deaths are related to cancer.¹ Early detection, effective monitoring of the disease and optimal treatments may bring cancer from a deadly to a chronic controllable disease. Liquid biopsies may effectively detect and monitor cancer through the analysis of blood. Not only under physiological, but also under pathological conditions, cells release extracellular vesicles (EVs) for communication or waste removal purposes.²⁻⁴ Hence, cancer cells may release EVs to the blood stream,⁵⁻⁷ and consequently, a fraction of the particles in blood will derive from tumors. Such tumor-derived EVs (tdEVs) may contain specific information about their parental cancer cells and, in general, reflect the state of the patient. Thus, identifying and characterizing tdEVs can provide relevant information for cancer diagnosis, selection of optimal treatment and monitoring treatment response.

The detection and characterization of tdEVs in blood has been challenging due to (1) their small size, which may be as small as 30 nm in diameter,⁸ (2) their size and density overlap with many other EVs and non-EV particles present in the blood, such as lipoproteins and (3) the limited knowledge on their chemical composition. Therefore, the utilization of tdEVs as cancer biomarkers will largely benefit from techniques that are able to (1) detect biological nanoparticles at the single particle level and (2) disclose physical and chemical features that can be used to distinguish tdEVs from other particles in blood and gain a better understanding about them.

The aim of this work is to detect and characterize biological nanoparticles in blood, specifically tdEVs, at the single particle level. Hence, this thesis explores various methods that enable in a novel way the detection and characterization of individual particles and the discrimination of tdEVs from other EVs and non-EV particles in a label-free manner. One method is the exploration of correlated scanning electron microscopy (SEM) and Raman spectroscopy. Another method is the development of synchronous Rayleigh and Raman spectroscopy. The thesis describes the implementation of those methods to biological nanoparticles in blood, from big to small, from cancer cells to tdEVs and from model particles to particles in the blood of cancer patients. This development opens an avenue to exploit the potential of tdEVs as cancer biomarkers and to study other particles in blood relevant to cancer and other diseases.

1.2 What are extracellular vesicles (EVs)?

Extracellular vesicles (EVs) are particles enclosed by a phospholipid bilayer and released by both eukaryotic and prokaryotic cells. The size range of EVs is very broad, ranging from 30 nm up to 5 μm in diameter.^{9–15} The release of EVs by cells is an evolutionarily conserved process that serves various functions, which are not all yet unveiled. Historically, EVs were believed to be waste products of cells. However, in the last decade, it has become increasingly clear that EVs serve not only functions of waste removal, but also of intercellular communication and coagulation.^{2–4} Because EVs originate from cells, they contain biomolecules present in the parent cells, such as lipids, proteins, nucleic acids and sugars. Hence, EVs may reflect the nature of the parent cell, which means that by studying EVs, the phenotype and genotype of parent cells can potentially be identified.

One of the first reports on EVs dates back to 1946, when Chargaff and West studied a “clotting factor” in plasma that promoted clotting in blood.¹⁶ In 1967, Wolf identified the “clotting factor” by electron microscopy and called it “platelet-dust”, which consisted of sub-micrometer lipid-rich particles originating from platelets.¹⁷ Various observations of EVs followed^{18–22} and many of these EVs were assumed to be released by outward budding of the cell membrane. However, a more complex biogenesis of EVs was described in the 1980s, which involved the fusion of multivesicular bodies (MVBs), also known as multivesicular endosomes, with the cell membrane.^{3,23,24} These types of EVs of endosomal origin were named “exosomes”.²⁵ Since then, the field of EVs has expanded rapidly with more than 25,000 publications according Web of Science (Figure 1.1).

EVs are highly heterogeneous in composition, size, origin, function and release mechanism. Hence, such vesicles have received many different names in the literature referring to their size (e.g. microvesicles, nanovesicles), their origin (e.g. platelet-derived EVs, prostasomes, oncosomes), their function (calcifying matrix vesicles, argosomes), their presence outside the cells (ectosomes, exovesicles) and their biogenesis (exosomes, microvesicles and apoptotic bodies).³ Figure 1.2 shows a snapshot of different cell types releasing EVs, some of which may be microvesicles (circles) and apoptotic bodies (arrows).

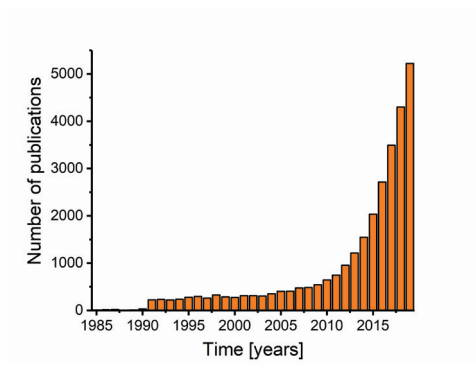


Figure 1.1. Number of publications per year for topic: “extracellular vesicle(s)” or “exosome(s)” or “microvesicle(s)” as reported by Web of Science.

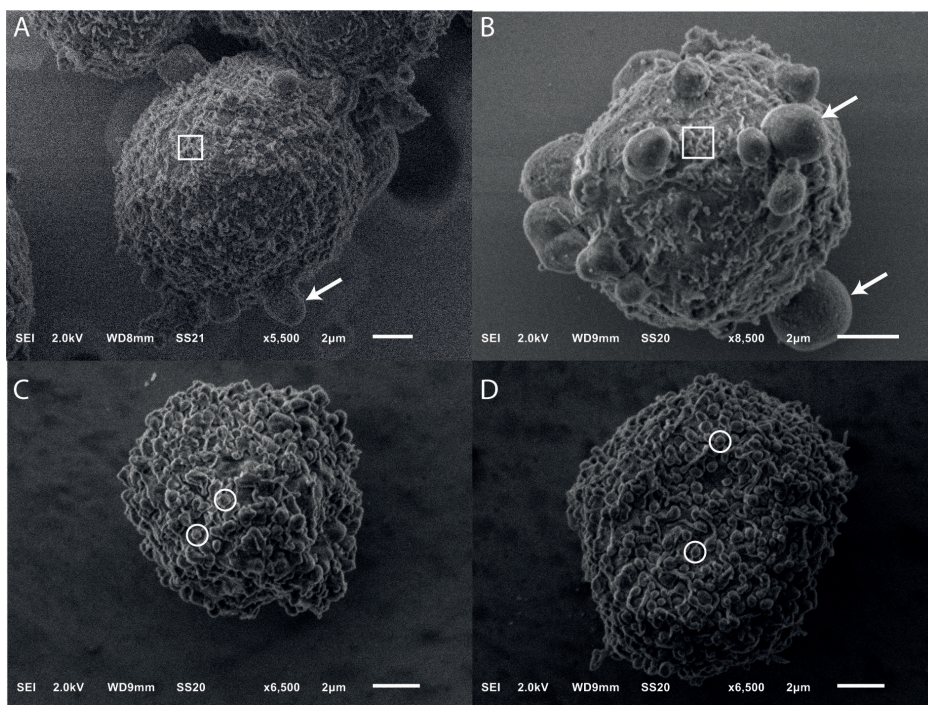


Figure 1.2. SKBR-3 (A), LNCaP (B), and PC3 (C and D) cells releasing EVs of various sizes indicated by arrows and circles. Squares indicate examples of microvilli. Images were taken with a scanning electron microscope. Scale bars denote 2 μm .

At present, the most common nomenclature for subgroups of EVs is based on their biogenesis (Figure 1.3). The endocytic pathway involves the invagination of the cell membrane forming lipid vesicles called early endosomes, which mature into late endosomes. During this process, inward budding of the endosome membrane forms intraluminal vesicles (ILVs), which contain

proteins, lipids and cytosol. The endosomes accumulate ILVs in their lumen and are then commonly referred to as multivesicular endosomes or MVBs. MVBs can fuse either with lysosomes for cargo degradation, or with the cell membrane to release the ILVs, then called exosomes.³ Exosomes have an estimated diameter between 30 and 150 nm.^{9–11} Microvesicles, also known as microparticles, are formed by direct budding from the cell membrane. They have an estimated diameter up to 1000 nm.^{10–13} Apoptotic bodies are formed when the cell undergoes apoptosis and membrane blebbing occurs. This type of EVs is among the largest, ranging between 1 and 5 μm in diameter and may contain fragments of genomic DNA.^{10,15,26} The mechanisms underlying the biogenesis and secretion of EVs have been reviewed elsewhere.^{3,27}

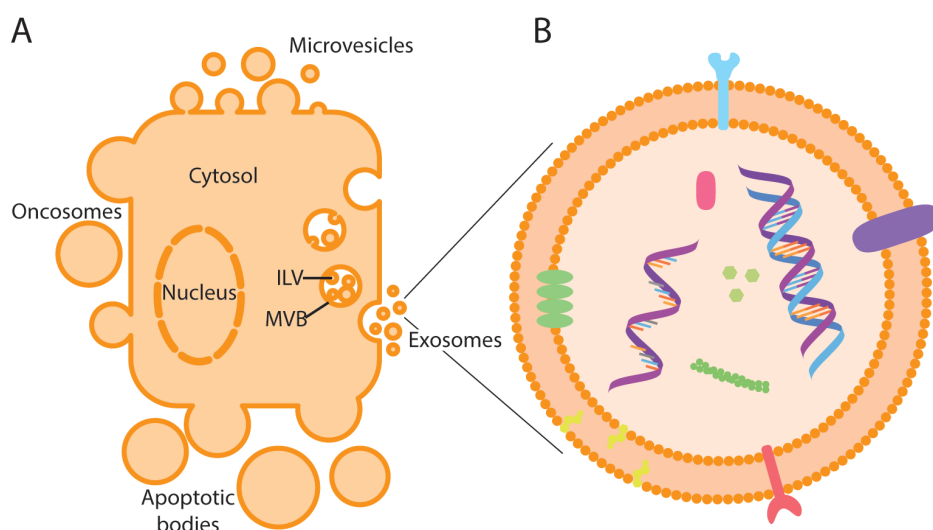


Figure 1.3. EV biogenesis. **(A)** Formation and release of exosomes, microvesicles, apoptotic bodies and oncosomes (in cancer cells). ILV: intraluminal vesicles, MVB: multivesicular bodies. **(B)** Schematic of an EV composed of proteins, lipids and nucleic acids.

1.3 Extracellular vesicles in cancer

In recent years, it has become accepted that body fluids, such as blood and urine, contain EVs.²⁸ Under physiological conditions, blood contains between 10^6 and 10^{12} EVs per mL,^{2,8,28} which originate from red blood cells (RBCs), platelets, leukocytes and the vessel wall.²⁹ However, diseased cells, such as cancer cells, also release EVs. Hence, in cancer, tumor-derived EVs (tdEVs) may be present within the circulation.^{5–7} Consequently, tdEVs may be used as diagnostic and prognostic biomarkers.

The first observations of tdEVs were made in the early 1980s, and tdEVs were attributed procoagulant activity associated with different types of malignancies.^{30,31} At present, the collected evidence suggests that cancer cells not only release EVs, but such tdEVs may affect all of the hallmarks of cancer described by Hanahan and Weinberg.¹⁰ It has been reported that malignant transformation leads to an increased production of tdEVs. This may enhance the transfer of activated oncogenes contained in tdEVs, which are released to the cellular surroundings, but may reach other tissues via the circulation.^{10,32} Hence, tdEVs are potential contributors to oncogenesis.¹¹ It has been shown that tdEVs are capable of transferring characteristics of cancer cells to normal fibroblasts and epithelial cells.^{10,33} tdEVs may also contribute to metastasis. For instance, tdEVs can sequester molecules involved in epithelial-mesenchymal transition³⁴ and it has been reported that tdEVs carry miRNAs that target the tight junctions between endothelial cells, destroying the natural barriers against metastasis.³⁵ tdEVs can also induce pre-metastatic niche formation and angiogenesis.^{10,36,37} Various studies have reported that tdEVs contribute to drug resistance by removing anticancer drugs out of a cancer cell or by expressing molecules that redirect the chemotherapy agents away from the cancer cells.^{11,38-40}

In peripheral blood, the concentration of large tdEVs for metastatic prostate, breast and colorectal patients, as identified by EpCAM enrichment and using cytokeratin immunofluorescent staining, ranges from 10 to 10³ tdEVs per mL and is strongly associated with poor clinical outcome.^{7,41-43} Similar outcomes have been reported for ovarian cancer, where the number of circulating tdEVs is suggested to be higher than in healthy controls and proportional to the cancer stage.^{11,44}

Because of the potential diagnostic and prognostic value of tdEVs and their relatively "easy access" via the circulation, there have been many efforts to isolate and characterize them. However, there are major technological and biological challenges. For example, the lack of standardized isolation and characterization methods for EVs, the low concentration of tdEVs compared to non-EV particles and other EVs in blood, and the heterogeneity of EVs in many aspects, including morphology,⁴⁵ size,⁴⁵⁻⁴⁷ membrane composition,^{41,47-50} and refractive index,^{51,52} complicate EV isolation, detection and enumeration. As tdEVs are outnumbered by EVs of other cellular origin and non-EV particles in blood, such as lipoprotein particles, in this thesis special focus is given to single particle analysis techniques, hence avoiding bulk analysis methods, whose inherent ensemble average precludes the identification of single particles.

In sum, utilization of tdEVs as cancer biomarker requires (1) the discrimination of EVs from non-EV particles, (2) the identification of the EVs cellular origin, and (3) the analysis of the EVs molecular content. This thesis is part of the efforts of a consortium of eight universities and 21 companies, who collaborate in the Dutch NWO Perspectief program *Cancer-ID*, aiming to develop and evaluate technology to detect tdEVs in blood as biomarker for cancer. Various techniques were developed or improved throughout the *Cancer-ID* program, including techniques that are commonly used in the EV field to validate samples, such as transmission electron microscopy (TEM) and flow cytometry (FCM). A brief description of the state-of-the-art is presented, including some of the techniques used within the *Cancer-ID* program.

1

1.4 Analysis techniques for single EV and non-EV particles

This section includes techniques assessed within the Cancer-ID program that can (1) detect single particles attached to a surface, such as atomic force microscopy (AFM), scanning electron microscopy (SEM) and transmission electron microscopy (TEM), and (2) detect single EVs in suspension, such as nanoparticle tracking analysis (NTA) and flow cytometry (FCM). Other technologies include immunomagnetic EpCAM (epithelial cell adhesion molecule) enrichment followed by fluorescence microscopic (FM) detection. Technologies that can measure either single or multiple particles attached to a substrate or in a suspension, such as Raman microscopy and hybrid AFM-SEM-Raman, will be further explained throughout the thesis.

1.4.1 Nanoparticle tracking analysis (NTA)

NTA measures the size distribution of particles between 50 to 1000 nm in diameter based on their Brownian motion. A laser illuminates particles in suspension, which consequently scatter light. The light scattered by the particles undergoing random motion is collected by a microscope objective and detected by an EMCCD camera (Figure 1.4). The random motion of the particles in the field of view is followed through a video sequence and the mean velocity of individual particles is computed and related to their size.⁵³

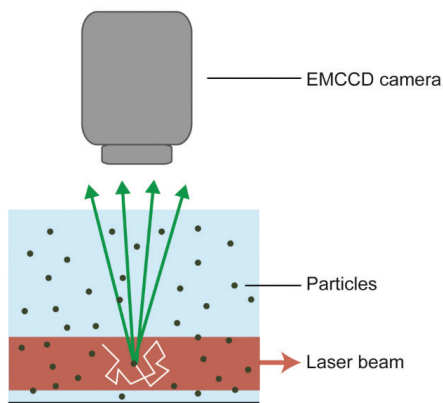


Figure 1.4. Schematic representation of the NTA setup.

1.4.2 Transmission electron microscopy (TEM)

TEM is considered a standard technique to confirm the presence of EVs in samples.⁵⁴ TEM transmits electrons through sufficiently thin (<100-200 nm for biological materials) samples to make images with nm resolution.⁵⁵ Particles from the sample are adhered to a carbon coated grid. Because EVs compete with other negatively charged particles for space on the grid, removal of soluble proteins and/or salts, for example by size exclusion chromatography (SEC)⁵⁶ and/or dilution, is required prior to incubation of the grid with EV samples. In addition, because TEM is performed in vacuum, EV samples are fixed with paraformaldehyde. After fixation and adhesion, the grid is placed on a droplet of contrast agent (uranyl acetate). A filter paper is used to remove the excess of contrast agent and the grid is dried at room temperature.⁵⁷

Next, the grid is exposed to an electron beam and images are generated based on the detected transmitted electrons (Figure 1.5). The contrast agent scatters electrons efficiently and stains the background more efficiently than the EVs. Consequently, EVs appear as bright particles on top of a dark background.

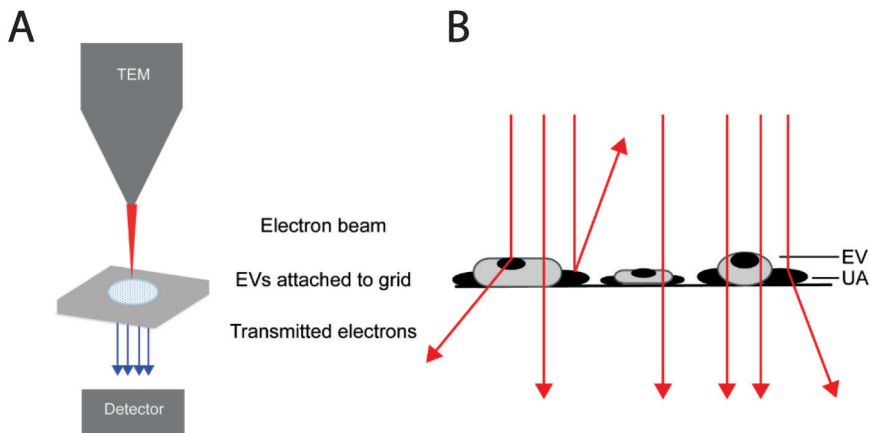


Figure 1.5. TEM of EV samples. Schematic representation of TEM imaging for EV samples. (A) The sample on a grid is exposed to an electron beam and images are constructed based on the detected transmitted electrons. (B) The uranyl acetate (UA) scatters electrons efficiently, which results in negative contrast. EVs and lipoprotein particles (LPs) have a low electron density and are seen as bright particles in a dark background.

1.4.3 Scanning Electron microscopy (SEM)

In SEM imaging, a focused beam of electrons scans the surface of a sample interacting with all atoms in the sample (Figure 1.6). Detection of the secondary electrons, originating from the outer layers of the sample, enables to visualize the topography of a sample. The amount of backscattered electrons, originating from the deeper layers of the sample, is associated with the atomic number of the atoms in the sample. EV samples can be fixed in paraformaldehyde, followed by gradual ethanol dehydration and chemical drying by using hexamethyldisilazane (HMDS). EVs are dehydrated and dried to maintain their morphological and surface features with minimal deformation in the vacuum chamber of the SEM.^{58,59} EV samples may be coated with gold to increase the image contrast and avoid surface charging. The sample must be placed on a conductive substrate during imaging.

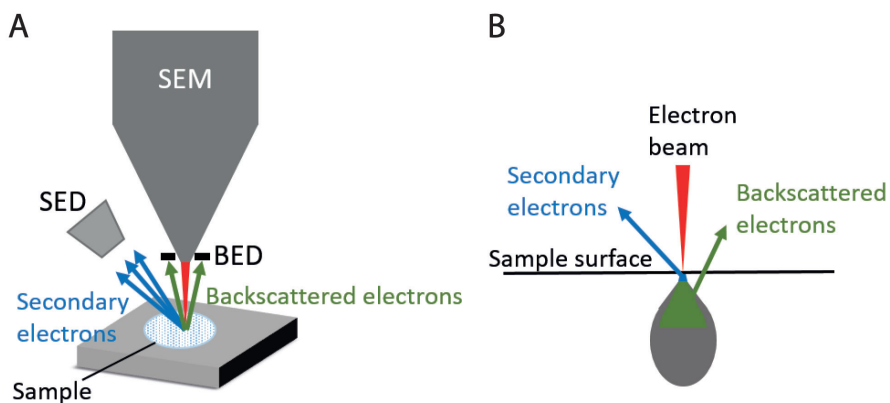


Figure 1.6. SEM of EV samples. (A) Schematic representation of a SEM setup. SED: secondary electron detector, BED: backscatter electron detector. (B) The sample is illuminated by the electron beam. Electrons interact with the sample at different depths, resulting in emitted electrons from the surface (secondary electrons) and from deeper layers (backscattered electrons).

1.4.4 Atomic force microscopy (AFM)

AFM is a very high resolution scanning probe microscopy useful for single particle analysis and topography imaging. Next to imaging, it is also possible to perform mechanical measurements with AFM.⁶⁰ During AFM imaging, a cantilever with a nm-sized tip probes the sample surface (Figure 1.7).⁶¹ Deflection of the cantilever is measured with a laser and photodiode. EVs can be added onto a poly-L-lysine coated coverslip and placed on the AFM.^{62–65} Acquired images can provide information about the topography of the sample surface. Mechanical properties can be obtained by applying a defined force perpendicular to the surface (indentation), providing force-indentation curves.

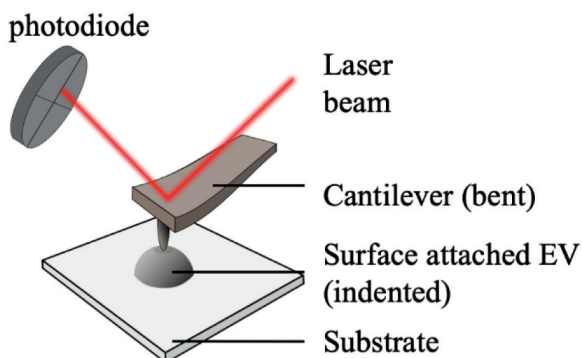


Figure 1.7. AFM EV samples. (A) Schematic representation of the AFM setup. In AFM, a cantilever interacts with the sample and the reflected laser beam is detected by a photodiode. The experiments are performed in liquid.

1.4.5 Flow cytometry (FCM)

In a flow cytometer, the sample is hydrodynamically focused with sheath fluid to intersect a laser beam (Figure 1.8A). Scattered light and fluorescence from the particle are collected by a forward scatter detector, a side scatter detector, and multiple fluorescence detectors (Figure 1.8B).⁶⁶ The measured scatter and fluorescent signals per particle can be represented and analyzed using scatter plots as shown in Figure S6.5. EV samples should be diluted in PBS to prevent swarm detection⁶⁷ and stained with fluorescently-labelled antibodies.

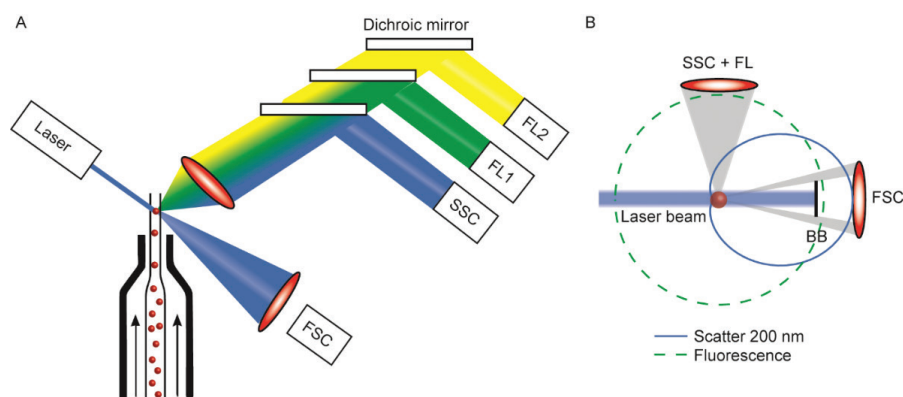


Figure 1.8. FCM of EV samples. (A) In FCM, a single particle in suspension is hydrodynamically focused with sheath fluid (arrows) to intersect a laser. Light coming from the particle is collected by a forward scatter detector (FSC), a side scatter detector (SSC), and multiple fluorescence detectors (FL1, FL2, etc.). (B) Fluorescence (green dashed line) is isotropic and can be used to determine antigen expression and cellular origin. Scatter (blue solid line) has an angular distribution that depends on the size and refractive index of the particle (here 200 nm polystyrene). Knowledge of the flow cytometer collection angles and Mie theory allows derivation of particle size and refractive index from the measured scatter signals.

1.4.6 Immunomagnetic EpCAM enrichment followed by fluorescence microscopic (FM) detection

It has been shown that CellSearch system can be used to enrich large tdEVs based on their EpCAM expression.⁴¹ Figure 1.9 indicates the flow: (1) blood is incubated with anti-EpCAM magnetic particles, which then bind to EpCAM-positive cells and EVs. (2) In the presence of a magnetic field, the magnetic particles coupled to the EpCAM-positive cells/EVs are separated from the rest of the blood. (3) EpCAM-enriched cells/EVs are fluorescently labelled. (4) The stained sample is loaded in a cartridge and placed between two magnets placed in such a way that all stained EpCAM-positive enriched particles homogeneously align on the glass slide on the surface of the cartridge. The cartridge is scanned using a fluorescence microscope (CellTracks Analyzer II). (5) The images are analyzed to identify tdEVs.

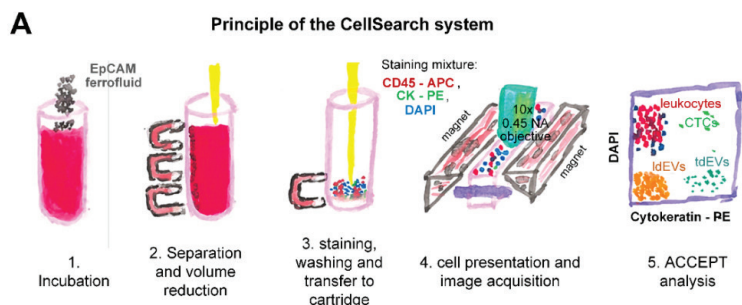


Figure 1.9. EpCAM immunomagnetic enrichment and FM detection of EV samples.

Besides FM and FCM, there are other methods that use fluorescence to detect and characterize EVs, such as stimulated emission depletion (STED) microscopy, fluorescence correlation spectroscopy and fluorescence NTA.⁵³

1.5 Thesis contents

Chapter 2 provides a theoretical background of the key principles behind the most used optical analytical technique in this thesis, namely Raman micro-spectroscopy. It explains Raman and Rayleigh scattering and the principle of optical trapping, which has been used to trap biological nanoparticles in suspension. The chapter ends with a brief literature overview about the use of Raman spectroscopy for EV characterization, current methods, findings and limitations.

Chapter 3 describes the implementation of correlative and integrated SEM and Raman micro-spectroscopy to cancer and non-cancer cells that enables their identification and characterization. The so-called SEM-Raman image cytometry is applied to non-labelled and non-metal coated cells as a first step before moving on to EVs, a much more challenging sample to work with. However, this is the first time such a method is applied to cells, so the developed sample preparation protocol and experimental design are presented. This chapter shows high resolution SEM images of cells correlated with their respective chemical fingerprint enabled by Raman spectroscopy. Here, Raman spectral features are used in principal component analysis (PCA) and hierarchical cluster analysis (HCA) to identify cells from different origins.

Chapter 4 brings SEM-Raman a step further to analyze individual EVs which are captured on antibody-functionalized stainless steel substrates. The downscaling challenges of going from cells (*chapter 3*) to EVs are solved by the development of a multi-modal platform for the specific capture of tdEVs and a proper workflow strategy. This chapter shows a multi-modal

analysis using SEM, Raman and AFM imaging to correlate size, morphology and chemical information at the single EV level. Based on Raman, it was possible to clearly distinguish tdEVs from contaminant particles, which differed in chemical composition.

Chapter 5 is the start of a series of chapters that move from detecting EVs on surfaces to doing it directly in suspension. This chapter presents a novel method for the detection and characterization of single EVs directly in suspension and in a label-free manner. The method is based on the synchronized detection of Rayleigh and Raman scattering from a single laser beam, which optically traps individual EVs. While Rayleigh scattering is used to detect when an individual particle is trapped, the synchronously acquired Raman spectrum labels each particle with chemical information. The method to trap and detect single particles is first validated with monodisperse polystyrene beads and then applied to tdEVs.

Chapter 6 shows the application of optical trapping and synchronized Rayleigh and Raman scattering (*chapter 5*) for the detection and characterization of single EVs and lipoprotein particles, which are a major component of blood plasma. The Raman spectra per particle type is shown and associated with relevant chemical information. By means of PCA on the Raman spectra of individual particles, we show that tdEVs can be distinguished from red blood cell-derived EVs and lipoprotein particles in a label-free manner and directly in suspension. Chapter 6 further addresses size determination of particles based on Rayleigh scattering.

Chapter 7 moves towards the analysis of single particles in the blood of cancer patients. This chapter presents a pilot study where optical trapping and synchronized Rayleigh and Raman scattering are used to interrogate plasma of metastasized castration-resistant prostate cancer patients and compare it to healthy controls at the individual particle level. PCA and HCA show a significant difference in terms of particle composition for some patients compared to healthy controls and these differences are discussed in an attempt to find the nature of the particles in cancer patients.

Chapter 8 discusses some findings related to chapters 3 and 4 about the interactions of organosilicon compounds with cell membranes.

Chapter 9 contains the general conclusion of this thesis, places this work into perspective and indicates recommendations for future research.

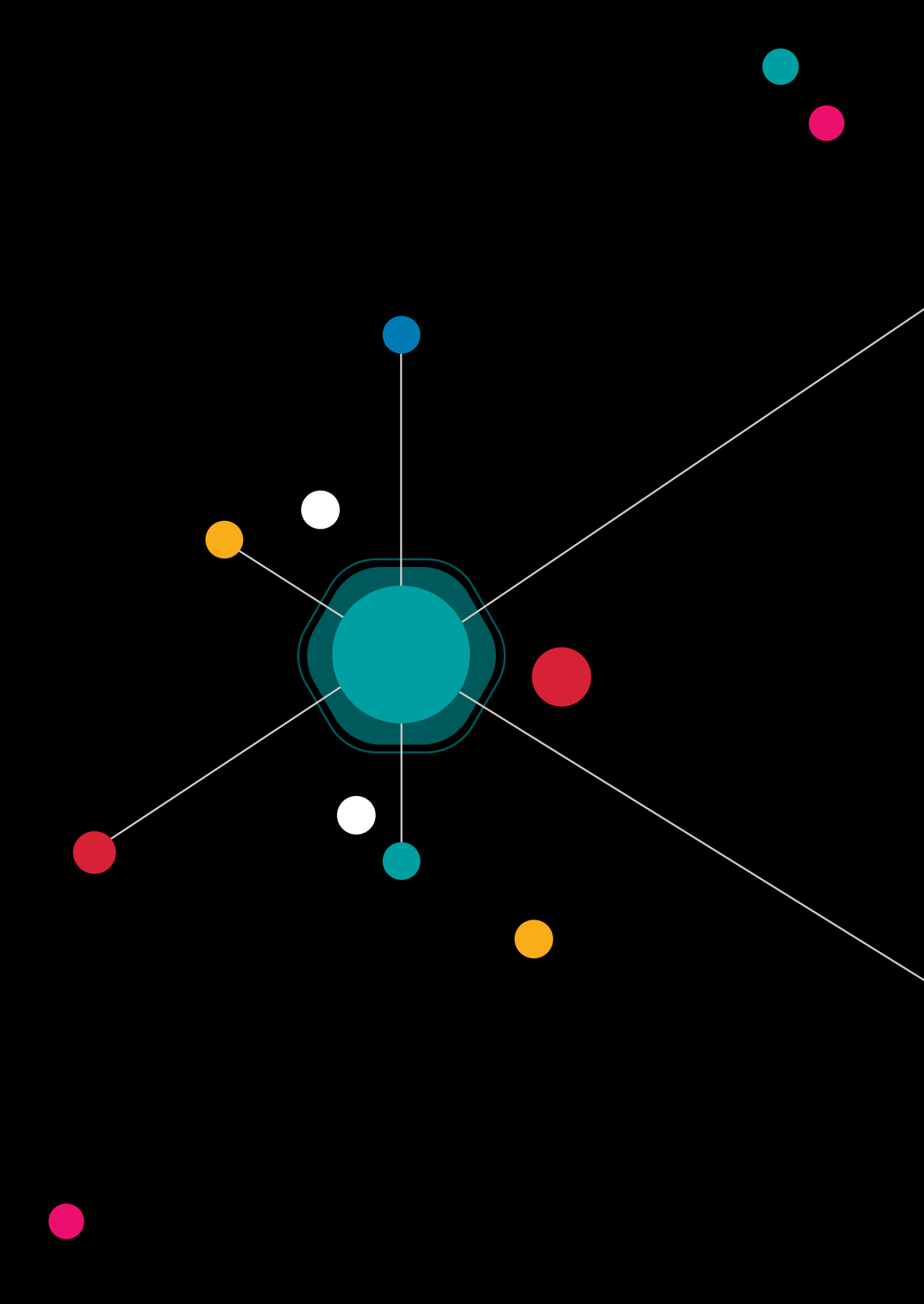
References

1. Global Cancer Observatory. International Agency for Research on Cancer; World Health Organization (2018). Available at: <http://gco.iarc.fr/>. (Accessed: 24th February 2020)
2. van der Pol, E., Böing, A. N., Harrison, P., Sturk, A. & Nieuwland, R. Classification, functions, and clinical relevance of extracellular vesicles. *Pharmacol. Rev.* 64, 676–705 (2012).
3. Colombo, M., Raposo, G. & Théry, C. Biogenesis, Secretion, and Intercellular Interactions of Exosomes and Other Extracellular Vesicles. *Annu. Rev. Cell Dev. Biol.* 30, 255–289 (2014).
4. Tkach, M. & Théry, C. Communication by Extracellular Vesicles: Where We Are and Where We Need to Go. *Cell* 164, 1226–1232 (2016).
5. Zwicker, J. I. et al. Tumor-derived tissue factor-bearing microparticles are associated with venous thromboembolic events in malignancy. *Clin. Cancer Res.* 15, 6830–40 (2009).
6. Li, J. et al. Claudin-containing exosomes in the peripheral circulation of women with ovarian cancer. *BMC Cancer* 9, 244 (2009).
7. Coumans, F. A. W., Doggen, C. J. M., Attard, G., de Bono, J. S. & Terstappen, L. W. M. M. All circulating EpCAM+CK+CD45- objects predict overall survival in castration-resistant prostate cancer. *Ann. Oncol. Off. J. Eur. Soc. Med. Oncol.* 21, 1851–7 (2010).
8. Arraud, N. et al. Extracellular vesicles from blood plasma: determination of their morphology, size, phenotype and concentration. *J. Thromb. Haemost.* 12, 614–627 (2014).
9. Théry, C., Zitvogel, L. & Amigorena, S. Exosomes: Composition, biogenesis and function. *Nature Reviews Immunology* 2, 569–579 (2002).
10. Kanada, M., Bachmann, M. H. & Contag, C. H. Signaling by Extracellular Vesicles Advances Cancer Hallmarks. *Trends in Cancer* 2, 84–94 (2016).
11. Shah, R., Patel, T. & Freedman, J. E. Circulating Extracellular Vesicles in Human Disease. *N. Engl. J. Med.* 379, 958–966 (2018).
12. Heijnen, H. F. G., Schiel, A. E., Fijnheer, R., Geuze, H. J. & Sixma, J. J. Activated platelets release two types of membrane vesicles: Microvesicles by surface shedding and exosomes derived from exocytosis of multivesicular bodies and α -granules. *Blood* 94, 3791–3799 (1999).
13. Dragovic, R. A. et al. Sizing and phenotyping of cellular vesicles using Nanoparticle Tracking Analysis. *Nanomedicine Nanotechnology, Biol. Med.* 7, 780–788 (2011).
14. Poon, I. K. H. et al. Unexpected link between an antibiotic, pannexin channels and apoptosis. *Nature* 507, 329–334 (2014).
15. Doyle, L. M. & Wang, M. Z. Overview of Extracellular Vesicles, Their Origin, Composition, Purpose, and Methods for Exosome Isolation and Analysis. *Cells* 8, 727 (2019).
16. Chargaff, E. & West, R. The biological significance of the thromboplastic protein of blood. *J. Biol. Chem.* 166, 189–197 (1946).
17. Wolf, P. The nature and significance of platelet products in human plasma. *Br. J. Haematol.* 13, 269–288 (1967).
18. Anderson, H. C. Vesicles associated with calcification in the matrix of epiphyseal cartilage. *J. Cell Biol.* 41, 59–72 (1969).

19. Dalton, A. J. Microvesicles and vesicles of multivesicular bodies versus 'virus like' particles. *J. Natl. Cancer Inst.* 54, 1137–1148 (1975).
20. Stegmayr, B. & Ronquist, G. Promotive effect on human sperm progressive motility by prostasomes. *Urol. Res.* 10, 253–257 (1982).
21. Ronquist, G. & Brody, I. The prostatic prostatic: its secretion and function in man. *BBA - Reviews on Biomembranes* 822, 203–218 (1985).
22. Crawford, N. The Presence of Contractile Proteins in Platelet Microparticles Isolated from Human and Animal Platelet-free Plasma. *Br. J. Haematol.* 21, 53–69 (1971).
23. Harding, C., Heuser, J. & Stahl, P. Receptor-mediated endocytosis of transferrin and recycling of the transferrin receptor in rat reticulocytes. *J. Cell Biol.* 97, 329–339 (1983).
24. Pan, B. T. & Johnstone, R. M. Fate of the transferrin receptor during maturation of sheep reticulocytes in vitro: Selective externalization of the receptor. *Cell* 33, 967–978 (1983).
25. Johnstone, R. M., Adam, M., Hammond, J. R., Orr, L. & Turbide, C. Vesicle formation during reticulocyte maturation. Association of plasma membrane activities with released vesicles (exosomes). *J. Biol. Chem.* 262, 9412–9420 (1987).
26. Atkin-Smith, G. K. et al. A novel mechanism of generating extracellular vesicles during apoptosis via a beads-on-a-string membrane structure. *Nat. Commun.* 6, 7439 (2015).
27. Morel, O., Jesel, L., Freyssinet, J. M. & Toti, F. Cellular mechanisms underlying the formation of circulating microparticles. *Arterioscler. Thromb. Vasc. Biol.* 31, 15–26 (2011).
28. Johnsen, K. B., Gudbergsson, J. M., Andresen, T. L. & Simonsen, J. B. What is the blood concentration of extracellular vesicles? Implications for the use of extracellular vesicles as blood-borne biomarkers of cancer. *Biochim Biophys Acta Rev Cancer* 1871, 109–116 (2019).
29. Berckmans, R. J. et al. Cell-derived microparticles circulate in healthy humans and support low grade thrombin generation. *Thromb. Haemost.* 85, 639–46 (2001).
30. Homesley, H. D. & Doellgast, G. J. Binding of Specific Peroxidase-labeled Antibody to Placental-type Phosphatase on Tumor-derived Membrane Fragments. *Cancer Res.* 40, 4064–4069 (1980).
31. Dvorak, H. F. et al. Tumor shedding and coagulation. *Science* (80-). 212, 923–924 (1981).
32. Lee, T. H. et al. Oncogenic ras-driven cancer cell vesiculation leads to emission of double-stranded DNA capable of interacting with target cells. *Biochem. Biophys. Res. Commun.* 451, 295–301 (2014).
33. Antonyak, M. A. et al. Cancer cell-derived microvesicles induce transformation by transferring tissue transglutaminase and fibronectin to recipient cells. *Proc. Natl. Acad. Sci. U. S. A.* 108, 4852–4857 (2011).
34. Jeppesen, D. K. et al. Quantitative proteomics of fractionated membrane and lumen exosome proteins from isogenic metastatic and nonmetastatic bladder cancer cells reveal differential expression of EMT factors. *Proteomics* 14, 699–712 (2014).
35. Zhou, W. et al. Cancer-Secreted miR-105 destroys vascular endothelial barriers to promote metastasis. *Cancer Cell* 25, 501–515 (2014).
36. Costa-Silva, B. et al. Pancreatic cancer exosomes initiate pre-metastatic niche formation in the liver. *Nat. Cell Biol.* 17, 816–826 (2015).
37. Al-Nedawi, K., Meehan, B., Kerbel, R. S., Allison, A. C. & Rak, A. Endothelial expression of autocrine VEGF upon the uptake of tumor-derived microvesicles containing oncogenic EGFR. *Proc. Natl. Acad. Sci. U. S. A.* 106, 3794–3799 (2009).

38. Muralidharan-Chari, V. et al. Microvesicle removal of anticancer drugs contributes to drug resistance in human pancreatic cancer cells. *Oncotarget* 7, 50365–50379 (2016).
39. Shedden, K., Xie, X. T., Chandaroy, P., Chang, Y. T. & Rosania, G. R. Expulsion of small molecules in vesicles shed by cancer cells: Association with gene expression and chemosensitivity profiles. *Cancer Res.* 63, 4331–4337 (2003).
40. Ciravolo, V. et al. Potential role of HER2-overexpressing exosomes in countering trastuzumab-based therapy. *J. Cell. Physiol.* 227, 658–667 (2012).
41. Nanou, A. et al. Circulating tumor cells, tumor-derived extracellular vesicles and plasma cytokeratins in castration-resistant prostate cancer patients. *Oncotarget* 9, 19283–19293 (2018).
42. Nanou, A. et al. Abstract 4464: Tumor-derived extracellular vesicles in blood of metastatic breast, colorectal, prostate, and non-small cell lung cancer patients associate with worse survival. in *AACR 2019 Proceedings: Abstract 4464 - American Association for Cancer Research 4464–4464* (2019). doi:10.1158/1538-7445.sabcs18-4464
43. Coumans, F., van Dalum, G. & Terstappen, L. L. W. M. M. L. W. M. M. CTC Technologies and Tools. *Cytom. A* 93, 1197–1201 (2018).
44. Taylor, D. D. & Gercel-Taylor, C. MicroRNA signatures of tumor-derived exosomes as diagnostic biomarkers of ovarian cancer. *Gynecol. Oncol.* 110, 13–21 (2008).
45. Rikkert, L. G., Nieuwland, R., Terstappen, L. W. M. M. & Coumans, F. A. W. Quality of extracellular vesicle images by transmission electron microscopy is operator and protocol dependent. *J Extracell Vesicles* 8, 1555419 (2019).
46. de Rond, L., Coumans, F. A. W. W., Nieuwland, R., van Leeuwen, T. G. & van der Pol, E. Deriving extracellular vesicle size from scatter intensities measured by flow cytometry. *Curr Protoc Cytom* 86, e43 (2018).
47. Beekman, P. et al. Immuno-capture of extracellular vesicles for individual multi-modal characterization using AFM, SEM and Raman spectroscopy. *Lab Chip* 19, 2526–2536 (2019).
48. Enciso-Martinez, A. et al. Synchronized Rayleigh and Raman scattering for the characterization of single optically trapped extracellular vesicles. *Nanomedicine Nanotechnology, Biol. Med.* 24, 102109 (2020).
49. Gool, E. L. et al. Surface Plasmon Resonance is an Analytically Sensitive Method for Antigen Profiling of Extracellular Vesicles. *Clin Chem* 63, 1633–1641 (2017).
50. De Rond, L. et al. Comparison of generic fluorescent markers for detection of extracellular vesicles by flow cytometry. *Clin. Chem.* 64, 680–689 (2018).
51. de Rond, L. et al. Refractive index to evaluate staining specificity of extracellular vesicles by flow cytometry. *J. Extracell. Vesicles* 8, 1643671 (2019).
52. van der Pol, E. et al. Absolute sizing and label-free identification of extracellular vesicles by flow cytometry. *Nanomedicine Nanotechnology, Biol. Med.* 14, 801–810 (2018).
53. Van Der Pol, E. et al. Optical and non-optical methods for detection and characterization of microparticles and exosomes. *J. Thromb. Haemost.* 8, 2596–2607 (2010).
54. Lötval, J. et al. Minimal experimental requirements for definition of extracellular vesicles and their functions: a position statement from the International Society for Extracellular Vesicles. *J. Extracell. Vesicles* 3, 10.3402/jev.v3.26913 (2014).
55. Pisitkun, T., Shen, R. F. & Knepper, M. A. Identification and proteomic profiling of exosomes in human urine. *Proc Natl Acad Sci U S A* 101, 13368–13373 (2004).

56. Böing, A. N. et al. Single-step isolation of extracellular vesicles by size-exclusion chromatography. *J. Extracell. Vesicles* 3, 10.3402/jev.v3.23430 (2014).
57. Keerthikumar, S. et al. Proteogenomic analysis reveals exosomes are more oncogenic than ectosomes. *Oncotarget* 6, 15375–15396 (2015).
58. Enciso-Martinez, A., Timmermans, F. J., Nanou, A., Terstappen, L. W. M. M. & Otto, C. SEM–Raman image cytometry of cells. *Analyst* 143, 4495–4502 (2018).
59. Nanou, A. et al. Scanning Electron Microscopy of Circulating Tumor Cells and Tumor-Derived Extracellular Vesicles. *Cancers (Basel)* 10, 416 (2018).
60. Krieg, M. et al. Atomic force microscopy-based mechanobiology. *Nat. Rev. Phys.* 1, 41–57 (2019).
61. Piontek, M. C. & Roos, W. H. Atomic Force Microscopy: An Introduction. *Methods Mol Biol* 1665, 243–258 (2018).
62. Vorselen, D., MacKintosh, F. C., Roos, W. H. & Wuite, G. J. Competition between Bending and Internal Pressure Governs the Mechanics of Fluid Nanovesicles. *ACS Nano* 11, 2628–2636 (2017).
63. Vorselen, D. et al. The fluid membrane determines mechanics of erythrocyte extracellular vesicles and is softened in hereditary spherocytosis. *Nat Commun* 9, 4960 (2018).
64. Sorkin, R. et al. Nanomechanics of Extracellular Vesicles Reveals Vesiculation Pathways. *Small* 14, e1801650 (2018).
65. Vorselen, D. et al. Multilamellar nanovesicles show distinct mechanical properties depending on their degree of lamellarity. *Nanoscale* 10, 5318–5324 (2018).
66. Brown, M. & Wittwer, C. Flow cytometry: Principles and clinical applications in hematology. *Clin. Chem.* 46, 1221–1229 (2000).
67. Van Der Pol, E., van Gemert, M. J. C., Sturk, A., Nieuwland, R. & Van Leeuwen, T. G. Single vs. swarm detection of microparticles and exosomes by flow cytometry. *J Thromb Haemost* 10, 919–930 (2012).



The image features a black background with several abstract elements. At the top, a white circle is connected to the left edge by a thin white line. Below it is a smaller yellow circle. In the center, the text 'Chapter 2' is written in a bold, white, sans-serif font, with 'Optical analytical techniques' in a smaller, regular font below it. On the right side, there is a blue circle above a larger white circle. On the left side, there is a white circle above a red circle. At the bottom left, a pink circle is connected to the left edge by a thin white line. At the bottom center, there is a red circle.

Chapter 2

Optical analytical techniques

2.1 Introduction

When light interacts with matter, different phenomena may occur (Figure 2.1). Depending on the material, light can be absorbed, reflected, scattered or transmitted. These interactions occur in varying proportions and the sum of absorbed (I_a), reflected (I_r), scattered (I_s) and transmitted light (I_t) equals the total amount of incident energy (I_0):

$$I_0 = I_a + I_r + I_s + I_t \quad (2.1)$$

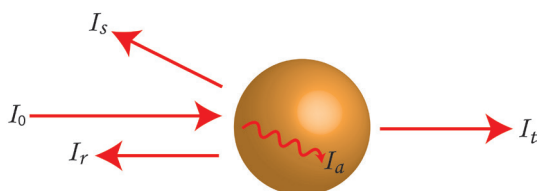


Figure 2.1. Light-matter interaction. Detectors may be positioned accordingly to detect the portion of light of interest.

The study of the interaction between electromagnetic radiation and matter is called spectroscopy and the type of electromagnetic radiation used gives rise to different spectroscopy techniques. Of particular interest are the processes of light absorption and scattering, because the study of these interactions yields for example molecular information about the material being impinged by the light. Each atom in a molecular system has a positive nucleus surrounded by a cloud of negatively charged electrons, which form chemical bonds with neighboring atoms. When light interacts with a molecule, the electric field of the incident light wave sets the electric charges of the molecule to oscillate. The oscillating charges emit light in all directions except for the direction of its oscillation. Most of the scattered light will have the same frequency as the incident light, which is referred to as *elastic* or *Rayleigh scattering*, while significantly less light will be scattered with a different frequency, the so-called *Raman scattering* (Figure 2.2).

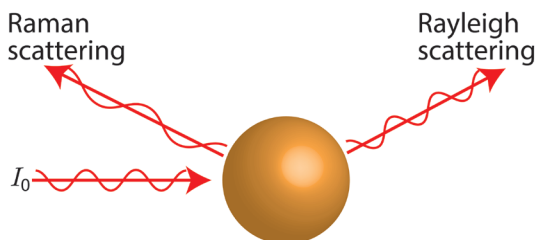


Figure 2.2. Rayleigh and Raman scattering.

2.2 Raman and Rayleigh scattering

The inelastic scattering had been predicted in 1923 by Adolf Smekal¹ and in 1928, the Raman effect was visualized by Sir C. V. Raman and K.S. Krishnan. They observed that some scattered light by liquids had a different color than the incident light, hence a wavelength shift.² The discovery of the Raman effect earned Raman the Nobel prize in physics in 1930. The Raman effect arises from the interactions between the electrons in a molecule and the electric field of the electromagnetic radiation. This interaction changes the polarizability of a molecule inducing a temporary dipole moment. The polarizability changes due to the incident oscillating electric field may be seen as shape changes in the electron clouds surrounding a molecule. The incident oscillating electric field distorts and transmit energy to the electron cloud, thereby generating an induced dipole moment in the molecule. This dipole moment oscillates with the frequency of the incident electric field of the electromagnetic radiation. Hence, it emits light whose intensity is proportional to the fourth power of the incident frequency ν_0 .³

$$I = \frac{2^5 \pi^4 \nu_0^4}{3 \epsilon_0 c^3} |\alpha|^2 I_0 \quad (2.2)$$

where ν_0 is the incident frequency, c the speed of light, α the polarizability and I_0 the intensity of the incident light. The molecular polarizability α is defined as the ability of a molecule to form a dipole when placed in an external electric field \vec{E} . The electric field vector \vec{E} of the incident electromagnetic radiation is expressed in scalar notation as:

$$E = E_0 \cos(2\pi\nu_0 t) \quad (2.3)$$

The induced dipole moment is defined as:

$$P = \alpha E = \alpha E_0 \cos(2\pi\nu_0 t) \quad (2.4)$$

A molecule exhibits vibrational modes, which contribute to the polarizability of the molecule, or in other words, the polarizability of a molecule can be modulated by a molecular vibration. Therefore, the induced dipole moment \vec{P} and the amplitude of the emitted light are modulated by the frequency of the molecular vibration. The polarizability of a molecule modulated by the molecular vibrations gives Raman spectroscopy its molecular specificity. The polarizability of a normal vibrational mode of frequency ν_k can be expressed in form of periodic motion:^{4,5}

$$\alpha_k = \alpha_0 + \left(\frac{\partial \alpha}{\partial q_k} \right)_0 q_k^0 \cos(2\pi\nu_k t + \varphi) \quad (2.5)$$

where α_0 is independent of the vibrational modes, $\partial\alpha/\partial q_k$ represents the change in polarizability α during a vibrational motion, q_k^0 represents the normal coordinate and φ is the phase of the vibrational oscillation, which is random for each molecule and gives rise to the incoherent nature of spontaneous Raman scattering. Multiple vibrational modes R can then be written as a sum of contributions of vibrational modes:

$$\alpha = \alpha_0 + \sum_k \left(\frac{\partial\alpha}{\partial q_k} \right)_0 q_k^0 \cos(2\pi\nu_k t) \quad (2.6)$$

Introducing equation (2.6) into (2.4), the expression for the induced dipole moment changes becomes:

$$P = \left(\alpha_0 + \sum_k \left(\frac{\partial\alpha}{\partial q_k} \right)_0 q_k^0 \cos(2\pi\nu_k t) \right) E_0 \cos(2\pi\nu_0 t)$$

$$P = \alpha_0 E_0 \cos(2\pi\nu_0 t) + \frac{1}{2} \sum_k \left(\frac{\partial\alpha}{\partial q_k} \right)_0 q_k^0 E_0 [\cos(2\pi(\nu_0 + \nu_k)t) + \cos(2\pi(\nu_0 - \nu_k)t)] \quad (2.7)$$

Equation 2.7 illustrates that the induced dipole moment oscillates not only with the incident frequency ν_0 , but also with frequencies $\nu_0 + \nu_k$ and $\nu_0 - \nu_k$. Hence, one frequency component of the emitted electromagnetic radiation by the molecule is equal to the frequency of the incident radiation ν_0 referred to as *elastic* or *Rayleigh scattering*. The frequency components $\nu_0 + \nu_k$ and $\nu_0 - \nu_k$ are the anti-Stokes and Stokes *Raman scattering*, respectively. Hence, the Raman bands are located symmetrically on both sides of the Rayleigh band of frequency ν_0 .

The classical description of the Raman effect can be complemented by a quantum-mechanical description, as shown in [Figure 2.3A](#) and [2.3B](#). When photons of energy $h\nu_0$ interact with a molecule with discrete energy levels, elastic collisions scatter photons of energy $h\nu_0$ (Rayleigh scattering) and inelastic collisions scatter photons of energies smaller for Stokes Raman scattering. It is higher for anti-Stokes Raman scattering. Rayleigh scattering of quanta with energy $h\nu_0$ has a higher probability than Raman scattering, during which vibrational energy is exchanged. Stokes scattering occurs when molecules in the vibrational ground state ($\nu_k = 0$) transit to a vibrational state of higher energy and photons with energy $h\nu^- = h\nu_0 - h\nu_k$ are emitted. In an anti-Stokes scattering process a transition from a vibrational excited state to a lower energy state occurs and photons are emitted with energy $h\nu^+ = h\nu_0 + h\nu_k$.⁴ Since the occupancy of states follows a Boltzmann distribution, most molecules are in their vibrational ground state at room temperature and the Stokes Raman process has a higher probability than the anti-Stokes Raman process. Therefore, in spontaneous Raman spectroscopy and imaging, the Stokes Raman spectrum is mostly used.

In Raman spectroscopy, the induced dipole moment and amplitude of the emitted radiations are modulated by the frequency of the molecular vibration. Because of the oscillating charges, the molecule behaves like an antenna that emits light with different frequency components. The light can be analyzed with a spectrometer and will result in the so-called Raman spectrum. An example of a Raman spectrum for the polyatomic molecule toluene is shown in (Figure 2.3C). A central band is visible (Rayleigh scattering of ν_0) as well as side bands of lower frequency (Stokes Raman scattering) that are specific to the molecule toluene. Raman spectrometers typically consist of an excitation laser that is focused on a sample with an optical objective. The Raman scattered light can be collected by the optical objective and dispersed in a spectrometer to finally reach the detector, which can be a charge coupled device (CCD) camera. By coupling the Raman spectrometer with a standard confocal microscope, the resolution can be significantly improved to a small focal depth. Confocal Raman spectroscopy measures a Raman spectrum per scanning point, which enables to image or map samples.⁶

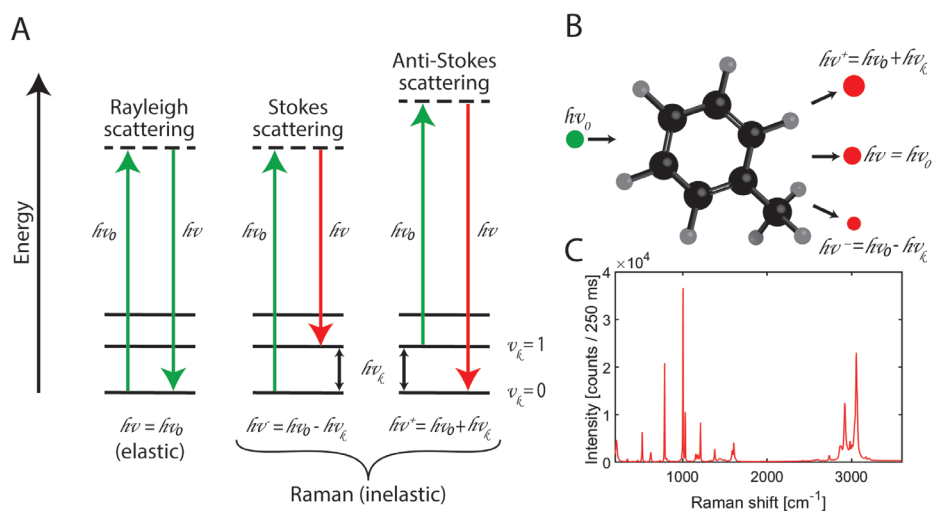


Figure 2.3. (A) Jablonski diagrams for Rayleigh, Stokes Raman and anti-Stokes Raman scattering. (B) Photons (green) with energy $h\nu_0$ hit the molecule toluene (C_7H_8), thereby scattering photons of energies $h\nu = h\nu_0$ (Rayleigh scattering), $h\nu^+ = h\nu_0 + h\nu_k$ (anti-Stokes Raman) and $h\nu^- = h\nu_0 - h\nu_k$ (Stokes Raman). (C) Stokes Raman spectrum of liquid toluene.

Electromagnetic radiation can be characterized by wavelength λ (cm) and wavenumber $\bar{\nu}$ (cm^{-1}):

$$\bar{\nu} = \frac{1}{\lambda} = \frac{\nu}{c} \quad (2.8)$$

Where c is the speed of light in centimeters per second, ν the frequency in cycles per second and λ the wavelength in centimeters.³ Since the Raman scattered light is frequency shifted with respect to the excitation wavelength, it is customary to write the relative wavenumbers as:

$$\bar{\nu}_{rel} = \frac{1}{\nu_0} - \frac{1}{\nu} \quad \bar{\nu}_{rel}[cm^{-1}] = \frac{10^7}{\nu_0[in\ nm]} - \frac{10^7}{\nu[in\ nm]} \quad (2.9)$$

Here, the exciting light and Rayleigh scattering have a shift of zero wavenumbers (0 cm^{-1}) and the Raman frequency components are shifted with respect to the Rayleigh band.⁴

The total Raman scattering intensity I_{Raman} depends on the Raman scattering cross section σ , the intensity of the excitation source I_0 and the number of molecules N in the measurement volume:

$$I_{Raman} = \sigma I_0 N \quad (2.10)$$

The Raman scattering cross section is different for each vibration in a molecule.

2.3 Confocal Raman micro-spectroscopy and resolution

Confocal microscopy has the advantage of spatially resolving features deep within transparent layers, such as coverslips, by simply focusing the laser beam to a diffraction-limited spot on the sample. Hence, a laser beam can be tightly focused in a voxel by an objective with numerical aperture $NA = \sin \theta$ (Figure 2.4). The diffraction limited focus, calculated for a plane wave and an objective with numerical aperture NA , gives rise to a minimum radius r_0 and a depth of field, which is two times the Rayleigh length Z_r , and based on the Rayleigh criterion:⁷

$$r_0 = \frac{0.61\lambda_0}{NA} \quad (2.11)$$

$$Z_r = \frac{2\lambda_0}{NA^2} \quad (2.12)$$

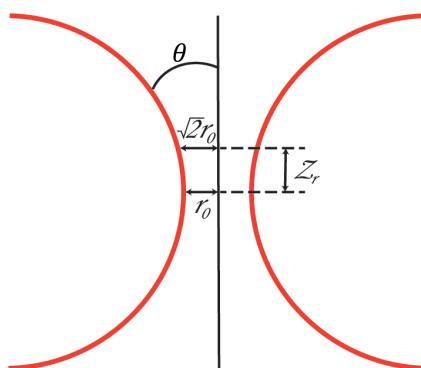


Figure 2.4. Beam profile in the focal spot.

Thus, for a home-built Raman microscope that uses a wavelength of 647.08 nm and an objective with a NA of 0.95, the minimum radius r_0 is 415 nm and the Rayleigh length Z_r is 1434 nm.

The depth resolution can further be increased by blocking part of the light that reaches the detector with a small aperture or pinhole. This suppresses out of focus light which helps in removing background contributions from the collected scattered light, thus enabling three-dimensional (3D) imaging. Hence, Raman spectra at different depths within the sample can be acquired by either moving the stage or the objective.

2.4 Optical trapping

The first observations that light can exert a force on a particle was made by Johannes Kepler in the seventeenth century, who explained that the tail of a comet points away from the sun due to radiation pressure.^{8,9} When light hits a particle in a medium of different refractive index, the light is reflected, refracted (or both). As light carries momentum, the deviation of light from its original path implies a change in momentum of the light. Hence, by conservation of momentum, the particle acquires a momentum that ultimately results in a net force on the particle that will accelerate it. This is the principle on how optical trapping of small particles works. Its discovery and technological application was made by Arthur Ashkin and earned him in 2018 the Nobel Prize in Physics.

In 1970, Ashkin showed that micrometer particles in suspension could be accelerated and trapped by forces of radiation pressure using laser light.¹⁰ Two basic optical forces are responsible for the acceleration and trapping of particles: a scattering force in the direction of the incident laser beam, and a gradient force in the direction of the intensity gradient of the beam.¹¹

Ray optics are used in [Figure 2.5](#) to indicate the optical forces arising from the interaction of a laser beam and a particle in the so-called Mie regime, where the diameter is large compared to wavelength of laser (λ_0). The particle, e.g. a polystyrene bead suspended in water, is located off axis in the lateral plane in the presence of a mildly focused Gaussian beam. For simplicity, only two rays of light are considered, i.e. "a" and "b", and surface reflections are neglected. When the rays "a" and "b" hit the particle, they will be refracted, resulting in forces F_a and F_b . Because of the Gaussian beam, the intensity of ray "a" is higher than ray "b", giving rise to a larger force F_a compared to force F_b . This results in a net force F_{net} that pushes the particle towards the center of the beam in the lateral plane and away from the incident beam. F_{net} can be decomposed in two force components. The first force component is known as the gradient force F_{grad} , which results from the gradient in light intensity and points towards the region of the beam with the highest intensity. The second force component is called the scattering force F_{scat} , which points in the direction of the incident light. Hence, when the particle is located in the center of the beam in the lateral plane, the net force becomes the scattering force F_{scat} .^{10,11}

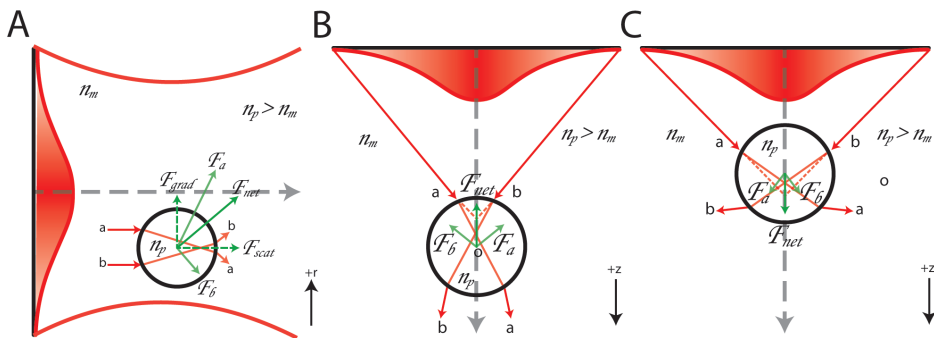


Figure 2.5. Optical forces using Ray optics for particles in the Mie regime with refractive index larger than the refractive index of the medium $n_p > n_m$. (A) Spherical particle in a mildly focused beam experiencing a gradient force F_{grad} toward $+r$ and a scattering force F_{scat} in the direction of the incident beam. By strongly focusing the laser beam, axial stability is achieved by a net force F_{net} that moves the particle towards the laser focus, either to $-z$ if the particle is below the focus (B) or to $+z$ if the particle is above the focus (C). Adapted from [11,12].

In the configuration of [Figure 2.5A](#), the particle is only trapped in the center of the beam axis but accelerated in the direction of the incident light. To achieve stable trapping in three dimensions, Ashkin used a strongly focused beam. The technique of trapping and manipulating particles with a strongly focused laser beam is also known as "optical tweezers".

Ray optics are useful to estimate the optical forces acting on particles in the Mie regime ($d \gg \lambda_0$), but for particles in the so-called Rayleigh regime, where the diameter d is much smaller than λ_0 ($d \leq 0.2\lambda_0$),¹³ wave optics approximations are used. The particles are then treated as point

dipoles that interact with an electromagnetic field. This results in a scattering force F_{scat} in the direction of the incident beam.¹³

$$F_{scat} = \frac{I_0}{c} \frac{128\pi^5 r^6}{3\lambda_0^4} \left(\frac{m^2 - 1}{m^2 + 2} \right)^2 n_m \quad (2.13)$$

where I_0 is the intensity of the laser, n_m is the refractive index of the medium and m is the effective refractive index (n_p/n_m). The gradient force F_{grad} for a particle of polarizability α is in the direction of the intensity gradient and is defined as:¹³

$$F_{grad} = -\frac{n_m}{2} \alpha \nabla E^2 = -\frac{n_m^3 r^3}{2} \left(\frac{m^2 - 1}{m^2 + 2} \right) \nabla E^2 \quad (2.14)$$

A necessary condition for stable trapping in the Rayleigh and Mie regime is that $F_{grad}/F_{scat} \geq 1$. This must be refined when other forces like those from Brownian motion and gravity are involved.

In this thesis, a strongly focused monochromatic laser beam will be used to optically trap particles and generate Rayleigh and Raman light scattering. The uniqueness of this approach opens up numerous clinical relevant applications by probing particles suspended in body fluids. The term “optical trapping” is used in this thesis because particles are only trapped but not manipulated.

2.5 Raman spectroscopy and EVs

Raman spectroscopy has been used for single and bulk compositional analysis of biological nanoparticles, such as EVs. This technique has enabled the acquisition of chemical fingerprints of particles without the need of markers such as antibody labels. For example, liposomes and phospholipid vesicles have been characterized by Raman spectroscopy.^{14–18} Lavielle et al. showed one of the first Raman spectra of bulk measurements of EVs derived from *Dictyostelium* cells.¹⁹ Bulk Raman measurements have been also performed by Lee et al., who obtained Raman signatures of EV clusters derived from prostate cancer cell lines and plasma.²⁰ Similarly, Gualerzi et al. have applied Raman spectroscopy for bulk characterization of EVs from stem and stromal cells, with their method involving air-drying of EV-containing drops.^{21,22} Tatischeff et al. studied EVs from *Dictyostelium discoideum* cells and from human urine by bulk optical trapping and Raman spectroscopy of small numbers of EVs (2–10).²³ The authors found EV subtypes that differed in nucleic acid, carotenoid and lipid content depending on cell growth and starvation conditions. They also showed spectral differences between EV samples deriving from different urine donors, suggesting individual variability and potential diagnostic value. Smith et al. trapped EVs from cancerous and non-cancerous cell lines, and by using

Raman spectroscopy followed by principal component analysis (PCA), they suggested that EV subpopulations are shared among cell lines.²⁴ In their study, the hypothesized single particle trapping was ensured by diluting the EV-containing samples. Carney et al. coupled Raman and fluorescence measurements of EVs to study the chemical composition of CD9⁺ EVs.²⁵ Penders et al. have identified single particles based on intensity values of characteristic Raman peaks passing over a threshold. Such threshold is selected based on the spectrum of an initial particle being trapped.¹⁶ Similarly, Kruglik et al. characterized liposomes and EVs from human urine and rat hepatocytes with Raman spectroscopy. Continuous acquisition of Raman spectra enabled the detection of single particles by the integration of the Raman spectra.²⁶ **Table 2.1** shows major Raman bands observed in EVs and their biomolecule assignments.

Table 2.1. Major Raman spectral bands observed in EVs and their biomolecule assignments

Raman shift [cm ⁻¹]	Assignment	Reference number
700/2	Cholesterol	[20, 23, 25]
710-713	Phospholipids	[21]
717	Phospholipids	[25]
718	Nucleic acids	[20]
720-820	Nucleic acids	[20]
725-751	Nucleic acids	[25]
748	Nucleic acids	[20]
752-760	Proteins (Trp)	[20, 25]
782/3	Nucleic acids	[18, 20, 22]
782-788	Nucleic acids	[25]
785/8	Nucleic acids (phosphate backbone)	[20, 21]
810-836	Nucleic acids	[25]
820-900	Phospholipids	[25]
828-837	Proteins	[25]
840	Saccharides/amines	[23]
	Proteins	[24]
853	Proteins (proline/hydroxyproline)	[20]
855	Proteins (Tyr)	[18, 21, 25]
878-880	Proteins	[25]
882	Proteins	[23, 24]
898	Nucleic acids	[24]
920	Proteins (proline/hydroxyproline)	[20]
928/30-940/60	Proteins	[21, 25]
1000/2/4/3/5	Proteins (Phe)	[18, 20, 21, 22, 24, 25]
1012	Proteins (Trp)	[25]
1032	Proteins (Phe)	[25]
1050-1160	Proteins and lipids	[25]

Table 2.1. (continued)

Raman shift [cm ⁻¹]	Assignment	Reference number
1053-1055	Proteins and lipids	[21]
1060	NA (phosphate backbone)	[20]
1063/65/66	Lipids	[18, 21, 23]
1085	Lipids	[18]
1090-1100	Nucleic acids	[25]
1094/95	Nucleic acids	[18, 24]
1125	Lipids	[18]
1127-1130	Proteins and phospholipids	[21]
1128	Nucleic acids	[24]
1130	Cholesterol	[20]
1150	Cholesterol	[24]
1155-1160	Carotenoids	[25]
1175-1177	Proteins (Tyr)	[25]
1200-1260	Nucleic acids	[25]
1200-1300	Amide III	[21]
1206	Proteins (proline/hydroxyproline)	[20]
1207-1210	Proteins (Phe, Tyr)	[25]
1208	Proteins (Trp)	[20]
1230-1305	Proteins (Amide III)	[25]
1240-1280	Proteins	[24]
1257	Proteins (Amide III)	[18]
1230-1305	Proteins (Amide III)	[25]
1265	Lipids	[24]
1260-1270	Lipids	[25]
1296/98	Lipids	[18, 19, 23]
1300	Lipids	[24]
1295-1305	Lipids	[25]
1330-1380	Nucleic acids	[25]
1339	Proteins	[18, 25]
1360/61	Proteins (Trp)	[20, 25]
1420	Nucleic acids	[24]
1440/1	Lipids and proteins	[18, 19]
1440/2	Cholesterol	[20, 24]
1445	Lipids	[24, 25]
1450	Proteins and lipids	[18, 20, 21, 22, 23, 25]
1455	Proteins	[24, 25]
1455-1457	Nucleic acids	[21, 25]
1490	Nucleic acids	[24, 25]
1515-1540	Carotenoids	[22, 25]

Table 2.1. (continued)

Raman shift [cm ⁻¹]	Assignment	Reference number
1550-1555	Proteins (Trp)	[20, 25]
1575	Nucleic acids	[18]
1570-1580	Nucleic acids	[24, 25]
1600-1690	Proteins (Amide I)	[21]
1603-1607	Proteins (Phe)	[19, 21, 25]
1615-1617	Proteins	[21, 25]
1619-1621	Proteins (Trp)	[25]
1640-1700	Proteins (Amide I)	[25]
1650/1	Lipids	[19, 23]
1650-1670	Lipids	[25]
1656	Proteins (Amide I)	[18]
	Lipids	[24]
1668	Amide I/Cholesteryl ester	[23]
1670-1690	Nucleic acids	[25]
1680	Proteins/cholesterol	[24]
1728	Lipids	[21]
1720-1750	Lipids	[25]
2600-3200	Lipids	[20]
2847	Lipids	[19]
2876	Lipids	[19]
2883	Lipids and proteins	[21]
2932	Proteins	[19]
2937-2940	Lipids and proteins	[21]
2940	Proteins	[20]

Phe: phenylalanine; Tyr: tyrosine; Trp: tryptophan.

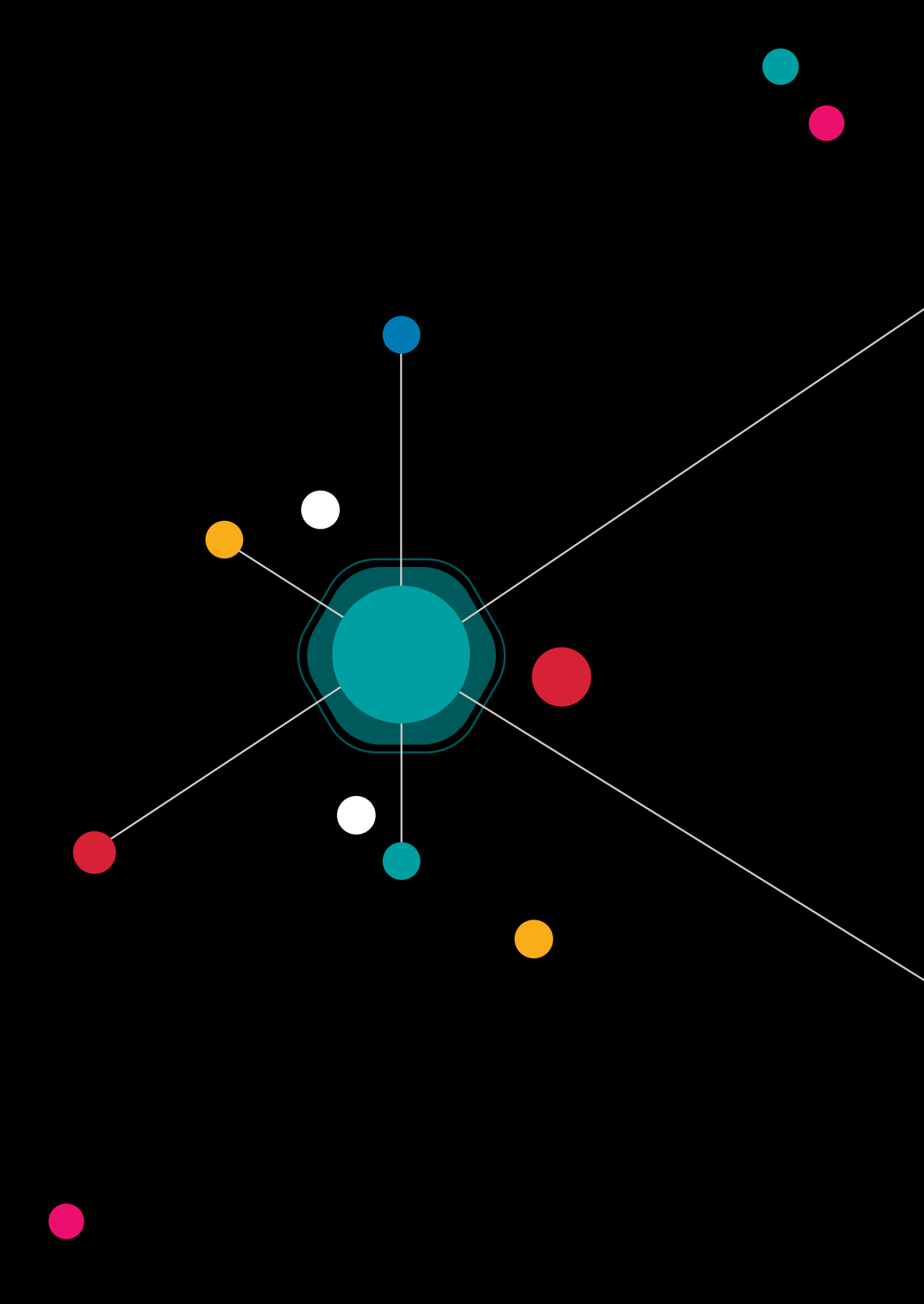
Surface-enhanced Raman spectroscopy (SERS) is another approach that has been used to detect and chemically characterize biological nanoparticles.²⁷⁻³⁶ The popularity of this technique relies on the enhanced Raman scattering compared to non-resonant Raman. There are two common approaches to perform SERS. The first approach enhances the Raman signal of molecules that make up the biological particles. For instance, surfaces with metal nanostructures or metal nanoparticles targeting EVs will enhance the molecules in close proximity (in the order of nanometers) of the plasmonic nanoparticle.²⁷⁻²⁹ A second SERS approach uses nanoprobes conjugated with molecules that target biological nanoparticles. For example, EVs may be labelled with plasmonic nanoparticles that are functionalized with antibodies and Raman reporters.^{35,36} Hence, similar to immuno-fluorescent staining, molecular specificity is achieved by antibody labelling and detection of the specific binding is much facilitated by the high intensity Raman signals of the Raman reporters.

One of the many challenges identified from the literature is the detection and characterization of individual biological nanoparticles. For techniques using optical trapping, sample dilution may avoid the trapping of multiple particles,²⁴ but long measurements are then required, decreasing the throughput of the technique. In addition, several studies using optical trapping have detected single particles on the basis of visible increases in the Raman spectrum. Nevertheless, small EVs have very low Raman signal, which can be overwhelmed by the water signal. This can hinder the detection of single particles with very low amount of material. Nonetheless, the efforts in the field of Raman spectroscopy for the detection and characterization of biological nanoparticles have evolved towards single particle analysis methods. The detection of single particles becomes more important when trying to identify rare EV populations, such as tdEVs, from other non-tumor EVs and non-EV particles. Therefore, to develop methods and study biological nanoparticles we aim, in the following chapters, at single particle detection and characterization.

References

1. Smekal, A. Zur Quantentheorie der Dispersion. *Naturwissenschaften* 11, 873–875 (1923).
2. Raman, C. V. & Krishnan, K. S. A new type of secondary radiation [11]. *Nature* 121, 501–502 (1928).
3. Urban, M. W. *Vibrational spectroscopy of molecules and macromolecules on surfaces*. (Wiley, 1993).
4. Schrader, B. The Raman spectrum. in *Infrared and Raman Spectroscopy: Methods and Applications* (ed. Schrader, B.) 18–26 (Wiley-VCH Verlag GmbH, 1995). doi:10.1002/9783527615438
5. Long, D. A. Classical Theory of Rayleigh and Raman Scattering. in *The Raman Effect* 31–48 (John Wiley & Sons, Ltd, 2003). doi:10.1002/0470845767.ch3
6. Smith, R., Wright, K. L. & Ashton, L. Raman spectroscopy: An evolving technique for live cell studies. *Analyst* 141, 3590–3600 (2016).
7. Overall, N. J. Confocal Raman microscopy: Performance, pitfalls, and best practice. *Appl. Spectrosc.* 63, (2009).
8. Nieminen, T. A., Knöner, G., Heckenberg, N. R. & Rubinsztein-Dunlop, H. Physics of Optical Tweezers. *Methods in Cell Biology* 82, 207–236 (2007).
9. Kepler, J. *De Cometis libelli tres... Autore Iohanne Keplero...* (Carmen J. Tanckii). (Typis Andreae Apergeri, 1619).
10. Ashkin, A. Acceleration and Trapping of Particles by Radiation Pressure. *Phys. Rev. Lett.* 24, 156–159 (1970).
11. Ashkin, A. History of optical trapping and manipulation of small neutral particles, atoms, and molecules. *IEEE J. Sel. Top. Quantum Electron.* 6, 841–856 (2000).
12. Ashkin, A. Optical trapping and manipulation of neutral particles using lasers. *Proc. Natl. Acad. Sci.* 94, 4853–4860 (1997).
13. Ashkin, A., Dziedzic, J. M. & Chu, S. Observation of a single-beam gradient force optical trap for dielectric particles. *Opt. Lett.* 11, 288–290 (1986).
14. Cherney, D. P., Conboy, J. C. & Harris, J. M. Optical-Trapping Raman Microscopy Detection of Single Unilamellar Lipid Vesicles. *Anal. Chem.* 75, 6621–6628 (2003).
15. Sanderson, J. M. & Ward, A. D. Analysis of liposomal membrane composition using Raman tweezers. *Chem. Commun.* 10, 1120–1121 (2004).
16. Penders, J. et al. Single Particle Automated Raman Trapping Analysis. *Nat. Commun.* 9, 4256 (2018).
17. Cherney, D. P., Bridges, T. E. & Harris, J. M. Optical trapping of unilamellar phospholipid vesicles: Investigation of the effect of optical forces on the lipid membrane shape by confocal-Raman microscopy. *Anal. Chem.* 76, 4920–4928 (2004).
18. Myers, G. A. & Harris, J. M. Confocal raman microscopy of pH-gradient-based 10 000-fold preconcentration of compounds within individual, optically trapped phospholipid vesicles. *Anal. Chem.* 83, 6098–6105 (2011).
19. Lavialle, F. et al. Nanovesicles released by Dictyostelium cells: A potential carrier for drug delivery. *Int. J. Pharm.* 380, 206–215 (2009).
20. Lee, W. et al. Label-Free Prostate Cancer Detection by Characterization of Extracellular Vesicles Using Raman Spectroscopy. *Anal. Chem.* 90, 11 (2018).
21. Gualerzi, A. et al. Raman spectroscopy uncovers biochemical tissue-related features of extracellular vesicles from mesenchymal stromal cells. *Sci. Rep.* 7, (2017).

22. Gualerzi, A. et al. Raman spectroscopy as a quick tool to assess purity of extracellular vesicle preparations and predict their functionality. *J. Extracell. Vesicles* 8, (2019).
23. Tatischeff, I. et al. Fast characterisation of cell-derived extracellular vesicles by nanoparticles tracking analysis, cryo-electron microscopy, and Raman tweezers microspectroscopy. *J. Extracell. Vesicles* 1, 229–238 (2012).
24. Smith, Z. J. et al. Single exosome study reveals subpopulations distributed among cell lines with variability related to membrane content (SI). *J. Extracell. Vesicles* 4, 28533 (2015).
25. Carney, R. P. et al. Multispectral Optical Tweezers for Biochemical Fingerprinting of CD9-Positive Exosome Subpopulations. *Anal. Chem.* 89, 5357–5363 (2017).
26. Kruglik, S. G. et al. Raman tweezers microspectroscopy of circa 100 nm extracellular vesicles. *Nanoscale* 11, 1661–1679 (2019).
27. Park, J. et al. Exosome Classification by Pattern Analysis of Surface-Enhanced Raman Spectroscopy Data for Lung Cancer Diagnosis. *Anal. Chem.* 89, 6695–6701 (2017).
28. Stremersch, S. et al. Identification of individual exosome-like vesicles by surface enhanced raman spectroscopy. *Small* 12, 3292–3301 (2016).
29. Lee, C. et al. 3D plasmonic nanobowl platform for the study of exosomes in solution. *Nanoscale* 7, 9290–9297 (2015).
30. Fraire, J. C. et al. Improved Label-Free Identification of Individual Exosome-like Vesicles with Au@Ag Nanoparticles as SERS Substrate. *ACS Appl. Mater. Interfaces* 11, 39424–39435 (2019).
31. Yan, Z. et al. A Label-free platform for identification of exosomes from different sources. *ACS Sensors* 4, 488–497 (2019).
32. Shin, H., Jeong, H., Park, J., Hong, S. & Choi, Y. Correlation between Cancerous Exosomes and Protein Markers Based on Surface-Enhanced Raman Spectroscopy (SERS) and Principal Component Analysis (PCA). *ACS Sensors* 3, 2637–2643 (2018).
33. Li, T. Da et al. An ultrasensitive polydopamine bi-functionalized SERS immunoassay for exosome-based diagnosis and classification of pancreatic cancer. *Chem. Sci.* 9, 5372–5382 (2018).
34. Lee, C., Carney, R., Lam, K. & Chan, J. W. SERS analysis of selectively captured exosomes using an integrin-specific peptide ligand. *J. Raman Spectrosc.* 48, 1771–1776 (2017).
35. Zong, S. et al. Facile detection of tumor-derived exosomes using magnetic nanobeads and SERS nanoprobe. *Anal. Methods* 8, 5001–5008 (2016).
36. Kwizera, E. A. et al. Molecular detection and analysis of exosomes using surface-enhanced Raman scattering gold nanorods and a miniaturized device. *Theranostics* 8, 2722–2738 (2018).





Chapter 3


SEM-Raman image cytometry of cells



A. Enciso-Martinez,* F. J. Timmermans,* A. Nanou, L. W. M. M. Terstappen and C. Otto

** authors contributed equally*

Analyst, 2018, 143, 4495-4502



Abstract

A correlative and integrated Scanning Electron Microscopy (SEM) and Raman micro-spectroscopy is presented that enables the characterization and identification of different cancer and non-cancer cells through SEM-Raman image cytometry. The hybrid microscope system enables the acquisition of high resolution SEM images of un-coated cells and the spatial correlation with chemical information as obtained from Raman micro-spectroscopic imaging. A sample preparation protocol and workflow is presented that is compatible with the demands of hybrid SEM-Raman microscopy. Use has been made of stainless steel cell substrates that are both conductive and give low optical response in Raman scattering. Correlative and integrated SEM-Raman micro-spectroscopy is illustrated with cells from blood and cells from a SKBR-3 breast cancer cell line.

3.1 Introduction

Correlative light and electron microscopy (CLEM) enables the combined optical and electron microscopic analysis of sample structures. Correlative analysis recently sparked interest for imaging of cells and cellular structures,¹⁻⁵ typically for the combination of light microscopic contrast with electron microscopic resolution. Of specific interest is Raman micro-spectroscopy as a label-free imaging technique that, based on inelastic light scattering from molecules, provides spectral characterization of compounds in the Raman microscopic focus. A confocal Raman microscope image is obtained by 2D- or 3D-stage scanning. Specimen characterization by high resolution scanning electron microscopy and hyperspectral Raman micro-spectroscopy is ideally achieved through an integration of a Raman microscope with the SEM vacuum chamber. Correlative SEM-Raman imaging is thus obtained.⁶ In order to enable 2D- and 3D Raman imaging with the required optical imaging accuracy, the sample is mounted on a sub-stage that is fixed on the SEM stage. Accurate motion enabled by the sub-stage is necessary for diffraction limited hyperspectral Raman microscopy. The SEM stage provides the course adjustments, e.g. those necessary to scan the sample from the SEM probe position to the Raman probe position. After arrival at the Raman probe position, the sub-stage enables to obtain Raman spectra from each point with sub-micrometer step-size precision in a user-selected region of interest. Correlative imaging is thus performed by a controlled motion of the sample. The Raman region of interest can be chosen on the basis of either the SEM image or the optical video image. The combination of stages preserves the functionalities of both the SEM and the Raman microscope and facilitates a flexible workflow in which correlated microscopy enables selection of multiple objects from the SEM image for subsequent Raman analysis.

Correlative SEM-Raman imaging of hematopoietic cells from healthy donors and cells from the breast cancer cell line SKBR-3 were performed to observe the diverse morphologies of different cell types in combination with cell type specific Raman characterization. This demonstrates for the first time the characterization of different cell types in an integrated correlative SEM – Raman microscope. This instrumentation can then be used to develop a library of cells including both spectral and morphological features of individual cell types, which becomes important when trying to objectively discriminate between cancerous and normal cells. In the existing literature, characterization of cells is performed either only with Raman⁷⁻⁹ or only by electron microscopy.^{10,11}

Challenges in correlative imaging include charging effects in SEM imaging due to the absence of conductive coatings, or the contamination of Raman spectra through electron beam induced

deposition (EBID) of amorphous carbon with SEM. Such challenges have been overcome by using a proper sample preparation protocol and workflow strategy.

For the experiments, a substrate for the cells is needed, which has to be both compatible with SEM and Raman microscopy. The substrate should be optically quiet to avoid contributions in the Raman spectrum not related to the object of interest and electrically conductive to limit charging of the cells during the electron beam illumination. In addition, a suitable sample preparation protocol is required, that preserves the cell morphology, and does not obscure the Raman spectra of cells. Therefore, no embedding medium or conductive coatings are applied as these will either suppress the Raman signal or contribute photoluminescence to the Raman spectra.¹²

In the present study, we report a sample preparation protocol and a workflow that is suitable for correlative SEM-Raman of cells. High resolution SEM imaging revealed morphological features, while Raman spectroscopy disclosed a spectral fingerprint for each cell type. SEM and Raman color-coded images (Raman maps) are used for cell recognition: neutrophilic granulocytes, lymphocytes and SKBR-3 cells. In addition, multivariate analysis of spectral features can be used for cell identification avoiding the need of fluorescent labels, contrast-enhancing agents or metal coatings.

3.2 Materials and methods

3.2.1 SEM-Raman compatible substrate

An optically quiet substrate improves the signal-to-noise ratio in Raman spectra. A common choice for a substrate material for cells in spontaneous Raman spectroscopy is CaF_2 .¹³ On the other hand, SEM relies on electrical currents passing through the material of interest, hence an electrically conductive sample substrate is required. However, CaF_2 has a poor conductivity and is therefore not a suitable substrate for application in SEM. We have found stainless steel substrates to be suitable for combined SEM-Raman operation. The stainless steel surface can be chemically modified to accommodate cell adhesion with a procedure that is similar to the treatment of CaF_2 . **Figure 3.1** shows a comparison of the Raman spectra of the substrate materials CaF_2 and stainless steel. Although stainless steel has a slightly higher contribution to the background in Raman spectra than CaF_2 , this background does not appreciably interfere with the quality of the Raman spectra. In comparison with quartz or glass as a substrate (spectra not shown), the relatively flat spectrum of stainless steel is an additional advantage.¹⁴ Stainless steel $\mu\text{Rim}^{\text{TM}}$ substrates were purchased from BioTools, Inc.

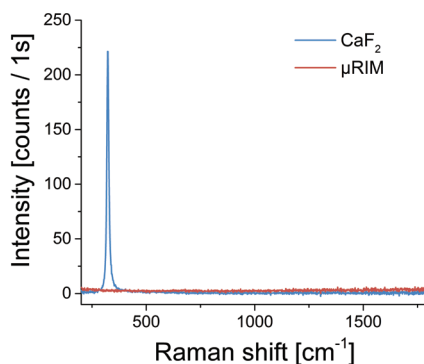


Figure 3.1. Mean Raman spectra of a CaF_2 and a stainless steel $\mu\text{RIM}^{\text{TM}}$ substrate. Raman acquisition is performed by a 2D raster scan of an area of $\sim 300 \mu\text{m}^2$ with a 785 nm laser excitation, 1 s integration time per pixel and 10.4 mW laser power.

3.2.2 Sample preparation

Blood from anonymous healthy donors was obtained after written informed consent. The blood samples were collected by venipuncture in Ethylenediaminetetraacetic acid (EDTA) vacutainer tubes (BD) from healthy donors, which was obtained from the TNW-ECTM-donor services (University of Twente, Enschede, The Netherlands). Blood collection was performed in accordance with the Dutch regulations and was approved by the Medical-ethical assessment committee Twente (METC Twente).

Red blood cells are prepared by a blood smear on a $\mu\text{Rim}^{\text{TM}}$ slide using 1 μL of whole blood. The sample contains mostly erythrocytes. Cells were fixed by submerging it three times in 100% v/v methanol for one second. The sample was dehydrated afterwards by immersing it in 100% ethanol for 20 minutes. In order to dry the sample, it was first incubated for five minutes in 1:1 v/v hexamethyldisilazane (HMDS): ethanol, and then in 100% HMDS for another five minutes. Finally, it was left overnight at room temperature (RT) for the HMDS residual to evaporate.

Leukocytes were isolated from whole blood. Ammonium chloride lysing buffer [154.95 mM NH_4Cl (Fisher Scientific), 9.99 mM KHCO_3 (Fisher Scientific), 0.099 mM EDTA (VWR Chemicals) in Milli-Q] with a pH of 7.25 was used to lyse the red blood cells. The blood was diluted 14 times in the lysing buffer and after five minutes leukocytes were collected and washed with 5mL cold (4°C) 1X phosphate buffered saline (PBS). Their fixation with 1% v/v paraformaldehyde (PFA) in PBS for 15 minutes at RT followed. Cells were collected by centrifugation at 300 g for five minutes and the pellet resuspended in 1X PBS. The sample was placed in the BDFACSAriaTM and neutrophilic granulocytes and lymphocytes were sorted based on their differences in forward

and right angle light scattering characteristics. The sorted cells were collected as pellets after centrifugation at 300g for five minutes. Cells were gradually dehydrated by incubation in increasing concentrations of ethanol: 70% v/v for three minutes and 80 and 90% v/v for five minutes each. Cells were collected as a pellet after being centrifuged at 400 g for five minutes and resuspended in 100% v/v ethanol. After an incubation of five minutes, an equal volume of HMDS was added to reach a 1:1 (v/v) ratio of HMDS: ethanol. Cells were pelleted down again and resuspended in 100% HMDS for three more minutes. Approximately 100 μ L of each sample population was added to μ RIM™ slides and samples were left drying overnight at RT.

SKBR-3 (ATCC) cells have been cultured in DMEM (Lonza) supplemented with 10% fetal bovine serum (FBS) (Sigma-Aldrich) and 1% 100 unit/mL Penicillin-Streptomycin (P/S) (Lonza) at 37 °C in a humidified atmosphere containing 5% CO₂. Dehydration and drying was performed as with the leukocytes.

3.2.3 SEM-Raman measurements

Correlative SEM-Raman imaging has been performed with an integrated Raman microspectrometer (HybriScan HSCMM_21) and a SEM (JEOL JSM-6610LA). Dehydrated and dried samples were placed in the SEM–Raman vacuum chamber for analysis. A region of interest (ROI) containing single or multiple cells was selected on the basis of a relatively low SEM magnification (~200-800x) and short acquisition time. Low electron dose was used to limit potential damage or EBID contamination of the sample before Raman spectroscopy. The SEM was operated at 2 kV acceleration voltage using secondary electron (SE) detection. A low acceleration voltage was chosen because these samples consist mainly of low atomic weight compounds with limited SEM contrast, which is improved by a lower electron energy that provides a stronger SE scattering coefficient.¹² Raman microscopy, with 785 nm laser excitation wavelength, was performed by 2D raster scan of ROIs (500 nm imaging step size) located with the SEM. The excitation power and spectral acquisition time (~10.5 mW, 1 s) were chosen to prevent sample damage and achieve a suitable signal intensity. After Raman analysis, the sample was moved back under the SEM lens to record a high resolution SEM image using a higher magnification (5000-10000x) and a longer exposure time. A low spot size setting (10-21), which also limits the probe current, was used to prevent surface charging.

3.2.4 Data processing

The Raman data was pre-treated with the following procedures: (1) Cosmic rays and outliers were removed from the data set. (2) Each ROI was divided in either cell or background pixels, the latter being discarded for multivariate analysis. (3) In the spectra, a residue of the HMDS

drying agent was observed after comparison with the HMDS spectrum and existing literature on Raman spectroscopy of cells.¹⁵ This contribution to the Raman spectra was subtracted using a linear least squares (LLS) fit. (4) Finally, baseline correction and denoising was performed using a function called BEADS.¹⁶ This removes a continuous fluorescence background contribution from the dataset and aids the multivariate analysis to distinguish the objects on the basis of the molecule-specific cellular Raman signal.¹⁷ Multivariate analysis of the Raman measurements was performed using a method of hierarchical cluster analysis (HCA) based on the principal component analysis (PCA) scores, resulting in cluster images (Raman maps). PCA was performed on the spectral region between 400 to 1800 cm^{-1} .

3.3 Results and discussion

3.3.1 Experimental design

In an integrated SEM-Raman microscope, low magnification SEM imaging enables to quickly assess the location of the cells for subsequent Raman imaging. In principle, SEM imaging captures the ultrastructure of cells in the sub-micrometer to nm range, while Raman spectroscopy enables the acquisition of complementary biochemical information. The correlation of both modalities results in combined morphological and chemical information for cell characterization and subsequent classification of the objects (*vide infra*).

The procedure to localize a ROI containing cells and perform SEM-Raman measurements is illustrated in [Figure 3.2](#). For this purpose, erythrocytes were used as an example for SEM-Raman characterization. The Raman spectrum of erythrocytes is well known for different excitation wavelengths, including 785 nm, which facilitates verification of initial experimental results and sample preparation procedure.⁷

A SEM image at a low magnification was first made to find ROIs ([Figure 3.2A](#)). Then, the motorized xy stage under the SEM was moved towards the Raman microscope objective with a precision of $\pm 1\mu\text{m}$. An optical video image was acquired ([Figure 3.2B](#)) and specific cells (red and blue rectangles in [Figure 3.2B](#)) were selected for Raman spectroscopy. After multivariate analysis, Raman maps were obtained ([Figure 3.2C](#)), which indicate clear differences among various cell types. The reported Raman cluster spectra in [Figure 2D](#) are color-coded according to the colors in the Raman map. The cluster spectra are averaged over all the pixels within the respective clusters. A good correspondence with the literature of the Raman peak positions was found.⁷ After acquiring the Raman signal, the xy-motorized stage returned the ROI to the same position ($\pm 1\mu\text{m}$) under the SEM lens and high-resolution SEM images of cells were taken.

Finally, an overlay of the SEM and Raman images (Figure 3.2E) discloses biochemical and morphological information of single cells. A more comprehensive investigation was performed to the correlative analysis of leukocytes and SKBR-3 cells. It will be shown that the different cell types can be distinguished based on their respective Raman spectra and SEM observed cell morphologies.

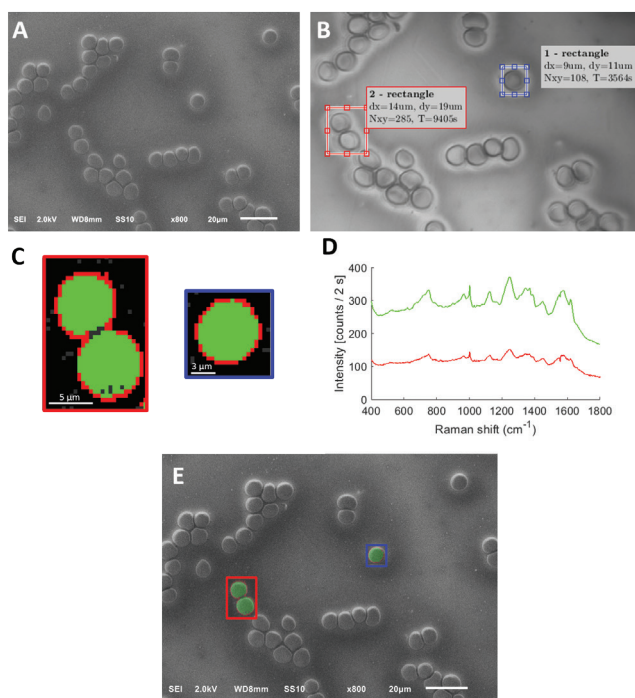


Figure 3.2. Strategy for localization of ROIs and further SEM-Raman characterization and image registration. SEM is used to scan the sample and find ROIs, i.e. clusters of erythrocytes as shown in panel (A). The xy-motorized stage then moves towards the Raman microscope objective and a bright field image is acquired (B). The optical image in panel (B) is used to select the cells of interest for further Raman acquisition. Panel (C) shows 2-level Raman maps resulting from HCA. Outliers are displayed as gray pixels. The corresponding Raman spectra with the same color coding is shown in panel (D). (E) Overlay image showing the Raman cluster image in conjunction with the SEM image, recorded with SE detection at 2.0 kV electron energy. Scale bars in SEM images denote 20 µm.

The measurement of cells in the vacuum chamber of the SEM required cells to be washed, dehydrated and dried (Materials and Methods, sample preparation). After preparation a clean substrate with RBCs is visible in Figure 3.2A. The samples were not treated for improved SEM contrast with a gold – or gold/palladium coatings, although ~5 nm thin layers of such coating can be accommodated by Raman spectroscopy.¹² In order to avoid charging and minimize cell damage due to the electron beam striking the sample, low acceleration voltages (2.0 kV electron energy) and spot size setting of 10-21 were used during SEM imaging.

3.3.2 SEM-Raman characterization of leukocytes and SKBR-3 cells

The correlative analysis of leukocytes and SKBR-3 cells with SEM and Raman is presented in **Figure 3.3**. This figure shows SEM and Raman maps of SKBR-3 cells and sorted neutrophils and lymphocytes by flow cytometry on the basis of their differences in forward and right angle light scattering characteristics. The Raman maps in columns A, C and E correspond to the SEM images of columns B, D and F, respectively. Scanning electron microscopy is performed on uncoated organic specimens. The absence of a conductive coating could result in some charging effects during electron imaging. Charges are more likely to be trapped at protrusions of the cell and will contribute to the gray-scale contrast in the SEM images. In addition, the use of a low probe current and longer imaging time provided a sufficient SEM resolution to distinguish surface features of the cells. The images in **Figure 3.3** directly reveal variation in surface roughness, shape and size, and as such enable to distinguish the three cell types from each other. The mean diameter sizes for neutrophils, lymphocytes and SKBR-3 cells was respectively 6.5 (± 0.7), 5.0 (± 0.3) and 11.8 (± 1.0) μm , with 15 cells of each type measured. All cells appear to have shrunken compared to typical values in aqueous environment.¹⁸⁻²⁰ Cell shrinkage has previously been found to be proportional to the drying duration.²¹ However, despite cell shrinkage during sample preparation, cell morphology was preserved after HMDS drying, without conceding on quality to standard and more complex drying methods for SEM, such as critical point drying.²¹

It can be observed that the three cell types have distinctly different morphologies. Neutrophilic granulocytes show short ruffles throughout their membrane, a courser surface compared to lymphocytes, and lack microvilli. Lymphocytes display a smoother membrane compared to neutrophilic granulocytes and lack short microvilli. SKBR-3 cells display microvilli on their surface and some membrane folding's. Short ruffles and the lack of microvilli in the cell membrane were expected for neutrophilic granulocytes.²² On the other hand, microvilli are expected in the surface of lymphocytes and SKBR-3 cells.^{22,23} The apparent absence of microvilli in the lymphocytes might be an artefact of the sample preparation protocol including cell sorting with FACS due to damage of the cytoskeleton.^{21,24,25} SEM imaging reveals the cells' ultrastructure, which serves as a feature for further cell identification. The morphological characterization of cells can be complemented by a chemical characterization technique such as Raman spectroscopy, as a step towards SEM-Raman image cytometry.

Multivariate analysis was performed simultaneously on all presented Raman measurements in **Figure 3.3**. This method reduced the full Raman dataset to clusters and corresponding images.

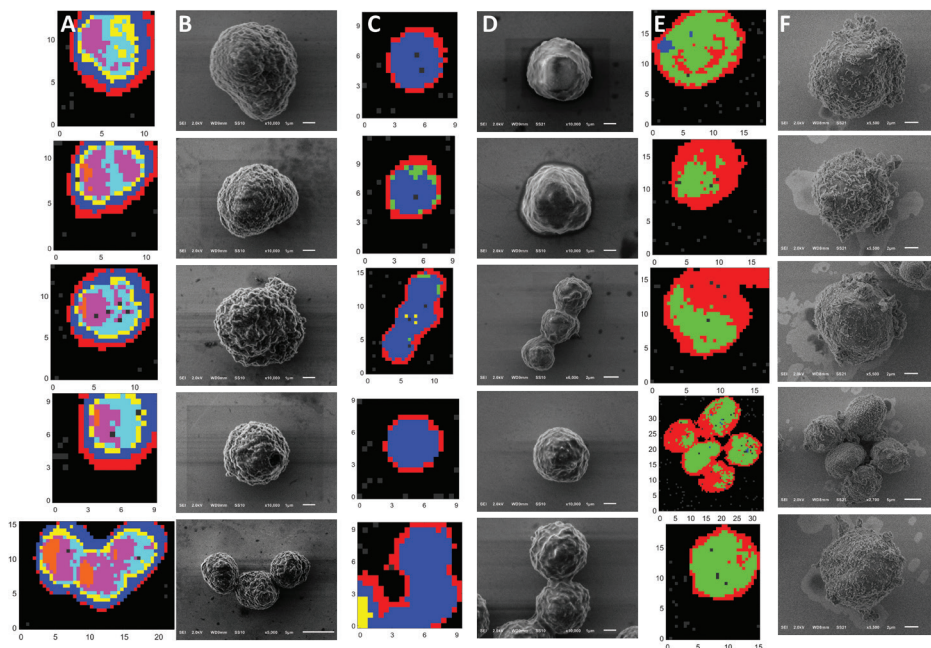


Figure 3.3. Raman maps (columns A, C and E) with their respective uncoated SEM images (columns B, D and F) of cells. Columns A and B show neutrophilic granulocytes, C and D lymphocytes and E and F SKBR-3 cells. Raman maps are measured with 10.5 mW excitation power, 1s integration time, and 500 nm scanning step size. Axes units in Raman maps are μm . Scale bars in SEM images denote from top to bottom in brackets, and left to right: [1, 1, 1, 1, 5], [1, 1, 2, 1, 1], and [2, 2, 2, 5, 2] μm .

The analysis was performed on pre-treated data, as discussed in the materials and methods section.

The Raman maps enable to distinguish neutrophils, lymphocytes and SKBR-3 cells as shown in [Figure 3.3](#). The three types of cells could be identified on the basis of the distribution and number and type of clusters per cell, and are shown in columns A, C and E in [Figure 3.3](#). Hence, color coded clusters can be assigned to specific cell types: light blue, pink, yellow and orange to neutrophilic granulocytes, blue mainly to lymphocytes and green to SKBR-3 cells.

The sample preparation protocol including cell fixation and dehydration preserves the Raman characteristics of cells. However, HMDS residual components are observed in the Raman spectra. Nevertheless, the HMDS contribution to the recorded spectra was subtracted using a LLS fitting procedure.

Although cluster analysis enables to distinguish cell types, a more clear interclass variation was obtained by comparing the average Raman spectra and the principal component scores of each cell type.

3.3.3 Spectral comparison and discrimination of leukocytes and SKBR-3 cell

The actual identification of cell types was performed based on the cell Raman spectra shown in [Figure 3.4](#). The presented Raman spectra were averaged over the measured cells shown in [Figure 3.3](#). It is noteworthy that while there are similarities between the spectra, characteristics specific for the respective cell types can be observed. These Raman bands are indicated in [Figure 3.4](#) with vertical lines and their respective Raman frequencies. Indicated Raman bands are at 679, 727, 781 and 1098 cm^{-1} specific for lymphocytes.⁸ The first two vibrational bands correspond to ring breathing modes of the nucleic acid bases (guanine and adenine, respectively).⁹ The 1098 cm^{-1} peak can be assigned to the O-P-O backbone in DNA.^{9,26} These vibrational modes indicate nucleic acid contributions. Although some of these bands are also visible in the Raman spectrum of the neutrophilic granulocytes, they are more prominent in the spectrum of the lymphocytes. This is explained by the fact that lymphocytes have a much larger nucleus which occupies around 90% of the cell compared to the smaller lobed nucleus of the neutrophilic granulocytes.⁹ The band at 1577 cm^{-1} is assigned to guanine and adenine.⁹ Again, this band is more prominent in the lymphocytes compared to the other two cell types. Raman bands from neutrophilic granulocytes are mostly overlapping with bands of the other cell types. Regarding the SKBR-3 cells, relatively prominent bands, compared to the other cell types, can be found at 743 and 1157 cm^{-1} . Other differences among cell types are found in the Raman profile between 820 and 870 cm^{-1} , associated with tyrosine.^{8,27} The averaged Raman spectrum of SKBR-3 cells shows other typical bands of this cell line that agree with the literature.²⁸ The Raman spectra in [Figure 3.4](#) result from averaging Raman contributions of various biomolecules, i.e. nucleic acids, proteins, lipids and carbohydrates over whole cells. Despite having Raman bands specific to a cell type, it is the resulting Raman spectrum profile that can serve as a fingerprint for further cell identification.

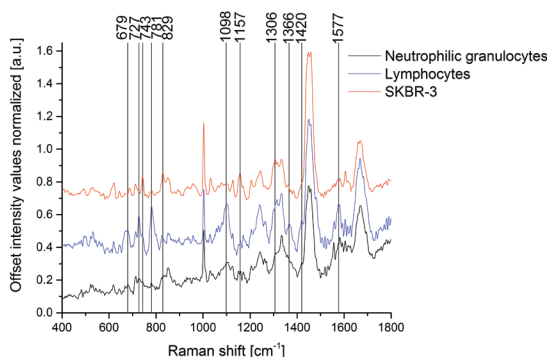


Figure 3.4. Comparison of Raman spectra of leukocytes and SKBR-3 cells. The presented spectra are averaged over the measured cells shown in Figure 3.3, normalized to one and smoothed by Savitzky-Golay 7-point filter. Vertical lines are drawn to highlight Raman bands showing specificity for different cell types and their corresponding Raman frequency values are indicated. The 679, 727, and 781 cm^{-1} bands are pronounced for lymphocytes, while SKBR-3 cells show clear peaks at 743 and 1157 cm^{-1} .

3.3.4 Principal component analysis

The spectral analysis of Figure 3.4 can be expanded by identifying the main sources of spectral variation via PCA. For this, the Raman spectra of 26 cells (9 neutrophilic granulocytes, 7 lymphocytes and 10 SKBR-3 cells) were selected after pre-treatment. Figure 3.5A shows the first, second and third principal component (PC1, PC2 and PC3, respectively) loadings. A good separation between the three cell types is visible in the two-dimensional scores plot (Figure 3.5B). Interestingly, neutrophilic granulocytes and SKBR-3 cells achieve a good separation along PC1, while lymphocytes and SKBR-3 cells are separable mainly along the PC3. An overlap of score values is seen mainly for leukocytes (blue and black dots). This might be due to regions of similar chemical composition among cells. Nevertheless, this does not prevent from cell discrimination because many Raman spectra are measured per cell, the majority of which would lie around the center of a cluster.

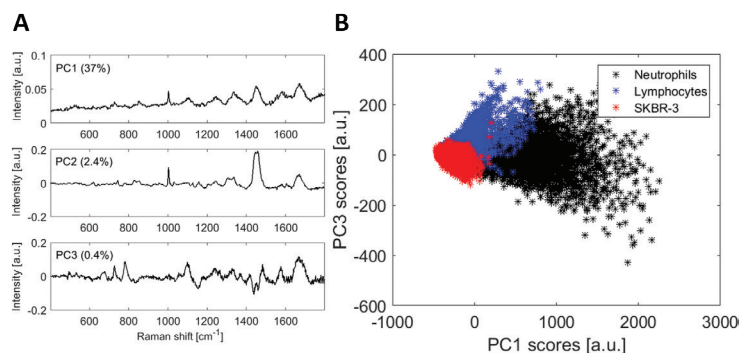


Figure 3.5. (A) First, second and third (from top to bottom) principal component loadings of the PCA. The input data in the analysis corresponds to a total of 26 cells (9 neutrophilic granulocytes, 7 lymphocytes and 10 SKBR-3 cells). (B) First and third principal component score plot. Three clusters are visible: neutrophilic granulocytes (black), lymphocytes (blue) and SKBR-3 cells (red).

3

3.3.5 Identification of unsorted leukocytes by means of SEM-Raman image cytometry

Leukocytes from a healthy blood donor patient were fixed, dehydrated and dried, but not sorted into different populations. SEM-Raman imaging was performed following the strategy shown in [Figure 3.2](#). After performing HCA on multiple cells, two groups of cells could be identified based on their Raman maps ([Figure 3.6](#)). We labelled each cell either as a lymphocyte or neutrophilic granulocyte assuming that the total cell population consisted by either one of these two cell types. Although lymphocytes and neutrophilic granulocytes constitute almost 90% of the leukocyte population,⁹ it is possible that we have imaged other cell types, e.g. monocytes, eosinophilic granulocytes or basophilic granulocytes.

The SEM-Raman overlays in [Figure 3.6 A, B and C](#) show one group of cells with smaller diameter and consisting mainly of two types of clusters: light and dark blue, whose corresponding average Raman spectra show the highest intensity for nucleic acid (NA) contributions ([Figure 3.6D](#)). Based on their sizes and Raman maps, this group of cells resemble the lymphocytes in [Figure 3.3](#); hence they have been labelled as such. The cluster distribution homogeneity in lymphocytes is related to their high nuclear-cytoplasmic ratio (~4:1). The second group of cells have a larger diameter and higher cluster heterogeneity, consisting mainly of three type of clusters (green, yellow and pink). Such cells resemble the neutrophilic granulocytes in [Figure 3.3](#) and have been labelled as such. The Raman maps of these cells do not show well defined nuclei and the reason might be their typical multi-lobed nuclei. In addition, cells belonging to the granulocyte family are known to have abundant cytoplasmic granules containing enzymes and metabolites^{8,9} that might contribute to the cluster heterogeneity in the Raman maps.

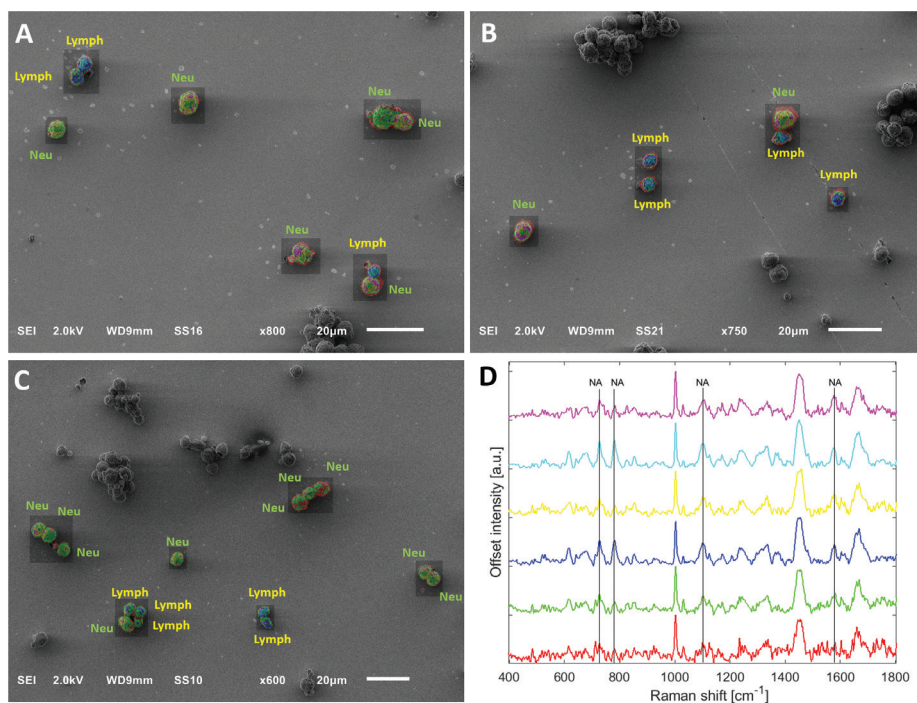


Figure 3.6. SEM-Raman overlay of unsorted leukocytes. Panels (A), (B) and (C) show SEM-Raman image overlays on an unsorted sample of leukocytes where labels have been assigned to cells based on a binary classification performed with HCA. The Raman maps shown on top of the SEM images are obtained after HCA using 6 clusters, whose respective Raman spectra are shown in panel (D), where the Raman peaks corresponding to nucleic acid (NA) contributions are indicated with vertical lines.

3.4 Conclusions

In this paper, we have demonstrated for the first time the characterization and identification of different cell types in an integrated correlative SEM-Raman microscope. Such approach allows us to obtain high resolution images of cells with electron microscopy correlated with their respective chemical fingerprint by means of Raman spectroscopy. As a first step, we successfully developed a sample preparation protocol and workflow for SEM-Raman characterization of cells. The preparation protocol enables to obtain morphological and chemical features of non-labelled and non-metal-coated cells in a vacuum environment. In order to discriminate among different cell types, the cell morphological features were complemented with Raman spectral features, which are based on the inherent chemical makeup of cells. In conjunction with PCA and HCA, we were able to identify breast cancer cells (SKBR-3) from lymphocytes and neutrophilic granulocytes. In addition, SEM-Raman overlay images of a random mixture of leukocytes

show the potential of this approach to distinguish various cells. A further improvement may be achieved in the future when the information from SEM images is actually included as features in a “multivariate” way.

The sample preparation protocol and workflow were specially developed for SEM-Raman. It can be applied to other biological samples as well to obtain a direct correlation of morphological and chemical information. This approach can be extended to characterize various cell types including cancer cells, such as circulating tumor cells (CTCs) and may shed some light on the heterogeneity of cancer cells, their interaction with the hematopoietic cells and the nature of the agents they secrete to communicate with their environment. The next step will be to use the morphological and chemical features of leucocytes and cancer cells to build a model for cell classification in order to detect CTCs from blood samples of cancer patients serving as a liquid biopsy. By combining CTC enrichment techniques with SEM-Raman image cytometry of cells we are approaching towards a new diagnostic tool for cancer cell recognition.

3

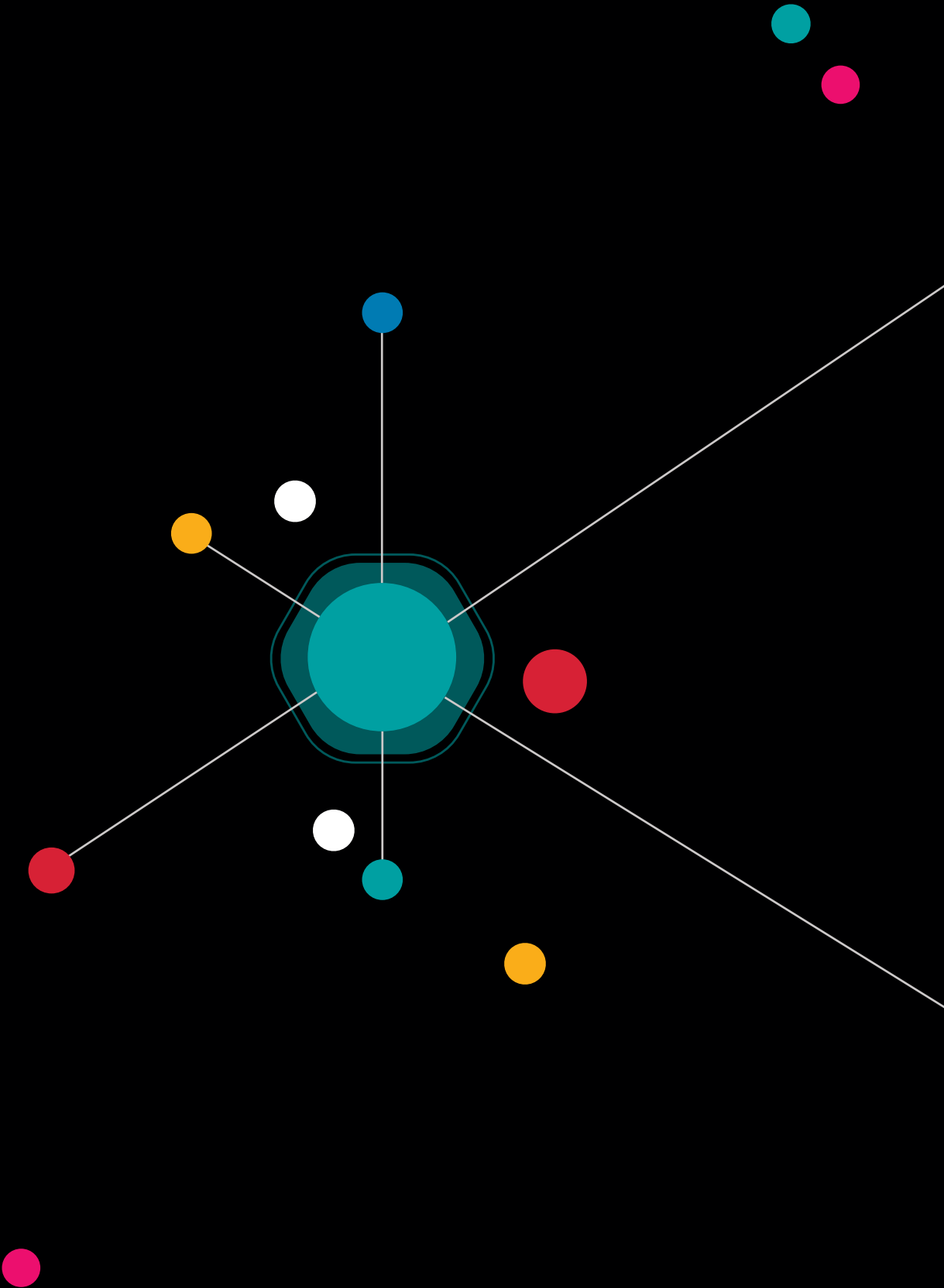
Acknowledgments

This work is part of the Perspectief Program Cancer ID with project number 14193, which is in part financed by the Netherlands Organization for Scientific Research (NWO).

References

1. de Boer, P., Hoogenboom, J. P. & G Giepmans, B. N. Correlated light and electron microscopy: ultrastructure lights up! *Nat. Methods* 12, 503–513 (2015).
2. Agronskaia, A. V et al. Integrated fluorescence and transmission electron microscopy. *J. Struct. Biol.* 164, 183–189 (2008).
3. Johnson, E. et al. Correlative in-resin super-resolution and electron microscopy using standard fluorescent proteins. *Sci. Rep.* 5, 1–8 (2015).
4. Löscherberger, A., Franke, C., Krohne, G., Van De Linde, S. & Sauer, M. Correlative super-resolution fluorescence and electron microscopy of the nuclear pore complex with molecular resolution. *J. Cell Sci.* 127, 4351–4355 (2014).
5. Liv, N. et al. Electron Microscopy of Living Cells During in Situ Fluorescence Microscopy. *ACS Nano* 10, 265–273 (2015).
6. Timmermans, F. J., Liszka, B., Lenferink, A. T. M., van Wolferen, H. A. G. M. & Otto, C. Integration of correlative Raman microscopy in a dualbeam FIB SEM. *J. Raman Spectrosc.* 47, 956–962 (2016).
7. Wood, B. R., Caspers, P., Puppels, G. J., Pandiancherri, S. & McNaughton, D. Resonance Raman spectroscopy of red blood cells using near-infrared laser excitation. *Anal. Bioanal. Chem.* 387, 1691–1703 (2007).
8. Bankapur, A. et al. Raman Tweezers Spectroscopy of Live, Single Red and White Blood Cells. *PLoS One* 5, e10427 (2010).
9. Ramoji, A. et al. Toward a Spectroscopic Hemogram: Raman Spectroscopic Differentiation of the Two Most Abundant Leukocytes from Peripheral Blood. *Anal. Chem.* 84, 5335–5342 (2012).
10. Canonico, B. et al. Evaluation of leukocyte stabilisation in TransFixR-treated blood samples by flow cytometry and transmission electron microscopy. *J. Immunol. Methods* 295, 67–78 (2004).
11. Rey Vázquez, G. & Guerrero, G. A. Characterization of blood cells and hematological parameters in *Cichlasoma dimerus* (Teleostei, Perciformes). *Tissue Cell* 39, 151–160 (2007).
12. Timmermans, F. J. & Otto, C. Contributed Review: Review of integrated correlative light and electron microscopy. *Cit. Rev. Sci. Instruments* 86, 011501 (2015).
13. Van Manen, H. J., Uzunbajakava, N., Van Bruggen, R., Roos, D. & Otto, C. Resonance Raman imaging of the NADPH oxidase subunit cytochrome b 558 in single neutrophilic granulocytes. *J. Am. Chem. Soc.* 125, 12112–12113 (2003).
14. Zhang, D. et al. Raman Detection of Proteomic Analytes. *Anal. Chem.* 75, 5703–5709 (2003).
15. Carteret, C. & Labrosse, A. Vibrational properties of polysiloxanes: From dimer to oligomers and polymers. 1. structural and vibrational properties of hexamethyldisiloxane (CH₃)₃SiOSi(CH₃)₃. *J. Raman Spectrosc.* 41, 996–1004 (2010).
16. Ning, X., Selesnick, I. W. & Duval, L. Chromatogram baseline estimation and denoising using sparsity (BEADS). *Chemom. Intell. Lab. Syst.* 139, 156–167 (2014).
17. Eilers, P. H. C. & Boelens, H. F. M. Baseline Correction with Asymmetric Least Squares Smoothing. (2005).
18. van Dalum, G., Lenferink, A. T. M. & Terstappen, L. W. M. M. 3. *Cancer Res.* 73, 1459–1459 (2013).
19. Heyn, R. M., Tubergen, D. G., Althouse, N. T. & Arbor, A. Lymphocyte Size Distribution: Determination in Normal Children and Adults and in Patients With Immunodeficiency States. *Am J Dis Child.* 125, 789–793 (1973).






20. Hallett, M. B. et al. Techniques for measuring and manipulating free Ca²⁺ in the cytosol and organelles of neutrophils. *J. Immunol. Methods* 232, 77–88 (1999).
21. Katsen-Globa, A., Puetz, N., Gepp, M. M., Neubauer, J. C. & Zimmermann, H. Study of SEM preparation artefacts with correlative microscopy: Cell shrinkage of adherent cells by HMDS-drying. *Scanning* 38, 625–633 (2016).
22. Majstorovich, S. et al. Lymphocyte microvilli are dynamic, actin-dependent structures that do not require Wiskott-Aldrich syndrome protein (WASp) for their morphology. *Blood* 104, 1396–1403 (2004).
23. Cavaliere, F. et al. Influence of the morphology of Lysozyme-shelled microparticles on the cellular association, uptake, and degradation in human breast adenocarcinoma cells. *Part. Part. Syst. Charact.* 30, 695–705 (2013).
24. Wollweber, L., Stracke, R. & Gothe, U. The use of a simple method to avoid cell shrinkage during SEM preparation. *J. Microsc.* 121, 185–189 (1981).
25. Schroeter, D., Spiess, E., Paweletz, N. & Benke, R. A procedure for rupture-free preparation of confluent grown monolayer cells for scanning electron microscopy. *J. Electron Microsc. Tech.* 1, 219–225 (1984).
26. Neugebauer, U., Clement, J. H., Bocklitz, T., Krafft, C. & Popp, J. Identification and differentiation of single cells from peripheral blood by Raman spectroscopic imaging. *J. Biophotonics* 3, 579–587 (2010).
27. Movasaghi, Z., Rehman, S., Rehman, I. U. I. U. & Zanyar Movasaghi, S. R. & D. I. U. R. Raman Spectroscopy of Biological Tissues. *Appl. Spectrosc. Rev.* 42, 493–541 (2007).
28. Tipping, W. J., Lee, M., Serrels, A., Brunton, V. G. & Hulme, A. N. Chem Soc Rev Stimulated Raman scattering microscopy: an emerging tool for drug discovery. *Chem. Soc. Rev.* 45, 2075–2089 (2016).





Chapter 4


Immuno-capture of extracellular vesicles for individual multi-modal characterization using AFM, SEM and Raman spectroscopy



P. Beekman,* A. Enciso-Martinez,* H. S. Rho, S. P. Pujari, A. Lenferink, Han Zuilhof, L.W.M.M. Terstappen, C. Otto and S. Le Gac

** authors contributed equally*

Lab Chip, 2019, 19, 2526-2536



Abstract

Tumor-derived extracellular vesicles (tdEVs) are promising blood biomarkers for cancer disease management. However, blood is a highly complex fluid that contains multiple objects in the same size range as tdEVs (30 nm – 1 μ m), which confuses an unimpeded observation of tdEVs. Here, we report a multi-modal analysis platform for the specific capture of tdEVs on antibody-functionalized stainless steel substrates, followed by their analysis using SEM, Raman spectroscopy and AFM, at the single EV level in terms of size and size distribution, and chemical fingerprint. After covalent attachment of anti-EpCAM (Epithelial Cell Adhesion Molecule) antibodies on stainless steel substrates, EV samples derived from a prostate cancer cell line (LNCaP) were flushed into a microfluidic device, assembled with this stainless steel substrate for capture. To track the captured objects between the different analytical instruments and subsequent correlative analysis, navigation markers were fabricated onto the substrate from a cyanoacrylate glue. Specific capture of tdEVs on the antibody-functionalized surface was demonstrated using SEM, AFM and Raman imaging, with excellent correlation between the data acquired by the individual techniques. The particle distribution was visualized with SEM. Furthermore, a characteristic lipid-protein band at 2850-2950 cm^{-1} was observed with Raman spectroscopy, and with AFM the size distribution and surface density of the captured EVs was assessed. Finally, correlation of SEM and Raman images enabled to discriminate tdEVs from cyanoacrylate glue particles, highlighting the capability of this multi-modal analysis platform for distinguishing tdEVs from contamination. The trans-instrumental compatibility of the stainless steel substrate and the possibility to spatially correlate the images of the different modalities with the help of the navigation markers opens new avenues to a wide spectrum of combinations of different analytical and imaging techniques for the study of more complex EV samples.

4.1 Introduction

Liquid biopsies have been proposed as an alternative to conventional approaches (e.g., magnetic resonance imaging or solid biopsies) for the disease management of cancer patients. In this non-invasive approach, a blood sample (7.5 ml) is analyzed for the presence and amount of circulating tumor cells (CTCs), tumor-derived EVs (tdEVs), cell free DNA (cf-DNA), miRNA and/or tumor-associated proteins or peptides.^{1,2} CTCs are well suited to characterize a tumor and to evaluate the heterogeneity for subsequent selection of the optimal treatment.³ The concentration of CTCs is however extremely low (~ 1 CTC mL⁻¹), especially when compared with that of blood cells ($\sim 10^9$ mL⁻¹).⁴ In contrast, tdEVs are much more abundant with concentrations up to 10^{10} tdEVs mL⁻¹.⁵ Importantly, the presence and amount of tdEVs in blood has been proven to strongly correlate with the survival of patients with metastatic prostate cancer.⁶ EVs are membrane-bound biological carriers of biomolecules, which are shed by all cell types. They are found in all body fluids,⁷ and exhibit a size ranging from 30 nm to 1 μ m.^{8,9} EVs are of great interest because of their implication in intercellular communication and pathogenesis;^{7,10,11} they show great promises not only for disease diagnosis but also for drug delivery.^{4,11–13} Altogether, EV analysis offers a promising approach for non-invasive cancer patient management as a result of the wealth of biological information they carry, some of which being potential biomarkers.¹⁴

However, blood is a highly complex fluid¹⁵ that contains lipoproteins, cell debris and protein aggregates, as well as EVs of non-cancerous origin, which are all in the same size and density range as tdEVs, and the same applies for less complex samples originating from cell culture media. In all these cases, tdEVs need to be selectively isolated and/or distinguished from EVs of non-cancerous origin and other small objects.^{16,17} Several methods have been proposed for EV isolation, among which ultracentrifugation and size-exclusion chromatography are the most popular.^{8,16,18–20} However, these isolation approaches yield highly heterogeneous samples containing tdEVs, other EVs, cell debris and molecular aggregates. Therefore, alternative approaches have been introduced that rely on the immuno-capture of targeted EVs, using either generic membrane markers (e.g., CD9, CD63 and CD81) to retrieve all exosomes/EVs from a sample,^{21,22} or specific membrane markers (e.g., EpCAM,⁶ EGFR,¹² HER2²³) to selectively isolate tdEVs. Microfluidic technology has proven to be instrumental for the immunocapture of EVs by controlling the surface dynamics (e.g., controlling flow rate when washing non-specifically bound species), and drastically reducing the distances over which EVs have to migrate before coming in contact with the functionalized surface. In addition, microfluidics facilitates controlled and sequential handling of (very small) samples.^{8,24}

A second main challenge is the high heterogeneity found in any purified EV sample, in terms of size and from a molecular perspective. Therefore, EVs must be thoroughly characterized for their possible and reliable recognition in heterogeneous samples. For that purpose, it is important to study individual EVs and not populations to avoid that ensemble averaging obscures differences. EVs have been analyzed using a great variety of techniques^{25–28} such as flow cytometry,^{29–31} confocal and non-confocal (fluorescence) microscopy,^{22,32} scanning electron microscopy (SEM),³³ atomic force microscopy (AFM),³⁴ Raman spectroscopy,³⁵ surface plasmon resonance (SPR),^{36,37} mass spectrometry (MS)³⁸ and μ NMR.³⁹ However, not all techniques allow the collection of information at the single EV level. Furthermore, to get comprehensive information on heterogeneous samples, different techniques yielding complementary information must be combined. In that context, Raman Spectroscopy, SEM and AFM are of great interest. Raman spectroscopy provides chemical information on a sample of interest in a label-free manner.^{40,41} SEM enables characterization of the size and morphology of intact EVs.^{42,43} Correlating this size and morphology information with Raman fingerprints confirms the cellular origin of individual EVs, and, in previous work, we have demonstrated that using this combination²³ cancer cells could be distinguished from non-cancer cells.^{44,45} Finally, AFM yields more detailed information on the size and morphology of EVs, and possibly, on their mechanical properties.^{30,46}

In this paper, we report the specific isolation of tdEVs obtained from prostate cancer cell lines on functionalized stainless-steel substrates followed by their *in situ* multi-modal characterization with SEM, Raman and AFM imaging (Figure 4.1). Stainless steel substrates were selected for their suitability for all considered modalities: this material gives little background in Raman (See SI 4.1);^{44,45} it is conductive; and mirror-polished stainless steel substrates have a low surface roughness level of ca. 7 nm, which is well-suited for the analysis of EVs by AFM. Here, and as depicted in Figure 4.2, stainless steel substrates were first functionalized with a monolayer of carboxydecyl phosphonic acid (CDPA),^{47–49} onto which antibodies targeting tdEVs were covalently anchored through carbodiimide-based bioconjugation chemistry.⁵⁰ The resulting monolayers were characterized with X-ray photoelectron spectroscopy (XPS) and infrared reflection-absorption spectroscopy (IRRAS), to optimize their formation with respect to the initial CDPA concentration. Next, EVs derived from human prostate cancer cell lines (LNCaP) were injected in a microfluidic channel assembled onto the functionalized stainless steel substrate, for their capture, which was confirmed using individual imaging techniques. For their multi-modal analysis, and to easily track individual EVs in the different instruments, navigation markers were fabricated on the functionalized substrates next to a region of interest (ROI). Finally, the captured EVs were successively analyzed by Raman imaging, SEM, and AFM, and data acquired by the different techniques correlated. The trans-instrumental compatibility

of the stainless steel substrate and the tracking possibility offered by the navigation markers opens gives the opportunity to apply a wide spectrum of combinations of different analytical and imaging techniques.

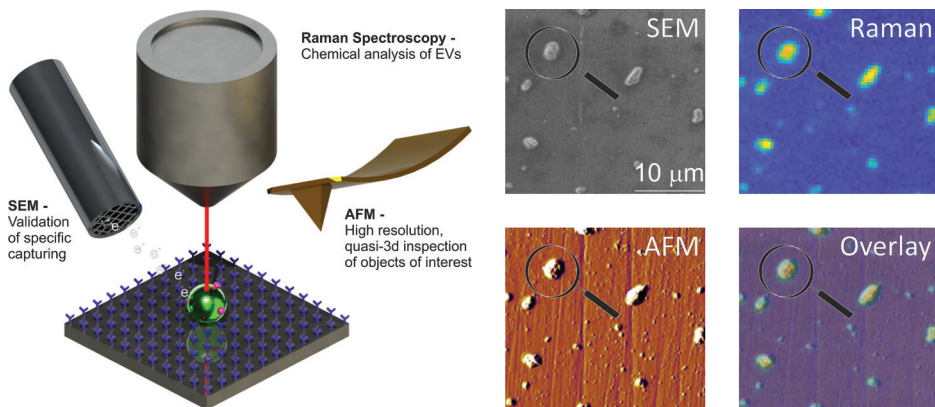


Figure 4.1. Multi-modal analysis of tdEVs on antibody-functionalized stainless steel substrates. After their selective capture on a stainless-steel surface functionalized with antibodies of interest (here Anti-EpCAM antibodies targeting tdEVs), EVs are successively imaged using Raman spectroscopy, SEM and AFM, and information collected from these different imaging modalities correlated to get a comprehensive picture on the captured objects.

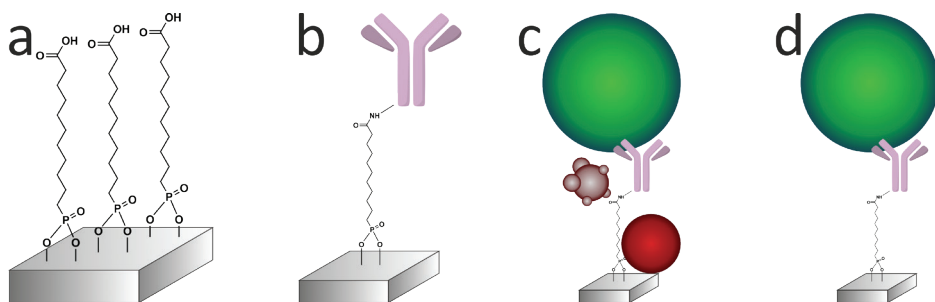


Figure 4.2. Different steps of surface modification and capture of the tdEVs on stainless steel substrates. a) An oxygen plasma-treated stainless steel substrate is functionalized with a carboxydecyl phosphonic acid (CDPA) monolayer. b) Anti-EpCAM antibodies are conjugated to the CDPA monolayer using NHS/carbodiimide chemistry. c) tdEVs (in green here) are specifically immuno-captured on the antibody-functionalized surface. d) The substrate is washed to remove non-specifically bound materials (in red and purple here), before retained EVs are fixed and dehydrated.

4.2 Experimental

4.2.1 Materials

1-Ethyl-3-(3-dimethylaminopropyl)carbodiimide (EDC), N-hydroxysuccinimide (NHS), acetone (VLSI grade), paraformaldehyde (PFA), phosphate-buffered saline (PBS), and 2-(N-morpholino)

ethanesulfonic acid were purchased from Merck (Zwijndrecht, The Netherlands). Ethanol (VLSI grade) and dichloromethane were purchased from VWR (Amsterdam, The Netherlands). Carboxydecyl phosphonic acid (CDPA) was purchased from Sikémia (Montpellier, France). Sylgard 184 poly(dimethylsiloxane) (PDMS) was purchased from Farnell (Utrecht, The Netherlands). SS316L Stainless steel foils (0.9 mm thickness, one side mirror polished) were purchased from Goodfellow Inc. (Bad Nauheim, Germany). Anti-EpCAM antibodies were produced at the University of Twente, The Netherlands (Medical Cell BioPhysics Laboratory) from VU1D9 hybridoma cells.

4.2.2 PDMS handling devices

Three different PDMS devices (a 6-mm diameter reservoir, a xurography channel and a navigation marker device) were used for different steps of the sample preparation, as depicted in [Figure 4.3](#). For all devices, PDMS was prepared and cured according to the same procedure. PDMS precursor and cross linker (10:1 weight ratio) were first thoroughly mixed, and subsequently degassed by centrifugation at 1000x g for 1 min. The resulting mixture was poured on different molds for the different devices, and degassed again in a desiccator for 15 min. Curing was performed at 80 °C overnight.

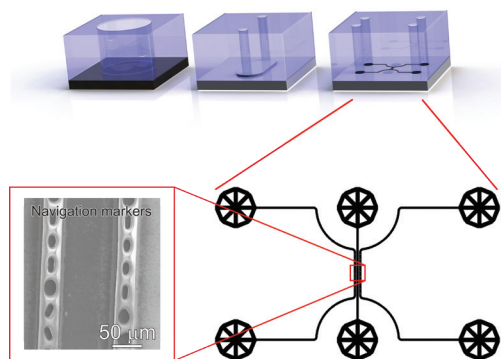


Figure 4.3. Various PDMS devices used in this work. *Top*, and from *left to right*: 6-mm diameter reservoir used for the immobilization of antibodies under static conditions on a CDPA monolayer; xurography microchannel ($6 \times 3 \times 0.2 \text{ mm}^3$) used for the capture of EVs and subsequent washing under mild flow conditions ($400 \mu\text{l}\cdot\text{min}^{-1}$); microfluidic device used for the fabrication of navigation markers next to a $50 \mu\text{m} \times 1 \text{ mm}$ sample region, subsequently considered for analysis using SEM, Raman and AFM. *Bottom, right*: Design of the microfluidic device used to fabricate the navigation markers, consisting of three microfluidic channels, two microchannels comprising pillars with various geometries, flanking one sample microchannel, all channels being $30 \mu\text{m}$ height \times $50 \mu\text{m}$ width \times 1 mm length, and (*left*) actual SEM image showing the navigation markers fabricated from cyanoacrylate glue injected in the side-channels and used to retrace the captured objects in the different imaging instruments.

PDMS Reservoir. A large 6-mm diameter PDMS reservoir was used for the antibody immobilization onto CDPA-functionalized stainless steel substrates. To this end, a 5-mm height PDMS layer was prepared in a petri dish. This PDMS layer was cut in 1 x 1 cm² pieces, in which a hole was punched with a Harris Uni-Core 6-mm biopsy punch (VWR International B.V., Amsterdam, The Netherlands).

Xurography channel. To capture EVs and their subsequent washing and fixation, a xurography microchannel was used. The mold for this device was produced using a desktop plotter (Silhouette Cameo 2, Silhouette, Wateringen), as follows. First, a 6 mm x 3 mm feature was cut out of a foil laminated with a 200- μ m thick adhesive layer, and subsequently placed at the bottom of a clean petri dish. The foil was removed to only leave the adhesive layer. After PDMS curing in this mold, inlets and outlets were punched using a 1-mm diameter Harris Uni-Core biopsy punch. The resulting device was placed on top of a stainless steel substrate after removal of the previously used PDMS reservoir.

Navigation marker device. For the multi-modal analysis, and after dehydration of the captured EVs (see section "Vesicle capture and dehydration"), navigation markers were fabricated on the stainless steel substrates for easy tracking of the captured EVs, using a microfluidic device comprising 3 microchannels: two microchannels featuring navigation markers (Figure 4.3) and flanking one sample channel. All channels were 30 μ m height x 50 μ m width x 1 mm length. The distance between the navigation markers and the sample region (80 μ m, center-to-center) was chosen to be compatible with the characteristic dimension of the field of view of the bright-field optical objectives in all instruments used in this work (i.e., ~200 μ m for the Raman system, 500 μ m for the AFM instrument and freely variable in the SEM, see SI 4.2).

The design of this microfluidic device was drawn in CleWin (WieWeb, Hengelo, The Netherlands), and the mold fabricated in the Nanolab cleanroom of the MESA+ Institute for Nanotechnology. Briefly, a <100> Si wafer was spin-coated with AZ-40XT resist (Microchemicals, Ulm, Germany) at 3000 RPM for 1 min to yield a 30- μ m thick layer. The photoresist was exposed, baked and developed according to the manufacturer's specifications. After PDMS casting on the finished mold, fluidic accesses were punched using a 1-mm diameter Harris Uni-Core biopsy punch. The PDMS device was placed on top of a functionalized stainless steel substrate after EV capture and dehydration. No specific care was required for alignment of the device, since the width of the sample region is much smaller than that of the xurography channel. Cyanoacrylate superglue (Tesa SE, Norderstedt, Germany) was injected in the side channels and cured for 30 min to create the navigation markers. After PDMS delamination, the designed micro-features were transferred to the stainless steel surface with high fidelity (Figure 4.3, bottom left).

4.2.3 CDPA monolayer formation and characterization on stainless steel substrates

CDPA monolayer formation. Stainless steel substrates were laser-cut into 1 cm x 1 cm substrates and cleaned in an ultrasonic bath in ethanol, acetone and dichloromethane (7 min for each solvent), followed by an oxygen plasma treatment for 3 min in a Diener Pico (Diener electronic, Bielefeld, Germany) at 250 W. Immediately after plasma treatment, the substrates were transferred to a solution of CDPA in ethanol for overnight incubation at 60 °C to form a CDPA monolayer (Figure 4.2a). Three CDPA concentrations were initially tested (0.1, 1 and 10 mM) to identify the optimal concentration. The resulting CDPA monolayer was subsequently cured in a vacuum oven at 130 °C for 1 h and finally washed in an ultrasonic bath in ethanol, acetone and dichloromethane (7 min for each solvent).

Infrared Reflection/Absorption Spectroscopy (IRRAS). IRRAS measurements were performed on a Bruker Tensor 27 using a Harrick Auto Seagull™ (Bruker Nederland B.V.). 2000 scans per measurement were recorded under an angle of incidence of 83° using a liquid nitrogen-cooled MCT (mercury-cadmium-telluride) detector. Measurements were taken in triplicates after 35 min of purging with argon to remove moisture and carbon dioxide. Data were averaged and normalized with respect to a reference (O₂ plasma-cleaned stainless steel) to yield relative absorption values.

X-ray Photoelectron Spectroscopy (XPS). XPS measurements were conducted on a JPS-9200 (JEOL, Japan) under ultra-high vacuum conditions with analyser pass energy of 10 eV using monochromatic Al K α X-ray radiation at 12 kV and 20 mA at an angle of incidence of 80°. Wide scans (0-800 eV) were recorded as well as narrow scans in the 280-300 eV region to more closely inspect the carbon binding energies.

4.2.4 Antibody conjugation onto the CDPA monolayer

VU1D9 (anti-EpCAM) antibodies were conjugated onto the CDPA monolayer using EDC/NHS chemistry (EDC = 1-ethyl-3-(3-dimethylaminopropyl)carbodiimide, NHS = N-hydroxysuccinimide) at room temperature (Figure 4.2b). In the PDMS reservoir, a solution of 40 mM NHS, 130 mM EDC and 50 mM 2-(N-morpholino)ethanesulfonic acid in Milli-Q (pH 5) was pipetted and left to react with the CDPA monolayer for 30 min. The substrate was subsequently rinsed with 50 μ l of a 5 mM acetic acid solution in Milli-Q to stop the reaction, followed by 100 μ l PBS. Next, the antibody solution at 20 μ g/mL in PBS was pipetted in the reservoir and incubated with the surface for 1 h, followed by extensive washing with PBS to remove unreacted chemicals. Finally,

unreacted NHS ester groups were blocked by a 0.1 M ethanolamine solution in Milli-Q for 30 min. The reservoirs were filled with PBS buffer until their use within 24 h.

4.2.5 Vesicle capture and dehydration

EVs were isolated from culture medium (see SI 4.3 for the isolation protocol) of the human prostate cancer cell line LNCaP, which is known to express epithelial cell adhesion molecules (EpCAM). To avoid any EV contamination from the serum added to the culture medium, the LNCaP cells were cultured in serum-free medium for 48 h before their isolation. Nanoparticle tracking analysis (NTA)⁵¹ of those isolated EVs revealed a concentration of 1.06×10^9 EVs ml⁻¹ (See SI 4.4). 25 μ l of this EV-containing suspension was introduced into the xurography channel (channel volume: 3.6 μ l) using a capillary pipette tip acting as an inlet reservoir, and left under static incubation for 1 h at room temperature. Channels were subsequently washed with 200 μ l of PBS at a flow-rate of 400 μ l min⁻¹ using a syringe-pump connected to the outlet reservoir and operated in withdrawal mode (Figure 4.2d). Captured EVs were next fixed in the channel with a 1% PFA solution in PBS. After fixation of the EVs, the PDMS device was removed, the sample rinsed in Milli-Q, dehydrated by immersion in a solution of 70% ethanol in Milli-Q (5 min) followed by immersion in pure ethanol (5 min), and finally dried overnight under ambient conditions. Various negative control experiments were conducted in this study, as summarized in Table S14.1: (i) no activation of the CDPA layer with EDC/NHS; (ii) no immobilization of anti-EpCAM antibodies; and (iii) no incubation with any EV sample.

4.2.6 Multi-modal analysis of the captured EVs on anti-EpCAM-conjugated stainless steel substrates

SEM measurements. SEM imaging was performed using a JEOL JSM-6610LA Analytical SEM (JEOL, Nieuw-Vennep, The Netherlands). The SEM was operated in high-vacuum mode, and images were recorded with secondary electron (SE) detection with a low acceleration voltage of 2 kV to avoid sample charging in the absence of conductive coatings.

Raman measurements. Hyperspectral Raman micro-spectroscopy was performed by 2D point scanning of a laser beam ($\lambda = 647.09$ nm) from a Coherent Innova 70C laser. The Raman scattered light was dispersed in a spectrometer and collected with a CCD sensor (Andor Newton DU-970-BV). The wavenumber interval per pixel is ~ 2.3 cm⁻¹ on average over the length of the sensor. The laser power was measured underneath the objective (40x, NA: 0.95) and adjusted to 10 mW. The laser focal spot ($d \sim 0.39$ μ m, $h \sim 1.2$ μ m) was focused on the substrate and a 30 μ m x 30 μ m ROI was scanned with a step size of 0.47 μ m and an illumination time of 250 ms per pixel. Using Matlab 2017b (Mathworks, Eindhoven, The Netherlands), after wavenumber

and intensity calibration, the data were pretreated by cosmic ray removal and noise reduction by singular value decomposition, maintaining five singular components. Raman spectra were acquired across the entire wavenumber range (0 – 3660 cm^{-1}). Multivariate analysis by means of principal component analysis (PCA) was performed in the high frequency spectral region between 2700 to 3200 cm^{-1} . PCA was used to extract the most relevant information from the data matrix and to represent it as a linear combination of orthogonal principal components (PC or loadings) with coefficients (scores) for the contribution of the variance to the data.⁵² For each loading, a single score value was assigned to each measured pixel in the ROI and a Raman image reconstructed based on the scores. A high score value for a certain loading means a high contribution of that loading to the corresponding pixel.

AFM measurements. AFM measurements were performed on an Asylum MFP-3D instrument (Asylum Research, Santa Barbara, USA) in AC air topography mode (i.e., tapping mode) with a scan rate of 0.1 Hz and a set point of 400 mV. An Olympus micro cantilever with a nominal spring constant of 2 N m^{-1} was used (resonant frequency \sim 70 kHz). The resulting graphs were processed with Gwyddion 2.5.1 SPM analysis software (www.gwyddion.net). A mean plane subtraction and 3rd order polynomial background removal was applied. For object analysis, a 25.0 ± 0.2 nm height threshold was applied to the data and circles were fitted to the remaining islands. A list of radii was exported to Matlab 2016a (Mathworks, Eindhoven, The Netherlands) for analysis and plotting of a size distribution histogram.

4.3 Results and discussion

4.3.1 Monolayer formation and characterization

To optimize the monolayer formation, different concentrations of carboxydecyl phosphonic acid (CDPA) were tested and the resulting CDPA monolayers analyzed using infrared reflection-absorption spectroscopy (IRRAS) to evaluate the surface coverage, molecular ordering, and the configurations of the carboxyl groups. Spectra recorded for stainless steel substrates functionalized with CDPA (1 mM solution), as well as for CDPA powder, are presented in [Figure 4.4a](#). Bands assigned to the anti-symmetric CH_2 stretch were found around 2914 cm^{-1} for all tested CDPA concentrations (see SI 4.5). These anti-symmetric CH_2 stretch bands are typically found between 2914 and 2930 cm^{-1} , and their exact values reflect the packing density of the monolayer. Low values, as observed here, suggest densely packed monolayers displaying a short-range inter-chain monolayer ordering.^{47,48,53–56} In all samples, the carboxyl band was detected at \sim 1720 cm^{-1} , which is attributed to acyclically dimerized carboxyl groups,⁵⁷ i.e., hydrogen-bonding dimerization with nearest neighbors. Higher absorption frequencies for

this band (towards 1740 cm^{-1}) indicate non-hydrogen-bonded species, and therefore a less dense monolayer. Lower frequencies ($\sim 1700\text{ cm}^{-1}$) would suggest cyclic dimerization as a result of multilayer formation. In the $1700\text{-}1740\text{ cm}^{-1}$ region, peak broadening was observed in the substrates functionalized with 0.1 and 10 mM solutions (see SI 4.5), indicating a lesser degree of ordering than for the substrates prepared with a 1 mM solution. The baseline across the relative samples revealed that the signal-to-noise ratio for the substrate prepared with a 1 mM solution was also significantly improved compared to the other samples. Therefore, on the basis of these results, further experiments were conducted using a 1 mM CDPA solution for the 1st-step functionalization of the stainless steel substrates.

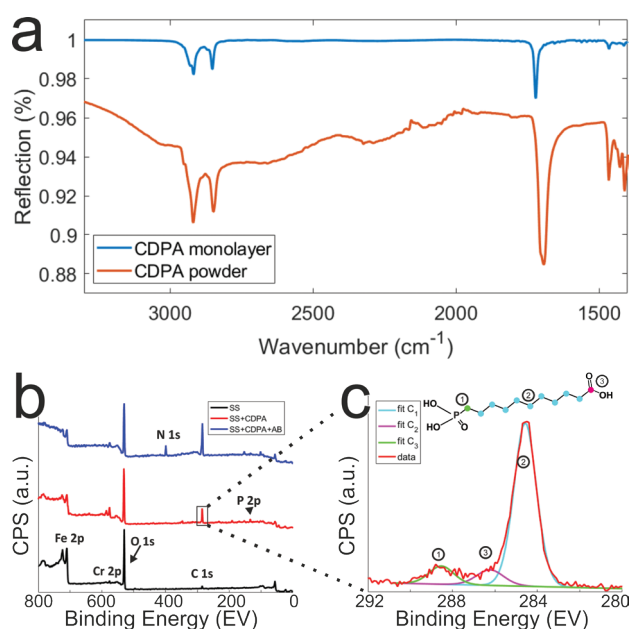


Figure 4.4. Chemical characterization of the stainless steel surfaces after the different surface modification steps. a) IR reflection-absorption (IRRAS) spectra (which are background corrected) of CDPA monolayers prepared on SS316L stainless steel substrates using a 1 mM CDPA solution (blue trace) and CDPA powder (red trace). b) XPS spectra recorded after the various surface modification steps, as depicted in Figure 2. Wide range scans acquired on a O_2 plasma-treated stainless steel substrate (SS, black trace), a stainless steel substrate functionalized with a CDPA monolayer (SS+CDPA, red trace); and after antibody conjugation on the CDPA monolayer (SS+CDPA+AB, blue trace). c) C 1s narrow scan showing fitted peaks corresponding to the different carbon species found in a CDPA molecule (*inset*).

After each surface modification step (oxygen plasma treatment, CDPA functionalization, antibody modification), the substrates were also analyzed using XPS (Figure 4.4b). Integration of the peak surface areas provides quantitative information about the proportion of elements found on the substrate. After O_2 plasma (black line, Figure 4.4b), relatively little carbon (C 1s signal at

~285 eV) was found on the stainless steel substrates, and this corresponds to adventitiously adsorbed carbon. A significant oxygen peak (O 1s peak at 532 eV) was detected as a result of the plasma treatment. Finally, various metals were present, such as Fe 2p (710 eV) and Cr 2p (575 eV). After formation of the CDPA monolayer, the signal corresponding to carbon became more intense, and a peak appeared at 134 eV, corresponding to P 2p. Integration of these two peaks reveals a C:P ratio of 11.2 : 1, which is in excellent agreement with the theoretically expected 11 : 1 ratio according to the molecular formula of CDPA (Figure 4.4c). Carbon atoms experiencing different electronic environments are characterized by different binding energies, and CDPA molecules comprise carbon atoms in three distinct environments, as depicted in Figure 4.4c. The C atom in the carbonyl group is observed at ~289 eV; the phosphorous-bound carbon at ~286.2 eV; and the alkyl chain carbon atoms at 285 eV. Integrating these different C 1s signals yields a ratio of ~8.8 : 1.1 : 1, which is again in good agreement with the molecular structure of CDPA (9 : 1 : 1).

After formation of the monolayer (red line, Figure 4.4b), signals originating from the metal elements decreased by a factor of ~1.5, indicating successful coverage of the surface by the CDPA monolayer. Using these XPS data, the monolayer thickness can be derived, together with the tilt angle of the CDPA molecules on the surface. The thickness (t) of the CDPA layer was calculated using $t = -\lambda \times \sin \theta \times \ln \left(\frac{Fe_{CDPA}}{Fe_0} \right)$,^{58,59} with λ being the attenuation length estimated for Fe 2p (1.4 nm), $\theta = 80^\circ$, and Fe_0 and Fe_{CDPA} the signal intensities (counts s⁻¹) for Fe 2p before and after grafting of the CDPA monolayer, respectively. A CDPA monolayer thickness of 1.2 ± 0.1 nm was found. Considering a molecular length of 1.30 nm for CDPA as determined by Chem3D (PerkinElmer Informatics, Inc.), this monolayer thickness corresponds to a tilt angle of $20 \pm 10^\circ$, which supports the IRRAS data that suggested the formation of a densely packed and ordered monolayer.

Finally, after antibody conjugation (Figure 4.4b, blue line), an N 1s signal appeared at 400 eV. The metal signal was further attenuated, which can be accounted for by the formation of a thicker layer on the substrates due to the size of the antibody molecules, which is in the same order of magnitude as the probing depth of the technique, *i.e.*, ~10 nm.

4.3.2 Capture of LNCaP-derived EVs on antibody-conjugated stainless steel substrates and uncorrelated analysis

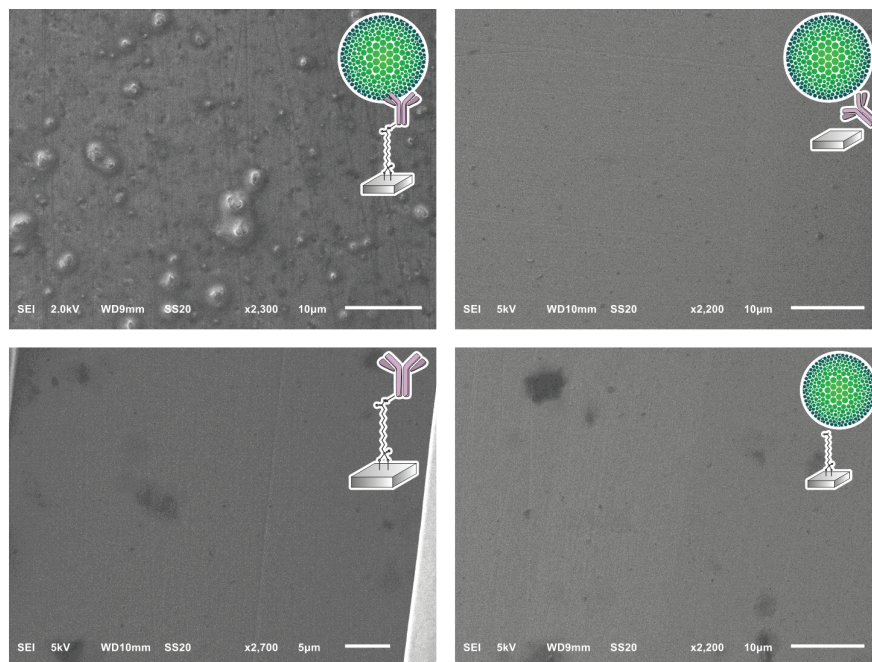
The antibody-conjugated surfaces were incubated with an EpCAM-positive tdEV sample prepared from LNCaP culture medium, and subsequently imaged with SEM to demonstrate their ability to immuno-capture tdEVs. As shown in Figure 4.5a, tdEVs were successfully and

specifically captured on the antibody-conjugated stainless steel surfaces, onto which quasi-spherical objects in the 100 nm – 1 μm size range were identified. In contrast, in negative controls, for which one step of surface functionalization was omitted or which were not exposed to tdEV sample (see Table SI4.1, and Figure SI4.6), nothing was captured in the surface (Figure 4.5a). Collectively, this experiment demonstrates the ability of our antibody-functionalized stainless steel substrates to successfully capture tdEVs.

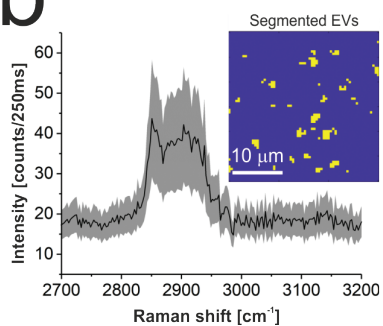
As a next step, the same substrates, after capture of the tdEVs, were analyzed using Raman spectroscopy and AFM imaging. Hyperspectral Raman images were acquired on 30 μm x 30 μm ROIs (64 x 64 pixels), and analyzed using PCA in the spectral region between 2700 to 3200 cm^{-1} that contains the most intense peaks. EVs were identified as regions with pixels of high intensity values in certain scores. Such pixels were next segmented and used not only as a mask to identify the locations corresponding to EVs in all the images, as depicted in the inset of Figure 4.5b, but also to compute a mean Raman spectrum for EVs, as presented in Figure 4.5b. This spectrum comprises a characteristic lipid-protein band at 2850 – 2950 cm^{-1} , and a clear peak at 2851 cm^{-1} that corresponds to the CH_2 symmetric stretch of lipids.⁶⁰

Finally, AFM images were used for quantitative analysis of the captured EVs. In five considered areas of 50 μm x 50 μm , a total of 5.4×10^3 tdEVs were detected, which corresponds to a surface density of 4.3×10^5 tdEVs mm^{-2} . These objects presented a size range of 54 to 3840 nm and an average diameter of 101 ± 111 nm, and Figure 4.5c shows the particle distribution up to 0.7 μm , since most of the particles were found in the 0-0.7 μm range. Noteworthy, the particle size distribution and average size as determined by AFM were overall in good agreement with data obtained using Nanoparticle Tracking Analysis (NTA), with yet a slight shift in the size distribution *i.e.*, 167 ± 91 nm (See SI4.4 and Figure 4.5c, blue line). The difference observed can be accounted for by the lower detection limit of the latter technique, or by shrinking of the EVs due to dehydration.^{51,61}

a



b



c

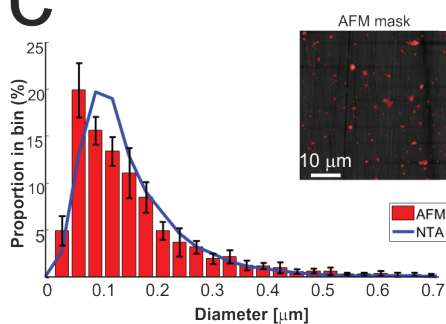


Figure 4.5. Analysis of the tdEVs captured on anti-EpCAM functionalized stainless steel substrates. a) SEM imaging revealing the specific capture of tdEVs (obtained from LNCaP cells) on anti-EpCAM functionalized stainless steel substrates (*top left*), while no object was captured on negative control samples (*top right*; without carbodiimide/NHS activation; *bottom left*; without functionalization with anti-EpCAM antibodies; and *bottom right*, without exposure to tdEV samples). b) Mean Raman spectrum (black line) and standard deviation (shaded area) of all EVs segmented from the ROI presented in the inset (30 μm x 30 μm and 64 x 64 pixels). The Raman spectrum (Raman shift range 2700-3200 cm^{-1}) shows a lipid-protein band (2850-2950 cm^{-1}) with a characteristic peak at 2851 cm^{-1} , which corresponds to the CH_2 symmetric stretch of lipids. In the inset, yellow pixels correspond to EVs and blue to the background. c) Size distribution of the surface-immobilized LNCaP-derived EVs determined by AFM (red histogram), and of the same sample in suspension before its immobilization on the surface as determined by NTA (blue line). Histogram: bin width 30 nm, error bars corresponding to the standard deviation ($n=5$). Inset: mask used for counting EVs on the AFM image, showing all objects detected with a height greater than 25 nm.

4.3.3 Multi-modal analysis using SEM, Raman and AFM imaging

Finally, tdEVs captured on functionalized stainless steel substrates were analyzed successively using SEM, Raman and AFM imaging for their multi-modal characterization, and this last series of analysis was performed after fabrication of navigation markers on the stainless steel substrates. To identify interesting ROIs, the samples were first analyzed with SEM at a low resolution. It should be noted that for this first step of SEM imaging, the ROIs were not extensively exposed to the electron beam to avoid electron beam-induced deposition (EBID) of amorphous carbon,⁶² which would hinder later analysis by Raman spectroscopy. Next, the distance between the measured location and the nearest set of markers was noted so as to find back the same region in the different imaging techniques. Following this, the same ROIs on the surface were successively imaged using hyperspectral Raman spectroscopy and SEM to characterize the EV size and morphology. Similarly, and with the help of the navigation markers, the ROIs were traced back and imaged with AFM. A key element in this multi-modal analytical process is the presence of navigation markers: due to their varying pitch, size and shape, each location in the sample region, as defined by the microchannel in the last PDMS device, can be matched to a unique combination of markers to assign spatial reference points to a ROI. This reference enables to retrieve objects of interest after transferring the stainless steel substrates between different instruments.

Figure 4.6 presents the images of this multi-modal analysis, for the individual techniques as well as overlaid images. Noteworthy, a very good correlation exists between the images acquired with the individual techniques, with similar patterns observed in all 3 techniques (Figures 4.6c, f, and i). Surprisingly, SEM imaging (Figure 4.6a) revealed the presence of two types of particles, which could easily be distinguished based on their morphology and size: on one hand, small and elongated objects with an aspect ratio of approximately 1:7, and, on the other hand, compact, solidified crystalline particles with irregular shapes and well-defined edges, and with a height comparable to their lateral size. The larger particles were identified as cyanoacrylate glue particles, while the smaller particles were captured tdEVs, which was confirmed by Raman imaging (vide infra). Glue particles are presumably created upon release of the last PDMS device used to fabricate the navigation markers. In SEM, tdEVs present a much lower contrast than glue particles due to differences in molecular density.

Multivariate analysis of the Raman data by PCA performed in the high frequency region (2700 and 3200 cm^{-1}) as before confirms the presence of distinct populations of objects on the stainless steel substrates, whose Raman profile was distinct enough, as observed from the loading vectors PC3 (for tdEVs) and PC1 (for glue particles), respectively, in Figures 4.6d and 4.6g. Measurements were conducted here on single EVs captured on the surface, and the signal-to-noise ratio was

better in the high frequency region, which was therefore solely considered for data analysis. Yet, it allowed distinguishing tdEVs from other particles. As before, a clear Raman peak was found in the PC3 (Figure 4.6d) loading at 2851 cm^{-1} , which corresponds to the CH_2 symmetric stretch of lipids, and a lipid-protein band between 2850 and 2950 cm^{-1} , which is characteristic of EVs. These bands were absent in the PC1 loading, and are indeed not expected for cyanoacrylate (glue) particles. In contrast, the PC1 loading (Figure 4.6g) presented a CH stretching region with a prominent peak at 2944 cm^{-1} and a CN stretching region with a peak at around 2247 cm^{-1} , which are both characteristic of cyanoacrylate glue.⁶³ It is worth noticing that the optical contrast of the images of scores is superior to the electron contrast in the SEM images, which clearly highlights the added value of correlative SEM-Raman imaging. The Raman images of the PC3 and PC1 scores in Figures 4.6e and 6h reveal the respective distribution of the EVs and glue particles.

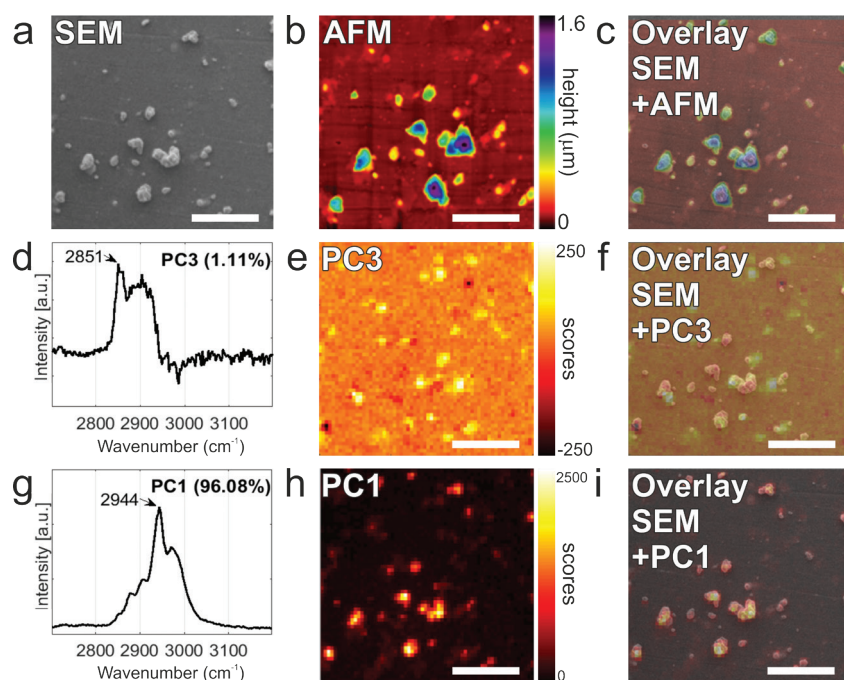


Figure 4.6. Multi-modal analysis of LNCaP-derived EVs on anti-EpCAM functionalized stainless steel substrates. a) SEM image of a selected ROI ($30\ \mu\text{m} \times 30\ \mu\text{m}$). b) Corresponding AFM height image of the same ROI. c) AFM – SEM overlaid image. d) Raman spectrum in the $2700\text{--}3200\text{ cm}^{-1}$ region of the PC3 displaying a characteristic lipid-protein band ($2850\text{--}2950\text{ cm}^{-1}$) specific to EVs, with a characteristic peak at 2851 cm^{-1} , which corresponds to the CH_2 symmetric stretch of lipids. e) Raman image of scores on PC3 (1.11%) showing the position of EVs in the Raman image. f) Overlay image showing excellent correspondence between the PC3 image of scores (h) with the SEM image (a). g) Raman spectrum in the $2700\text{--}3200\text{ cm}^{-1}$ region corresponding to the PC1 displaying a $\nu(\text{CH})$ stretching region of the cyanoacrylate glue with a characteristic peak at 2944 cm^{-1} . h) Raman image of scores on PC1 (96.08%) showing the position of the glue particles in the Raman image. i) Overlay image showing excellent correspondence between the Raman image of scores on PC1 (e) with the SEM image presented in (a).

As a last analytical modality, AFM was employed to characterize the objects captured on the surface. Although AFM is typically slower than SEM, its resolution is higher, which allows detecting both more and smaller particles compared to the two other techniques. The resolution of particles below $\sim 0.5 \mu\text{m}$ in SEM is complicated by the low contrast in lieu of gold coating of the sample, whereas it became apparent only from AFM analysis that the majority of particles is in fact smaller than $\sim 120 \text{ nm}$ (See [Figure 4.5c](#)). Moreover, AFM provides quasi-3D morphological information, which is of great interest to characterize the height of the captured EVs. Given also the low contrast in SEM due to the low acceleration voltages, the AFM data is altogether more suitable for studying the size distribution of captured EVs ([Figure 4.5c](#)). [Figure 4.6b](#) presents an AFM image corresponding to the previously discussed Raman and SEM images, and [Figure 4.6c](#) an overlay image of the AFM and SEM data, showing good agreement between the data acquired by both techniques. In future studies, AFM could also be considered to examine the mechanical properties of the captured EVs (e.g., by nanoindentation⁶⁴).

Altogether, data acquired by AFM are fully in line with both Raman and SEM data, and they all demonstrate the specific capture of tdEVs by the covalently bound antibodies on the stainless steel substrates.

4.4 Conclusion

We reported here a platform for the selective capture of tumor derived EVs (tdEVs) followed by their multi-modal analysis using SEM, Raman and AFM imaging to correlate size, morphological and chemical information at the individual EV level. Stainless steel, selected here for its suitability for all three imaging techniques, was first chemically modified with a CDPA monolayer onto which anti-EpCAM antibodies targeting tumor-derived EVs were immobilized. IRRAS and XPS characterization of the CDPA-functionalized surfaces revealed a densely packed and well-ordered monolayer, and XPS confirmed proper immobilization of the antibodies. Furthermore, EVs isolated from LNCaP prostate cancer cell lines were successfully captured on the antibody-conjugated stainless steel substrates, and successively analyzed using Raman spectroscopy, SEM and AFM. The integration of navigation markers on the stainless steel substrates after EV capture was instrumental here to track back individual EVs between the different analytical techniques. However, their fabrication using cyanoacrylate injected in patterned PDMS channels resulted in the creation of glue particles, which were detected together with the EVs. In future work, therefore, such navigation markers should be machined in the substrate and not onto the substrate to alleviate these contamination issues. Nonetheless, good agreement was found

between the three techniques considered here, with excellent overlay of the images acquired by the individual modalities.

As a proof of concept, in this paper, tdEVs isolated from cancerous cell lines were captured and analyzed. As a next step, the same platform will be challenged with more complex samples, such as blood samples, after implementation of anti-fouling moieties, *e.g.*, based on polyethylene glycol (PEG). Furthermore, the proposed multi-modal approach can easily be expanded in the future to other optical (*e.g.*, confocal fluorescence microscopy or infrared spectroscopy), electron (*e.g.*, energy-dispersive X-ray spectroscopy) and probe (*e.g.*, force spectroscopy) microscopy techniques as well as other analysis techniques, *e.g.*, surface plasmon resonance (SPR) and mass spectroscopy (MS).

Acknowledgments

The authors would like to thank Naoual Ouazzani Chahdi for her experimental contribution. This work is part of the Perspectief Program Cancer ID with project numbers 14193 and 14196, which is funded by the Netherlands Organization for Scientific Research (NWO) and co-financed by JEOL Europe B.V., Hybriscan Technologies B.V., Aquamarijn Micro Filtration B.V. and Lionix International.

References

1. Poudineh, M., Sargent, E. H. E. H., Pantel, K. & Kelley, S. O. S. O. Profiling circulating tumour cells and other biomarkers of invasive cancers. *Nat. Biomed. Eng.* 2, 72–84 (2018).
2. Vaidyanathan, R., Soon, R. H., Zhang, P., Jiang, K. & Lim, C. T. Cancer Diagnosis: From Tumor to Liquid Biopsy and Beyond. *Lab Chip* (2018). doi:10.1039/C8LC00684A
3. Alix-Panabières, C. & Pantel, K. Circulating tumor cells: Liquid biopsy of cancer. *Clin. Chem.* 59, 110–118 (2013).
4. Coumans, F. A. W. F. A. W., Ligthart, S. T. S. T., Uhr, J. W. J. W. & Terstappen, L. W. M. M. L. W. M. M. Challenges in the enumeration and phenotyping of CTC. *Clin. Cancer Res.* 18, 5711–5718 (2012).
5. Coumans, F., van Dalum, G. & Terstappen, L. L. W. M. M. L. W. M. M. CTC Technologies and Tools. *Cytom. A* 93, 1197–1201 (2018).
6. Nanou, A. et al. Circulating tumor cells, tumor-derived extracellular vesicles and plasma cytokeratins in castration-resistant prostate cancer patients. *Oncotarget* 9, 19283–19293 (2018).
7. Yáñez-Mó, M. et al. Biological properties of extracellular vesicles and their physiological functions. *J. Extracell. Vesicles* 4, 1–60 (2015).
8. Sunkara, V., Woo, H.-K. & Cho, Y.-K. Emerging techniques in the isolation and characterization of extracellular vesicles and their roles in cancer diagnostics and prognostics. *Analyst* 141, 371–381 (2016).
9. Liga, A., Vliegthart, A. D. B. D. B., Oosthuizen, W., Dear, J. W. W. & Kersaudy-Kerhoas, M. Exosome isolation: A microfluidic road-map. *Lab Chip* 15, 2388–2394 (2015).
10. György, B. et al. Membrane vesicles, current state-of-the-art: Emerging role of extracellular vesicles. *Cell. Mol. Life Sci.* 68, 2667–2688 (2011).
11. Xu, R., Greening, D. W., Zhu, H., Takahashi, N. & Simpson, R. J. Extracellular vesicle isolation and characterization : toward clinical application. *J Clin Invest* 126, 1152–1162 (2016).
12. Reátegui, E. et al. Engineered nanointerfaces for microfluidic isolation and molecular profiling of tumor-specific extracellular vesicles. *Nat. Commun.* 9, 2018 (2018).
13. Zhu, Q., Heon, M., Zhao, Z. & He, M. Microfluidic engineering of exosomes: Editing cellular messages for precision therapeutics. *Lab Chip* 18, 1690–1703 (2018).
14. Raposo, G. & Stoorvogel, W. Extracellular vesicles: Exosomes, microvesicles, and friends. *J. Cell Biol.* 200, 373–383 (2013).
15. Im, H. et al. Label-free detection and molecular profiling of exosomes with a nano-plasmonic sensor. *Nat. Biotechnol.* 32, 490–5 (2014).
16. Witwer, K. W. et al. Standardization of sample collection, isolation and analysis methods in extracellular vesicle research. *J. Extracell. Vesicles* 2, 2013 (2013).
17. Yuana, Y. et al. Handling and storage of human body fluids for analysis of extracellular vesicles. *J. Extracell. Vesicles* 4, 2015 (2015).
18. Tauro, B. J. B. J. et al. Comparison of ultracentrifugation, density gradient separation, and immunoaffinity capture methods for isolating human colon cancer cell line LIM1863-derived exosomes. *Methods* 56, 293–304 (2012).
19. Yoshioka, Y. et al. Ultra-sensitive liquid biopsy of circulating extracellular vesicles using ExoScreen. *Nat. Commun.* 5, 3591 (2014).

20. Willms, E., Cabañas, C., Mäger, I., Wood, M. J. A. & Vader, P. Extracellular vesicle heterogeneity: Subpopulations, isolation techniques, and diverse functions in cancer progression. *Front. Immunol.* 9, 2018 (2018).
21. Kanwar, S. S. S. S., Dunlay, C. J. C. J., Simeone, D. M. D. M. & Nagrath, S. Microfluidic device (ExoChip) for on-chip isolation, quantification and characterization of circulating exosomes. *Lab Chip* 14, 1891–1900 (2014).
22. Koliha, N. et al. A novel multiplex bead-based platform highlights the diversity of extracellular vesicles. *J. Extracell. Vesicles* 5, 2016 (2016).
23. Yadav, S. et al. An Electrochemical Method for the Detection of Disease-Specific Exosomes. *ChemElectroChem* 4, 967–971 (2017).
24. Guo, S. C., Tao, S. C. & Dawn, H. Microfluidics-based on-a-chip systems for isolating and analysing extracellular vesicles. *J. Extracell. Vesicles* 7, (2018).
25. Coumans, F. A. W. F. A. W. et al. Methodological guidelines to study extracellular vesicles. *Circ. Res.* 120, 1632–1648 (2017).
26. Im, H., Lee, K., Weissleder, R., Lee, H. & Castro, C. M. C. M. Novel nanosensing technologies for exosome detection and profiling. *Lab Chip* 17, 2892–2898 (2017).
27. Contreras-Naranjo, J. C. J. C., Wu, H.-J. H. J. & Ugaz, V. M. V. M. Microfluidics for exosome isolation and analysis: Enabling liquid biopsy for personalized medicine. *Lab Chip* 17, 3558–3577 (2017).
28. Hisey, C. L., Dorayappan, K. D. P. K. D. P., Cohn, D. E. D. E., Selvendiran, K. & Hansford, D. J. D. J. Microfluidic affinity separation chip for selective capture and release of label-free ovarian cancer exosomes. *Lab Chip* 18, 3144–3153 (2018).
29. Kormelink, T. G. T. G. et al. Prerequisites for the analysis and sorting of extracellular vesicle subpopulations by high-resolution flow cytometry. *Cytom. Part A* 89, 135–147 (2016).
30. Yuana, Y. et al. Atomic force microscopy: A novel approach to the detection of nanosized blood microparticles. *J. Thromb. Haemost.* 8, 315–323 (2010).
31. van der Pol, E. et al. Standardization of extracellular vesicle measurements by flow cytometry through vesicle diameter approximation. *J. Thromb. Haemost.* 16, 1236–1245 (2018).
32. Zhang, P. et al. Ultrasensitive Quantification of Tumor mRNAs in Extracellular Vesicles with Integrated Microfluidic Digital Analysis Chip. *Lab Chip* 18, 3790–3801 (2018).
33. Zhang, P., He, M. & Zeng, Y. Ultrasensitive microfluidic analysis of circulating exosomes using a nanostructured graphene oxide/polydopamine coating. *Lab Chip* 16, 3033–3042 (2016).
34. Sebaihi, N., De Boeck, B., Yuana, Y., Nieuwland, R. & Pétry, J. Dimensional characterization of extracellular vesicles using atomic force microscopy. *Meas. Sci. Technol.* 28, 8pp (2017).
35. Lee, W. et al. Label-Free Prostate Cancer Detection by Characterization of Extracellular Vesicles Using Raman Spectroscopy. *Anal. Chem.* 90, 11 (2018).
36. Shpacovitch, V. & Hergenröder, R. Optical and surface plasmonic approaches to characterize extracellular vesicles. A review. *Anal. Chim. Acta* 1005, 1–15 (2018).
37. Obeid, S. et al. Development of a NanoBioAnalytical platform for "on-chip" qualification and quantification of platelet-derived microparticles. *Biosens. Bioelectron.* 93, 250–259 (2017).
38. Pocsfalvi, G. et al. Mass spectrometry of extracellular vesicles. *Mass Spectrom. Rev.* 35, 3–21
39. Shao, H. et al. Protein typing of circulating microvesicles allows real-time monitoring of glioblastoma therapy. *Nat. Med.* 18, 1835–1840 (2012).

40. Tatischeff, I. et al. Fast characterisation of cell-derived extracellular vesicles by nanoparticles tracking analysis, cryo-electron microscopy, and Raman tweezers microspectroscopy. *J. Extracell. Vesicles* 1, 229–238 (2012).
41. Krafft, C. et al. A specific spectral signature of serum and plasma-derived extracellular vesicles for cancer screening. *Nanomedicine Nanotechnology, Biol. Med.* 13, 1–7 (2016).
42. Eswaran, N., Agaram Sundaram, V., Rao, K. A. & Thalaivarisai Balasundaram, S. Simple isolation and characterization of seminal plasma extracellular vesicle and its total RNA in an academic lab. *3 Biotech* 8, 1–6 (2018).
43. Kondratov, K. A. et al. A Study of Extracellular Vesicles Isolated from Blood Plasma Conducted by Low-Voltage Scanning Electron Microscopy. *Cell tissue biol.* 11, 181–190 (2017).
44. Timmermans, F. J. & Otto, C. Contributed Review: Review of integrated correlative light and electron microscopy. *Cit. Rev. Sci. Instruments* 86, 011501 (2015).
45. Enciso-Martinez, A., Timmermans, F. J., Nanou, A., Terstappen, L. W. M. M. & Otto, C. SEM–Raman image cytometry of cells. *Analyst* 143, 4495–4502 (2018).
46. Sharma, S. et al. Structural-Mechanical Characterization. *ACS Nano* 4, 1921–1926 (2010).
47. Kosian, M., Smulders, M. M. J. M. J. & Zuilhof, H. Structure and Long-Term Stability of Alkylphosphonic Acid Monolayers on SS316L Stainless Steel. *Langmuir* 32, 1047–1057 (2016).
48. Raman, A., Dubey, M., Gouzman, I. & Gawalt, E. S. E. S. Formation of self-assembled monolayers of alkylphosphonic acid on the native oxide surface of SS316L. *Langmuir* 22, 6469–6472 (2006).
49. Tizazu, G., Adawi, A. M. A. M., Leggett, G. J. G. J. & Lidzey, D. G. D. G. Photopatterning, etching, and derivatization of self-assembled monolayers of phosphonic acids on the native oxide of titanium. *Langmuir* 25, 10746–10753 (2009).
50. Hermanson, G. T. *Bioconjugate Techniques*. (Academic Press, 2013). doi:10.1016/B978-0-12-382239-0.00004-2
51. van der Pol, E. et al. Particle size distribution of exosomes and microvesicles determined by transmission electron microscopy, flow cytometry, nanoparticle tracking analysis, and resistive pulse sensing. *J. Thromb. Haemost.* 12, 1182–1192 (2014).
52. Abdi, H. & Williams, L. J. L. J. Principal component analysis. *Wiley Interdiscip. Rev. Comput. Stat.* 2, 433–459 (2010).
53. Ter Maat, J. et al. Organic modification and subsequent biofunctionalization of porous anodic alumina using terminal alkynes. *Langmuir* 27, 13606–13617 (2011).
54. Porter, M. D. M. D., Bright, T. B. T. B., Allara, D. L. D. L. & Chidsey, C. E. C. E. Spontaneously Organized Molecular Assemblies. 4. Structural Characterization of n-Alkyl Thiol Monolayers on Gold by Optical Ellipsometry, Infrared Spectroscopy, and Electrochemistry. *J. Am. Chem. Soc.* 109, 3559–3568 (1987).
55. Maoz, R. & Sagiv, J. On the formation and structure of self-assembling monolayers. I. A comparative attractiveness study of Langmuir-Blodgett and adsorbed films on flat substrates and glass microbeads. *J. Colloid Interface Sci.* 100, 465–496 (1984).
56. Debrassi, A. et al. Versatile (bio)functionalization of bromo-terminated phosphonate-modified porous aluminum oxide. *Langmuir* 31, 5633–5644 (2015).
57. Arnold, R., Azzam, W., Terfort, A. & Wöll, C. Preparation, modification, and crystallinity of aliphatic and aromatic carboxylic acid terminated self-assembled monolayers. *Langmuir* 18, 3980–3992 (2002).

Chapter 4

58. Bain, C. D. C. D. & Whitesides, G. M. G. M. Attenuation lengths of photoelectrons in hydrocarbon films. *J. Phys. Chem.* 93, 1670–1673 (1989).
59. Laibinis, P. E. P. E., Bain, C. D. C. D. & Whitesides, G. M. G. M. Attenuation of photoelectrons in monolayers of n-alkanethiols adsorbed on copper, silver, and gold. *J. Phys. Chem.* 95, 7017–7021 (1991).
60. Movasaghi, Z., Rehman, S., Rehman, I. U. I. U. & Zanyar Movasaghi, S. R. & D. I. U. R. Raman Spectroscopy of Biological Tissues. *Appl. Spectrosc. Rev.* 42, 493–541 (2007).
61. Van Der Pol, E. et al. Optical and non-optical methods for detection and characterization of microparticles and exosomes. *J. Thromb. Haemost.* 8, 2596–2607 (2010).
62. Timmermans, F. J. J., Chang, L., Van Wolferen, H. A. G. M. A. G. M., Lenferink, A. T. M. T. M. & Otto, C. Observation of whispering gallery modes through electron beam-induced deposition. 42, 1337–1340 (2017).
63. Edwards, H. G. M. H. G. M. & Day, J. S. J. S. Fourier transform Raman spectroscopic studies of the curing of cyanoacrylate glue. *J. Raman Spectrosc.* 35, 555–560 (2004).
64. Roos, B. W. H. & Wuite, G. J. L. Nanoindentation Studies Reveal Material Properties of Viruses. *Adv. Mater.* 1187–1192 (2009). doi:10.1002/adma.200801709

Supporting Information

Control experiments

Table SI4.1. Overview of the experiments included in this study – EV capture on the antibody-conjugated substrates and negative control experiments.

	EDC/NHS activation	Antibody	EVs
Sample <i>EVs to be analyzed</i>	+	+	+
Control i	-	+	+
Control ii	+	-	+
Control iii	+	+	-

SI 4.1 Raman Spectroscopy of stainless steel

In order to assess the suitability of functionalized stainless steel as a substrate for Raman spectroscopy, an area of 40 μm x 40 μm was scanned with a laser power of 35 mW and an illumination time of 250 ms with a step size of 1 μm . The spectrum of clean stainless steel is comparable to standard CaF_2 and commercial stainless steel ($\mu\text{RIM}^{\text{TM}}$, BioTools) used as substrate for Raman spectroscopy. A quartz spectrum is also shown for comparison.

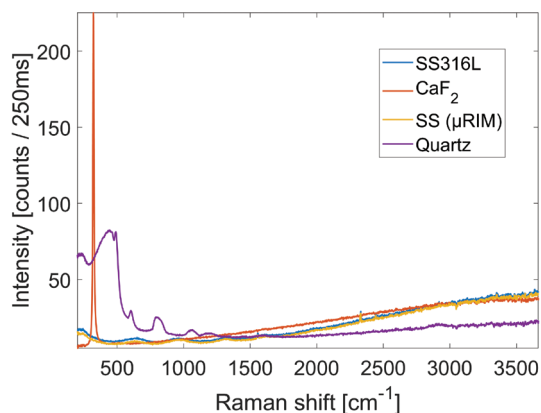


Figure SI4.1. Mean Raman spectra of stainless steel (SS316L), CaF_2 , stainless steel ($\mu\text{RIM}^{\text{TM}}$) and Quartz.

SI 4.2 Navigation markers

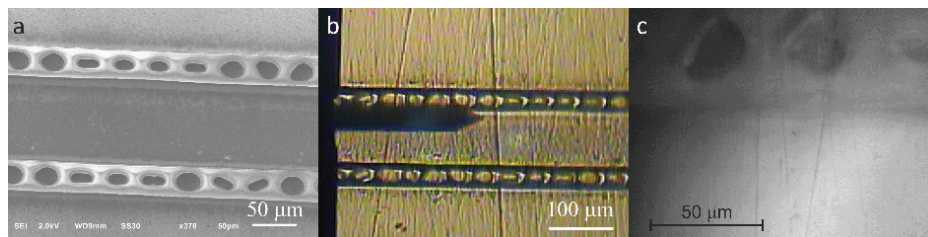


Figure SI4.2. Navigation markers patterned on the stainless steel substrates next to the sample region, using cyanoacrylate glue. a) SEM image of the sample region flanked by the navigation markers; navigation markers as seen through the sample stage optics of the AFM (b) and the Raman spectroscopy imaging setup (c). Knowing the position of a particular object of interest relative to a (unique) combination of navigation features allows easily retracing it in all instruments.

SI 4.3 EV isolation protocol from prostate cancer cell lines (LNCaP)

The LNCaP Prostate cancer cell line purchased at the American Type Culture Collection (ATCC) was used to produce prostate tumor-derived EVs. LNCaP cells were cultured at 37 °C and 5% CO₂ in RPMI-1640 with L-glutamine medium (Lonza, cat.# BE12-702F) supplemented with 10% v/v fetal bovine serum, 10 units/mL penicillin, and 10 µg/mL streptomycin. The initial cell density was 10,000 cells/cm² as recommended by the ATCC. Medium was refreshed every second day. When cells reached 80–90% confluence, they were washed three times with PBS and FBS-free RPMI medium supplemented with 1 unit/mL penicillin and 1 µg/mL streptomycin was added to the cells. After 48 h of cell culture, the cell supernatant was collected and centrifuged at 1000g for 30 min. The pellet containing dead or apoptotic cells and the largest EVs was discarded. The supernatant was pooled, and aliquots of 50 µL were frozen in liquid nitrogen and stored at –80 °C. The size distribution of the harvested EVs was assessed with nanoparticle tracking analysis (NTA) (See SI 4.4).

SI 4.4 NTA measurements of LNCaP EVs

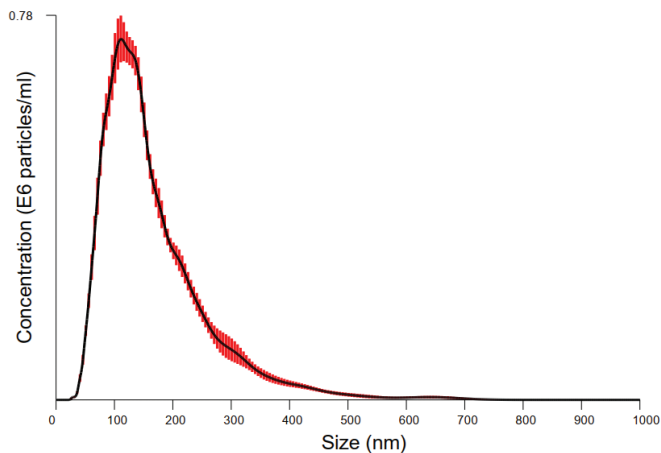


Figure SI4.4. NTA average concentration over 10 samples. Measured using a NanoSight 500 dark field microscope (Nanosight, Amesbury, UK). 5607 particles were measured with an average diameter of 167 ± 91 nm (diameter \pm s.d.), corresponding to a total concentration (before 10x dilution) of 1.06×10^9 ml⁻¹. The raw data from this measurement was used to obtain a histogram compatible with the AFM data from Figure 4.5c.

4

SI 4.5 IRRAS measurements of CDPA as monolayer on stainless steel substrates, and as a powder

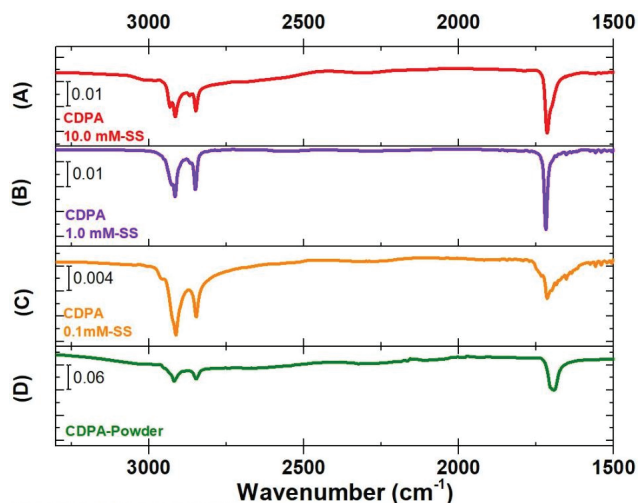


Figure SI4.5. IRRAS reflection spectra for CDPA monolayers prepared using a CDPA concentration of (A) 0.1 mM, (B) 1 mM, and (C) 10 mM, and using CDPA powder.

SI 4.6 Influence of flow dynamics on capturing efficiency

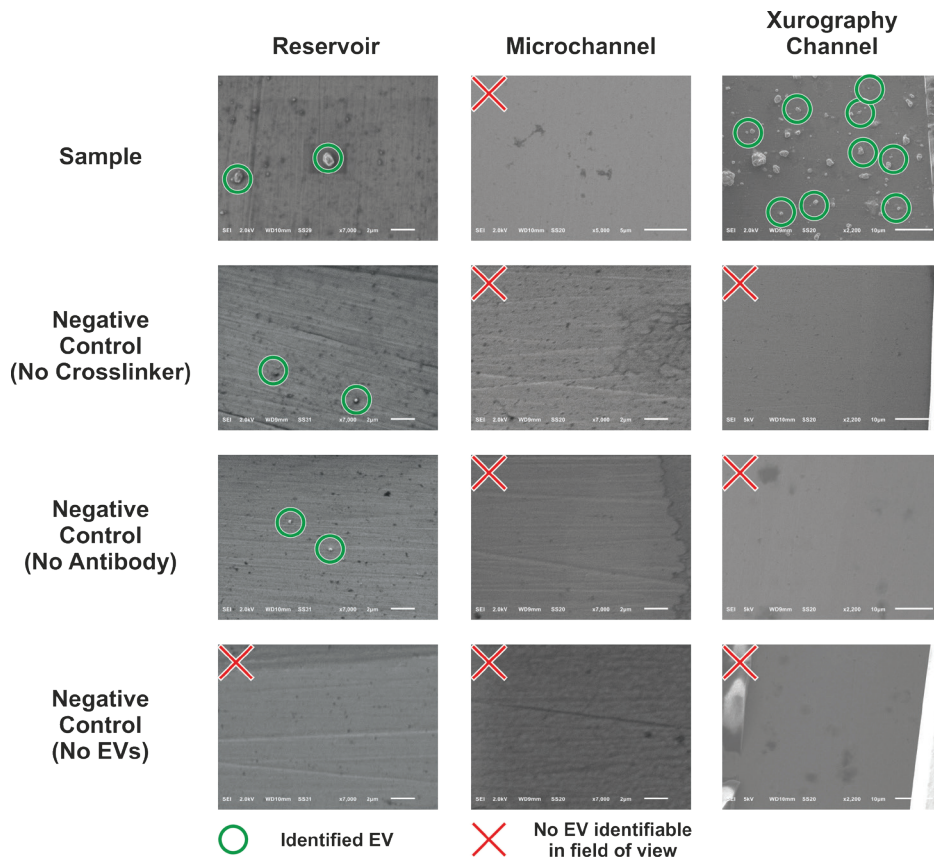
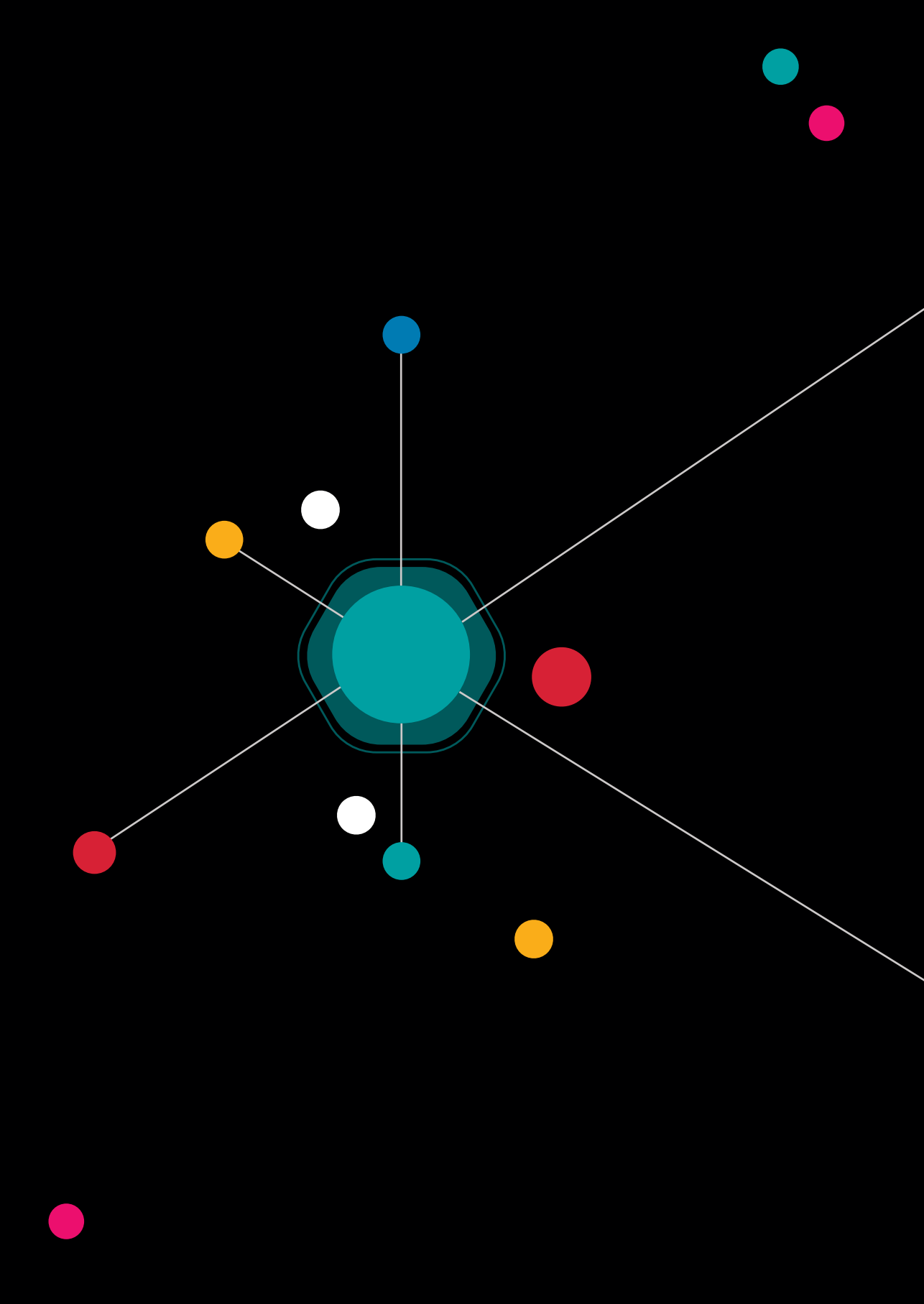


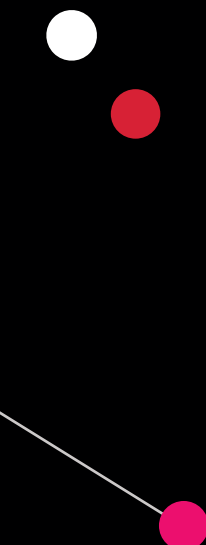

Figure SI4.6. SEM images; comparison of contrast between specifically and non-specifically bound species in various fluidic systems. In a reservoir (left column, scale bar: 2 μm), where EVs are incubated and dehydration agents are exchanged under semi-static conditions, there is an apparent lack of a force to remove physisorbed EVs as can be seen from the negative controls. Using a microchannel of 20- μm height (middle column, scale bars: 5 μm (top) and 2 μm) entails imposing shear forces so high that specifically bound species are also removed when introducing dehydration agents. An intermediate option, use of exceptionally high (~200 μm) microchannels produced by xurography (right column, scale bars: 10 μm) yielded expected results, where EVs were only identified in the positive control.






Chapter 5

Synchronized Rayleigh and Raman scattering for the characterization of single optically trapped extracellular vesicles



A. Enciso-Martinez, E. van der Pol, A.T.M. Lenferink, L.W.M.M. Terstappen, T.G. van Leeuwen and C. Otto

Nanomed Nanotechnol Biol Med, 2020, 24, 102109



Abstract

Extracellular vesicles (EVs) can be used as biomarkers in diseases like cancer, as their lineage of origin and molecular composition depend on the presence of cancer cells. Recognition of tumor-derived EVs (tdEVs) from other particles and EVs in body fluids requires characterization of single EVs to exploit their biomarker potential. We present here a new method based on synchronized Rayleigh and Raman light scattering from a single laser beam, which optically traps single EVs. Rapidly measured sequences of the Rayleigh scattering amplitude show precisely when an individual EV is trapped and the synchronously acquired Raman spectrum labels every time interval with chemical information. Raman spectra of many single EVs can thus be acquired with great fidelity in an automated manner by blocking the laser beam at regular time intervals. This new method enables single EV characterization from fluids at the single particle level.

5.1 Introduction

Recent studies have shown that small lipid-membrane-bound vesicles called Extracellular vesicles (EVs) derived from cancer cells play a role in tumor cell proliferation, migration, invasion, and metastasis,^{1–3} and the peripheral blood load of relatively large tumor-derived EVs is strongly associated with poor clinical outcome.⁴ The EVs, which may be as small as 50 nm,⁵ are able to transport proteins, nucleic acids and membrane components to neighboring or distant cells, influencing cellular behaviors. Hence, EVs derived from diseased cells, such as cancer cells, could trigger oncogenic signals and promote tumor development.² Tumor-derived extracellular vesicles (tdEVs) can be present in body fluids, such as blood.^{6–10} However, their identification and characterization is challenging due to their heterogeneity, ultra-small size, low refractive index, size overlap with physiological EVs and contaminants in body fluids, and the lack of knowledge on their chemical composition. Specially, their broad size range overlaps not only with non-tdEVs, but also with lipoproteins and protein aggregates that fall in the EV size range.¹¹ Thus, the ensemble average inherent to bulk analysis methods require a sensitivity which techniques like ELISA or western blot unlikely have. Single particle analysis may overcome this problem and pave the road towards identification of rare tdEV populations.

There are well established methods for single particle analysis, such as nanoparticle tracking analysis (NTA), resistive pulse sensing and flow cytometry that together can provide the size, number, concentration, electrophoretic mobility and refractive index of EVs. However, these methods fail in providing information on the chemical composition of EVs, which is essential to identify their origin. In recent years, Raman spectroscopy (RS) has been used to contribute chemical information of EVs and tdEVs.^{12–17} RS is a label-free chemical characterization technique based on the inelastic scattering of light by molecules. RS combined with optical tweezers, provides Raman spectra of particles trapped in the focal spot. Pioneered by Ashkin,^{18,19} optical tweezers use a diffraction limited beam to stably trap a particle in three dimensions. Particles in Brownian motion that enter the trapping focal spot experience a net force that brings them to the axial center of the laser beam waist slightly displaced from the focal plane.

Previous studies demonstrate trapping of single solid particles in the size range of EVs, such as silica beads, polystyrene beads and viruses.^{20,21} The trapping of single particles has been complemented with characterization techniques such as fluorescence spectroscopy²² and Raman spectroscopy.²³ Although EVs have also been studied with Raman, single EV Raman measurements have never been experimentally confirmed. Indirect evidence has been used in some studies to presume single EV or liposome trapping and chemical characterization.^{13,14,17,24}



However, the unequivocal prove that a trapping event involves a single EV and the ability to trap EVs at sufficiently high rates has not yet been shown.

Here, we propose a new method to optically trap single EVs and simultaneously disclose their inherent chemical composition by means of RS. The method distinguishes individual particle trapping events by the detected Rayleigh scattered light while synchronously measured Raman spectra enables the chemical characterization of individual EVs. Rayleigh – and Raman scattering are, respectively, elastic and inelastic scattering of light by particles in a medium. Further, our method involves a purge of the optical trap at regular time intervals. Hence, long time series of Rayleigh-Raman scattering events can be acquired starting each time from an empty trap. In this way, many individual trapping events can be acquired in an automated manner. Our method can be directly applied to diluted EV samples and does not require any EV isolation steps. The Raman spectra of multiple individual EVs enable a chemical fingerprint of the sample. We introduce and validate the method with polystyrene (PS) and silica (Si) beads. Subsequently, we show that synchronous Rayleigh-Raman scattering enables the identification of single EVs on the basis of the Raman spectral signature, which is related to their molecular composition.

5.2 Methods

5.2.1 PC3-derived EVs

PC3 cells provided by the American Type Culture Collection (ATCC) were used as a model to produce prostate cancer-derived EVs. Cells were cultured at 37 °C and 5% CO₂ in RPMI-1640 with L-glutamine medium (Lonza, Cat. No.: BE12-702F) supplemented with 10% (v/v) fetal bovine serum (FBS), 10 units/mL penicillin and 10 µg/mL streptomycin. The initial cell density was 10,000 cells/cm² as recommended by the ATCC. Medium was refreshed every second day. At 80 to 90% confluence, cells were washed three times with phosphate buffer solution (PBS) and cultured in FBS-free RPMI-1640 with L-glutamine medium (Lonza, Cat. No.: BE12-702F) supplemented with 1 unit/mL penicillin and 1 µg/mL streptomycin. After 2-3 days of cell culture, cell supernatant was collected in a 15 mL tube (Cellstar® tubes, Greiner Bio-one) and centrifuged at 800 g at room temperature for 10 min (Centrifuge 5804, Eppendorf) . The pellet containing dead or apoptotic cells and large cell fragments was discarded. The collected supernatant containing PC3-derived EVs was stored in aliquots of 500 µL (Micro tube 0,5 mL, PP, SARSTEDT) at -80 °C. Samples were thawed in a water bath at 37°C before use. EV size distribution was determined using NTA (NanoSight NS500). An EV concentration of 1.9x10⁹ particles/mL with a mean diameter (+/- standard deviation) of 157 (+/- 79) nm was found (Figure S5.1).

5.2.2 Polystyrene (Ps) and Silica (Si) beads

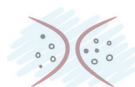
To validate our technology, we used NIST traceable polystyrene (PS) beads (Nanosphere; Thermo Fisher, Waltham, MA, USA) with mean diameters of 100, 125, 147, 296 and 799 nm and plain silica (Si) beads (Silica Kisker, Steinfurt, Germany) with mean diameters of 182, 315, 405 and 548 nm. The concentration was determined by NTA (NS500, Malvern, UK). Diameters of the silica beads were obtained by TEM. The corresponding refractive indices of PS and Si beads are 1.586 and 1.464, respectively. The suspensions of beads were diluted in MiliQ to a concentration of 3×10^8 - 3×10^9 particles/mL to optimize the single particle trapping rate. PS and Si particle suspensions were vortexed for 3 sec and re-suspended 3 times before experiments to prevent particle aggregation that may have occurred during storage. A suspension of 50 μ L of each monodisperse sample of beads was then used for synchronous Rayleigh – and Raman scattering measurements.

5.2.3 Sample preparation

PS beads, Si beads, and EVs derived from PC3 cells were used in a concentration of 3.6×10^8 - 5×10^{10} particles/mL and diluted in MiliQ (beads) or PBS (EVs) to this concentration if necessary. A 50 μ L suspension of each particle type was placed on a well glass slide (BMS Microscopes; 1.0-1.2 mm thick, Cat. no.: 12290). The sample was covered with a glass cover slip (VWR Ltd, thickness No. 1, diameter: 22mm, Cat. no.: 631-0158) and sealed with glue (EVO-STIK, Impact) onto the well glass slide (Figure 5.1A). The glue was then cured at room temperature for ~30 minutes. The closed well glass slide was placed on the microscope table under the objective of the Rayleigh-Raman spectrometer.

5.2.4 Optical setup and measurements

The Rayleigh-Raman spectrometer is based on a home-built Raman spectrometer integrated with the base of an upright optical microscope (Olympus BX41). A single laser beam from a Coherent Innova 70C laser ($\lambda_{\text{exc}} = 647.089$ nm) was used for optical trapping and illuminating beads and EVs. Rayleigh and Raman scattering was collected with a cover glass corrected dry objective (Olympus, 40x, NA: 0.95). Rayleigh and Raman scattering were separated in a homebuilt spectrometer and simultaneously detected with a single CCD camera. The spectrometer had an average dispersion of ~ 2.3 cm^{-1} (0.11 nm) wavenumber per pixel over the CCD camera surface with 1600 pixels along the dispersive axis and 200 pixels perpendicular to this axis. The spectral resolution was ~ 3.0 cm^{-1} . The laser power was measured underneath the objective and adjusted to 70 mW. By moving the objective along the z-axis, the laser focal spot is focused inside the solution, ~ 37 μm below the cover slip. The focal spot has a theoretical diameter of 370 nm and a Rayleigh range of 1160 nm based on full width half maximum. Rayleigh and Raman scattering



spectra were typically acquired 256 times with an acquisition time of 38 ms over a period of ~9.7 seconds. The trapped particles were then released from the optical trap by blocking the laser beam with a shutter for ~1 second. This measurement cycle was repeated, typically, 100 times, which resulted in $100 \times 256 = 25600$ Rayleigh-Raman spectra per measurement.

5.2.5 Backscattering calculations

Light scattering calculations based on Mie theory were used to relate the measured backscattering to the diameter and refractive index of PS and Si beads. The Rayleigh scattering intensity was compared with Mie scattering calculations of the intensity averaged over the collection angle of the microscope objective as a function of particle diameter. From these measurements it was theoretically predicted that with the present embodiment of the setup the Rayleigh light scattering signal was sufficiently intense to detect trapping of individual EVs, in spite of the small refractive index difference of EVs ($n = 1.37$)²⁵ from water ($n = 1.33$). We use the Mie scripts of Mätzler²⁶ in MATLAB (2018b, MathWorks, USA) to calculate the amplitude scattering matrix elements, which describe the relation between the incident and scattered field amplitudes of a sphere. Our model incorporates particle diameter and refractive index (RI), RI of the medium, the illumination wavelength, and the numerical aperture of the microscope.

5.3 Results

Brownian motion of EVs in suspension occasionally brings the EVs sufficiently close to the trap to experience a net trapping force directing towards the focal spot. Once an EV is trapped, an intense increase in the amplitude of the Rayleigh light scattering occurs, and this can be seen as a discrete step in a time trace (Figure 5.1B). Such time trace results from the integration of the Rayleigh band over 50 pixels around 0 cm^{-1} plotted over time. As long as the shutter to the laser remains open, successive trapping and accumulation of particles occur until the focal volume becomes saturated with particles. Hence, monitoring the time trace over prolonged time enables to distinguish between zero (baseline), single (first step) and multiple trapping events, which can be enumerated (Figure 5.1B and 5.1C). Synchronous acquisition of Raman spectra with the Rayleigh scattering allows us to assign a Raman spectrum to individual particles trapped (Figure 5.1D). Purging the laser focus from trapped particles at regular time intervals enables the acquisition of many single EV trapping events in an automated manner over long periods of time, thus monitoring the composition of a suspension of EVs on the level of individual, single EVs with fidelity. Rayleigh and Raman scattering spectra were typically acquired 256 times with an acquisition time of 38 ms over a total period of ~9.7 seconds per cycle. After purging the laser focus a new cycle started.

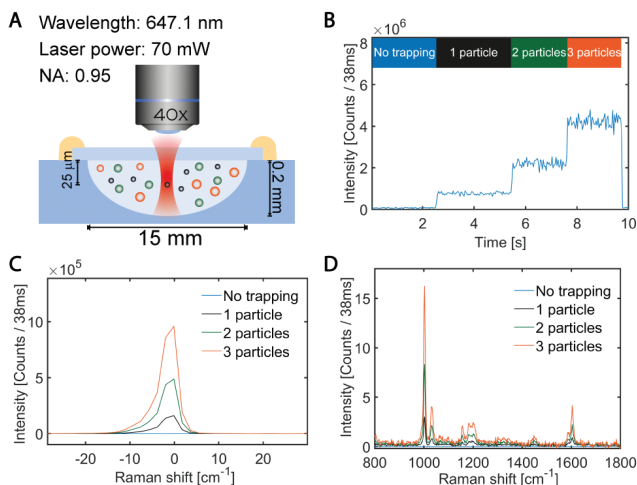


Figure 5.1. (A) Schematic overview of the setup. Particles in suspension are loaded in a well glass slide that is mounted under a microscope objective. (B) Rayleigh scattering intensity versus time clearly shows trapping of single PS beads ($\varnothing=125$ nm). Color labels at the top in (B), indicating the number of particles in the trap, correspond to the color of the traces in (C) and (D). (C) Intensity versus Raman shift for Rayleigh scattering without trapped particles, or with 1, 2 and 3 particles being trapped. (D) Raman scattering signals when no particle is trapped and when 1, 2 and 3 particles are trapped in the laser focal spot.

To validate our technology, single PS and Si beads of various sizes (SI) were optically trapped and synchronous Raman acquisition was performed. To increase the event throughput of our Rayleigh-Raman setup we have automated the trapping and release of particles by acquiring both Rayleigh and Raman scattering signals overtime while closing a laser shutter to purge the trap from particles. Subsequent opening of the shutter starts another cycle of trapping events from an empty trap. For example, Figure 5.2A shows the intensity time traces of both, the Rayleigh and the Raman scattering signals of 100 nm polystyrene beads. Integrating the characteristic 1003 cm^{-1} polystyrene Raman peak and plotting the intensity versus time results in a step-wise time trace that correlates with the Rayleigh time trace. This correlation confirms that the trapped particles indeed are polystyrene beads.

Figure 5.2B shows a magnification of a part of the time trace in Figure 5.2A. In the absence of particles in the laser focus, both scattering signals show a constant baseline. Trapping events can easily be observed from stepwise increases in the amplitude of the scattering signals. These signals increase upon the arrival and trapping of the first, second, third and fourth bead (labelled as 1, 2, 3 and 4, respectively in Figure 5.2B). The average Rayleigh signal per time interval (0, 1, 2, 3 and 4 in Figure 5.2B) is shown in Figure 5.2C. Synchronous Raman acquisition labels each time interval with a Raman spectrum. The average Raman spectra of polystyrene for the five time intervals in Figure 5.2B are shown in Figure 5.2D.



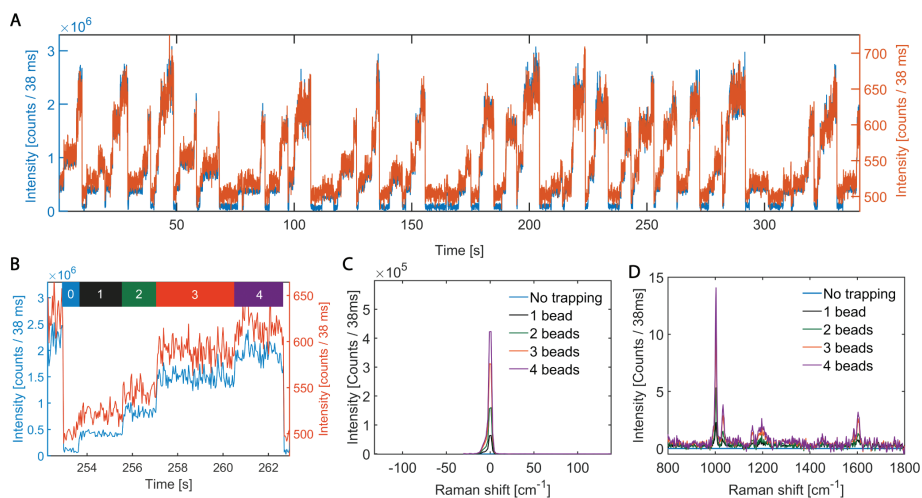


Figure 5.2. Rayleigh and Raman scattering signals of PS beads ($\varnothing=100$ nm). **(A)** Time trace of 35 cycles of Rayleigh (blue) and Raman (orange) scattering signals. This dataset contains $35 \times 256 = 8960$ spectra. **(B)** Magnified cycle from **(A)** to highlight the coincidences in the time traces of both, Rayleigh and Raman scattering signals for 4 trapping events (labelled as 0, 1, 2, 3 and 4), with **(C)** and **(D)** showing the corresponding Rayleigh and Raman scattering signals.

The discrete nature of the time traces can be better visualized by segmenting all the levels in the Rayleigh signal and plotting the median value of each level versus time, as shown in [Figure 5.3A](#). Here, the time trace corresponds to the trapping and release of polystyrene beads with a diameter of 125 nm. The median values of each level in the Rayleigh intensity time traces are represented with a triangle. [Figure 5.3B](#) shows a typical boxplot with a low standard deviation of the Rayleigh scattering intensities corresponding to the discrete trapping of beads. Five levels of scattering can be identified, namely the baseline (no trapped beads), and the first -, second -, third - and fourth step or trapping event. [Figure 5.3C](#) (black squares and red circles, right axis) shows the experimentally obtained backscatter intensity of the PS ($n=1.586$) and Si ($n=1.464$) beads in water ($n=1.3317$) versus their diameter. The backscatter intensity values correspond to the amplitude of the Rayleigh scattering for the first trapping events (e.g. blue box in [Figure 5.3B](#)). These values have been plotted versus diameter and theoretically described by Mie theory, taking into account the diameter and refractive index of the beads as well as the optical configuration of the setup. Mie theory predicts an angle-dependent oscillatory behavior of the scattering cross section ([Figure 5.3C](#), left axis) for the collected backscattered light.

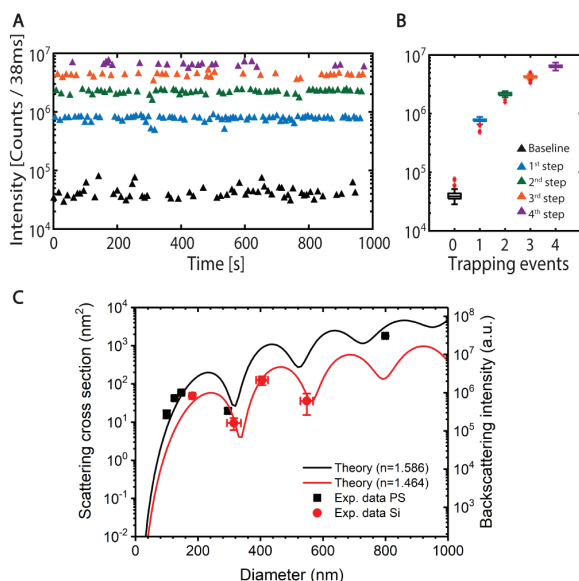
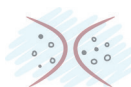


Figure 5.3. (A) Rayleigh scattering intensity of PS beads ($\varnothing=125$ nm), after time trace segmentation, and (B) its corresponding boxplot. (C) Prediction of the back-scattered signals (lines) from PS beads (black) and Si beads (red). The left vertical axis depicts the cross-section and the right vertical axis depicts the counts per 38 ms. Vertical error bars are SD of measured amplitudes. Horizontal error bars are SD of size distributions as provided by manufacturer.

After developing and validating a procedure to trap single beads and measuring their Rayleigh scattering and Raman spectrum, we proceeded to investigate suspensions of EVs derived from a prostate cancer cell line (PC3 EVs) by synchronized Rayleigh – Raman scattering. Their intensity time traces are shown in Figure 5.4A. The associated Raman scattering time trace was obtained from the integration of the lipid-protein band in the Raman spectrum between 2811 cm^{-1} and 3023 cm^{-1} . The Rayleigh – and Raman time traces show synchronous steps associated with trapping events and provide a tool to confirm the presence of a single EV in the trap. The mean Rayleigh intensity for PC3 EVs is 1.74×10^5 with a SD of 1.6×10^5 ($n=94$). Figure 5.4B shows a magnified portion of the time trace in Figure 5.4A with four time intervals labelled as 0, 1, 2, 3 and 4, corresponding to no trapping, first, second, third and fourth trapping events, respectively. The synchronously measured Raman spectra are extracted from the time trace and correspond to the Raman fingerprint of the particles trapped at the respective time intervals. Figure 5.4C shows the Raman spectra of four different single PC3 EVs that correspond to the four time intervals presented in Figure 5.4B.

To obtain a Raman fingerprint of PC3 EVs, we segmented the first particle trapping events from the Rayleigh time traces and thus obtained the time intervals where individual EVs generated a Raman spectrum. Figure 5.4D shows the mean Raman spectra after baseline correction and



noise removal for 94 PC3 EVs. Typical lipid and protein bands are shown at 1004, 1128, 1300, 1340, 1443, 1607, 1636-1690 cm^{-1} , as well as in the high frequency region between 2811 and 3023 cm^{-1} . Among other Raman peaks found in PC3 EVs are: 1247 (Amide III)²⁷ and 1663 (DNA and Amide I of proteins)²⁷, further confirming the trapping of EVs.

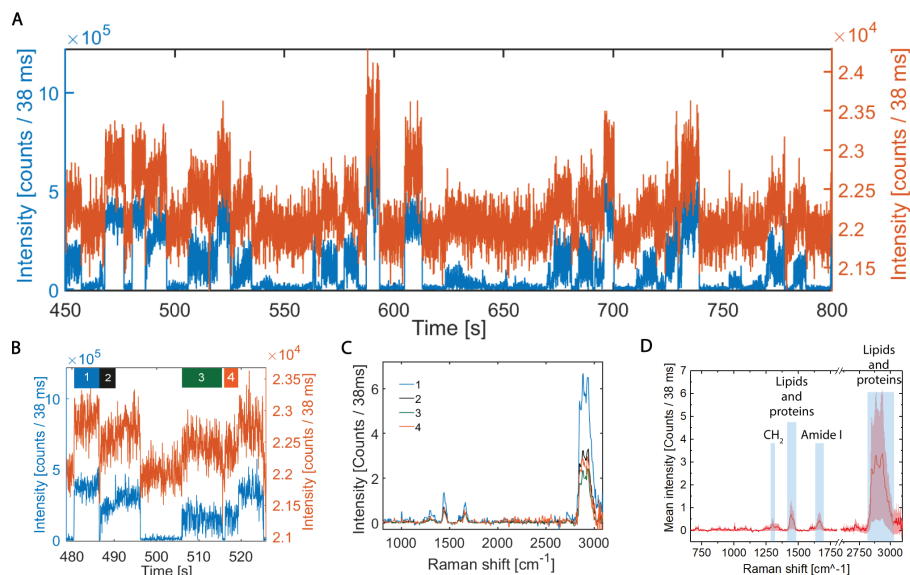


Figure 5.4. Rayleigh and Raman scattering signals of PC3 EVs. **(A)** Time trace of Rayleigh (blue) and Raman (orange) scattering signals. This dataset contains 100 cycles \times 256 = 25600 spectra. **(B)** Magnified cycle from **(A)** indicating 4 time intervals with single trapped PC3 EVs (labelled as 1, 2, 3 and 4), whose corresponding Raman spectra are shown in **(C)**. **(D)** Mean Raman spectrum (thick line) and SD (shaded area) for 94 PC3 EVs.

5.4 Discussion

Identification and characterization of a sub-population of EVs (e.g. tdEVs) requires a method working at the single EV level. To achieve this, optical trapping and subsequent chemical characterization by Raman spectroscopy has been shown to be an attractive approach, because it is essentially a label-free approach that requires minimal sample preparation and enables chemical characterization of EVs in fluids. However, previous studies have shown that Raman spectroscopy requires long integration times of many seconds up to minutes,¹³⁻¹⁷ leading to the problem of trapping multiple particles. One option is to decrease the concentration of EVs and avoid any multiple trapping events, but the disadvantage is that at such low concentrations the chance of actually trapping an EV of interest, such as tdEVs, becomes low, and the acquisition of a sufficient large number of Raman spectra from single EVs may take many hours.

In this study, we have successfully investigated a new approach of synchronized Rayleigh and Raman scattering, that enables to measure Raman spectra of single EVs from samples with 1.9×10^9 EVs/mL at a reasonable high trapping rate. In this approach, the Rayleigh scattering was used to detect the arrival of each individual particle in the trap from a large increase in the Rayleigh scattering signal. Synchronously, the Raman scattering signal was obtained with the same acquisition time as the Rayleigh scattering signal. Integration over the lipid-protein high frequency band enabled to obtain Raman time traces that coincide with the Rayleigh time traces. The time synchronicity is essential to enable an unequivocal relation between single EV trapping events visualized with Rayleigh scattering and the characteristic Raman fingerprint of that EV.

In order to establish the method of synchronous Rayleigh – Raman scattering, we first measured PS and Si beads in suspension. PS and Si beads with a refractive index of 1.586 and 1.464, and a diameter down to 100 nm and 182 nm, respectively, were easily trapped. Individual trapping events could be detected (Figure 5.2) and the time-synchronized Raman scattering assigned the familiar polystyrene spectrum to each PS particle. Mie theory was used to predict the scattering cross section of single PS and Si beads of different sizes. The prediction is in agreement with the experimental backscatter intensity values obtained from optically trapped single PS and Si beads.

Unlike PS and Si beads, EVs have a lower refractive index (1.35 – 1.40),^{25,28–31} making their refractive index contrast small with respect to the aqueous solution with a refractive index of 1.3317. Such small refractive index contrast also results in a decrease of the trapping force. However, we were able to trap and identify single PC3 EVs from a sample containing EVs with a diameter of 157 (+/- 79) nm, according to NTA. In addition, the low integration time (38 ms) and subsequent automated data analysis allowed the identification of single EVs in the focal spot and Raman spectra acquisition from approximately 400 single-EVs per hour. The signal processing that we have implemented automated the computation of Raman and Rayleigh time traces and segmented the step-wise signal to identify single and multiple trapping events with their respective Raman spectra.

Previous studies have claimed single EV trapping based on an increase of the Raman scattering signal.^{14,15,17} Our approach integrates the Rayleigh scattering signal as a way to monitor and prove the trapping of single EVs. This enables the identification of smaller particles as the Rayleigh signal is much stronger ($\times \sim 10^3$ to 10^4) than Raman scattering, whose weak scattering process can miss the detection of very small particles. Our method has the additional advantage of identifying single EVs irrespective of their Raman spectra due to the fact that it does not rely



on thresholding of a characteristic Raman peak or band integration. This becomes critical when trying to identify rare EV populations within a mixture of many other EV types. While the Rayleigh scattering signal allows the detection of single particles irrespective of their chemical composition, the Raman signal is used to identify the type of particles trapped. Other studies have relied on fluorescence signal to identify single EVs.¹³ Immunostaining can disclose molecular-specific information, but it complicates sample preparation and workflow and requires specific markers to be used for rare EV populations. Our method is label-free and does not require additional steps to disclose the chemical information of an EV from its medium.

Although label-free Raman spectroscopy is not specific to molecules, the global information in Raman spectra enables to differentiate among different vesicles as previous studies of non-labelled EVs have demonstrated.¹³⁻¹⁶ Our results show that the spectral region between 2811-3023 cm^{-1} , assigned to proteins and lipids, is the highest Raman intensity band for EVs (around 3x higher than the highest peak in the fingerprint region for PC3 EVs). This region in the Raman spectrum between 2811-3023 cm^{-1} enables an identification of different types of small single EVs and eventually tdEVs in plasma from cancer patients. The throughput of our technique can still be improved, e.g. by increasing the length of the time traces.

In conclusion, by synchronous acquisition of Rayleigh and Raman light scattering during optical trapping of sub-micrometer particles in suspension, we have been able to identify single trapping events at a high rate. This method could allow the identification of rare populations of EVs, such as tdEVs, where otherwise the ensemble average occludes the signal from single rare EVs. The synchronized detection of Rayleigh – Raman scattering and the ability to characterize single individual nanoparticles opens a vast number of applications in different fields, e.g. identification of micro-plastics in contaminated water, virus detection, atmospheric science and catalysis,²³ among others.

References

1. Vader, P., Breakefield, X. O. & Wood, M. J. A. Extracellular vesicles: Emerging targets for cancer therapy. *Trends Mol. Med.* 20, 385–393 (2014).
2. Katsuda, T., Kosaka, N. & Ochiya, T. The roles of extracellular vesicles in cancer biology: Toward the development of novel cancer biomarkers. *Proteomics* 14, 412–425 (2014).
3. Kanada, M., Bachmann, M. H. & Contag, C. H. Signaling by Extracellular Vesicles Advances Cancer Hallmarks. *Trends in Cancer* 2, 84–94 (2016).
4. Nanou, A. et al. Abstract 4464: Tumor-derived extracellular vesicles in blood of metastatic breast, colorectal, prostate, and non-small cell lung cancer patients associate with worse survival. in *AACR 2019 Proceedings: Abstract 4464 - American Association for Cancer Research 4464–4464* (2019). doi:10.1158/1538-7445.sabcs18-4464
5. Brisson, A. R., Tan, S., Linares, R., Gounou, C. & Arraud, N. Extracellular vesicles from activated platelets: a semiquantitative cryo-electron microscopy and immuno-gold labeling study. *Platelets* 28, 263–271 (2017).
6. Zwicker, J. I. et al. Tumor-derived tissue factor-bearing microparticles are associated with venous thromboembolic events in malignancy. *Clin. Cancer Res.* 15, 6830–40 (2009).
7. Li, J. et al. Claudin-containing exosomes in the peripheral circulation of women with ovarian cancer. *BMC Cancer* 9, 244 (2009).
8. Coumans, F. A. W., Doggen, C. J. M., Attard, G., de Bono, J. S. & Terstappen, L. W. M. M. All circulating EpCAM+CK+CD45- objects predict overall survival in castration-resistant prostate cancer. *Ann. Oncol. Off. J. Eur. Soc. Med. Oncol.* 21, 1851–7 (2010).
9. Nanou, A. et al. Circulating tumor cells, tumor-derived extracellular vesicles and plasma cytokeratins in castration-resistant prostate cancer patients. *Oncotarget* 9, 19283–19293 (2018).
10. Wit, S. et al. Single tube liquid biopsy for advanced non-small cell lung cancer. *Int. J. Cancer* 144, 3127–3137 (2019).
11. Buzás, E. I. et al. Single particle analysis : Methods for detection of platelet extracellular vesicles in suspension (excluding flow cytometry) Single particle analysis : Methods for detection of platelet extracellular vesicles in suspension (excluding flow cytometry). *Platelets* 00, 1–7 (2017).
12. Krafft, C. et al. A specific spectral signature of serum and plasma-derived extracellular vesicles for cancer screening. *Nanomedicine Nanotechnology, Biol. Med.* 13, 1–7 (2016).
13. Carney, R. P. et al. Multispectral Optical Tweezers for Biochemical Fingerprinting of CD9-Positive Exosome Subpopulations. *Anal. Chem.* 89, 5357–5363 (2017).
14. Smith, Z. J. et al. Single exosome study reveals subpopulations distributed among cell lines with variability related to membrane content (S). *J. Extracell. Vesicles* 4, 28533 (2015).
15. Kruglik, S. G. et al. Raman tweezers microspectroscopy of circa 100 nm extracellular vesicles. *Nanoscale* 11, 1661–1679 (2019).
16. Lee, W. et al. Label-Free Prostate Cancer Detection by Characterization of Extracellular Vesicles Using Raman Spectroscopy. *Anal. Chem.* 90, 11 (2018).
17. Penders, J. et al. Single Particle Automated Raman Trapping Analysis. *Nat. Commun.* 9, 4256 (2018).
18. Ashkin, A. Acceleration and Trapping of Particles by Radiation Pressure. *Phys. Rev. Lett.* 24, 156–159 (1970).



19. Ashkin, A., Dziedzic, J. M. & Chu, S. Observation of a single-beam gradient force optical trap for dielectric particles. *Opt. Lett.* 11, 288–290 (1986).
20. Liu, T. H., Chiang, W. Y., Usman, A. & Masuhara, H. Optical Trapping Dynamics of a Single Polystyrene Sphere: Continuous Wave versus Femtosecond Lasers. *J. Phys. Chem. C* 120, 2392–2399 (2016).
21. Ashkin, A. & Dziedzic, J. M. Optical trapping and manipulation of viruses and bacteria. *Science* 235, 1517–20 (1987).
22. Pang, Y., Song, H., Kim, J. H., Hou, X. & Cheng, W. Optical trapping of individual human immunodeficiency viruses in culture fluid reveals heterogeneity with single-molecule resolution. *Nat. Nanotechnol.* 9, 624–630 (2014).
23. Rkiouak, L. et al. Optical trapping and Raman spectroscopy of solid particles. *Phys. Chem. Chem. Phys.* 16, 11426–11434 (2014).
24. Chan, J. W., Winhold, H., Lane, S. M. & Huser, T. Optical trapping and coherent anti-Stokes Raman scattering (CARS) spectroscopy of submicron-size particles. *IEEE J. Sel. Top. Quantum Electron.* 11, 858–863 (2005).
25. Van Der Pol, E., Coumans, F. A. W., Sturk, A., Nieuwland, R. & van Leeuwen, T. G. Refractive Index Determination of Nanoparticles in Suspension Using Nanoparticle Tracking Analysis. 14, 6195–6201 (2014).
26. Mätzler, C. MATLAB Functions for Mie Scattering and Absorption Version 2. (2002).
27. Movasaghi, Z., Rehman, S., Rehman, I. U. I. U. & Zanyar Movasaghi, S. R. & D. I. U. R. Raman Spectroscopy of Biological Tissues. *Appl. Spectrosc. Rev.* 42, 493–541 (2007).
28. M. Rupert, borah L. et al. Effective Refractive Index and Lipid Content of Extracellular Vesicles Revealed Using Optical Waveguide Scattering and Fluorescence Microscopy. *Langmuir* 34, 8522–8531 (2018).
29. Gardiner, C. et al. Measurement of refractive index by nanoparticle tracking analysis reveals heterogeneity in extracellular vesicles. *J. Extracell. Vesicles* 3, (2014).
30. Konokhova, A. I. et al. Light-scattering flow cytometry for identification and characterization of blood microparticles. *J. Biomed. Opt.* 17, 057006 (2012).
31. van der Pol, E. et al. Absolute sizing and label-free identification of extracellular vesicles by flow cytometry. *Nanomedicine Nanotechnology, Biol. Med.* 14, 801–810 (2018).

Supporting Information

PC3-derived EVs

EV size distribution was determined using nanoparticle tracking analysis (NanoSight NS500). An EV concentration of 1.9×10^9 particles/mL with a mean diameter (\pm standard deviation) of 157 (\pm 79) nm was found (Figure S5.1).

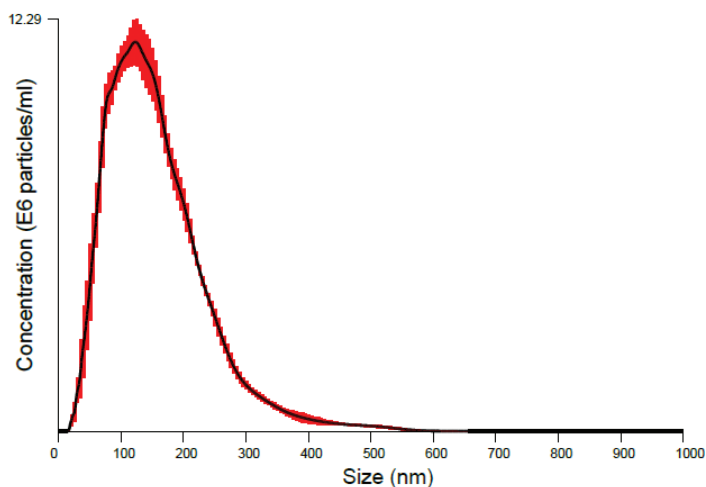
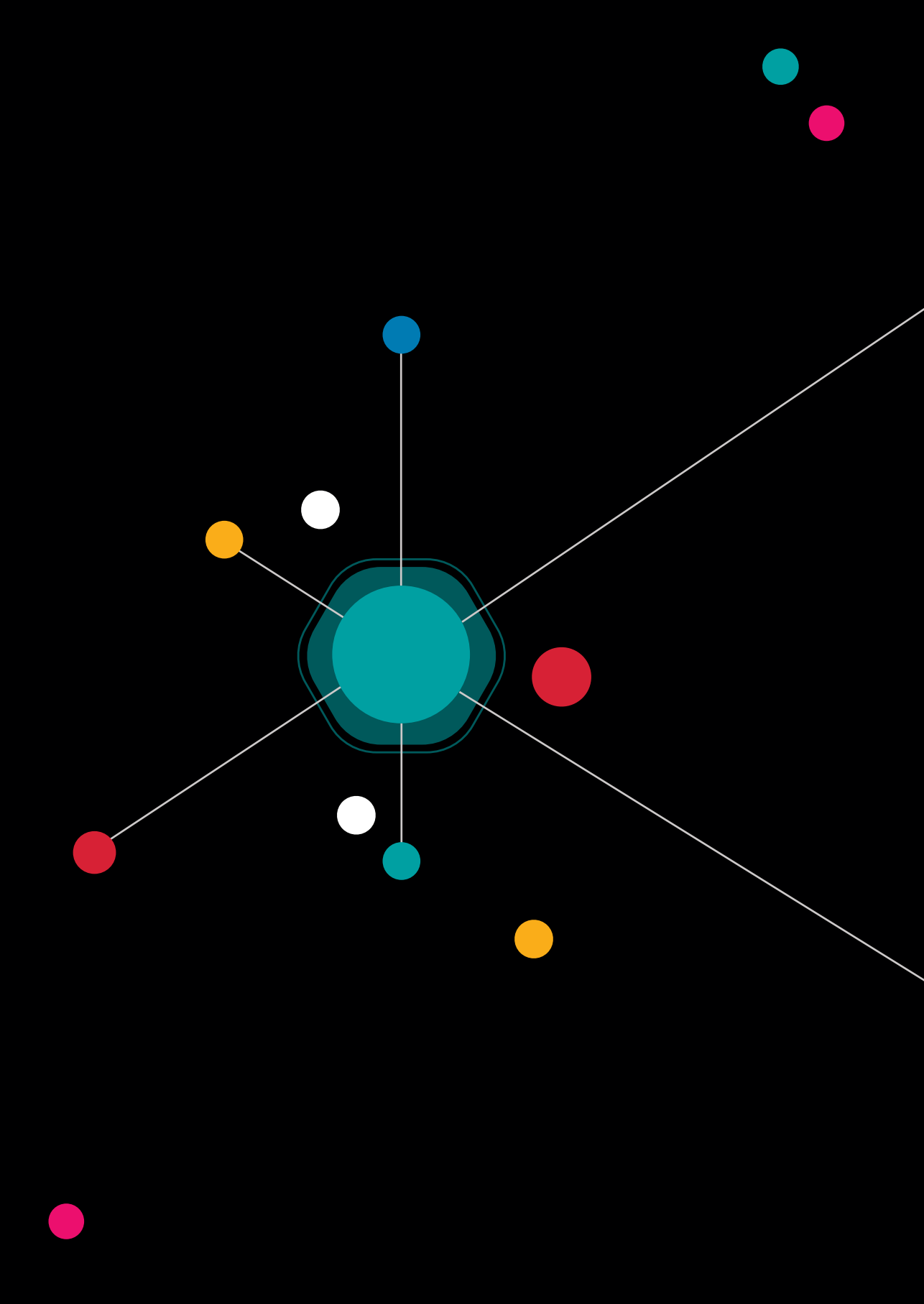


Figure S5.1. Characterization of PC3-derived EVs by Nanoparticle Tracking Analysis. Black line indicates the average size distribution and red error bars indicate the standard error of the mean. Measurements were done in an undiluted sample with a sCMOS camera; shutter, 8.9 ms; gain, 250; threshold, 6). Five videos of 60 s were captured at 22.0 °C and analyzed by NTA v2.3 (NanoSight), assuming a medium viscosity of 0.95 cP.

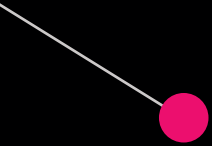











Chapter 6

Label-free identification and chemical characterization of single EVs and lipoproteins by synchronous Rayleigh and Raman scattering



A. Enciso-Martinez, E. van der Pol, C.M. Hau, R. Nieuwland, T.G. van Leeuwen, L.W.M.M. Terstappen and C. Otto

Journal of Extracellular Vesicles, 2020, 9, 1730134



Abstract

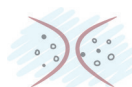
Extracellular vesicles (EVs) present in blood originate from cells of different origin such as red blood cells, platelets and leukocytes. In cancer patients, a small portion of EVs originate from tumor cells and their load is associated with poor clinical outcome. Identification of these tumor-derived extracellular vesicles (tdEVs) is difficult as they are outnumbered by EVs of different tissue of origin as well a large number of lipoproteins (LPs) that are in the same size range. In order to detect tdEVs from the abundant presence of other particles, single particle techniques are necessary. Here, synchronous Rayleigh and Raman scattering is used for that purpose. This combination of light scattering techniques identifies optically trapped single particles on the basis of Rayleigh scattering and distinguishes differences in chemical composition of particle populations based on Raman scattering. Here, we show that tdEVs can be distinguished from RBC EVs and LPs in a label-free manner and directly in suspension.

6.1 Introduction

Extracellular vesicles (EVs) are spherical particles enclosed by a lipid membrane that are released by prokaryotic and eukaryotic cells. EVs play a key role in intercellular communication,¹ that enables cells to send and receive messages encoded in the biomolecules that make up the EVs, namely lipids, proteins, nucleic acids and sugars. In recent years, it has become accepted that body fluids, such as blood, urine and cerebrospinal fluid contain EVs.² Under physiological conditions, blood contains 10^6 - 10^{12} EVs per mL²⁻⁴ which originate from blood cells and the vessel wall.⁵ However, in pathological conditions for example, cancer cells may release EVs. Hence, in cancer, tumor-derived EVs (tdEVs) may be present within the circulation.⁶⁻⁸ In peripheral blood, the concentration of tdEVs, as identified after EpCAM enrichment and using cytokeratin immunofluorescent staining, ranges from 10 to 10^3 EVs per mL and is strongly associated with poor clinical outcome.⁸⁻¹¹ In these studies, only the larger tdEVs were identified and new studies are still needed to determine the frequency and characteristics of the smaller tdEVs. In addition, characterization of the composition of tdEVs may contain information to determine the optimal therapy.

Isolating, identifying and characterizing tdEVs is challenging due to the (1) heterogeneity of EVs, (2) limited knowledge on the chemical composition of EVs, (3) low light scattering efficiency, and (4) size overlap between EVs and non-EV particles, such as lipoproteins (LPs). The smallest EVs range in diameter from 30 nm to 50 nm, depending on the sample, whereas the largest EVs exceed 1 μm .^{4,12-14} These small size ranges together with a refractive index (RI) below typically 1.42 make that EVs scatter light inefficiently. In addition, EV isolation methods lack standardization and the study of EVs can be biased depending on the isolation method used.^{15,16} Therefore, isolation methods that avoid altering the physical and chemical properties of EVs are preferred. Specific labeling of tdEVs is particularly relevant for blood plasma samples, where tdEVs are outnumbered by lipoproteins.^{2,11} Although size exclusion chromatography (SEC) based on CL-2B can efficiently remove small lipoproteins (\sim <70 nm),¹⁷ bigger lipoproteins in the size range of EVs, such as very low-density lipoproteins (VLDL) and chylomicrons (CM), remain present. Bulk analysis methods, such as western blot and mass spectroscopy, are useful to characterize the EV composition in a label-free manner, but not at the single particle level. The inherent averaging of bulk particle analysis methods precludes the detection of rare EV populations, such as tdEVs. Therefore, a technique that can identify and characterize single tdEVs is an important step to exploit tdEVs as biomarker for cancer.

Detection of single EVs by elastic light scattering has been proven to be a feasible approach.¹⁸⁻²⁰ The light that illuminates a particle is partially scattered with the same energy as the incident



light, a phenomenon known as Rayleigh scattering. In addition to Rayleigh scattering, light can also be scattered inelastically, after which the light is shifted in frequency. The shifts in frequency will become visible when a monochromatic laser source is used for illumination. The spectrum resulting from this so-called Raman scattering directly depends on the molecules that the particle is composed of. Hence, Raman scattering provides information about the chemical composition of the EVs. The scattered light can be collected and even the light scattered by single EVs can be detected.²⁰ Furthermore, if the laser illuminating a particle is tightly focused, the particle near the focus will experience a net force directing it to the axial center of the laser beam where the particle remains optically trapped as long as the laser is on.²⁰⁻²⁸ Synchronized Rayleigh and Raman scattering of optically trapped single particles enables single particle label-free analysis.²⁰

Here, we hypothesize and show that single EVs from different cellular origin are characterized by a different Raman spectrum in dependence of their variation in molecular composition. Furthermore, we will show that lipoprotein particles can be distinguished from EVs directly in suspension without labelling. As a proof of principle, we demonstrate here label-free differentiation of single red blood cell (RBC) EVs, lipoproteins and prostate cancer EVs in plasma.

6.2 Materials and methods

6.2.1 Tumor derived EVs

The two prostate cancer cell lines PC-3 and LNCaP American Type Culture Collection (ATCC, CRL-1435 and CRL-1740, USA) were used as a model to produce tdEVs. Both cell lines were cultured at 37 °C and 5% CO₂ in RPMI-1640 with L-glutamine medium (Lonza, Cat. No.: 12-702F) supplemented with 10% (v/v) fetal bovine serum (FBS), 10 units/mL penicillin and 10 µg/mL streptomycin. The initial cell density was 10,000 cells/cm² as recommended by the ATCC. Medium was refreshed every second day. At 80-90% confluence, cells were washed three times with phosphate buffer solution (PBS) and cultured in FBS-free RPMI-1640 with L-glutamine medium (Lonza, Basel, Switzerland, Cat. No.: 12-702F) supplemented with 1 unit/mL penicillin and 1 µg/mL streptomycin. After 2-3 days of cell culture, cell supernatant was collected in a 15 mL tube (Cellstar® tubes, Greiner Bio-one BV, Alphen a/d Rijn, The Netherlands) and centrifuged at 500-800 xg at room temperature for 10 min (Centrifuge 5804, Eppendorf, Hamburg, Germany). The pellet containing dead or apoptotic cells and large cell fragments was discarded. The collected supernatants containing PC-3 and LNCaP EVs were stored in aliquots at -80 °C. Samples were thawed in a water bath at 37 °C before use. EV size distribution and concentration were determined by both nanoparticle tracking analysis (NTA) (NanoSight NS500, UK) and flow cytometry (SI).

6.2.2 Red blood cell (RBC) derived EVs

RBC EVs were obtained from a RBC concentrate (150 mL, Sanquin Bloodbank, Amsterdam, The Netherlands) and diluted 1:1 with filtered PBS. Samples were centrifuged three times at 1560 xg for 20 min at 20 °C using a Rotina 46RS centrifuge (Hettich, Tuttlingen, Germany). The EV-containing supernatant was pooled and deposited in aliquots of 50 μ L, which were snap frozen in N₂ (l) for 15 min and stored at -80 °C until use. Samples were thawed in a water bath at 37 °C before use. EV size distribution and concentration were determined by both NTA (NanoSight NS500, UK) and flow cytometry (SI).

6.2.3 “Platelet particles”

With the term “platelet particles”, we refer to platelet-derived EVs and lipoproteins particles (LPs) present in platelet concentrate, which can be optically trapped (*vide infra*). Platelet concentrate (100 mL, Sanquin Bloodbank, Amsterdam, The Netherlands) was diluted 1:1 with filtered PBS. Next, 40 mL acid citrate dextrose (ACD; 0.85 mol/L trisodiumcitrate, 0.11 M D-glucose and 0.071 M citric acid) was added and the suspension was centrifuged for 20 min at 800 xg, 20 °C. Thereafter, the supernatant was centrifuged (20 min at 1560 xg, 20 °C). This centrifugation procedure was repeated twice to ensure removal of platelets. The supernatant was pooled and deposited in aliquots of 50 μ L, which were snap frozen in N₂ (l) for 15 min and stored at -80 °C until use. Samples were thawed in a water bath at 37 °C before use. Particle size distribution and concentration were determined by both NTA (NanoSight NS500, UK) and flow cytometry (SI).

6.2.4 Plasma

Blood from anonymous healthy donors was obtained from the TNW-ECTM-donor services (University of Twente, Enschede, The Netherlands) after written informed consent. The blood sample was collected by venipuncture in CellSave preservative tubes (10 mL, Menarini - Silicon Biosystems Inc, Huntington Valley, PA, USA). Blood was centrifuged (Centrifuge 5804, Eppendorf, Hamburg, Germany) in a CellSearch conical tube for 10 min at 800 xg without brake (on deceleration). Plasma was taken up to 1 cm above the red blood cell layer and stored in 1.5 mL tubes (Greiner Bio-one, Alphen a/d Rijn, The Netherlands, Cat. No.: 616201) at -80 °C until use. The particle size distribution and concentration were determined by flow cytometry (SI) only, due to the small sample availability. With the term “plasma particles”, we refer to all particles present in plasma, including EVs and LPs.

6.2.5 Lipoprotein particles (LPs)

From all types of lipoprotein particles, we expect that our Raman setup, flow cytometer and nanoparticle tracking analysis (NTA) primarily measure chylomicrons (CM) and very low-density lipoproteins (VLDL). Therefore, we acquired CM from human plasma (Sigma-Aldrich Chemie



N.V., Netherlands, SRP6304) with a purity of $\geq 95\%$ (SDS-PAGE), as specified by the provider. VLDL from human plasma were acquired (Sigma-Aldrich Chemie N.V., Netherlands, 437647) with a purity of $\geq 95\%$ of total lipoprotein content by electrophoresis, as specified by the provider.

6.2.6 Nanoparticle tracking analysis (NTA)

All samples except plasma (due to limited sample availability) were characterized with NTA (NanoSight NS500, Malvern, UK) to confirm the presence of submicrometer particles and obtain an order of magnitude estimate of the concentration of particles exceeding the minimum detectable size. For EVs, the minimum detectable diameter of the used instrument is 70-90 nm¹⁴. For detailed NTA settings see SI.

6.2.7 Flow cytometry (FCM)

To confirm the presence of EVs and LPs, FCM (A60-Micro, Apogee, UK; Rosetta Calibration, Exometry, The Netherlands) was performed on all the samples. In short, we triggered on side scattering using a threshold of 14 arbitrary units, corresponding to a side scattering cross section of $\sim 10 \text{ nm}^2$ (Rosetta Calibration, Exometry, The Netherlands). The flow rate was $3.01 \mu\text{L}/\text{min}$. To calibrate the side scattering detector, Rosetta Calibration was applied²⁹, which assumes that EVs are core-shell particles with a 5 nm thick shell of refractive index (RI) $n_{\text{shell}}=1.48$ and a core of RI $n_{\text{core}}=1.40$. Two μm APC Quantitative (Q-APC) beads (BD Biosciences, San Jose, CA, USA) and SPHERO™ PE MESF beads (Spherotech Inc., Illinois, USA) were used to calibrate the fluorescence detectors. We applied the flow cytometry scatter ratio (Flow-SR) to determine the effective RI,¹⁹ allowing differentiation between LPs and EVs.³⁰ Table 1 of this manuscript reports the *Concentration FCM total*, *Concentration FCM RI<1.42*, *Concentration RI>1.45*, and *Concentration FCM labeled EVs*. *Concentration FCM total* are all detected particles exceeding the side scattering cross section of $\sim 10 \text{ nm}^2$. Assuming that EVs match the aforementioned RI distribution, this corresponds to EVs of 162 nm and larger in diameter. *Concentration FCM RI<1.42* are all detected particles for which Flow-SR can be applied (200-800 nm in diameter and ~ 1 order of magnitude above the detection limits for forward and side scatter) and which have a RI<1.42. As previously confirmed,^{19,30} most of these particles are EVs. *Concentration RI>1.45* are all detected particles for which Flow-SR can be applied (200-800 nm in diameter and ~ 1 order of magnitude above the detection limits for forward and side scatter) and which have a RI>1.45. As previously confirmed,^{19,30} most of these particles are LPs. Gates are shown in [Figure S6.5](#).

6.2.8 Sample preparation

In synchronized Rayleigh and Raman scattering, the PC-3 EVs, LNCaP EVs, RBC EVs, “platelet particles” and “plasma particles” were, if necessary, diluted in PBS up to a concentration of

$\sim 10^{10}$ particles/mL. A 50 μL suspension of each particle type was placed on a well glass slide (BMS Microscopes; 1.0-1.2 mm thick, Cat. no.: 12290). The sample was covered with a glass cover slip (VWR Ltd, thickness No. 1, diameter: 22 mm, Cat. no.: 631-0158) and sealed with glue (EVO-STIK, Impact) onto the well glass slide to avoid evaporation.²⁰ The glue was then cured at room temperature for ~ 30 min. The closed well glass slide was placed under the microscope objective of the Rayleigh-Raman spectrometer.

6.2.9 Optical setup and measurements

The Rayleigh-Raman spectrometer is based on a home-built Raman spectrometer integrated with the base of an upright optical microscope (Olympus BX41). A single laser beam from a Coherent Innova 70C laser ($\lambda_{\text{exc}} = 647.089$ nm) was used for illuminating and trapping particles.²⁰ Rayleigh and Raman scattering were collected with a cover glass corrected dry objective (Olympus, 40x, NA: 0.95), separated in a homebuilt spectrometer and simultaneously detected with a single CCD camera (Andor Newton DU-970-BV). The spectrometer had an average dispersion of ~ 2.3 cm^{-1} (0.11 nm) wavenumber per pixel over the CCD camera surface with 1600 pixels along the dispersive axis and 200 pixels along the other axis. The spectral resolution was ~ 3.0 cm^{-1} . For further details about the Rayleigh-Raman spectrometer see SI. The laser power was measured underneath the objective and adjusted to 70 mW. By moving the objective along the z-axis, the laser focal spot is focused inside the solution, ~ 37 μm below the cover slip. The focal spot has a theoretical diameter of 0.4 μm and a Rayleigh range of 1.2 μm based on full width half maximum. 256 Rayleigh-Raman spectra were acquired with an acquisition time of 38 ms each over a period of 9.7 s. The trapped particles were then released from the optical trap by blocking the laser beam with a shutter for 1 s. This measurement cycle was repeated 100 times, which resulted in $100 \times 256 = 25600$ Rayleigh-Raman spectra per measurement. In total, we characterized 481 individual particles.

6

6.3 Data analysis

6.3.1 Calibration

The intensity and wavelength of the Rayleigh-Raman spectrometer was calibrated to convert the raw, measured data from pixels vs relative counts to calibrated data in wavenumber (cm^{-1}) vs counts. The pixel-to-wavenumber conversion was performed with a Raman spectrum from toluene, which has peaks of known relative wavenumber shift with respect to the exciting laser line at 0 cm^{-1} shift, and an argon-mercury lamp with narrow emission lines known with picometer accuracy. The wavelength-dependent transmission of the setup and the pixel-to-pixel variation in the detection sensitivity of the CCD camera was corrected with an intensity calibration. This



intensity calibration was performed by acquisition of a white light spectrum from a tungsten halogen light source (AvaLight-Hal; Avantes BV, Apeldoorn, The Netherlands) that results in the light detection efficiency for the entire setup per pixel. The offset of the detector depends on the detector parameters and was obtained from a measurement without any light falling onto the detector. The spectrum of the entire light path through the setup with the laser on, but without a sample, was acquired to determine the background spectrum, which was subtracted from the measured data. All software was developed in-house with MATLAB (2017b, MathWorks, USA).

6.3.2 Time traces

The Rayleigh-Raman spectra comprised a dataset composed of 25600 spectra per measurement of 100 cycles. Rayleigh time traces were obtained by integrating the Rayleigh band, centered between -33 and 58 cm^{-1} . The Raman time traces resulted from integrating a lipid-protein Raman band from 2811 to 3023 cm^{-1} . The Rayleigh and Raman bands were localized and integrated using the trapezoidal method with unit spacing. Before the integration of the lipid-protein Raman band, singular value decomposition (SVD) was performed on the Raman spectra to improve the signal-to-noise ratio.^{31,32} The first 32 S-components were selected for reconstruction of the data. The integrated Rayleigh and Raman values of each cycle were concatenated and plotted versus time, allowing the selection of time intervals of interest.

6.3.3 Segmentation of time traces

The Rayleigh scattering time traces were used to identify the time intervals corresponding to single trapping events. Single trapping events are visualized as step-wise increases in the Rayleigh signal.²⁰ These steps were manually segmented and their time intervals were used to select the corresponding Raman spectra. A Raman spectrum of a single particle was thus acquired as the average Raman spectrum during the length of one step. All the molecules in the Raman focal spot contribute to the Raman spectra. However, we are only interested in the contribution of a single particle in the focal spot and not the background. Hence, to account for any background contribution (e.g. water or soluble particles), the immediate previous segment to the step was also segmented and the corresponding Raman spectrum was used for background subtraction by a linear least squares (LLS) fit. All software was developed in-house with MATLAB (2017b, MathWorks, USA).

6.3.4 Backscattering calculations

To assess the diameter range of the optically trapped particles, we compared the measured and theoretical backscattering intensities. To calibrate the backscattering intensities, we related the measured backscattering intensities of polystyrene beads (PS) (Nanosphere; Thermo Fisher, Waltham, MA, USA) with mean diameters of 100, 125, 147, 296 and 799 nm to their theoretical

backscattering cross section by least square fitting. Theoretical backscattering cross sections were calculated as a function of particle diameter with step sizes of 10 nm using the Mie theory scripts of Mätzler³³ in MATLAB (2018b) and incorporating the particle diameter and RI, RI of the medium, the numerical aperture of the microscope objective (NA=0.95) and the wavelength (647.1 nm), polarization and intensity of light. Details, equations and limitations of the applied model are extensively described and published.²⁹ Note that we let the optical axis of the microscope objective overlap with the negative z-axis of the Cartesian coordinate system, as defined in Figure 3 of de Rond et al.,²⁹ and that the integral of equation 4²⁹ was numerically solved in 24 steps for both the azimuthal and polar angles. We assumed a RI of 1.586 for polystyrene³⁴ and 1.464 for silica.³⁵ Silica beads (Si) (Silica Kisker, Steinfurt, Germany) were used to validate our model for particles with a lower RI than PS. Because EVs have a low (<1.42) but heterogeneous RI,³⁰ they were modelled as a core-shell particle with the core containing predominantly water ($n_{\text{H}_2\text{O}}=1.33$) and dissolved biological molecules, together giving rise to a lower and upper boundary core RI $n_{\text{coreLower}}=1.36$ and $n_{\text{coreUpper}}=1.40$, respectively; a shell consisting mostly of lipid molecules ($n_{\text{lipids}}=1.49$) and embedded proteins ($n_{\text{protein}}=1.44$), together giving rise to a shell RI $n_{\text{shell}}=1.48$ with a thickness of 6 nm.

6

6.3.5 Multivariate analysis

Following the segmentation of the time traces and background subtraction by LLS fit, the full dataset comprised a total of 481 Raman spectra corresponding to 481 individual particles: PC-3 EVs (n=94), LNCaP EVs (n=75), RBCs EVs (n=56), “platelet particles” (n=103) and “plasma particles” (n=153). The mean Raman spectra per sample type was computed for spectral comparison. The Raman spectrum of each particle was interpolated to the same wavenumber axis and baseline correction and de-noising were performed on the full dataset using a function called BEADS.³⁶ The cut-off frequency used was 0.006 cycles/sample, a regularization parameter of 0.0050, 0.0500 and 0.0400, a first-order filter and an asymmetry ratio of 6. Next, each Raman spectrum was normalized to have a mean of zero and a standard deviation of one. Finally, principal component analysis (PCA) was performed on the mean centered data in the spectral regions 800-1780 cm^{-1} and 2800-3080 cm^{-1} . Data analysis was performed using MATLAB (2017b, MathWorks, USA) and Eigenvector (Eigenvector Research, Inc., Washington, US) software.

6.4 Results

6.4.1 Pre-characterization of samples by NTA and flow cytometry

Table 6.1 shows the particle concentration as measured by NTA and FCM. The particle distributions from NTA confirmed that the majority of particles have a size range smaller than



600 nm (SI). The estimated concentrations are 10^9 tdEVs per mL and 10^{10} RBC EVs and “platelet particles” per mL. In addition, assuming a RI<1.42 for EVs, FCM confirmed the presence of mainly EVs in the PC-3, LNCaP and RBC samples. EVs and LPs were present in both the plasma and platelet concentrate samples, assuming a RI<1.42 for EVs and RI>1.45 for LPs.

Table 6.1. Sample pre-characterization by NTA and FCM. Particle sample concentrations (C_p) as given by NTA (Concentration NTA) and FCM (Concentration FCM total). Concentration FCM RI<1.42 are all detected particles between 200 and 800 nm in diameter and ~1 order of magnitude above the detection limits for forward and side scatter, and which have an RI <1.42. Concentration RI>1.45 are all detected particles between 200 and 800 nm in diameter and ~1 order of magnitude above the detection limits for forward and side scatter, and which have an RI >1.45. ^aValue missing due to limited sample availability.

	Concentration NTA (mL ⁻¹)	Concentration FCM total (mL ⁻¹)	Concentration FCM RI<1.42 (mL ⁻¹)	Concentration FCM RI>1.45 (mL ⁻¹)
PC-3 EVs	1.9×10^9	3.8×10^8	6.5×10^7	9.1×10^5
LNCaP EVs	1.1×10^9	6.8×10^8	9.5×10^7	4.4×10^6
RBC EVs	4.3×10^{10}	4.1×10^9	3×10^9	1.1×10^9
“Platelet particles”	8.4×10^{10}	2.3×10^{10}	1.9×10^{10}	3.7×10^9
“Plasma particles”	NA ^a	1.6×10^{11}	2×10^{10}	7.7×10^9

6.4.2 Detection of single EVs

We start by demonstrating trapping and detection by synchronous Rayleigh-Raman scattering of single EVs²⁰ originating from different cells and LPs. [Figure 6.1A](#) and [6.1B](#) show the Rayleigh and Raman scattering signals of multiple trapping cycles during 900 s corresponding to LNCaP and RBC EVs, respectively. Rayleigh time traces of the rest of the samples are shown in [Figure S6.7](#). The laser beam is unblocked and blocked at the start and end of a cycle of 9.7 s. Although not shown in the time traces, the laser remains blocked for 1 s between cycles to enable enough time for the particles to be released from the focal spot. The associated Raman scattering signals were obtained from the integration of the lipid-protein band ($2811\text{-}3023\text{ cm}^{-1}$) in the Raman spectrum. Because the Rayleigh scattering signal is much more intense than the Raman scattering signal, optical trapping can be much better studied using the Rayleigh signal. The Raman signals, on the other hand, contain information about the chemical composition of the trapped particles. [Figure 6.1A](#) and [6.1B](#) show a clear correlation between Rayleigh and Raman signal pairs for each sample, with cross-correlation coefficients of 0.81 for the LNCaP EVs and 0.93 for the RBC EVs. The cross-correlation coefficients for PC-3, plasma and platelet time traces are 0.92, 0.82, 0.87, respectively.

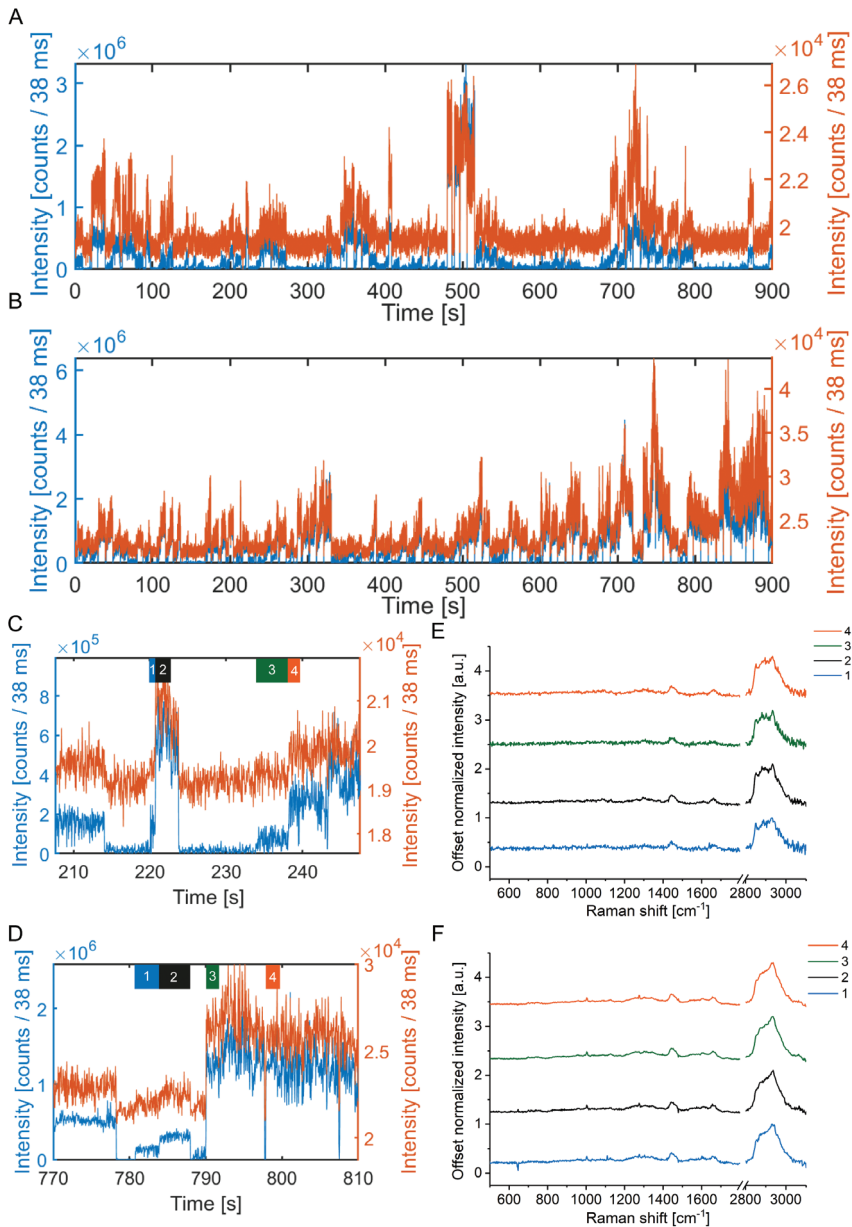


Figure 6.1. Synchronous intensity time traces of Rayleigh (blue) and Raman (orange) scattering signals from (A) LNCaP EVs and (B) RBC EVs, resulting from peak integration of the Rayleigh peak located between -33 and 58 cm^{-1} and a lipid-protein band between 2811 and 3023 cm^{-1} . (A) and (B) are a concatenation of multiple cycles of Rayleigh and Raman scattering signals with an integration time of 38 ms and a cycle duration of 9.7 s. (C) and (D) show a magnification of (A) and (B) respectively, indicating four time intervals (labels at the top of the plots) corresponding to the trapping of (C) single LNCaP EVs and (D) single RBC EVs. (E) and (F) display Raman spectra of single LNCaP and RBC EVs, respectively. The color-coded Raman spectra in (E) and (F) correspond to the 4 time points in (C) and (D), respectively.



When plotted on 40 s intervals, it becomes apparent that the Rayleigh scattering signals show discrete steps in time (Figure 6.1C and 6.1D), which indicates single trapping events. Thus, the Rayleigh scattering signal can be used to define the time intervals for extraction of the Raman spectrum corresponding to a single particle. In Figure 6.1C and 6.1D, we labelled four trapping events. Whereas each step is caused by a single particle entering the focal spot, only the first step corresponds to a time interval where only 1 particle is present in the focal spot. Figure 6.1E and 6.1F shows the background corrected Raman spectra corresponding to the numbered time traces in Figure 6.1C and 6.1D, respectively. The lipid-protein band ($2811\text{-}3023\text{ cm}^{-1}$) has higher intensity than the Raman bands in the fingerprint region ($500\text{-}1800\text{ cm}^{-1}$) and spectral differences are visible between LNCaP EVs (Figure 6.1E) and RBC EVs (Figure 6.1F).

6.4.3 Spectral characterization of various EVs types and LPs

To differentiate EVs from other particles, such as LPs, and to identify EVs of different cellular origin, we segmented single particle trapping events from the Rayleigh time traces and obtained the time intervals where individual EVs contributed to a Raman spectrum. The mean Raman spectra after baseline correction and noise removal are shown in Figure 6.2A for 56 individual RBC EVs, 94 PC-3 EVs, 75 LNCaP EVs, 153 “plasma particles” and 103 “platelet particles”. The mean Raman spectra of all EV types show lipid and protein bands at 1126 , $1297\text{-}1303$, $1441\text{-}1443$, $1655\text{-}1659$, and $2811\text{-}3030\text{ cm}^{-1}$. PC-3 and LNCaP EVs have a similar mean Raman spectrum (cross-correlation coefficient of 0.996). RBCs, PC-3 and LNCaP EVs show corresponding bands at 1004 , 1340 , $1607\text{-}1609\text{ cm}^{-1}$ and a higher protein-to-lipid ratio than “plasma particles” and “platelet particles”. “Plasma particles” and “platelet particles” share a similar spectral profile, as quantified by a cross-correlation coefficient of 0.997. The mean Raman spectra of PC-3 and LNCaP EVs show peaks specific to this type of EVs: $1243\text{-}1245$ (Amide III),³⁷ $1321\text{-}1323$ (guanine),³⁷ 1663 (Amide I),³⁷ among others. In addition, the protein marker band at 1004 cm^{-1} from the amino acid phenylalanine is clearly visible in all EV types but not in the “plasma particles” and “platelet particles”.

The spectral differences between the various particle types can be further detailed by principal component analysis (PCA), which discloses the main sources of spectral variation in the data set comprising 481 individual particles. Figure 6.2C shows two principal component loadings (PC1 and PC2) that together account for 73.7% of the variance in the full dataset. PC1 shows more lipid features than PC2, which in turn displays more protein features. Figure 6.2B depicts a scatter plot in which each dot represents a single particle with a certain value for PC1 and PC2. Particles with similar scores for principle components have similar Raman spectra (and

similar chemical content) and are clustered together. The higher the score value of a particle for a principal component, the larger the contribution of that principal component.

When plotting the scores values of PC1 against PC2, three main clusters can be identified: 1) RBC EVs, 2) PC-3 and LNCaP EVs (tdEVs) and 3) “plasma particles” and “platelet particles”. The ellipses around each particle type represent the 95% confidence interval. The results show that EVs can be distinguished from particles present in the plasma and platelet samples. Furthermore, tdEVs can be distinguished from RBC EVs. Most of the EVs are negative for PC1 (Figure 6.2B), while most of the “platelet particles” and “plasma particles” are positive for PC1, which indicates that there is a larger protein contribution for EVs than for “platelet particles” and “plasma particles”. In addition, most of the “plasma particles” and “platelet particles” show a very similar Raman profile and they fall in the same cluster. In FigureB, most of the “plasma particles” and “platelet particles” are positive for PC1 and negative or close to zero for PC2, which indicates that these particles have a high PC1 contribution, which mainly shows a lipid profile. These loadings suggest that the trapped events in RBC, PC-3, LNCaP are EVs, whereas the trapped events in plasma and platelet concentrates are LPs. To verify that most of the particles in our plasma and platelet samples are LPs, we performed Raman spectroscopy on commercially available LPs. Figure 6.3 shows that the mean Raman spectra of CM and VLDL shows a lipid profile highly similar to “plasma particles” and “platelet particles”. Hence, the abundance of trapped “plasma particles” and “platelet particles” are indeed LPs, and those LPs can be clearly differentiated from EVs without labeling based on their chemical composition.



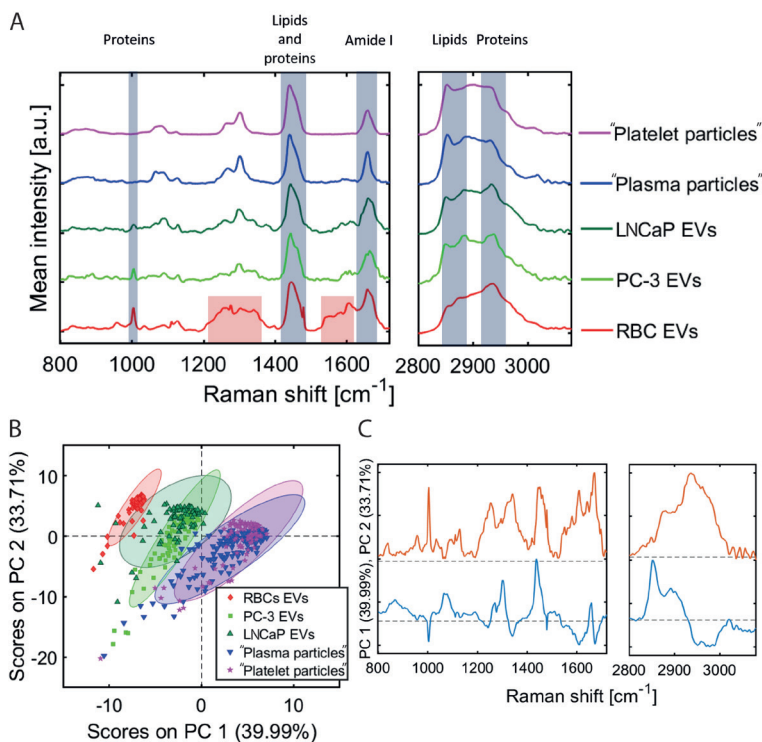


Figure 6.2. Principal component analysis of EVs. **(A)** Mean Raman spectra of single RBCs EVs ($n=56$), PC-3 EVs ($n=94$), LNCaP EVs ($n=75$), "plasma particles" ($n=153$) and "platelet particles" ($n=103$) displaying common Raman bands to all EV types: 1298-1300 (CH_2), 1442 (lipids and proteins), 1656 (Amide I), 2811-3023 (lipids and proteins) cm^{-1} . **(B)** First and second principal component scores. Ellipse represents the 95% confidence interval. **(C)** First two principal component loadings resulting from PCA analysis on the dataset of 481 single particles. The cumulative variance of these loadings represents 73.7%. The largest spectral variations are at the following locations: 1004, 1301, 1437, 1443, 1445, 1479, 1609, 1659, 1671, 2850, 2883, and 2933 cm^{-1} .

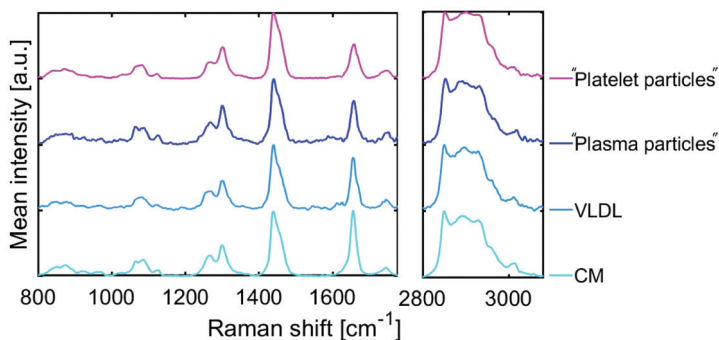


Figure 6.3. Normalized mean Raman spectra of CM ($n=98$), VLDL ($n=118$), "plasma particles" ($n=153$) and "platelet particles" ($n=103$). Baseline and noise removal were performed on each individual Raman spectrum belonging to a single particle.

6.4.4 EV size estimation based on Rayleigh scattering

To establish a relationship between the measured Rayleigh scattering intensity of the optically trapped particles and their diameter, **Figure 6.4** shows the Rayleigh scattering distribution from single trapped LNCaP EVs, PC-3 EVs, RBC EVs, “plasma particles” and “platelet particles”. Panel A shows that the interquartile range (IQR) for all the particle types is overlapping and the spread of plasma and platelet particles is larger than that of the EV types. The Rayleigh values for PC-3 and LNCaP EVs mainly overlap and the spread marked by the whiskers is between 5.2×10^3 and 5.7×10^5 . Because the Rayleigh scattering distribution does not follow a normal distribution, a non-parametric distribution (kernel distribution) was fitted to the density function of the Rayleigh scattering values of single particles (**Figure 6.4B**).

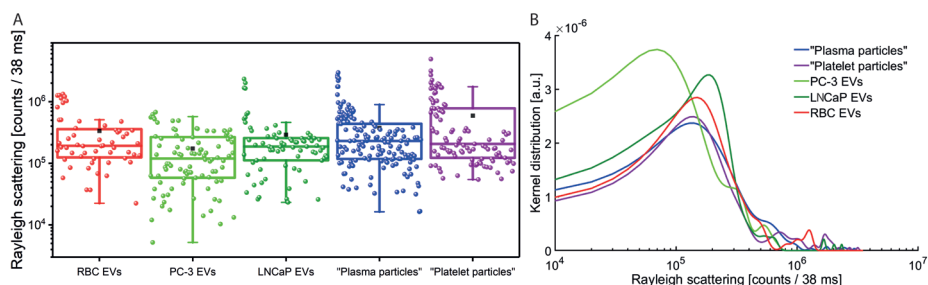
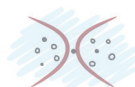


Figure 6.4. Rayleigh scattering distributions. **(A)** The boxplots (dots represent single particles) show the Rayleigh scattering distributions for RBC EVs, LNCaP EVs, PC-3 EVs, “plasma particles” and “platelet particles”. The boxes range from the 25th percentile to the 75th percentile, which corresponds to the interquartile range (IQR). The mean is indicated by the black squares. The whiskers range are within $1.5 \times$ IQR. **(B)** Kernel distribution of the Rayleigh scattering intensity of single EVs and non-EV particles.

Next, we calibrated the measured Rayleigh scattering intensities with a Mie scattering model by using PS beads with an RI of 1.586. With calibration, we mean that we related the measured backscattering intensity in arbitrary units to the theoretical scattering cross section in nm^2 . Next, Si beads were used to validate the model for particles with a lower RI than PS. The collection of light in the backscatter direction causes sharp oscillations, which are somewhat smoothed by averaging over the finite collection angle of the microscope objective. The theoretically determined backscattering cross section is the cross section related to the scattering of light towards the objective (NA=0.95) (**Figure 6.5**, left axis). The experimentally obtained backscatter intensity (data points in **Figure 6.5A**, right axis) of PS and Si beads is in agreement with the Mie calculations ($R^2=0.999$). The green curves in **Figure 6.5A** and **5B** depict the simulated backscattering cross sections (left axis) and thus the corresponding backscattering intensity (right axis) from EVs. Despite the small RI difference between EVs ($n_{\text{core}} \approx 1.37$)³⁸ and water ($n=1.33$), we show that sub-micrometer EVs exceed the detection limit of our instrument (black line in **Figure 5B**) by measuring and calibrating the Rayleigh backscattering intensity. Hence, the



measured Rayleigh backscattering intensity enables to select the Raman scattering intensities of individually trapped EVs in the sub-micrometer range. It can be noticed that for particles with diameters above 200 nm the Rayleigh scattering of EVs is much lower than for PS or Si beads, which can be related to the molecular composition and density of molecules of EVs.

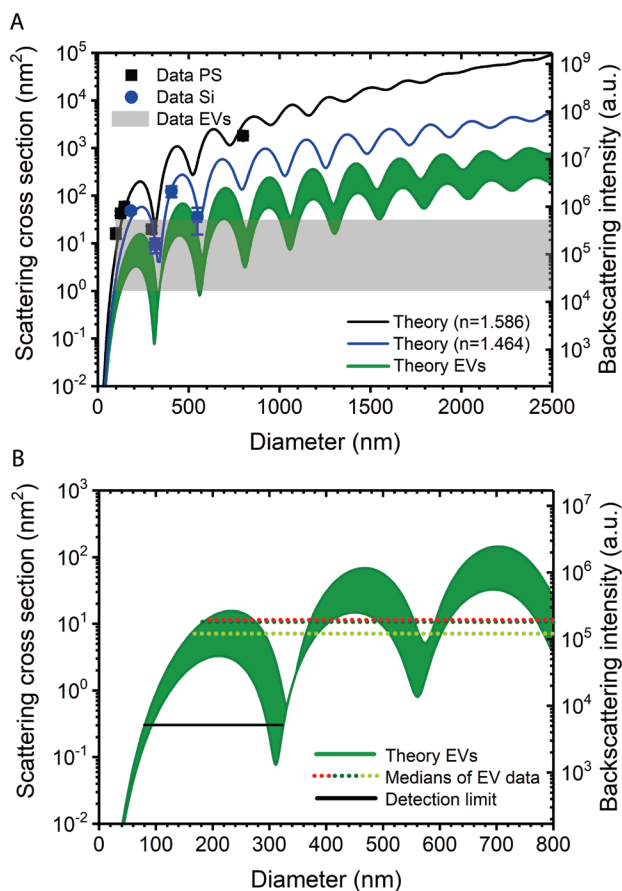


Figure 6.5. (A) Prediction of the back-scattered signals (lines) for linearly polarized light at a wavelength 647.1 nm from a PS beads (black), Si beads (blue) and EVs (green) using Mie theory. The left vertical axis depicts the cross-section integrated over the backscattering angles with an NA of 0.95. The right vertical axis depicts the counts per 38 ms measured on PS beads (back squares) and Si beads (blue dots). Vertical error bars indicate the SD of measured amplitudes and horizontal error bars are SD of size distributions as provided by manufacturer. The refractive indices used to model the particles were: Ps = 1.586, Si = 1.464, $EV_{core} = 1.36$ and $EV_{shell} = 1.48$ (lower boundary), $EV_{core} = 1.40$ and $EV_{shell} = 1.48$ (upper boundary) with a shell thickness of 6 nm for lower and upper boundaries. The gray area corresponds to the Rayleigh scattering intensity range from PC-3, LNCaP and RBC EVs in Figure 4A, with upper and lower boundaries that correspond to the mean value of the upper and lower whiskers. (B) Magnification of (A) showing the median Rayleigh scattering values for RBC EVs (red), LNCaP EVs (dark green) and PC-3 EVs (light green). The detection limit (black line) corresponds to the lowest whisker value in Figure 4A, which is for PC-3 EVs.

The oscillatory behavior of the Mie curves as a function of particle size (green curves in [Figure 6.5](#)) precludes that a unique solution of the size of the EVs can be extracted on the basis of the measured Rayleigh backscattering (gray area in [Figure 6.5A](#)). However, we can estimate the size range of the particles that are optically trapped. For instance, the gray area in [Figure 6.5A](#) corresponds to the Rayleigh scattering values of all EVs with a median value of 1.87×10^5 counts / 38 ms and mean lower and upper boundaries (whiskers in [Figure 6.4A](#)) of 1.7×10^4 and 5.14×10^5 , respectively. The black line in [Figure 6.5B](#) indicates the detection limit of the Rayleigh scattering based on the lowest Rayleigh intensity corresponding to a visible trapping event (lowest whisker in [Figure 6.4A](#)). Thus, the estimated diameter range of the smallest detectable EVs is between 80 to 320 nm.

6.5 Discussion

The identification and phenotyping of single and rare EVs in plasma, such as tdEVs, is challenging due to (1) their overlap in size with other biological nanoparticles, specially lipoproteins (LPs) and platelets, (2) the low number of EV surface antigens that are available for antibody labelling, and (3) the lack of chemical characterization methods at the single EV level.^{2,39,40} Previously, we demonstrated the trapping of single EVs in suspension, identified those single trapping events by triggering on Rayleigh scattering and, synchronously, obtained their chemical composition by Raman scattering.²⁰

In this study, we demonstrated that synchronous Rayleigh-Raman scattering of optically trapped particles enables to differentiate single EVs from LPs and to differentiate tdEVs from RBC EVs without labeling. The samples in our study were characterized also with NTA and FCM. Here, tdEVs were represented by EVs derived from prostate cancer cell lines. It is assumed that all particles from LNCaP and PC-3 are tdEVs and all particles from RBC concentrate are EVs. By synchronous acquisition of both Rayleigh and Raman scattering, we trapped single particles and disclosed their chemical fingerprint.

The identification of individual particles was enabled by a short acquisition time (38 ms) and triggering on Rayleigh scattering. Rayleigh scattering is much more intense than the Raman scattering, which allowed identification of small particles that are not visible in the Raman time traces. Hence, the Rayleigh time traces show clearer steps when a particle is trapped. Examples of intensity difference in Rayleigh and Raman scattering are visible in [Figure 6.1C](#) and [6.1D](#), before step 3 and from step 1 to 2, respectively. Here, the Rayleigh signal shows clear steps which are absent or not clear in the Raman signal. The Raman time traces result from



the integration of the lipid-protein band ($2811\text{-}3023\text{ cm}^{-1}$), which is the highest intensity Raman band for EVs and LPs.

The experimental identification of single vs multiple nanoparticles depends to a great extent on the particle concentration. Hence, two strategies can be followed to avoid trapping of multiple particles regarded as one: (1) dilute the suspension of particles and (2) decrease the illumination time. Dilution aims at decreasing the probability of trapping multiple particles during the integration time by a reduction of the concentration and given the stochastic nature of the trapping process. However, the time required to measure a statistical significant number of particles increases, lowering the throughput of the technique. Decreasing the illumination time enables time traces of higher temporal resolution, allowing a better distinction of particles entering the focal spot, but decreasing the signal-to-noise ratio. In this study we chose a tradeoff between concentration of particles and illumination time. The highest concentration of particles we measured was $C_p = 4.25 \times 10^{10}$ particles/mL (NTA) for the RBC EVs. With an estimated microscopic focal volume of 1.82 fL using the Rayleigh criterion, the number of particles in the focal volume when the laser is blocked is approximately 0.0774. For the RBC EV sample, the time trace contains segments that change more gradually as compared to a less concentrated sample like PC-3 EVs (Figure 6.1A and 6.1B). The gradual change is caused by the rapid accumulation of particles in the trap, making it difficult to distinguish and segment single trapping events and decreasing the amount of Raman spectra per particle; hence decreasing the signal-to-noise-ratio. Therefore, we used concentrations equal or lower than C_p .

The hereby presented method enabled the label-free distinction of tdEVs, i.e. PC-3 and LNCaP, from RBC EVs and LPs in plasma and platelet concentrates with a 95% confidence interval (Figure 6.2B). The Raman spectra of EVs show a larger contribution of proteins compared to LPs. For instance, phenylalanine is clearly visible in EVs (1004 cm^{-1}) while not detected in lipoproteins. In addition, the lipid-protein band ($2811\text{-}3023\text{ cm}^{-1}$) shows a higher protein contribution for EVs than for LPs. PCA suggested that most of the particles trapped in plasma and platelet concentrates are LPs. To further verify this, we compared the Raman fingerprint of the trapped LPs with commercially available LPs isolated by electrophoresis (Figure 6.3). The Raman spectra of the particles trapped in plasma and platelet concentrates correlates with the one measured on the commercial LPs and with.⁴¹ We mainly measure LPs in plasma, which agrees with previous studies that estimate the LP frequency in plasma to be much larger than the EV frequency.²

The difference between tdEVs and RBC EVs may come from the presence of derivatives of hemoglobin.⁴² PC-3 and LNCaP EVs are not distinguished from each other and two possible explanations are that the chemical differences among these EVs derived from prostate cancer cells is too small to detect, or there is a high heterogeneity within each EV type, which has been previously suggested.²⁵

The size of the trapped particles can be estimated by Mie theory based on the Rayleigh scattering. Rayleigh scattering depends on size and RI of the particles. It is known that the particle size distribution of EVs in body fluids are not normally distributed. Hence, the Rayleigh scattered light by EVs in blood will also not have a normal distribution. Indeed, the Rayleigh distributions of [Figure 6.4](#) reveal a lognormal distribution, rather than a normal distribution. By comparing the EV values for the Rayleigh backscattering cross section with the Mie model in [Figure 6.5](#), it was estimated that the lowest size range of particles probed is between 80 and 320 nm. Detecting smaller particles is challenging because their signal is overwhelmed by the background noise ([Figure S6.8](#)). The NTA distributions ([Figures S6.1-S6.4](#)) suggest that the size range of the trapped EVs corresponds with the range up to 600 nm in the Mie model ([Figure 6.5](#)).

The label-free and non-destructive Rayleigh-Raman method allows identification and differentiation of single EVs from lipoproteins, and tdEVs from RBC EVs. Additional Raman and Rayleigh analysis discloses the chemical composition of particles and estimates their size range. The data suggests that the origin of single particles present in plasma can be traced based on their unique Raman molecular fingerprint. Hence, the label-free method of synchronous Rayleigh and Raman provides a way to verify the nature of EVs and other particles in body fluids for diagnostic and prognostic purposes.

Acknowledgments

The authors thank Aufried T.M. Lenferink from the department of Medical Cell BioPhysics, University of Twente, Enschede, The Netherlands, for excellent support during the Raman measurements and Leonie de Rond from the department of Biomedical Engineering and Physics, Amsterdam UMC, University of Amsterdam, Amsterdam, The Netherlands for measuring the FCM data of RBC and platelet samples.



References

1. Kanada, M., Bachmann, M. H. & Contag, C. H. Signaling by Extracellular Vesicles Advances Cancer Hallmarks. *Trends in Cancer* 2, 84–94 (2016).
2. Johnsen, K. B., Gudbergsson, J. M., Andresen, T. L. & Simonsen, J. B. What is the blood concentration of extracellular vesicles? Implications for the use of extracellular vesicles as blood-borne biomarkers of cancer. *Biochim Biophys Acta Rev Cancer* 1871, 109–116 (2019).
3. van der Pol, E., Böing, A. N., Harrison, P., Sturk, A. & Nieuwland, R. Classification, functions, and clinical relevance of extracellular vesicles. *Pharmacol. Rev.* 64, 676–705 (2012).
4. Arraud, N. et al. Extracellular vesicles from blood plasma: determination of their morphology, size, phenotype and concentration. *J. Thromb. Haemost.* 12, 614–627 (2014).
5. Berckmans, R. J. et al. Cell-derived microparticles circulate in healthy humans and support low grade thrombin generation. *Thromb. Haemost.* 85, 639–46 (2001).
6. Zwicker, J. I. et al. Tumor-derived tissue factor-bearing microparticles are associated with venous thromboembolic events in malignancy. *Clin. Cancer Res.* 15, 6830–40 (2009).
7. Li, J. et al. Claudin-containing exosomes in the peripheral circulation of women with ovarian cancer. *BMC Cancer* 9, 244 (2009).
8. Coumans, F. A. W., Doggen, C. J. M., Attard, G., de Bono, J. S. & Terstappen, L. W. M. M. All circulating EpCAM+CK+CD45- objects predict overall survival in castration-resistant prostate cancer. *Ann. Oncol. Off. J. Eur. Soc. Med. Oncol.* 21, 1851–7 (2010).
9. Nanou, A. et al. Circulating tumor cells, tumor-derived extracellular vesicles and plasma cytokeratins in castration-resistant prostate cancer patients. *Oncotarget* 9, 19283–19293 (2018).
10. Nanou, A. et al. Abstract 4464: Tumor-derived extracellular vesicles in blood of metastatic breast, colorectal, prostate, and non-small cell lung cancer patients associate with worse survival. in *AACR 2019 Proceedings: Abstract 4464 - American Association for Cancer Research 4464–4464* (2019). doi:10.1158/1538-7445.sabcs18-4464
11. Coumans, F., van Dalum, G. & Terstappen, L. L. W. M. L. W. M. M. CTC Technologies and Tools. *Cytom. A* 93, 1197–1201 (2018).
12. Kotrbová, A. et al. TEM ExosomeAnalyzer: a computer-assisted software tool for quantitative evaluation of extracellular vesicles in transmission electron microscopy images. *J. Extracell. Vesicles* 8, (2019).
13. Zabeo, D. et al. Exosomes purified from a single cell type have diverse morphology. *J. Extracell. Vesicles* 6, (2017).
14. van der Pol, E. et al. Particle size distribution of exosomes and microvesicles determined by transmission electron microscopy, flow cytometry, nanoparticle tracking analysis, and resistive pulse sensing. *J. Thromb. Haemost.* 12, 1182–1192 (2014).
15. Ramirez, M. I. et al. Technical challenges of working with extracellular vesicles. *Nanoscale* 10, 881–906 (2018).
16. Gualerzi, A. et al. Raman spectroscopy as a quick tool to assess purity of extracellular vesicle preparations and predict their functionality. *J. Extracell. Vesicles* 8, (2019).
17. Böing, A. N. et al. Single-step isolation of extracellular vesicles by size-exclusion chromatography. *J. Extracell. Vesicles* 3, 10.3402/jev.v3.23430 (2014).

18. Van Der Pol, E., van Gemert, M. J. C., Sturk, A., Nieuwland, R. & Van Leeuwen, T. G. Single vs. swarm detection of microparticles and exosomes by flow cytometry. *J Thromb Haemost* 10, 919–930 (2012).
19. van der Pol, E. et al. Absolute sizing and label-free identification of extracellular vesicles by flow cytometry. *Nanomedicine Nanotechnology, Biol. Med.* 14, 801–810 (2018).
20. Enciso-Martinez, A. et al. Synchronized Rayleigh and Raman scattering for the characterization of single optically trapped extracellular vesicles. *Nanomedicine Nanotechnology, Biol. Med.* 24, 102109 (2020).
21. Ashkin, A. Acceleration and Trapping of Particles by Radiation Pressure. *Phys. Rev. Lett.* 24, 156–159 (1970).
22. Ashkin, A., Dziedzic, J. M. & Chu, S. Observation of a single-beam gradient force optical trap for dielectric particles. *Opt. Lett.* 11, 288–290 (1986).
23. Penders, J. et al. Single Particle Automated Raman Trapping Analysis. *Nat. Commun.* 9, 4256 (2018).
24. Kruglik, S. G. et al. Raman tweezers microspectroscopy of circa 100 nm extracellular vesicles. *Nanoscale* 11, 1661–1679 (2019).
25. Smith, Z. J. et al. Single exosome study reveals subpopulations distributed among cell lines with variability related to membrane content (SI). *J. Extracell. Vesicles* 4, 28533 (2015).
26. Lee, W. et al. Label-Free Prostate Cancer Detection by Characterization of Extracellular Vesicles Using Raman Spectroscopy. *Anal. Chem.* 90, 11 (2018).
27. Tatischeff, I. et al. Fast characterisation of cell-derived extracellular vesicles by nanoparticles tracking analysis, cryo-electron microscopy, and Raman tweezers microspectroscopy. *J. Extracell. Vesicles* 1, 229–238 (2012).
28. Carney, R. P. et al. Multispectral Optical Tweezers for Biochemical Fingerprinting of CD9-Positive Exosome Subpopulations. *Anal. Chem.* 89, 5357–5363 (2017).
29. de Rond, L., Coumans, F. A. W. W., Nieuwland, R., van Leeuwen, T. G. & van der Pol, E. Deriving extracellular vesicle size from scatter intensities measured by flow cytometry. *Curr Protoc Cytom* 86, e43 (2018).
30. de Rond, L. et al. Refractive index to evaluate staining specificity of extracellular vesicles by flow cytometry. *J. Extracell. Vesicles* 8, 1643671 (2019).
31. Uzunbajakava, N. et al. Nonresonant confocal Raman imaging of DNA and protein distribution in apoptotic cells. *Biophys. J.* 84, 3968–81 (2003).
32. Van Manen, H. J., Uzunbajakava, N., Van Bruggen, R., Roos, D. & Otto, C. Resonance Raman imaging of the NADPH oxidase subunit cytochrome b 558 in single neutrophilic granulocytes. *J. Am. Chem. Soc.* 125, 12112–12113 (2003).
33. Mätzler, C. MATLAB Functions for Mie Scattering and Absorption Version 2. (2002).
34. Sultanova, N. G., Zlatarov, B. A., Sultanova, N., Kasarova, S. & Nikolov, I. Dispersion Properties of Optical Polymers. 9 doi:10.12693/APhysPolA.116.585
35. Bass, M. et al. Handbook of Optics, Third Edition Volume IV: Optical Properties of Materials, Nonlinear Optics, Quantum Optics. *Zhurnal Eksperimental'noi i Teoreticheskoi Fiziki* (McGraw-Hill, Inc., 2009).
36. Ning, X., Selesnick, I. W. & Duval, L. Chromatogram baseline estimation and denoising using sparsity (BEADS). *Chemom. Intell. Lab. Syst.* 139, 156–167 (2014).
37. Movasaghi, Z., Rehman, S., Rehman, I. U. I. U. & Zanyar Movasaghi, S. R. & D. I. U. R. Raman Spectroscopy of Biological Tissues. *Appl. Spectrosc. Rev.* 42, 493–541 (2007).
38. Van Der Pol, E., Coumans, F. A. W., Sturk, A., Nieuwland, R. & van Leeuwen, T. G. Refractive Index Determination of Nanoparticles in Suspension Using Nanoparticle Tracking Analysis. 14, 6195–6201 (2014).



Chapter 6

39. De Rond, L. et al. Comparison of generic fluorescent markers for detection of extracellular vesicles by flow cytometry. *Clin. Chem.* 64, 680–689 (2018).
40. Aass, H. C. D. et al. Fluorescent particles in the antibody solution result in false TF- and CD14-positive microparticles in flow cytometric analysis. *Cytom. Part A* 79A, 990–999 (2011).
41. Chan, J. W., Motton, D., Rutledge, J. C., Keim, N. L. & Huser, T. Raman Spectroscopic Analysis of Biochemical Changes in Individual Triglyceride-Rich Lipoproteins in the Pre-and Postprandial State. (2005). doi:10.1021/ac050692f
42. Wood, B. R., Caspers, P., Puppels, G. J., Pandiancherri, S. & McNaughton, D. Resonance Raman spectroscopy of red blood cells using near-infrared laser excitation. *Anal. Bioanal. Chem.* 387, 1691–1703 (2007).

Supporting information

Nanoparticle tracking analysis characterization

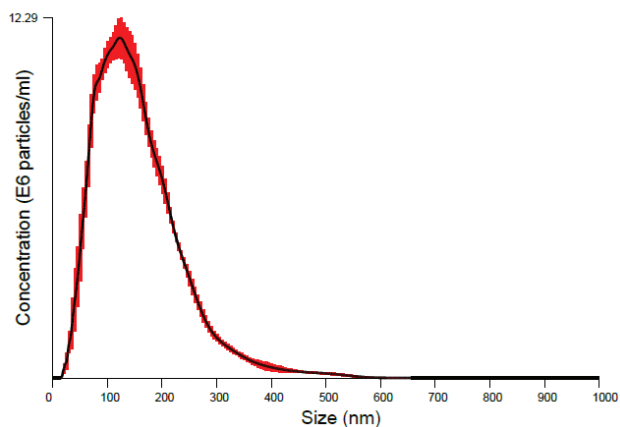


Figure S6.1. PC-3 EV diameter distribution was determined using nanoparticle tracking analysis (NanoSight NS500). An EV concentration of 1.9×10^9 particles/mL with a mean diameter (\pm standard deviation) of 157 (± 79) nm was found. Black line indicates the average size distribution and red error bars indicate ± 1 standard error of the mean. Measurements were done with a sCMOS camera, shutter length of 8.9 ms, gain of 250 and detection threshold of 6. Five videos of 60 s were captured at 22.0 °C and analyzed by NTA v2.3 (NanoSight), assuming a medium viscosity of 0.95 cP.

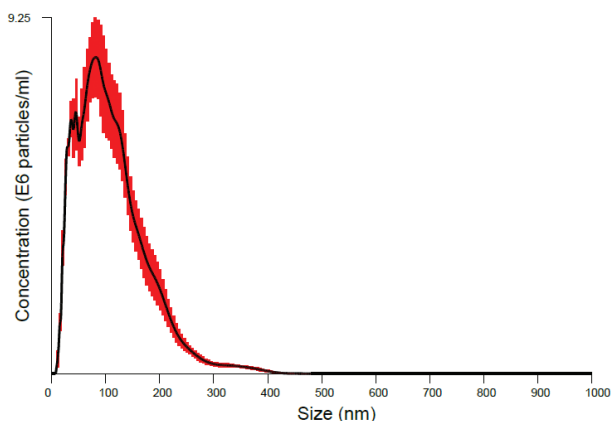


Figure S6.2. LNCaP EV diameter distribution was determined using nanoparticle tracking analysis (NanoSight NS500). An EV concentration of 1.1×10^9 particles/mL with a mean diameter (\pm standard deviation) of 109 (± 64) nm was found. Black line indicates the average size distribution and red error bars indicate ± 1 standard error of the mean. Measurements were done with a sCMOS camera, shutter length of 5 ms, gain of 250 and detection threshold of 7. Five videos of 60 s were captured at 22.0 °C and analyzed by NTA v2.3 (NanoSight), assuming a medium viscosity of 0.95 cP.



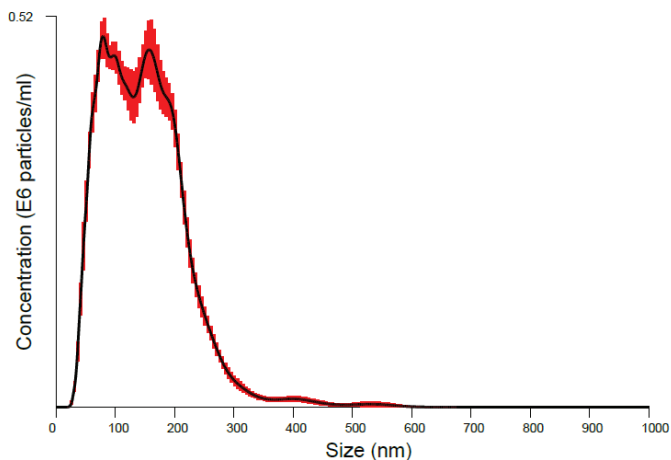


Figure S6.3. RBC EV diameter distribution was determined using nanoparticle tracking analysis (NTA NS500; Nanosight, Amesbury, UK). An EV concentration of 4.25×10^{10} particles/mL with a mean diameter (\pm standard deviation) of $148 (\pm 70)$ nm was found. Black line indicates the average size distribution and red error bars indicate ± 1 standard error of the mean. Measurements were done with an electron multiplying charge-coupled device (EMCCD) camera, shutter length of 33 ms, gain of 400 and detection threshold of 10. Ten videos of 30 s were captured at 22.0°C and analyzed by NTA v2.3 (NanoSight), assuming a medium viscosity of 0.95 cP.

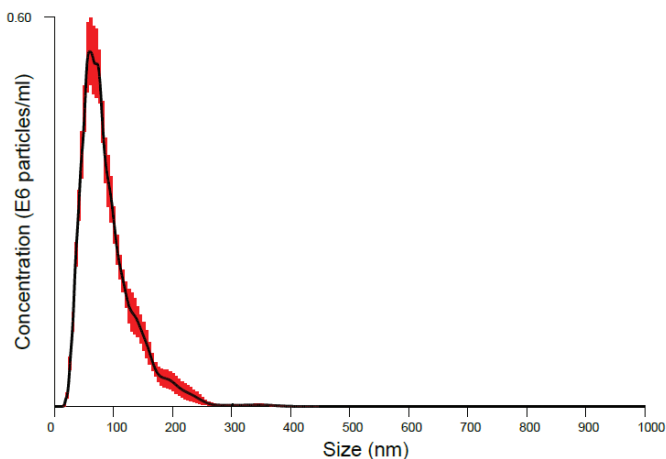


Figure S6.4. "Platelet particles" diameter distribution was determined using nanoparticle tracking analysis (NTA NS500; Nanosight, Amesbury, UK). An EV concentration of 8.4×10^{10} particles/mL with a mean diameter (\pm standard deviation) of $89 (\pm 43)$ nm was found. Black line indicates the average size distribution and red error bars indicate ± 1 standard error of the mean. Measurements were done with an electron multiplying charge-coupled device (EMCCD) camera, shutter length of 33 ms, gain of 400 and detection threshold of 10. Ten videos of 30 s were captured at 22.0°C and analyzed by NTA v2.3 (NanoSight), assuming a medium viscosity of 0.95 cP.

Flow cytometry

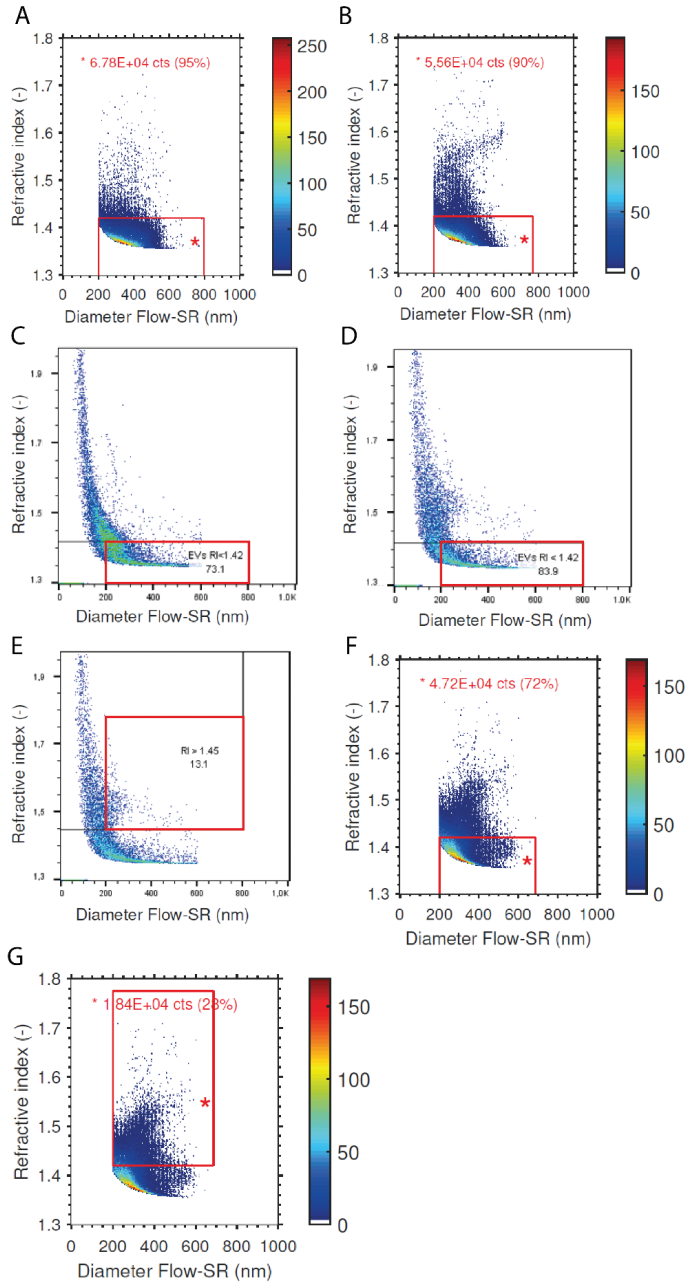
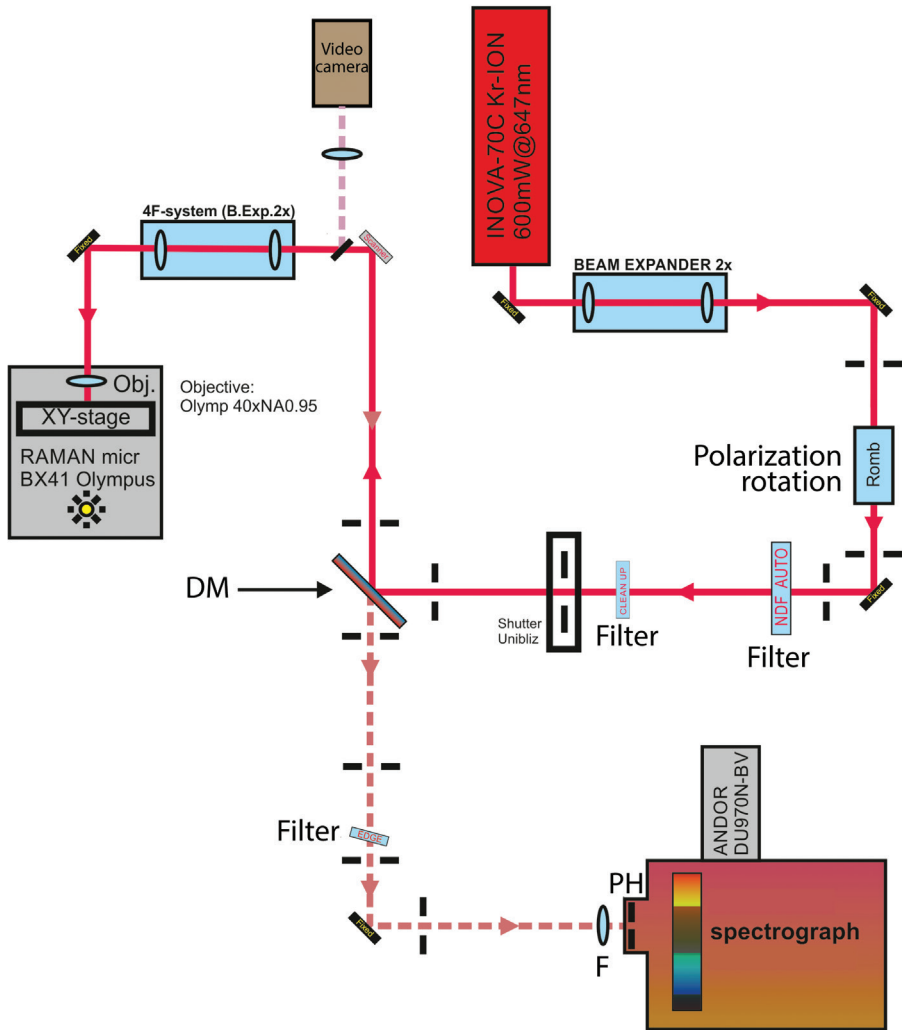


Figure S6.5. Flow cytometry scatter ratio (Flow-SR). (A) PC-3 EVs (RI < 1.42). (B) LNCaP EVs (RI < 1.42). (C) RBC EVs (RI < 1.42). (D) "Platelet particles" (RI < 1.42). (E) "Platelet particles" (RI > 1.45). (F) "Plasma particles" (RI < 1.42). (G) "Plasma particles" (RI > 1.45)



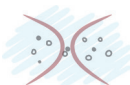
Rayleigh-Raman spectrometer

This setup is based on a homebuilt confocal Raman microscope (Figure S6.6). Laser light is generated by a Coherent Innova 70C laser ($\lambda_{\text{exc}} = 647.089$) and expanded by a beam expander. The laser light is reflected by a dichroic mirror (DM), again expanded (2x) by the 4F-system used for beam steering. The expanded laser beam passes through the microscope objective (40x, NA: 0.95; Olympus Nederland B.V., Leiderdorp, The Netherlands) and illuminates the sample. The Rayleigh and Raman scattered light are epi-detected and propagate together until the dichroic beam splitter is reached. This component reduces the Rayleigh scattering, which is further reduced after passing through an edge filter. The light is guided to the entrance pinhole (PH = 15 μm) of the spectrograph by mirrors and an image of the focal plane underneath the objective is made on the pinhole plane by lens ($F = 30$ mm). The spatially filtered light is dispersed in a home-built spectrograph such that the wavelength region of 646-849 nm (-30 cm^{-1} to 3670 cm^{-1}) illuminates the CCD camera (Andor Newton DU970N-BV, 1600 \times 200 pixels).



6

Figure S6.6. Homebuilt confocal Raman microscope.



Rayleigh time traces

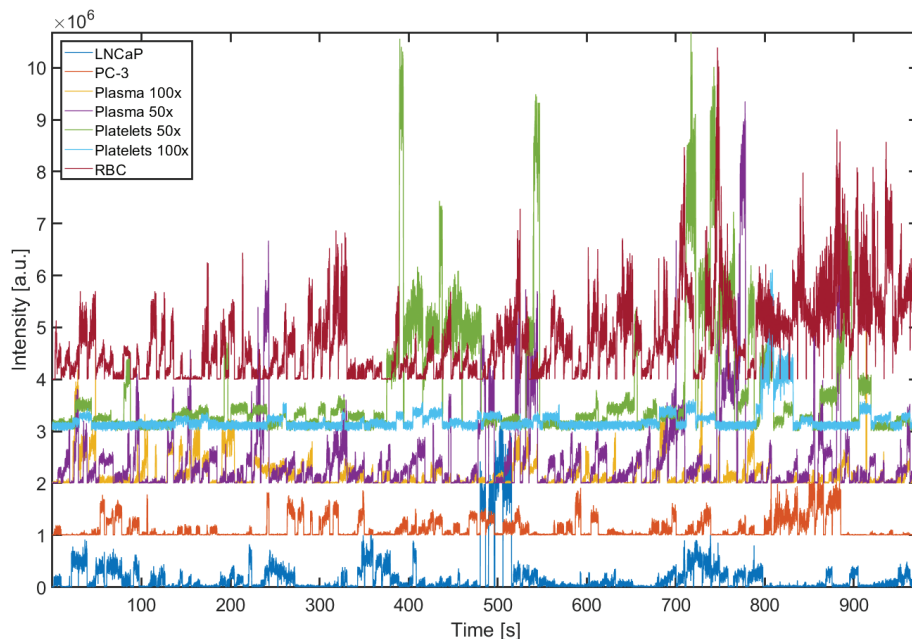


Figure S6.7. Rayleigh scattering signals of LNCaP sample, PC-3 sample, plasma sample (50x and 100x), platelet sample (50x and 100x) and RBC sample, resulting from peak integration of the Rayleigh peak located between -33 and 58 cm^{-1} .

Rayleigh-Raman scattering of phosphate-buffered saline

50 μL of phosphate-buffered saline 1x (PBS) was placed on a well glass slide (BMS Microscopes; 1.0-1.2 mm thick, Cat. no.: 12290). The sample was covered with a glass cover slip (VWR Ltd, thickness No. 1, diameter: 22mm, Cat. no.: 631-0158) and sealed with glued (EVO-STIK, Impact) onto the well glass slide. The glue was then cured at room temperature for ~ 30 minutes. The closed well glass slide was placed under the microscope objective of the Rayleigh-Raman spectrometer. The laser focal spot was focused inside the solution, ~ 37 μm below the cover slip. Rayleigh and Raman scattering spectra were typically acquired 256 times with an acquisition time of 38 ms over a period of ~ 9.7 seconds. The laser with a power of 70 mW, was then blocked for ~ 1 second. This measurement cycle was repeated 100 times, which resulted in 25600 Rayleigh-Raman spectra per measurement. [Figure S6.8](#) shows the Rayleigh scattering time trace with no visible trapping events.

The mean Rayleigh intensity of PBS is 6.1202×10^3 counts / 38 ms with a standard deviation (s) of 7.1397×10^3 . The coefficient of variation (c_v) is 1.17 and is defined as:

$$c_v = \frac{s}{\bar{x}}$$

being s the sample standard deviation and \bar{x} the sample mean.

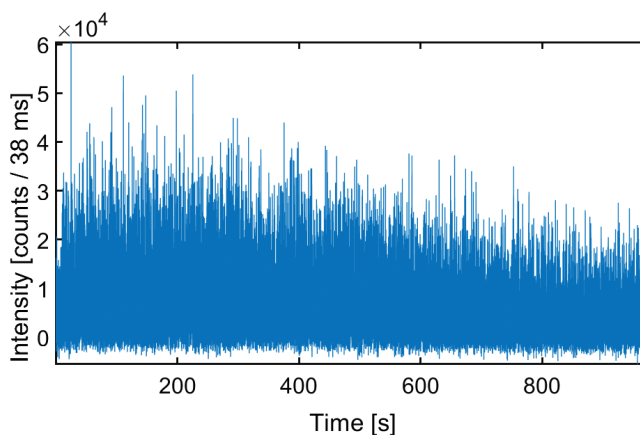


Figure S6.8. Rayleigh scattering time trace of PBS with a mean intensity of 6.120×10^3 counts / 38 ms and an SD of 7.139×10^3 .

The mean Raman spectrum of PBS over the entire time trace is shown in [Figure S6.9](#).

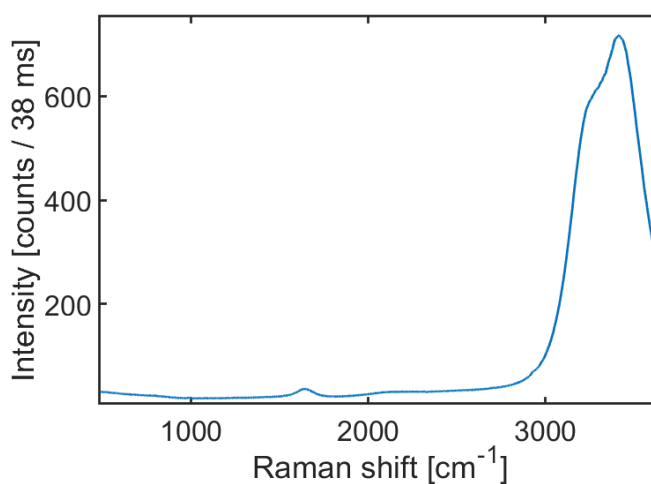


Figure S6.9. Mean Raman spectrum of PBS from 25600 Raman spectra with an integration time of 38 ms and a laser power of 70 mW.



The mean Raman spectrum and standard deviation of particles

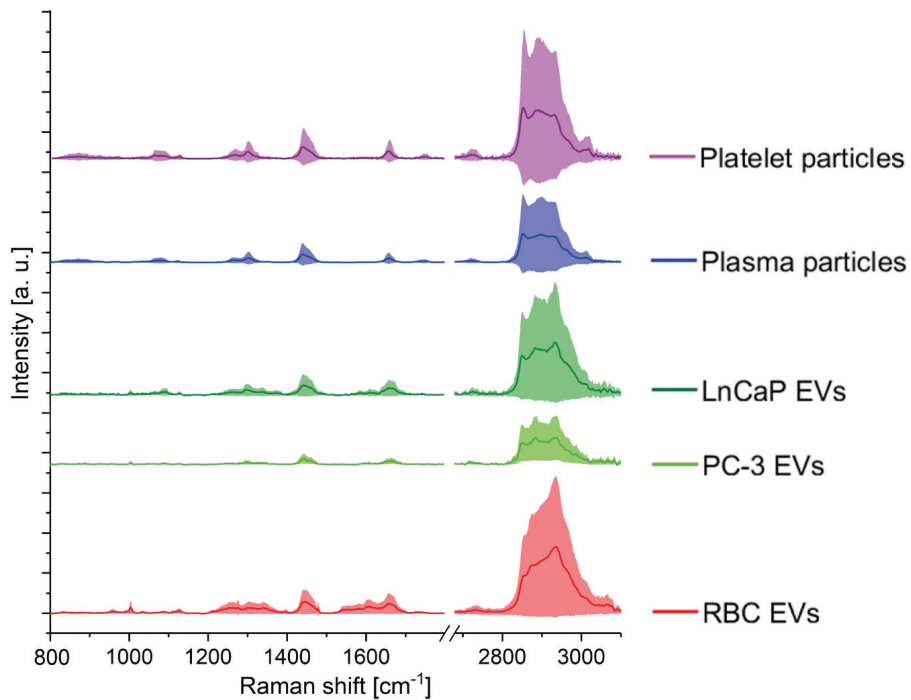
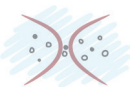
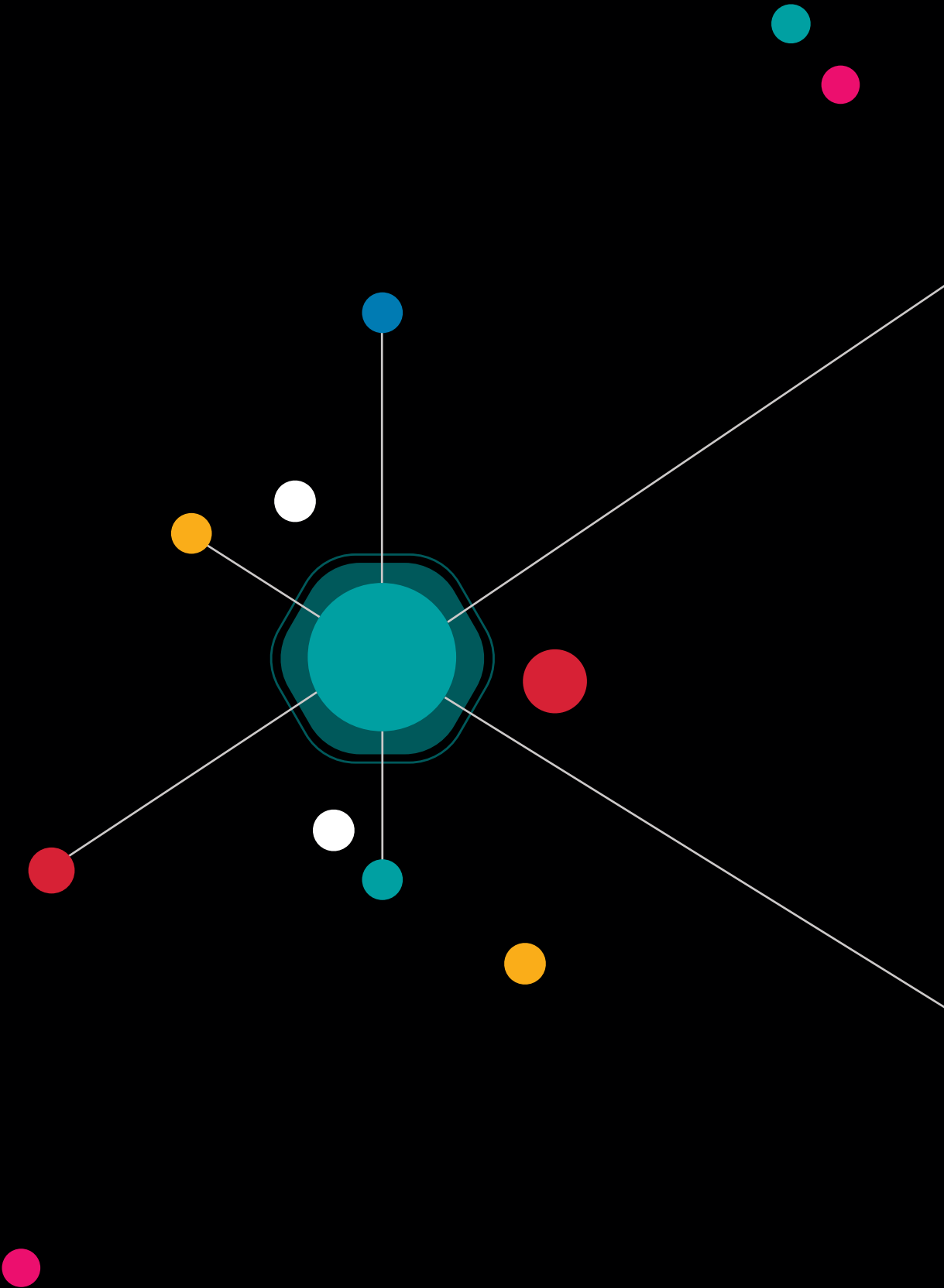


Figure S6.10. Mean Raman spectra and standard deviation of single RBCs EVs (n=56), PC-3 EVs (n=94), LNCaP EVs (n=75), "plasma particles" (n=153) and "platelet particles" (n=103).













Chapter 7

Label-free detection and
characterization of single
submicrometer particles in plasma of
prostate cancer patients



A. Enciso-Martinez, E. van der Pol, C.M. Hau, T.M. de Reijke, R. Nieuwland,
L.W.M.M. Terstappen and C. Otto

Manuscript in preparation



Abstract

The presence of large ($> 1 \mu\text{m}$) tumor-derived extracellular vesicles (tdEVs) in the blood cell fraction of metastatic castration-resistant prostate cancer (mCRPC) patients has proven to be prognostic. However, the majority of tdEVs are expected in the cell-free plasma fraction. Little is known about the chemical composition of single tdEVs and other submicrometer particles in the plasma of mCRPC patients. In this pilot study, we interrogate individual particles in the plasma of mCRPC patients (N=5) and compare it to healthy controls (N=14). Single EV analysis was achieved with optically trapping and simultaneous acquisition of both Rayleigh and Raman scattering to, respectively detect single trapping events and disclose their chemical composition. We identified various types of lipoprotein particles (LPs) as well as other particle types in a label-free manner and directly in suspension. Differences between particles from some patients and donors are visible after multivariate and cluster analysis of the Raman spectra of the particles. The results support the feasibility of optical trapping and synchronized Rayleigh and Raman scattering (OT-sRRs) for particle analysis in plasma from human donors. Further studies on a larger cohort of donors with well described clinical data is necessary to expand the diagnostic potential of the proposed methods.

7.1 Introduction

Prostate cancer (PCa) is the second most common cancer in men.^{1,2} Patients with metastatic PCa are treated by an androgen deprivation therapy to reduce the androgen hormones, which are required by cancer cells to grow. When patients relapse, PCa progresses into metastatic castration-resistant prostate cancer (mCRPC). In mCRPC, reactivation of androgen receptor axis occurs and the cancer remains dependent on androgen signaling.³ Current treatments including enzalutamide and abiraterone either target the androgen receptor directly or suppress de novo synthesis of androgens.³⁻⁵ Although these agents improve the survival of mCRPC patients, a significant number of patients experience primary resistance, and in time the remainder of the patients will acquire secondary resistance.^{3,5}

The response to treatment is monitored by radiographic data, clinical data or prostate specific antigen (PSA) measurements.³ Evaluation of the treatment response by radiographic or clinical data implies a late assessment in case the treatment is ineffective. The concentration of PSA is a prognostic marker in the early stages of PCa, but in mCRPC patients the PSA concentration should be combined with clinical data and ultimately other biomarkers.⁶ The detection of the actual presence of circulating tumor cells (CTCs) in the blood of mCRPC significantly improves the ability to monitor the efficacy of treatment.⁷⁻⁹ The main problem with counting CTCs is their low concentration in the blood, and enumeration of the more abundant tumor derived extracellular vesicles (tdEVs) are equally prognostic as compared to CTCs.¹⁰⁻¹³

The tdEVs measured in the aforementioned studies are relatively large ($> 1 \mu\text{m}$) as they were detected after EpCAM immunomagnetic enrichment from the blood cell fraction after removal of the plasma. Because plasma itself is now one of the major sources for studies on blood-derived EVs, including tdEVs, one may expect that measuring “small tdEVs” in cell-free plasma may offer even more clinically relevant information. Unfortunately, in plasma tdEVs are outnumbered by EVs of non-tumor origin, lipoprotein particles (LPs), soluble proteins, etc., which makes detection of the rare tdEVs challenging.

In this pilot study, we used single particle optical trapping and synchronized Rayleigh and Raman scattering (OT-sRRs)^{14,15} to measure the chemical profiles of submicrometer particles in plasma of 5 mCRPC patients and 14 healthy donors. The chemical fingerprint of the particles together with multivariate analysis and hierarchical cluster analysis (HCA) enabled us to identify different groups of particles as well as to differentiate between some patient and control groups.



7.2 Materials and methods

7.2.1 Plasma from healthy donors and cancer patients

Blood was obtained from non-fasting healthy donors and mCRPC patients (both N=5) after written informed consent in accordance with the Helsinki Declaration and approved by the medical-ethical assessment committee of the Academic Medical Center, University of Amsterdam (NL 64623.018.18). Refer to [Table S7.1](#) for donors clinical data. Whole blood was collected from each donor using a 21G needle, and the first vacutainer was discarded. Next, three citrate vacutainers of 2.7 mL (BD Biosciences, San Jose, CA) were collected and mixed gently by inversion. The vacutainers were centrifuged at 2500 *g* for 15 minutes at 20 °C without brake (Rotina 380R, Hettich, Tuttlingen, Germany). Plasma was collected up to 0.5 cm above the pellet, pooled and centrifuged in a conical base tube (10 mL; Sarstedt, Nimbrecht, Germany) at 2500 *g* for 15 minutes at 20 °C. The supernatant was deposited in aliquots of 75 μ L (Sarstedt), which were snap frozen in liquid N₂ and stored at -80 °C until use. Blood was also obtained from nine anonymous non-fasting healthy donors from the TNW-ECTM donor services of the University of Twente (Enschede, The Netherlands) after written informed consent. Blood collection was performed in accordance with the Dutch regulations and was approved by the medical-ethical assessment committee Twente (METC Twente). Whole blood was collected by venipuncture in ethylenediaminetetraacetic acid (EDTA) vacutainer tubes (BD). Blood was transferred to 15 mL CellSearch® conical tubes, followed by centrifugation (centrifuge 5804, Eppendorf, Hamburg, Germany) at 800 *g* without brake for 10 minutes at room temperature. Plasma was collected up to 1 cm above the buffy coat and stored in 1.5 mL tubes (Greiner Bio-one) at -80 °C until use. Samples were thawed in a water bath at 37 °C immediately before use.

7.2.2 Lipoprotein particles (LPs)

Human high density lipoprotein (HDL), low density lipoprotein (LDL), very low density lipoprotein (VLDL) and chylomicrons (CM) were acquired from Sigma-Aldrich Chemie N. V. (The Netherlands). HDL (Cat. No.: L8039), LDL (Cat. No.: 437644), VLDL (Cat. No.: 437647) and CM (Cat. No.: SRP6304) had a purity of \geq 95% by electrophoresis, as specified by the provider.

7.2.3 LNCaP-derived EVs

Cells from the prostate cancer cell line LNCaP (ATCC, CRL-1740, USA) were cultured at 37 °C and 5% CO₂ in RPMI-1640 with L-glutamine medium (Lonza, Cat. No.: 12-702F) supplemented with 10% (v/v) fetal bovine serum (FBS), 10 units/mL penicillin and 10 mg/mL streptomycin. Cells were seeded at a density of 10,000 cells/cm² as recommended by ATCC and medium was refreshed every second day. At 80-90% confluence, cells were washed three times with

phosphate buffer solution (PBS) and cultured in FBS-free RPMI-1640 with L-glutamine medium (Lonza, Cat. No.: 12-702F) supplemented with 1 unit/mL penicillin and 1 $\mu\text{g/mL}$ streptomycin. After 2-3 days of culture, cell supernatant was collected in a 15 mL tube (Cellstar® tubes, Greiner Bio-one BV, Alphen a/d Rijn, The Netherlands) and centrifuged at 500 g at room temperature for 10 minutes (centrifuge 5804, Eppendorf, Hamburg, Germany). Next, the supernatant containing LNCaP-derived EVs was collected and stored in aliquots (Greiner Bio-one) at $-80\text{ }^{\circ}\text{C}$ until use. Samples were thawed in a water bath at $37\text{ }^{\circ}\text{C}$ immediately before use. LNCaP-derived EVs are referred to as LNCaP EVs throughout the text.

7.2.4 Red blood cell (RBC) - derived EVs

RBC-derived EVs were obtained from RBC concentrate (150 mL, Sanquin Bloodbank, Amsterdam, The Netherlands) and diluted 1:1 with filtered PBS. Samples were centrifuged three times at 1560 g for 20 minutes at $20\text{ }^{\circ}\text{C}$ (Rotina 46RS centrifuge, Hettich, Tuttlingen, Germany). The supernatant containing EVs was pooled and distributed in aliquots of 50 μL , which were snap frozen in liquid N_2 for 15 minutes and stored in aliquots (Sarstedt) at $-80\text{ }^{\circ}\text{C}$ until use. Samples were thawed in a water bath at $37\text{ }^{\circ}\text{C}$ before use. RBC-derived EVs are referred to as RBC EVs throughout the text.

7.2.5 Sample preparation for OT-sRRs

Before synchronized Rayleigh and Raman scattering (sRRs) measurement, all samples were, if necessary, diluted in PBS to achieve a trapping rate of 3 to 4 particles/minute and avoid simultaneous trapping of multiple particles. Next, 50 μL of each sample was loaded on a well glass slide (BMS Microscopes; 1.0-1.2 mm thick). Each sample was covered with a glass cover slip (VWR Ltd, thickness No. 1, diameter: 22 mm) and sealed with glue (EVO-STIK, Impact) onto the well glass slide to avoid evaporation. The glue was left to dry at room temperature for ~ 30 minutes. The sealed well glass slide was placed under the microscope objective of the Rayleigh-Raman spectrometer. For the patients ($N=5$) and healthy controls ($N=5$), three samples per donor were prepared and measured alternating between samples from patients and controls.

7.2.6 Rayleigh-Raman spectrometer and data acquisition

The Rayleigh-Raman spectrometer has been described in detail elsewhere.^{14,15} In short, the Rayleigh-Raman spectrometer is based on a home-built Raman spectrometer integrated with the base of an upright optical microscope (Olympus BX41). A single laser beam from a Coherent Innova 70C laser ($\lambda_{\text{exc}}=647.089\text{ nm}$) was used for illuminating and trapping particles.¹⁴ Rayleigh and Raman scattering were collected with a cover glass corrected dry objective (Olympus, 40x, NA: 0.95), separated in a homebuilt spectrometer and simultaneously detected with a single



CCD camera (Andor Newton DU-970-BV). The spectrometer had an average dispersion of $\sim 2.3 \text{ cm}^{-1}$ (0.11 nm) wavenumber per pixel over the CCD camera surface with 1600 pixels along the dispersive axis and 200 pixels along the other axis. The spectral resolution was $\sim 3.0 \text{ cm}^{-1}$. The laser power was measured underneath the objective and adjusted to 70 mW. By moving the objective along the z-axis, the laser focal spot is focused inside the solution, $\sim 37 \text{ }\mu\text{m}$ below the cover slip. The focal spot has a theoretical diameter of $0.4 \text{ }\mu\text{m}$ and a Rayleigh range of $1.2 \text{ }\mu\text{m}$ based on full width half maximum. 256 Rayleigh-Raman spectra were acquired with an acquisition time of 38 ms each over a period of 9.7 s. The trapped particles were then released from the optical trap by blocking the laser beam with a shutter for 1 s. This measurement cycle was repeated 100 times, which resulted in $100 \times 256 = 25600$ Rayleigh-Raman spectra per measurement. In total, we characterized 2521 individual particles.

7.3 Data analysis

7.3.1 Calibration

The intensity and wavelength of the Rayleigh-Raman spectrometer was calibrated to convert the raw, measured data from pixels vs relative counts to calibrated data in wavenumber (cm^{-1}) vs counts. The calibration procedure has been described elsewhere.¹⁵

7.3.2 Time traces

Because particle trapping is a dynamic process, time traces of the Rayleigh and Raman signals were made. Rayleigh time traces were obtained by integrating the Rayleigh band, centered between -20 and 10 cm^{-1} . The Raman time traces resulted from integrating a lipid-protein Raman band from 2811 to 3023 cm^{-1} . The Rayleigh and Raman bands were localized and integrated using the trapezoidal method with unit spacing. Before integration of the lipid-protein Raman band, singular value decomposition (SVD) was performed on the Raman spectra to improve the signal-to-noise ratio.^{16,17} The first 32 S-components were selected for reconstruction of the data. The integrated Rayleigh and Raman values of each cycle were concatenated and plotted versus time, allowing the selection of time intervals of interest.

7.3.3 Segmentation of time traces

The Rayleigh scattering time traces were used to identify the time intervals corresponding to single trapping events. Single trapping events are visualized as step-wise increases in the Rayleigh signal.^{14,15} These steps were manually segmented and their time intervals were used to select the corresponding Raman spectra. A Raman spectrum of a single particle was thus acquired as the average Raman spectrum during the length of one step. Because all molecules

in the Raman focal spot will contribute to the Raman spectra, i.e. not only the trapped particle but also the background as from water or soluble components, the immediate previous segment to the step was also segmented and the corresponding Raman spectrum was used for background subtraction by a linear least squares (LLS) fit. All software was developed in-house with Matlab (2017b, MathWorks, USA).

7.3.4 Multivariate analysis

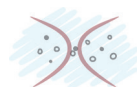
Following the segmentation of the time traces and background subtraction by LLS fit, the full dataset comprised 2521 Raman spectra corresponding to 2521 individual trapped and measured particles. The mean Raman spectra per sample type was computed for spectral comparison. The Raman spectrum of each particle was interpolated to the same wavenumber axis and baseline correction and de-noising were performed on the full dataset using a function called BEADS.¹⁸ BEADS was executed with the following parameter choices: cut-off frequency: 0.006 cycles/sample, regularization parameter: 0.003, 0.030 and 0.024, filter: first-order filter, asymmetry ratio: 6. Next, each Raman spectrum was normalized to have a mean of zero and a standard deviation of one. For comparison, spectral cross-correlation coefficients (CC) were computed on some Raman spectra in the spectral region 600-1800 cm^{-1} using the Matlab (2017b, MathWorks, USA) function "crosscorr". Finally, principal component analysis (PCA) was performed on the mean centered data in the spectral regions 600-1800 cm^{-1} and 2680-3080 cm^{-1} . Hierarchical cluster analysis was performed by first creating a hierarchical tree based on the PCA score values corresponding to each single particle and then clustering them based on their Euclidean distances. The dendrogram of the clustering process can be used to guide the selection of the number of clusters. Data analysis was performed using Matlab (2017b, Mathworks, USA).

7

7.4 Results

To chemically characterize particles in plasma, single particles from the healthy donors (N=14) were optically trapped and their corresponding Raman spectrum was acquired. **Figure 7.1A** shows the mean Raman spectra of n particles per donor with common lipid and protein bands indicated (refer to **Table 7.1**). Some differences are also visible such as in the lipid-protein band between 2811 and 3023 cm^{-1} . Because LPs outnumber EVs in plasma, we hypothesize that most of the trapped particles are LPs.

To verify the type of trapped particles in healthy donors, we compared the Raman spectra of the trapped particles to spectra of four commercially available LPs (see "Lipoprotein particles" under "Materials and Methods"). **Figure 7.1B** shows the mean Raman spectra of chylomicrons (CM),



very low density lipoproteins (VLDL), low density lipoproteins (LDL), high density lipoproteins (HDL) and the mean Raman spectrum of all healthy donors. This last spectrum highly resembles the VLDL and CM spectra (CC: 0.9859 and 0.9748, respectively), showing a clear contribution of these LPs to the mean Raman spectrum of healthy donors. The largest LPs in size, namely CM and VLDL, show a similar Raman fingerprint (CC: 0.9853). LDL and HDL show also a similar fingerprint (CC: 0.9477). **Figure 7.1B** further shows that Raman spectra of LDL and HDL have characteristic traces of cholesterol (refer to **Table 7.1**). Although the main contribution to the Raman spectra of healthy donors comes from VLDL and CM, there are other particles trapped with a different chemical composition.

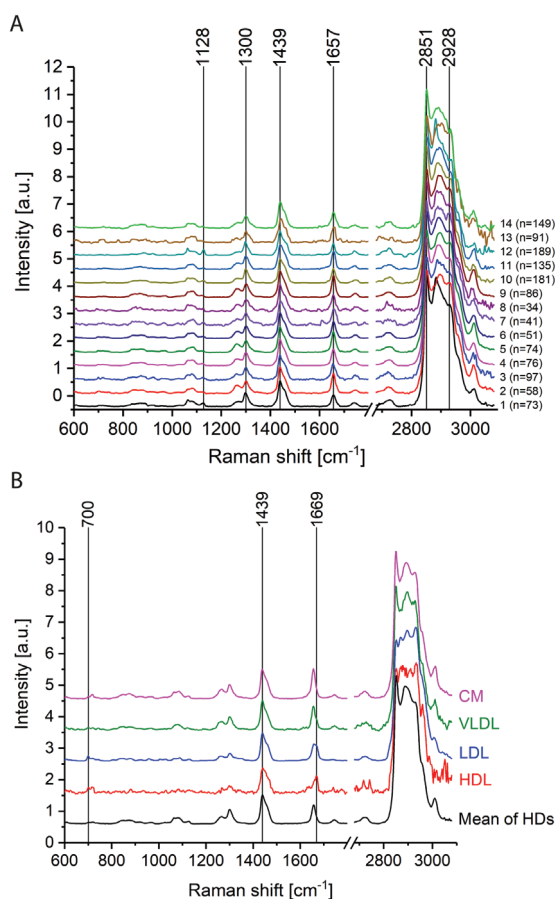


Figure 7.1. (A) Mean Raman spectra of n particles per healthy donor from a total of 14 healthy donors (HDs). The indicated Raman bands correspond to protein and lipid assignments (refer to Table 7.1). (B) Mean Raman spectra of all particles from the healthy donors and LPs: high density lipoproteins (HDL) and low density lipoproteins (LDL), very low density lipoproteins (VLDL), chylomicrons (CM). The indicated Raman bands correspond to cholesterol assignments.

To analyze each particle individually, PCA was performed on the entire dataset of healthy donors and lipoprotein particles. [Figure 7.2A](#) shows score plots in principal component (PC) 1 - PC2 space and PC1 - PC3 space, where each dot represents a single particle. VLDL and CM particles overlap with particles from healthy donors, while HDL and LDL particles can be separated from the rest of the particles along PC1. Along PC2, two types of particles can be identified, namely LPs with negative score values for PC1, and other particles present in healthy donors with positive score values. Hence, PC1 indicates wavenumber positions (positive and negative peaks in [Figure 7.2B](#)) that are key to distinguish LPs from the rest of the particles. Along PC2, HDL and LDL particles can be distinguished from VLDL and CM particles.

Hierarchical cluster analysis (HCA), performed on the score values, shows particles clustered into five groups indicated by different colors in [Figure 7.2C](#). The HCA clusters HDL and LDL together (cluster 4). In addition, HCA clusters VLDL and CM particles together with a number of particles from healthy donors (cluster 5). Other particles from healthy donors are clustered into 3 groups (clusters 1, 2 and 3). The mean Raman spectrum of each cluster is shown in [Figure 7.2D](#). All clusters show a lipid profile with a clear triglyceride contribution (refer to [Table 7.1](#)). Cluster 4, which groups LDL and HDL show clear cholesterol peaks (refer to [Table 7.1](#)). Although clusters 1, 2 and 3 show a clear lipid profile, there are clear differences compared to the other clusters, e.g. the lipid-protein band profile ($2811\text{-}3023\text{ cm}^{-1}$). Hence, it is unclear what is the nature of the particles in clusters 1, 2 and 3. The particles in cluster 4 can be assigned to HDL and LDL, while the particles in cluster 5 to VLDL and CM.



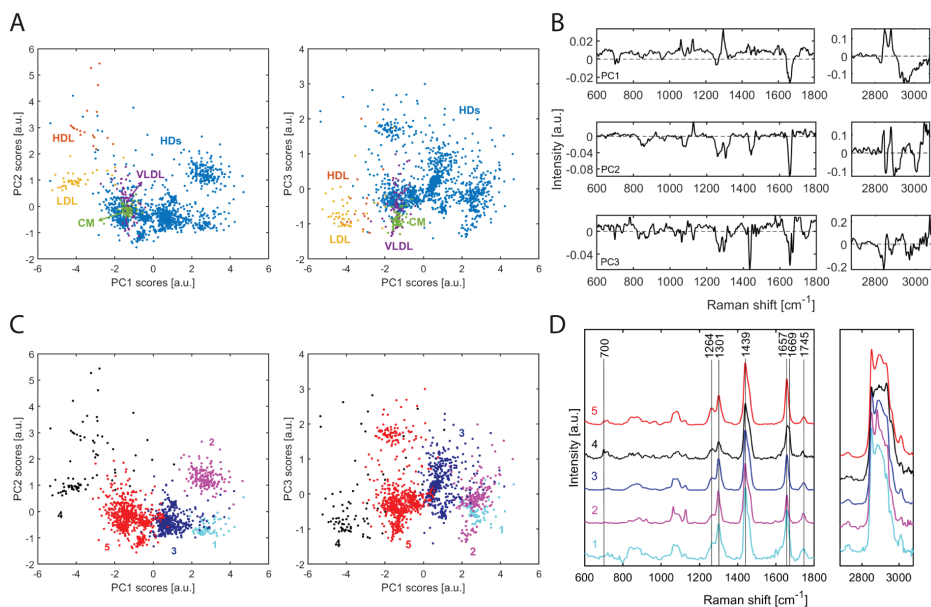


Figure 7.2. Healthy donors (HDs) and LPs. **(A)** First, second and third principal component scores corresponding to single particles from healthy donors (blue) and LPs: HDL (orange), LDL (yellow), VLDL (magenta) and CM (green). **(B)** First three principal component loadings resulting from PCA on the combined fingerprint (600-1800 cm^{-1}) and high frequency (2680-3080 cm^{-1}) regions. **(C)** First, second and third principal component scores color-clustered into five clusters after HCA. **(D)** Mean Raman spectra per cluster in (C). The indicated Raman bands correspond to triglyceride and cholesterol assignments (refer to Table 7.1).

To determine whether cancer patients have a different subpopulation of particles in plasma compared to healthy donors, OT-sRRs was performed on plasma from mCRPC patients ($N=5$) and compared to healthy donors ($N=14$). **Figure 7.3** shows the mean Raman spectra of n particles per patient and the mean Raman spectrum of all 14 healthy donors. The mean Raman spectrum of healthy donors resembles more the Raman spectra of patients 1 and 5 (CC: 0.9908 and 0.9843, respectively) than the one from patients 2, 3 and 4 (CC: 0.9229, 0.8517 and 0.8959, respectively). Patients 2, 3 and 4 share Raman bands indicated in black in **Figure 7.3**. Additional clear spectral bands are present in patient 4 indicated in magenta.

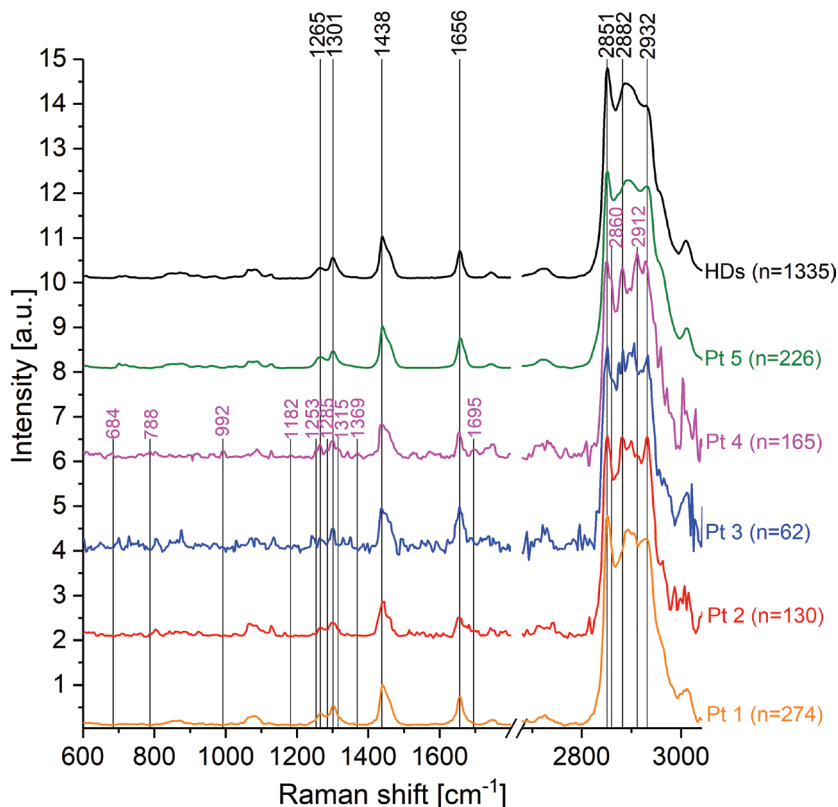


Figure 7.3. Mean Raman spectra of patients (Pt, N=5) and healthy donors (HDs, N=14). The indicated Raman bands are assigned in Table 7.1.

To compare all the trapped particles in the plasma of mCRPC patients and healthy donors at the single particle level, PCA was performed over the entire data set consisting of 2192 single particles. **Figure 7.4A** shows the score plot of PC1 against PC2 where each dot represents a single particle. Three out of the five patients can be clearly distinguished from the healthy donors, i.e. particles from patients 2 and 3 overlap with each other and particles from patient 4 separate from the rest of the particles along PC2. These particles are distinguished by high score values in PC2, which means that PC2 has a high contribution to the Raman spectra of those particles. Interestingly, PC2 shows peaks that indicate nucleic acid contributions indicated in **Figure 7.4B**. To compare the particles of all donors with each other, HCA was performed on the score values (**Figure 7.4C**). All particles from patients 2 and 3 cluster together in cluster 4 and 95% of the particles from patient 4 clusters in cluster 5. The other 5% of particles from patient 4 clusters together with patients 2 and 3 in cluster 4. The mean Raman spectra per cluster is shown in **Figure 7.4D**. Similar results are obtained when including in the PCA only samples from patients and healthy controls (both N=5) processed with same protocol as described in section 7.2.1 (see **Figure S7.1**).



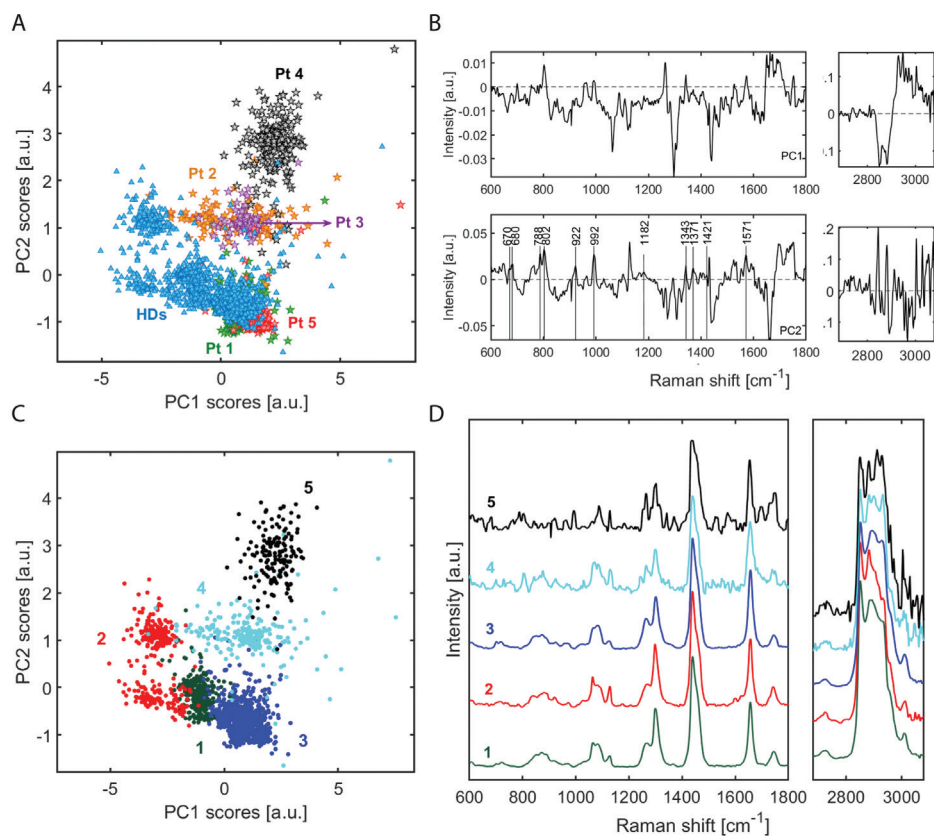
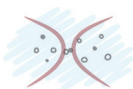


Figure 7.4. Multivariate analysis of mCRPC patients (N=5) and healthy donors (N=14). The full data set consists of $n=2192$ particles. **(A)** First and second principal component scores corresponding to single particles from healthy donors (triangles) and patients 1 to 5 (stars). **(B)** First two principal component loadings resulting from PCA on the combined fingerprint (600-1800 cm^{-1}) and high frequency (2680-3080 cm^{-1}) regions. The labels in PC2 indicate nucleic acid contributions. **(C)** First and second principal component scores color-clustered into five clusters after HCA. **(D)** Mean Raman spectra per cluster in (D).

Because it is expected that the majority of the particles in plasma are LPs, we performed a PCA on all samples and included commercially available LPs (i.e. HDL, LDL, VLDL and CM). EVs from LNCaP cells and RBCs were also included in the analysis as reference particles. Figure 7.5A shows a scores plot where single LPs, LNCaP and RBC EVs have been added to the PCA analysis of Figure 7.4A. While LNCaP EVs do not overlap with particles from any of the patients, RBC EVs do not overlap with particles from any of both healthy donors and patients. When clustering all the particles into 8 clusters based on their PC scores, it can be seen in Figure 7.5B that LNCaP EVs and particles from mCRPC patients do not group in the same cluster. LNCaP and RBC EVs cluster in clusters 1 and 2, respectively. All VLDL and CM group in cluster 6, together with 43% of particles from healthy donors and 99% of particles from patient 1 (see Table S7.2). HDL and

LDL mainly group in cluster 5, together with 96% of particles from patient 5. All particles from patients 2 and 3 cluster together in cluster 7 and 94% of the particles from patient 4 group in its own cluster 8. Particles from healthy donors group mainly into three clusters (clusters 3, 4 and 6) and one of these clusters (cluster 6) corresponds to VLDL and CM particles.

The main difference between the cluster analysis of [Figure 7.4](#) and [Figure 7.5](#) are the additional three clusters in [Figure 7.5B](#), assigned to HDL & LDL, LNCaP and RBC EVs. To compare the spectral differences among clusters, [Figure 7.5C](#) shows the mean Raman spectrum per cluster. The Raman spectra of clusters 1 and 2, corresponding to LNCaP and RBC EVs, show characteristic phenylalanine Raman bands at 1004 and 1583 cm^{-1} , which are not visible in other clusters.



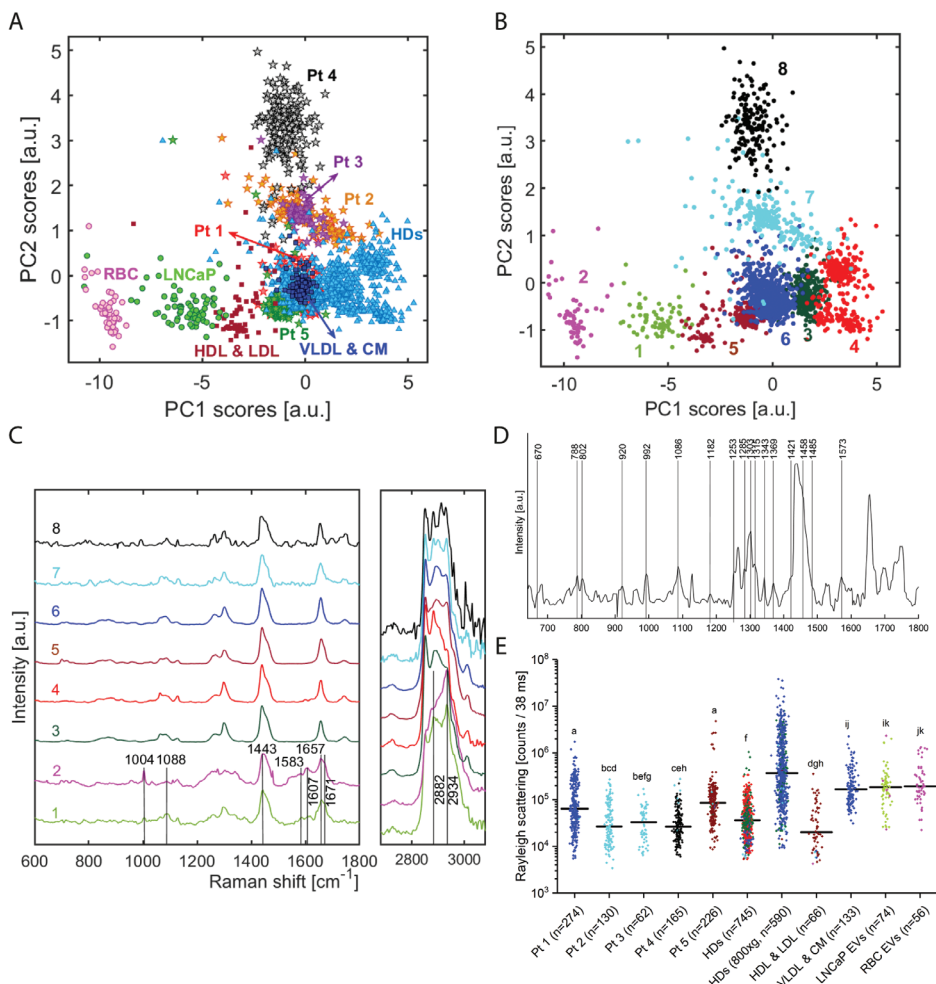


Figure 7.5. (A) First and second principal component scores corresponding to single particles from healthy donors (triangles), patients 1 to 5 (stars), LPs (squares), RBC and LNCaP EVs (circles). (B) First and second principal component scores color-clustered into eight clusters after HCA. (C) Mean Raman spectra per cluster in (B). The indicated Raman bands correspond to protein assignments. (D) Magnification of the Raman spectrum of cluster 8. The indicated Raman bands correspond to nucleic acid assignments. (E) Rayleigh scattering values of single particles color-coded based on clusters in (B) and (C). Black bars denote the medians. Samples sharing a letter are not significantly different at the 0.05 level according to the nonparametric Mann-Whitney U test.

Figure 7.5E shows the Rayleigh scattering distribution per sample type. Here, the HD samples have been separated into two groups based on their sample preparation protocol (see section 7.2.1). All distributions are not normally distributed and the ones from patients 2, 3 and 4 are not significantly different from each other, but significantly different from patients 1 and 5 that show higher medians. The distribution of healthy donors ($n = 795$) is significantly different compared to all, but patient 3. Furthermore, Figure 7.5E relates the Rayleigh scattering with the

Raman scattering by assigning each particle (i.e. each dot) to its respective cluster as in [Figure 7.5B](#). Despite the broad Rayleigh scattering range, clusters are homogeneously distributed per sample along the Rayleigh scattering axis.

Table 7.1. Biomolecule assignments of Raman bands [cm^{-1}]. For reference see also Table 2.1 in *chapter 2*.

Triglycerides	Cholesterol	Nucleic acids	Proteins	Lipids
1264	700	670	1004	716
1301	1439	788	1088	1088
1657	1669	802	1128	1300
1745		920	1443-1452	1439
		992	1583	1657
		1086	1607	2851/2
		1182	1655-1671	2882
		1253	2882	
		1285	2928-2934	
		1303		
		1315		
		1343		
		1369		
		1421		
		1458		
		1485		
		1573		

7.5 Discussion

To determine the composition of particles in plasma of mCRPC patients and to determine whether such particles differ from those present in plasma of healthy donors, we detected and characterized single particles using OT-sRRs.^{14,15} This technique enabled the label-free detection of particles in suspension and disclosed a Raman spectrum per individual particle, which is related to their chemical composition.

We first explored the composition of particles that are present in the plasma of healthy donors and compared it to that of commercially available LPs, as LPs are the most abundant particles in plasma.^{19,20} Cluster analysis, based on the Raman spectrum of the particles, showed that 45% of particles from all healthy donors cluster together with VLDL and CM. HDL and LDL cluster together but separate from healthy donors. Although the majority of particles in plasma are expected to be HDL and LDL,^{19,20} [Figure 7.2](#) suggests that we do not tend to trap these LPs. This may be due to the increase in trapping force with larger particles, increasing thus the chances



of trapping large over small LPs. All particles from healthy donors and LPs share Raman bands that correspond to lipids, for instance at 1301, 1441, 1657 and 2851/2 cm^{-1} . The mean Raman spectrum of cluster 5, which is composed of VLDL, CM and particles from healthy donors, shows Raman peaks which indicate the presence of triglycerides, e.g. 1264, 1301, 1657 and 1745 cm^{-1} (Figure 7.2).²¹ This further confirms the identification of VLDL and CM, as these particles are rich in triglycerides compared to LDL and HDL.^{22,23} These last two show cholesterol peaks at 702, 958, 1441, 1659 cm^{-1} .²¹ Cholesterol esters are the more predominant lipids in LDL and the second most predominant in HDL.²³ The particles from healthy donors in clusters 1, 2 and 3 show a lipid Raman profile, and their lipid-protein band (2811–3023 cm^{-1}) shows a higher lipid contribution than for all the other particles.

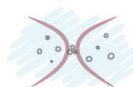
After identifying the major types of particles in plasma of healthy donors, we investigated the particles present in plasma of mCRPC patients. Interestingly, patients 2, 3 and 4 could be discriminated from the healthy donors based on their chemical particle composition (Figures 7.4C and 7.4D). Patients 2 and 3 show particles with similar composition, but different to patient 4. Patients 1 and 5 cluster together with a subgroup of healthy donors (cluster 3, Figure 7.4C), suggesting that the particles from patients 1 and 5 are LPs, while the particles from patients 2, 3 and 4 show a higher protein contribution.

To understand the nature of the particles present in the plasma of patients, we included in the PCA and HCA reference particles, such as LNCaP EVs, RBC EVs and commercially available LPs. The results in Figure 7.5 show that particles from patient 1 cluster with VLDL, CM and with around 44% of the particles from healthy donors, suggesting that particles from patient 1 correspond to LPs, specifically VLDL and/or CM. This can be further confirmed by looking at the mean Raman spectrum of particles from patient 1 (Figure 7.3), which shows characteristic peaks of triglyceride-rich particles, such as VLDL and CM.²² The majority of the particles from patient 5 cluster with HDL and LDL. The mean Raman spectrum of the particles from patient 5 shows Raman peaks at 700, 958, 1441 and 1659 cm^{-1} , indicating the presence of cholesterol, which is a main component in LDL and HDL.^{21,23} The lipid profile of the plasma of patient 5 showed high values for total cholesterol and LDL-cholesterol (Table S7.1), further confirming that these particles are LPs, i.e. LDL. Patients 2 and 3 cluster together separate from patient 4. Although the particles from these three patients show higher protein contribution than the particles from healthy donors, which include LPs, it is not clear what kind of particles are those from patients 2, 3 and 4, as they do not overlap with the reference particles we used. LNCaP EVs were used as a model for tdEVs in mCRPC patients. However, LNCaP EVs do not cluster with any of the particles from the patients, even though the LNCaP EVs show also high protein

contribution.¹⁵ Thus, we did not trap particles with a chemical composition similar to LNCaP EVs, so further investigation is required to determine the type of particles present in patients 2, 3 and 4.

The Rayleigh scattering distribution from patients 2, 3 and 4 have lower medians than patients 1 and 5. Assuming that all particles have similar refractive index, the ones from patients 2, 3 and 4 would be smaller in size than those from patients 1 and 5, as well as those from EVs. This also accounts for the noisier Raman spectra of patients 2, 3 and 4. All the particles of patients 2 and 3 grouped in a single cluster (cluster 7), although cluster 7 also contains very few particles from patients 1 and 5, as well as from healthy donors and LPs (refer to [Table S7.2](#)). On the other hand, 95% of the particles in patient 4, fall in the same cluster (cluster 8) and no other particle from other samples are grouped in the same cluster 8. Hence, the Raman spectrum of cluster 8 ([Figure 7.5C](#)) corresponds to the mean Raman spectrum of 95% of the particles in patient 4. Interestingly, the Raman spectrum of the particles of patient 4 shows bands (see labels in [Figure 7.5D](#)) that indicate the presence of nucleic acids, either inside the particles or bound to their outer surface. This patient shows the highest PSA level of all patients and may suggest the presence of a large amount of tumor plasma DNA, which is frequently observed in these patients.^{24–31} However, further studies are needed to clarify the exact nature of these particles.

Although it may be expected that most of the trapped particles would cluster together with the LPs, cluster analysis showed that only around 50% of the particles from healthy donors clustered together with LPs (i.e. VLDL and/or CM). The rest of the particles from healthy donors grouped into 2 clusters both showing a lipid profile, similar to VLDL and CM, but with a different protein-to-lipid ratio. More important, 3 out of the 5 patients showed a clear separation from all the particles of healthy donors and even though they did not cluster with LNCaP EVs, the composition of the particles might be related to an altered lipid metabolism, which has been increasingly recognized in cancer.^{32–34} In an effort to survive and proliferate in the tumor microenvironment, cancer cells undergo metabolic reprogramming with lipid alterations.^{35,36} These alterations can be reflected in serum concentrations of LPs as well as in their composition.^{37,38} This pilot study suggests that the composition of particles in plasma of mCRPC patients can disclose important changes that occur in cancer and it may be surmised that varying concentrations and/or particle composition may provide information on whether or not a certain treatment will be effective. If tdEVs are to be found in plasma of cancer patients, a prior enrichment of these EVs would be beneficial to increase their concentration. Nevertheless, the significant differences observed in the general particle profile of the plasma fraction of some patients compared to healthy controls motivates further research with a larger cohort of patients. Moreover, the utilization



of other submicrometer particles, such as LPs, next to tdEVs, as cancer biomarkers should not be underestimated.

Acknowledgments

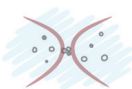
The authors thank Linda Rikkert from the Laboratory of Experimental Clinical Chemistry, Amsterdam UMC, University of Amsterdam, Amsterdam, The Netherlands for patient sample collection and handling, and Aufried T. M. Lenferink from the Department of Medical Cell BioPhysics, University of Twente, Enschede, The Netherlands, for excellent support during the Raman measurements.

References

1. Global Cancer Observatory. International Agency for Research on Cancer; World Health Organization (2018). Available at: <http://gco.iarc.fr/>. (Accessed: 24th February 2020)
2. Roy, S. & Morgan, S. C. Who Dies From Prostate Cancer? An Analysis of the Surveillance, Epidemiology and End Results Database. *Clin. Oncol.* 31, 630–636 (2019).
3. Antonarakis, E. S. et al. AR-V7 and resistance to enzalutamide and abiraterone in prostate cancer. *N. Engl. J. Med.* 371, 1028–1038 (2014).
4. Romanel, A. et al. Plasma AR and abiraterone-resistant prostate cancer. *Sci. Transl. Med.* 7, 312re10–312re10 (2015).
5. Crona, D. J. & Whang, Y. E. Androgen receptor-dependent and -independent mechanisms involved in prostate cancer therapy resistance. *Cancers* 9, 67 (2017).
6. Karzai, F. H., Madan, R. A. & Figg, W. D. Beyond PSA: Managing modern therapeutic options in metastatic castration-resistant prostate cancer. *Southern Medical Journal* 108, 224–228 (2015).
7. De Bono, J. S. et al. Circulating tumor cells predict survival benefit from treatment in metastatic castration-resistant prostate cancer. *Clin. Cancer Res.* 14, 6302–6309 (2008).
8. Lorente, D. et al. Circulating tumour cell increase as a biomarker of disease progression in metastatic castration-resistant prostate cancer patients with low baseline CTC counts. *Ann. Oncol.* 29, 1554–1560 (2018).
9. Lorente, D. et al. Decline in Circulating Tumor Cell Count and Treatment Outcome in Advanced Prostate Cancer. *Eur. Urol.* 70, 985–992 (2016).
10. Coumans, F. A. W., Doggen, C. J. M., Attard, G., de Bono, J. S. & Terstappen, L. W. M. M. All circulating EpCAM+CK+CD45- objects predict overall survival in castration-resistant prostate cancer. *Ann. Oncol. Off. J. Eur. Soc. Med. Oncol.* 21, 1851–7 (2010).
11. Nanou, A. et al. Abstract 4464: Tumor-derived extracellular vesicles in blood of metastatic breast, colorectal, prostate, and non-small cell lung cancer patients associate with worse survival. in AACR 2019 Proceedings: Abstract 4464 - American Association for Cancer Research 4464–4464 (2019). doi:10.1158/1538-7445.sabcs18-4464
12. Nanou, A. et al. Circulating tumor cells, tumor-derived extracellular vesicles and plasma cytokeratins in castration-resistant prostate cancer patients. *Oncotarget* 9, 19283–19293 (2018).
13. Coumans, F., van Dalum, G. & Terstappen, L. L. W. M. L. W. M. M. CTC Technologies and Tools. *Cytom. A* 93, 1197–1201 (2018).
14. Enciso-Martinez, A. et al. Synchronized Rayleigh and Raman scattering for the characterization of single optically trapped extracellular vesicles. *Nanomedicine Nanotechnology, Biol. Med.* 24, 102109 (2020).
15. Enciso-Martinez, A. et al. Label-free identification and chemical characterisation of single extracellular vesicles and lipoproteins by synchronous Rayleigh and Raman scattering. *J. Extracell. Vesicles* 9, 1730134 (2020).
16. Uzunbajakava, N. et al. Nonresonant confocal Raman imaging of DNA and protein distribution in apoptotic cells. *Biophys. J.* 84, 3968–81 (2003).
17. Van Manen, H. J., Uzunbajakava, N., Van Bruggen, R., Roos, D. & Otto, C. Resonance Raman imaging of the NADPH oxidase subunit cytochrome b 558 in single neutrophilic granulocytes. *J. Am. Chem. Soc.* 125, 12112–12113 (2003).



18. Ning, X., Selesnick, I. W. & Duval, L. Chromatogram baseline estimation and denoising using sparsity (BEADS). *Chemom. Intell. Lab. Syst.* 139, 156–167 (2014).
19. Simonsen, J. B. What are we looking at? Extracellular vesicles, lipoproteins, or both? *Circ Res* 121, 920–922 (2017).
20. Johnsen, K. B., Gudbergsson, J. M., Andresen, T. L. & Simonsen, J. B. What is the blood concentration of extracellular vesicles? Implications for the use of extracellular vesicles as blood-borne biomarkers of cancer. *Biochim Biophys Acta Rev Cancer* 1871, 109–116 (2019).
21. Movasaghi, Z., Rehman, S., Rehman, I. U. I. U. & Zanyar Movasaghi, S. R. & D. I. U. R. Raman Spectroscopy of Biological Tissues. *Appl. Spectrosc. Rev.* 42, 493–541 (2007).
22. Chan, J. W., Motton, D., Rutledge, J. C., Keim, N. L. & Huser, T. Raman Spectroscopic Analysis of Biochemical Changes in Individual Triglyceride-Rich Lipoproteins in the Pre-and Postprandial State. (2005). doi:10.1021/ac050692f
23. Satyanarayana, U. & Chakrapani, U. *Biochemistry*. (Elsevier Health Sciences APAC, 2013).
24. Schwarzenbach, H., Hoon, D. S. B. & Pantel, K. Cell-free nucleic acids as biomarkers in cancer patients. *Nature Reviews Cancer* 11, 426–437 (2011).
25. Khalaf, D. et al. Circulating tumor DNA (ctDNA) and correlations with clinical prognostic factors in patients with metastatic castration-resistant prostate cancer (mCRPC). *J. Clin. Oncol.* 35, 186–186 (2017).
26. Anker, P., Mulcahy, H. & Stroun, M. Circulating nucleic acids in plasma and serum as a noninvasive investigation for cancer: Time for large-scale clinical studies? *International Journal of Cancer* 103, 149–152 (2003).
27. Taback, B., O'Day, S. J. & Hoon, D. S. B. Quantification of circulating DNA in the plasma and serum of cancer patients. in *Annals of the New York Academy of Sciences* 1022, 17–24 (New York Academy of Sciences, 2004).
28. Conteduca, V. et al. Circulating tumor DNA fraction (ctDNA) as a surrogate predictive biomarker in metastatic castration-resistant prostate cancer (mCRPC). *J. Clin. Oncol.* 37, 5039–5039 (2019).
29. Jahr, S. et al. DNA fragments in the blood plasma of cancer patients: Quantitations and evidence for their origin from apoptotic and necrotic cells. *Cancer Res.* 61, 1659–1665 (2001).
30. Heitzer, E. et al. Tumor-associated copy number changes in the circulation of patients with prostate cancer identified through whole-genome sequencing. *Genome Med.* 5, 30 (2013).
31. Belic, J. et al. Genomic alterations in plasma DNA from patients with metastasized prostate cancer receiving abiraterone or enzalutamide. *Int. J. Cancer* 143, 1236–1248 (2018).
32. Yue, S. et al. Cholesteryl ester accumulation induced by PTEN loss and PI3K/AKT activation underlies human prostate cancer aggressiveness. *Cell Metab.* 19, 393–406 (2014).
33. Santos, C. R. & Schulze, A. Lipid metabolism in cancer. *FEBS J.* 279, 2610–2623 (2012).
34. Zhang, F., Du, G. & Profes-Sor, A. Dysregulated lipid metabolism in cancer. *World J Biol Chem* 3, (2012).
35. Beloribi-Djefaffia, S., Vasseur, S. & Guillaumond, F. Lipid metabolic reprogramming in cancer cells. *Oncogenesis* 5, e189–e189 (2016).
36. Gomaschi, M. Role of Lipoproteins in the Microenvironment of Hormone-Dependent Cancers. *Trends in Endocrinology and Metabolism* 31, 256–268 (2020).
37. Muntoni, S. et al. Serum lipoproteins and cancer. *Nutr. Metab. Cardiovasc. Dis.* 19, 218–225 (2009).
38. Barclay, M. et al. Lipoproteins in Cancer Patients. *CA. Cancer J. Clin.* 21, 202–212 (1971).



Supporting Information

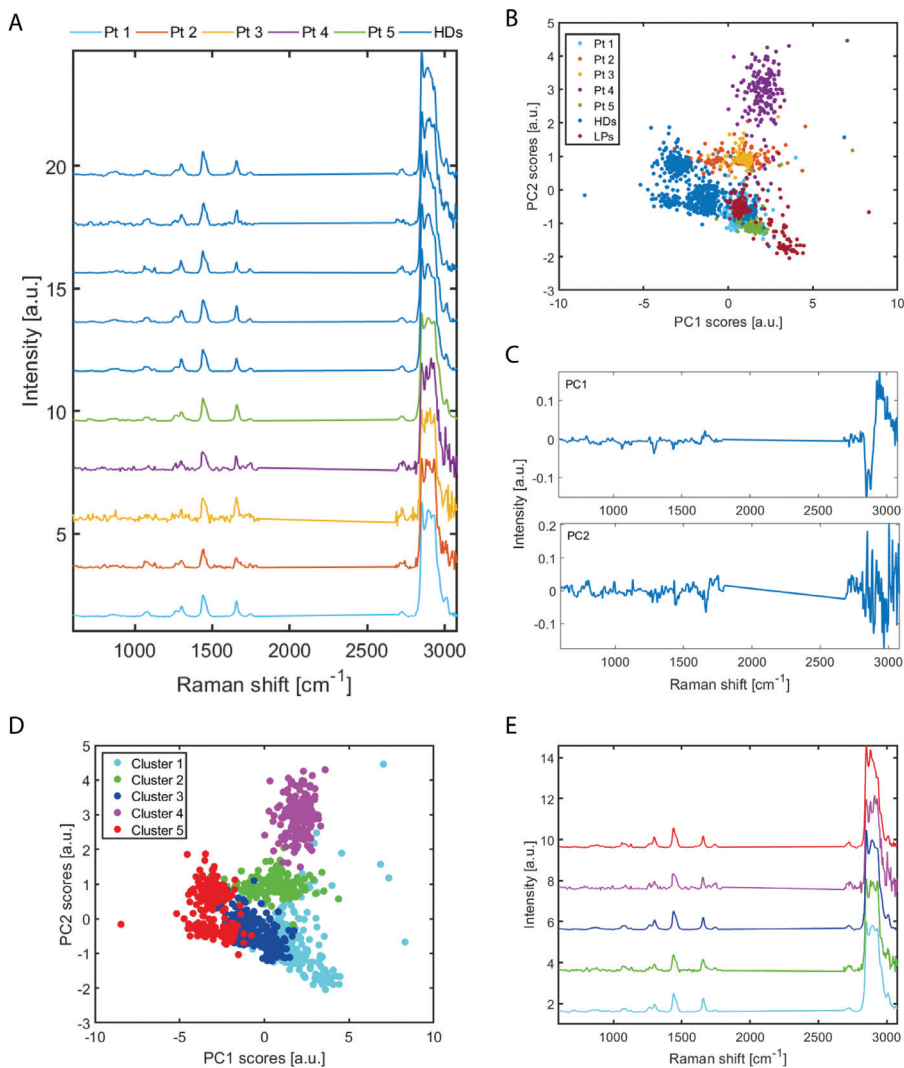


Figure S7.1. Multivariate analysis of mCRPC patients (N=5), healthy donors (HDs, N=5) and LPs. **(A)** Mean Raman spectra of single trapped particles from patients and healthy donors. **(B)** First and second principal component scores corresponding to single particles from healthy donors (blue), patients 1 to 5 and LPs (brown). **(C)** First two principal component loadings resulting from PCA on the combined fingerprint (600-1800 cm^{-1}) and high frequency (2680-3080 cm^{-1}) regions. **(D)** First and second principal component scores color-clustered into five clusters after HCA. **(E)** Mean Raman spectra per cluster in (D).

Table S7.1. Metastasized castration-resistant prostate cancer (mCRPC) patients and healthy donors clinical data.

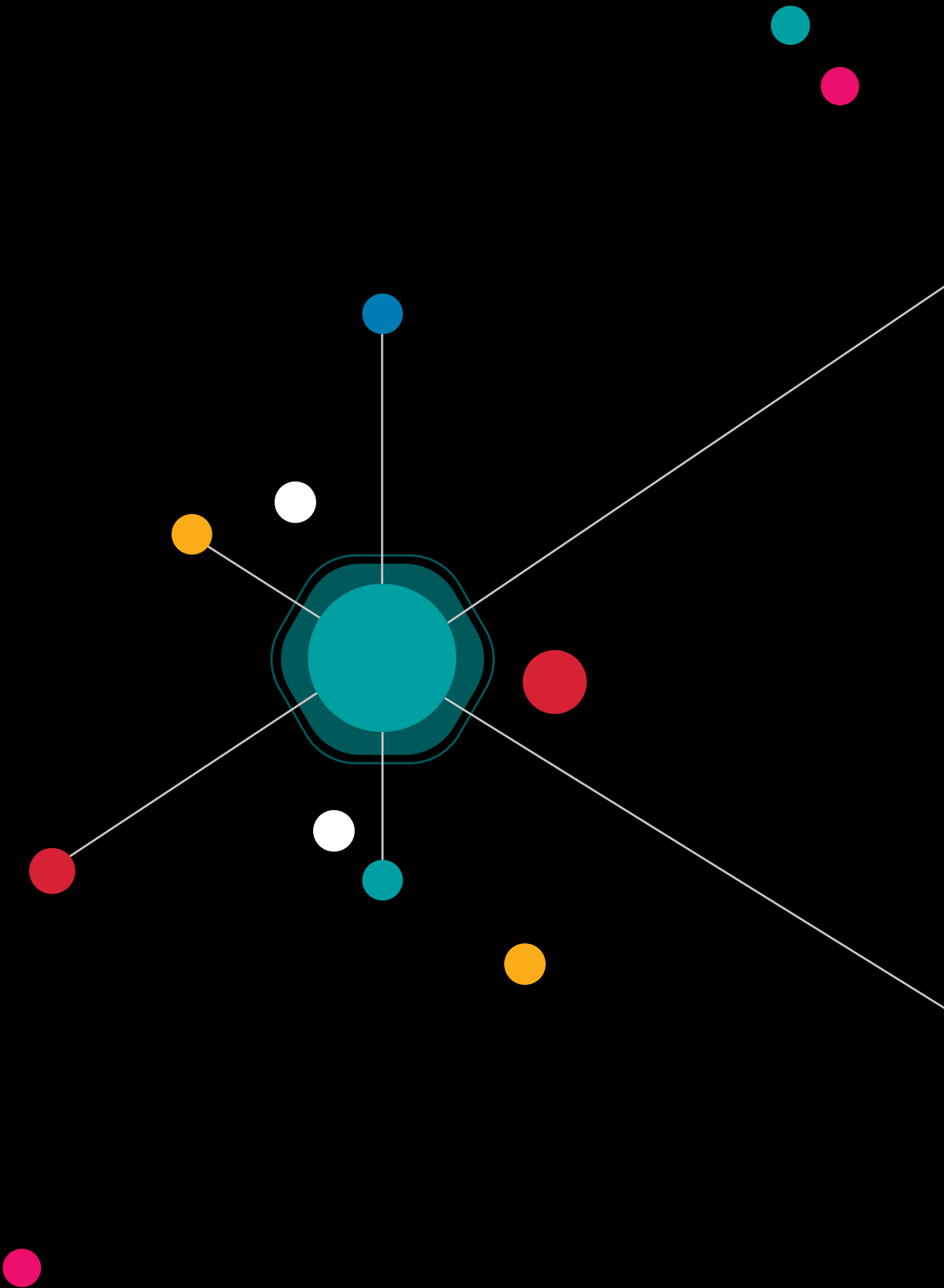
Donors	Date of cancer diagnosis	Date of CRPC diagnosis	Current treatment	Age	PSA*	LDH	ALP	tChol	HDL	LDL	TGL
<i>Pt 1</i>	05/2017	10/2018	Abiraterone prednisone	66	0.6	202.9	1.6	3.89	1.27	2.13	1.08
<i>Pt 2</i>	2006	04/2018	Enzalutamide	86	3.4	165.4	1.4	5.44	1.57	3.24	1.41
<i>Pt 3</i>	2000	04/2018	Abiraterone prednisone	75	1.2	175.6	5.0	3.15	1.37	1.39	0.86
<i>Pt 4</i>				77	17.6	165.3	3.3	5.45	2.22	2.82	0.92
<i>Pt 5</i>				82	10.4	240.3	6.4	5.75	1.36	3.59	1.78
<i>HD Min</i>	NA	NA	NA	19	NA	125.8	1.2	3.45	0.93	1.81	0.42
<i>HD Max</i>	NA	NA	NA	40	NA	270.3	3.2	4.38	1.45	2.47	1.93

Pt: patient; HD: healthy donor (N=5); PSA: prostate specific antigen; *last determined PSA level before inclusion; LDH: Lactate dehydrogenase (U/L 37C), ALP: Alkaline phosphatase (U/L 37C), tChol: total cholesterol (mmol/L), HDL: high density lipoproteins (mmol/L), LDL: low density lipoproteins cholesterol (mmol/L), TGL: Triglyceride (mmol/L).

Table S7.2. Number of particles assigned per cluster corresponding to Figure 5

	1	2	3	4	5	6	7	8	Total
Pt 1	0	0	0	0	0	272	2	0	274
Pt 2	0	0	0	0	0	0	130	0	130
Pt 3	0	0	0	0	0	0	62	0	62
Pt 4	0	0	0	0	0	0	9	156	165
Pt 5	0	0	2	0	218	4	2	0	226
HDs	0	0	410	325	3	580	17	0	1335
HDL & LDL	0	1	0	0	60	2	3	0	66
VLDL & CM	0	0	0	0	0	133	0	0	133
LNCaP EVs	67	7	0	0	0	0	0	0	74
RBC EVs	0	56	0	0	0	0	0	0	56








Chapter 8


Organosilicon uptake by biological membranes



P. Beekman,* A. Enciso-Martinez,* S.P. Pujari, L.W.M.M. Terstappen, H.T. Zuilhof,
S. Le Gac, C. Otto

** authors contributed equally*

Submitted for publication



Abstract

Organosilicon compounds are ubiquitous in everyday use. Application of several of these compounds in food, cosmetics and pharmaceuticals is widespread on the assumption that these materials are not systemically adsorbed.¹⁻⁴ However, here the interactions of various organosilicon compounds (simeticone, hexamethyldisilazane and poly(dimethylsiloxane)) with cell membranes and model lipid membranes are characterized with a range of analytical chemistry tools to demonstrate that complexations of these compounds occur in or on the cell membrane and that they can be covalent in nature. The increasing application of organosilicon compounds as replacement of plastics calls for a better awareness and understanding of these interactions. Moreover, with many biotechnology tools relying on organosilicon materials, it is important to understand the bias on characterization results induced by silicone leaching.

8.1 Introduction

Organosilicon compounds, which are silicon-containing hydrocarbons, have a wide range of accepted usage.¹ Examples include silicones like poly(dimethylsiloxane) (PDMS) which is accepted by the European Food Safety Authority (EFSA) as a food additive,⁵ and widely used in the field of microfluidics.⁶ The silicone-based over-the-counter drug simeticone is used as gastro-intestinal surfactant to treat colic in infants.⁷ Interestingly, there is no dosage limitation for this drug since it is claimed not to be absorbed systemically and it has been generally recognized as safe since before the FDA started Over-The-Counter Drug Review in 1972.⁸ However, despite the widespread use of silicones in products for use in humans, there relatively little literature regarding the possible interactions between silicone molecules and lipid membranes and, potentially, other biomolecules vital to living organisms. Moreover, various research disciplines use silicones for a broad range of applications. Leaching of low-molecular weight components into the samples under study may greatly influence results,^{6,9} for instance in lab-on-a-chip research and scanning electron microscopy (SEM) studies, which we briefly clarify below:

- 1) In the lab-on-a-chip field,^{10,11} the massive adoption of PDMS for the production of microfluidic and organ-on-a-chip platforms can be attributed to the ease of fabrication, its optical transparency, its gas-permeability, which is particularly attractive for cell culture experiments, and its elastomeric properties. Finally, PDMS has proven to be biocompatible in the sense that it does not significantly affect cell viability, also for very sensitive cells like mouse and human embryos.^{12–14} In-vivo short term studies reported no significant changes in the survival of rats fed with diets containing up to 10% PDMS.^{15,16} However, to our knowledge, systemic uptake was never comprehensively studied. In contrast, it has been demonstrated that PDMS microenvironments do modulate gene expression significantly,¹⁷ especially in comparison with other polymers.¹⁸
- 2) In SEM studies, biological samples require pretreatment before they can be placed in a vacuum chamber for imaging. Fixation, dehydration, drying and coating with an electrically conductive layer are typically required. Dehydration and drying seem to be the most critical steps as they can give rise to artifacts, such as specimen shrinkage and distortion.^{19–24} A common method for drying uses hexamethyldisilazane (HMDS).^{25,26} The mechanism by which HMDS acts on biological specimens has been poorly described. It is known to react via transfer of trimethylsilyl groups,²⁷ which can happen with, e.g. sugars and amino acids in biological specimens. In this process proteins crosslink to fix the biological specimen, avoiding its collapse during drying.²⁶

Based on preliminary observations of silicone residue in lipid membranes after incubation in microfluidic channels and HMDS-drying (*vide infra*), we set to investigate whether organosilicons, broadly speaking, interact with molecules found in biological membranes. To illustrate the generality of the silicone-membrane interactions, three different organosilicon sources were included in this study (See SI8.1 for structural information):

- 1) PDMS (Sylgard 184), whose oligomers leach from incompletely cured microfluidic channels;
- 2) HMDS used for dehydration in electron microscopy (EM) sample preparation; and
- 3) Infacol, an over-the-counter drug, containing simeticone, an organosilicon compound similar to PDMS, mixed with silica particles.

Two different specimens were considered: cells (LNCaP and HT-29 cell lines) and supported lipid bilayers (SLBs) prepared from synthetic but naturally abundant dioleoyl-phosphatidyl choline (DOPC).²⁸ SLBs are widely used as models of cellular membranes;²⁹ here, they allow studying oligomer interactions with phospholipid molecules using X-ray Photoelectron Spectroscopy (XPS).

The interactions between silicones and biological membranes were studied using four analytical techniques: a) Confocal Raman micro-spectroscopy, to probe the presence of specific chemical bonds down to 400 nm spatial resolution and map the spectra in a hyperspectral image; b) Auger Electron Spectroscopy (AES), to identify atomic species present at the surface of a sample, and which allows overlay with EM images to show the spatial distribution of species; c) XPS, to investigate with high elemental sensitivity whether silicon is present in natively silicon-free samples of SLBs after incubation with silicones; and d) Infrared spectroscopy (IR), to probe chemical bonds and for the presence of organosilicon compounds.

8.2 Materials and methods

A schematic overview of the sample preparation and subsequent characterization steps is presented in [Figure 8.1](#). Each individual step will be discussed in more detail in the following sections.

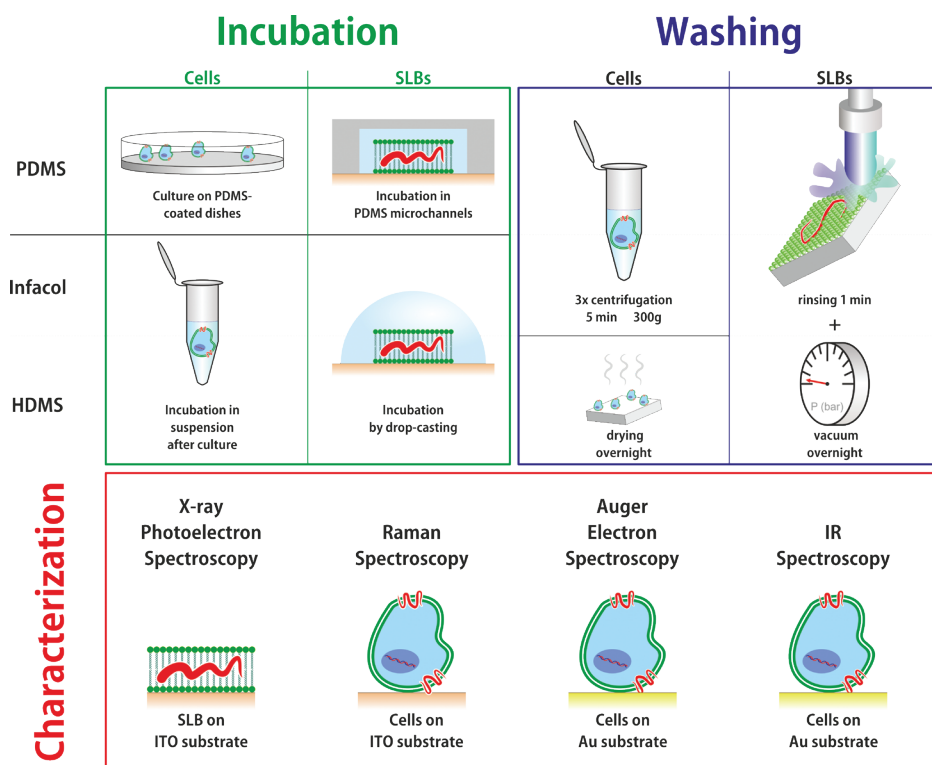


Figure 8.1. Overview of sample preparation and characterization steps. Cells and SLBs were first incubated with PDMS, Infacol or HDMS on substrates conforming to the requirements of the intended characterization instruments. The organosilicon compounds are presented as “red wavy lines” and their hypothetical interaction with membranes (vide infra) is here suggested. The excess of organosilicon compounds was removed before samples were characterized with various techniques.

8.2.1 Materials

PDMS was prepared using Sylgard 184 (Dow Corning) purchased from Farnell, Utrecht, The Netherlands. Infacol (TEVA) was purchased from Die Grenze, Almelo, The Netherlands. 1,2-dioleoyl-sn-glycero-3-phosphocholine (DOPC) was purchased from Avanti Polar Lipids, Alabama, US. All other chemicals were obtained from Sigma Aldrich, Zwijndrecht, The Netherlands, unless otherwise specified. In all experiments, phosphate buffered saline (PBS) was prepared at pH 7.4 filtered through a 0.2- μm syringe filter before use.

Indium Tin Oxide (ITO) coated fused silica substrates were used in combination with XPS. This material was chosen because of its low Raman background signal and its suitability for chemical surface modification. For Auger Electron Spectroscopy and IR, gold-coated fused silica substrates were used. Coating was performed in the cleanroom of the MESA+ Institute

for Nanotechnology by sputtering.³⁰ After sputtering, the chips were cut by dicing to a size of 1×1 cm².

8.2.2 Cell culture

Cells from a prostate cancer cell line (LNCaP) or colon cancer cell line (HT-29), purchased from the American Type Culture Collection (ATCC), were cultured in RPMI-1640 medium with L-glutamine (Lonza) supplemented with 1% penicillin and 1% streptomycin (Westburg, Amersfoort, The Netherlands) in an incubator at 37°C and with 5% CO₂, medium being refreshed every 3 days and cells being reseeded at a density of 10⁴ cells/cm². For experiments, 8 × 10⁶ cells were harvested using a 0.25% Trypsin solution (Thermo Fisher, Amsterdam, The Netherlands). Subsequently, the cells were fixed in 1% paraformaldehyde (PFA) for 15 min and washed three times in PBS by centrifuging at 300 g for 5 min. Finally, the sample was split in 6 equal fractions, each containing 1.3 × 10⁶ cells. Fixation alters the chemical state of several proteins but since it is necessary for some experiments it was done even in samples to be measured with Raman to keep results consistent (also with data not discussed in this paper). No Si species are introduced this way, so fixation cannot interfere with our conclusions.

8.2.3 Supported lipid bilayers

Supported lipid bilayers (SLBs) were formed by fusing small unilamellar vesicles on the ITO-coated surface. A DOPC solution in chloroform was dried under vacuum, to yield a lipid film on the walls of a glass vial. This lipid film was re-hydrated in PBS to reach a DOPC concentration of 10 mg/ml and ultrasonicated for 15 min to form small unilamellar vesicles (SUVs). ITO substrates were cleaned ultrasonically in dichloromethane, acetone and ethanol for 3 min each, followed by 30 min of O₂-plasma treatment in a Diener Pico (Diener electronic, Bielefeld, Germany) at 250 W. The cleaned surfaces were incubated with a diluted SUV suspension (1 mg/mL in PBS) at room temperature overnight. After incubation, the substrates were thoroughly rinsed with PBS. Before their characterization with XPS, all SLB samples were dried under vacuum overnight.

8.2.4 Sample preparation – organosilicon

Sticky PDMS microchannels were fabricated using xurography, as previously reported by us.³¹ Briefly, Sylgard 184 precursor was thoroughly mixed with the curing agent in a 10:1 weight ratio and degassed by centrifugation at 1000 g for 1 min. A mold was prepared by cutting a 0.2-mm thick adhesive film to yield 3×6 mm² patterns that were laminated in the bottom of a clean petri dish. The PDMS prepolymer/curing agent mixture was poured over the mold and degassed again under vacuum, before being cured at 80°C for 30 min yielding a sticky solid. Inlet and outlet holes were punched with a Harris Uni-Core 1-mm biopsy punch (VWR International B.V.,

Amsterdam, The Netherlands). For control experiments, PDMS microchannels were prepared using the same protocol, but more thoroughly cured at 80°C overnight. Before bonding, the latter PDMS microchannel devices were ultrasonicated in ethanol for 15 min before plasma activation. Solutions were exchanged in these microchannels by pipetting manually in the inlets.

Infacol consists of a 40 mg/ml solution of simeticone in water with various additives, e.g. dispersing and flavoring agents. Simeticone consists primarily of poly(dimethylsiloxane) with molecular weight ranging between 14 and 21 kDa, mixed with silicon dioxide (4-7%).³² Before use, *Infacol* was diluted to 1 mg/ml in PBS. Solid particles of few microns in diameter that remained in the solution, were removed by filtering the solution (0.2- μ m syringe filter) before experimentation with cells.

Hexamethyldisilazane (HMDS) was used as is, from a recently purchased bottle, extracted through a septum under perfusion with nitrogen by a syringe. Prior to HMDS-drying, cells were dehydrated with ethanol. Since Raman bands from ethanol were not observed neither in the HMDS-dried cells, nor in the control cells, it was concluded that ethanol was successfully evaporated from the cells.

8.2.5 PDMS interactions with cells and SLBs

For Auger Electron Spectroscopy (AES), cells were alternatively grown on a 1-mm thick PDMS layer prepared in a petri dish and cured for 30 min at 80°C. HT-29 cells were seeded at a density of 10^4 cells/cm² and left to proliferate for 48 h in RPMI medium supplemented with 1% penicillin and 1% streptomycin at 37°C in a 5% CO₂ atmosphere. Cell adhesion to the PDMS layer after 48 h was comparable to that in standard culture flasks. After trypsinization, cells were fixed for 15 min in 1% paraformaldehyde and washed 3 times with Milli-Q water by centrifugation (300 g, 5 min).

Experiments with SLBs were conducted in sticky microchannels placed on the top of cleaned ITO substrates. A DOPC SUV suspension was injected in the microchannel, and left overnight for incubation at room temperature to yield a SLB on the ITO-coated substrate. As for the cells, channels were rinsed with PBS and after delamination of the PDMS, the substrates were rinsed thoroughly with deionized water before analysis with XPS.

8.2.6 HMDS interactions with cells and SLBs

Fixed LNCaP cells in suspension (MilliQ) were dehydrated in increasing concentrations of ethanol (70-100%), followed by HMDS-drying and deposited on flat substrates overnight.³³ As a negative control, the HMDS-drying step was omitted and cells in 100% ethanol were dried

on the substrates overnight. ITO-coated and gold-coated fused-silica substrates were used for Raman and AES spectroscopy, respectively. SLBs prepared on a gold-coated fused-silica substrate were fully immersed in 1 ml of HMDS and dried under vacuum overnight.

8.2.7 Simeticone interactions with cells and SLBs

Fixed HT-29 cells were immersed in diluted Infacol solution and left overnight. Before characterization, cells were washed twice in PBS. For AES analysis, cells were deposited on gold-coated silica substrates. SLBs were immersed in 1 ml undiluted Infacol and dried under vacuum overnight after thorough rinsing.

8.2.8 Raman spectroscopy

An in-house Raman spectrometer was employed, that has been described in detail elsewhere.³¹ Briefly, 2D point scanning of a laser beam ($\lambda = 647.09$ nm) from a Coherent Innova 70C laser was performed. The Raman scattered light was dispersed in a spectrometer and collected with a CCD camera (Andor Newton DU-970-BV). The laser power was measured underneath the objective (40 \times , NA: 0.95; Olympus) and adjusted to 35 mW. The laser focal spot was focused 5 μm above the substrate to ensure it was close to the center of the cells. A 20 μm \times 20 μm area was scanned with a step size of 0.31 μm and an illumination time of 100 ms per pixel. Hyperspectral images are created by integrating the Raman band between 450 and 550 cm^{-1} , which contains the high intensity band 490 cm^{-1} , which is visible in all cells dried with HMDS. The area value of each pixel is converted to a color in a heat map scale.

8.2.9 XPS measurements

By using XPS, the atomic composition of the SLBs was characterized after incubation with organosilicon compounds (HMDS, PDMS and Infacol) and compared to control SLBs (no incubation) and bare ITO. By using this technique, with a probing depth of ~ 10 nm, a signal was detected from the entire SLB and the outer surface of the substrate. As such, this technique gave a comprehensive overview of the elemental composition of a lipid bilayer. Measurements were performed using a JEOL 9200 with a monochromatic Al K α X-ray source operated at 12 kV, with a beam current of 20 mA. The analyzer pass energy was set to 10 eV. Wide scans (0 – 800 eV) were recorded for inspection of all present elements. Narrow scans in the range of 90 – 105 eV were acquired to provide more detailed information about silicon presence. Spectra were fitted by Casa XPS software (www.casaxps.com) for quantification.

8.2.10 Auger Electron Spectroscopy

AES was performed using a JEOL Ltd. JAMP-9500F field emission scanning Auger microprobe. Briefly, this instrument probes chemical bonds by irradiating a surface locally with a focused electron beam and measuring the energetic spectrum of electrons emitted through the Auger effect. These secondary electrons with relatively low energy primarily originate from a 2-3 nm layer at the surface. Scanning this beam with a small irradiation spot size allows the acquisition of hyperspectral images with a sub-micron spatial resolution. In conjunction, the instrument can be operated in scanning electron microscopy (SEM) mode, for comparing the morphological appearance of the sample.

Cells incubated with HMDS and Infacol and cells cultured on PDMS dishes were compared to non-incubated cells (negative controls). Areas with around 20 to 200 cells were divided into fields of 256x256 pixels which were scanned in the narrow bands for gold (Au_{MNN} , 2015 eV), silicon (Si_{LMM} , 92 eV), carbon (C_{KLL} , 263 eV) and nitrogen (N_{KLL} , 375 eV) with a dwell time of 100 ms per pixel. Narrow band signals were integrated and background subtracted in Spectra Inspection Software (JEOL). The resulting bitmaps were converted to binary images and diluted in ImageJ. Across every row of [Figure 8.2c](#), the images were treated with the same threshold settings.

8.2.11 IR spectroscopy

The samples inspected with AES were next analyzed using IR spectroscopy on an Attenuated Total Reflection (ATR) with Alpha-P spectrometer from Bruker (Billerica, MA, USA). All spectra were obtained by averaging 32 scans. The resolution was set at 4 cm^{-1} . All spectra were recorded at room temperature and ambient atmosphere. These samples were also measured by using reflection FTIR spectra using a 50- μm diameter aperture in a Bruker Hyperion 1000 spectrometer equipped with a 15 \times objective coupled to a Bruker Tensor 27 FTIR spectrometer. A liquid nitrogen cooled MCT wideband detector is used to detect a spectral range from 4000–600 cm^{-1} . A background spectrum was collected from plasma cleaned gold surfaces. In addition to these samples, a gold substrate was coated with PDMS to compare the magnitude of the signal from silicone compounds found in cells to those found in pure polymer. Sylgard 184 base and curing agent were mixed in a 10:1 weight ratio and a droplet of this mixture was placed on a cleaned gold surface and spread uniformly using a clean glass microscope slide, resulting in a thin (several μm), coating. This sample was stored at room temperature and measured after 12 hours.

8.3 Results and discussion

The interaction of HMDS with cells was assessed by Raman spectroscopy. [Figure 8.2a](#) shows the mean Raman spectrum of cells dried in absence ([Figure 8.2a \(1\)](#)) and presence ([Figure 8.2a \(2\)](#)) of HMDS. HMDS-dried cells show four main peaks (490, 710, 2906 and 2964 cm^{-1}) that are not detected in the negative control samples. The contribution of the 490 cm^{-1} peak is clearly visible from the high intensity pixels in cells dried with HMDS, contrary to negative control cells. Spectra (3) and (4) in [Figure S18.4](#) correspond, respectively, to a cell dried with HMDS and to a cluster of dried cells with excess HMDS. Both, (3) and (4) display peaks at 490 and 710 cm^{-1} . The cell contribution to the Raman spectrum in (4) is not significant compared to the peaks at 490 and 710 cm^{-1} . The spectrum in [Figure 8.2a \(3\)](#) corresponds to liquid HMDS, the highest intensity peaks being indicated with arrows at 569, 685, 2900 and 2958 cm^{-1} . Similar high intensity peaks are found in the spectra of cells dried with HMDS (2), yet with a clear shift. [Figure 8.2b](#) shows Raman images of cells dried with (left column) and without (negative control, right column) HMDS, obtained by integration of the band between 450 and 550 cm^{-1} , confirming the absence of such a HMDS-related band in the negative control cells.

The presence of HMDS in the Raman spectra of cells dried with this compound reveals that HMDS does not fully evaporate despite its 24-mbar vapor pressure at room temperature. Furthermore, since HMDS-specific peaks are shifted, it is proposed here that HMDS has reacted with molecules in the cell, either in its membrane or its interior ([Figure 8.2b](#)).

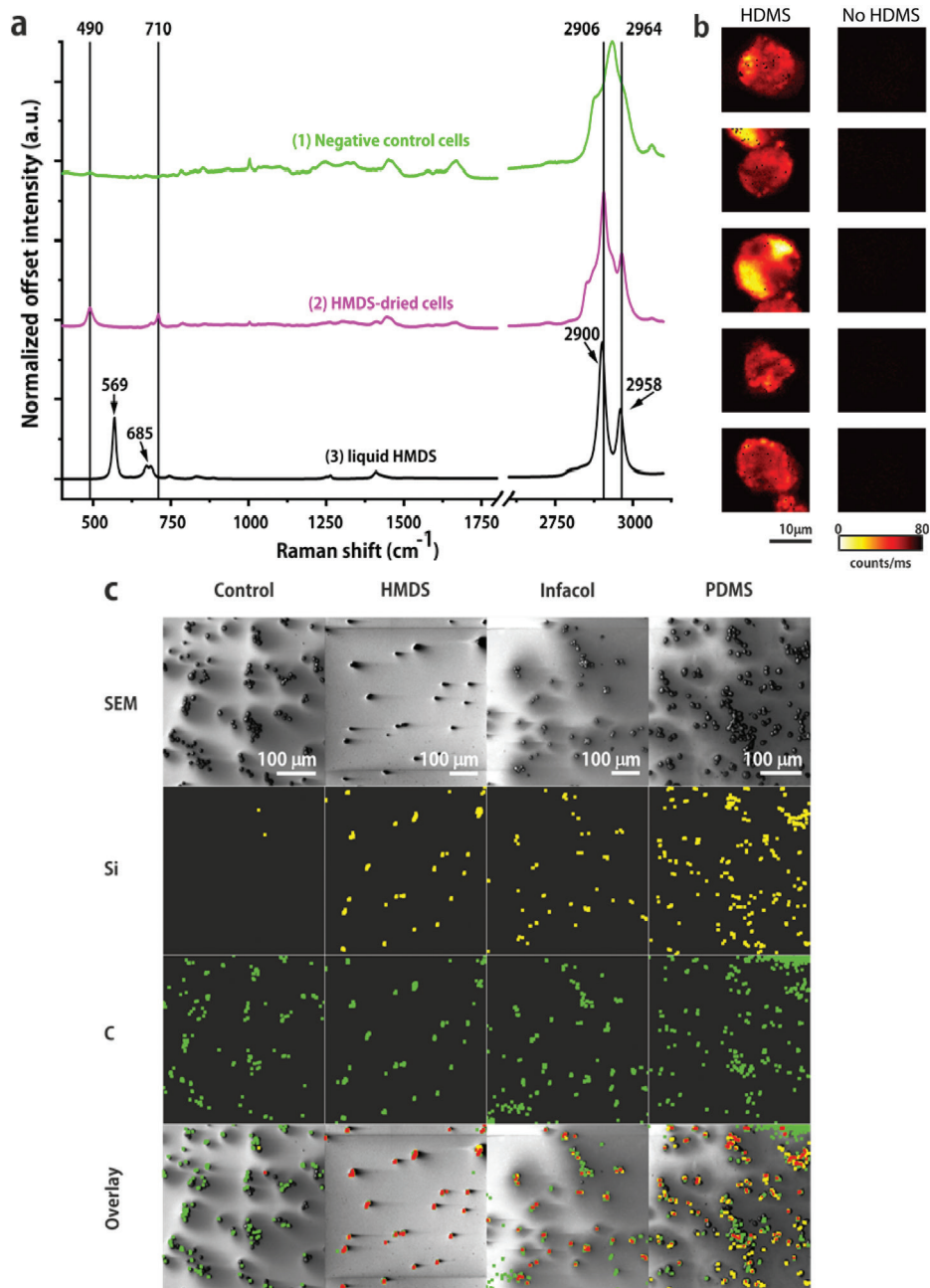


Figure 8.2. Imaging spectroscopic analysis of individual cells. (a) Normalized mean Raman spectra of: (1) 5 negative control cells (green), (2) 5 HMDS-dried cells (magenta), (3) neat (liquid) HMDS (black). (b) Raman images of HMDS-dried cells (left column) and negative control cells (right column) obtained by integration of the band between 450 and 550 cm^{-1} , the region in which the peak assigned to Si-C bonds is located. Raman images were acquired with 35 mW laser excitation power, 100 ms illumination time and 0.31 μm scanning step size. (c) AES/

SEM inspection of the silicon (yellow) and carbon (green) content of cells incubated with silicones compared to non-incubated samples (negative controls). In the same locations, overlapping with cells as shown by SEM, both silicon and carbon are found (overlapping dilated pixels corresponding to both Si and C are indicated in red). The original AES spectra revealing also the presence of N 1s in all cells are provided in SI8.2.

Since AES has a probing depth of only 3 nm, it only detects elements either in or on the cell membrane. Thus, AES was next used to get more information about the localization of the embedded Si species. As depicted in [Figure 8.2c](#), in all incubated samples a Si_{LMM} signal was detected, which was almost entirely absent in the negative control samples. In all samples including the negative control, as expected, the presence of carbon atoms was revealed.

Using XPS, with a probing depth of ~ 10 nm, a signal is detected from the entire SLB and the outer surface of the substrate. XPS wide scans (see [Figure 8.3a](#)) revealed, as expected, the presence of a C 1s signal at 285 eV after formation of a SLB (red), as well as a marked decrease in the signal coming from the ITO (Indium-Tin-Oxide) substrate (e.g. the peak attributed to In 3d at 444 eV). The respective atomic fractions of In 3d, C 1s and Si species per sample indicate that the C 1s signal strongly increased after incubation of the SLBs with any of the organosilicon compounds. This increased carbon signal was accompanied by the emergence of Si 2s and Si 2p peaks at ~ 153 eV and ~ 102 eV, respectively, and the concomitant additional decrease of the In 3d signal ([Figure 8.3b](#)). Noteworthy, a faint Si 2p signal (shifted to ~ 102.5 eV; typically a factor ~ 7 lower than the three categories above) was consistently observed in the non-incubated SLB samples.

The same SLB samples, that were used for AES measurements, were analyzed by IR spectroscopy. Full IR spectra are provided in SI8.3. Close inspection of the $1180\text{--}1300\text{ cm}^{-1}$ region unveils an absorption band for pure PDMS at 1257 cm^{-1} , corresponding to the symmetric stretch of the Si-C bond.³⁴ In the same region, broad bands were found in cell samples incubated with organosilicon compounds, but they were typically red-shifted to $\sim 1230\text{ cm}^{-1}$.²⁷ Interestingly, this band was absent in all control samples, suggesting that this absorption band could be associated with the presence of organosilicon species in the cell samples. This shift can be the result of a change in environment of the polymer species, e.g. by confinement within the cell membrane³⁵ and concomitant change in dipolar interactions.

Previously, it was demonstrated elsewhere³⁶ that small hydrophobic molecules such as drugs and hormones can absorb into a PDMS matrix. Similarly, PDMS can release precursor molecules that have not fully crosslinked in solutions. Regehr et al. reported the presence of uncrosslinked PDMS polymers in cells.⁹ The results presented here suggest that apolar organosilicon compounds *in general* can embed within various biological *membranes*, driven by physicochemical interactions rather than active uptake.

Raman spectroscopy identified the presence of HMDS in cells dried in its presence. The shift of HMDS-related Raman peaks from liquid, neat HMDS to HMDS-dried in cells suggests that HMDS had reacted with molecules in cells and/or their membranes. Raman spectroscopic imaging of single cells (Figure 8.2b) reveals that organosilicon compounds are also present intracellularly, presumably at lipid-rich areas such as the membrane organelles.

AES results collectively suggest that the presence of Si originates from the incubation of the cells with silicones. Furthermore, these results indicate that these Si-containing compounds are located in the outer 3 nm of the cells, i.e. in or on the plasma membrane of the cells, which does not exclude their presence elsewhere, depending on the compound.

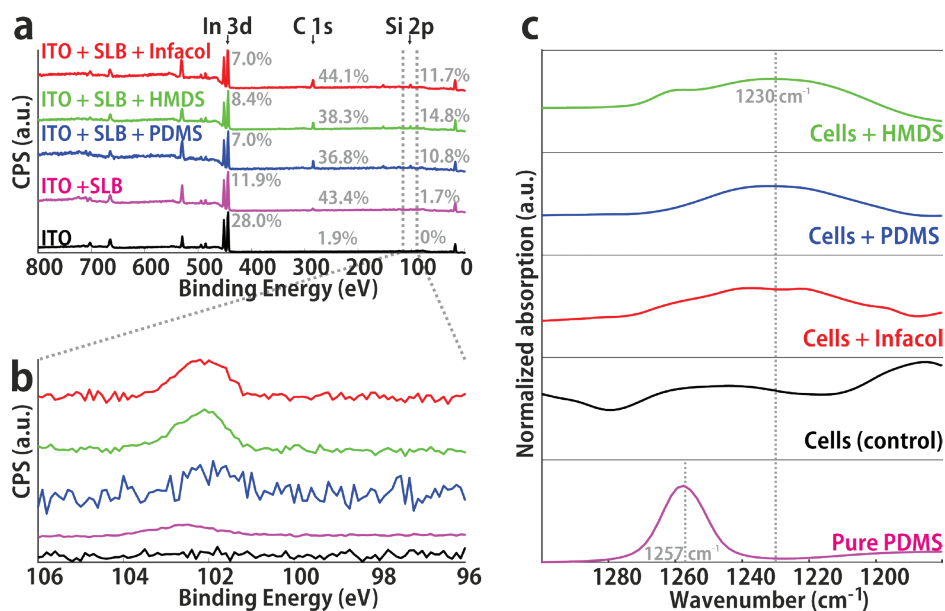


Figure 8.3. Spectroscopic analysis by XPS and IR of biological membranes in the form of SLBs and biological cells. (a) XPS wide scan showing all atomic species present; carbon content (285 eV) increases after SLB formation and again after silicone introduction. The relative contribution of In 3d (444eV) decreases after incubation steps. (b) XPS narrow scan in the Si 2p region, showing a significant increase after silicone introduction. The presence of a trace amount of Si 2p in DOPC supported lipid bilayers (magenta) indicates a minor impurity of the chemicals. (c) Si-C region in IR spectra obtained from pure PDMS and cells incubated with various organosilicon compounds. Incubated cells show a shift in a peak ($\sim 1250\text{ cm}^{-1} \rightarrow \sim 1230\text{ cm}^{-1}$) compared to negative control cells.

Similar interactions were found in SLBs acting here as simplified models for cell membranes, suggesting that the incorporation of silicones into membranes is a passive process, i.e. not driven by membrane proteins or other endocytic processes. The fact that, using XPS, traces of silicon were observed in DOPC SLBs, potentially as a result of packaging, sample handling

or storage, further illustrates the energetic favorability of apolar organosilicon compounds to interact with the phospholipid aliphatic chains.

The previous results strongly suggest that organosilicon compounds are retained in biological systems and more precisely, associate with lipids in biological membranes. Although the precise interaction is not clear, it is unlikely that a chemical reaction occurred between, on one hand, PDMS and (components of) Infacol and, on the other hand, biological specimens, or that any electrostatic interactions took place, since none of the silicones discussed here are charged. The exact location of the silicones – adsorbed on the outside of the membranes or embedded in the membrane – is at present not clear, as both areas would be observed with AES. Embedding in the membrane is most probable, assuming hydrophobic interactions between the trimethyl silyl moieties and the lipid tail environment.

PDMS and (components of) Infacol were not observed inside the cells, but HMDS, having a much lower molecular weight, was able to transfer into the intracellular compartment. Some understanding can be derived from a thermodynamic argument, which is that the polymer molecules in the vicinity of lipids have lower interfacial energy than those surrounded by water. From this reasoning, it follows that the larger the molecule, the more stable the coordination, which may explain that PDMS (1.5 – 6 kDa) and Infacol (14 – 21 kDa) were not observed inside cells, but HMDS, with a lower molecular weight, was able to transfer into the intracellular compartment. To minimize the contact with water, the polymers (with a length of several tens of nanometers) would need to be completely internalized within the phospholipid membrane (with a thickness of around 5 nanometers), thereby stretching out to fit in this quasi-2D landscape (Figure 8.4, right panel). This reduction in solvation energy³⁷ is balanced by an entropic cost, as it is entropically more favorable for polymers to assume a disordered, i.e. coiled or globular conformation^{38,39} (Figure 8.4, left panel) and since trimethyl silyl groups are large compared to linear alkanes. Alternatively, the polymer molecules may also span the membrane in multiple regions, much like a transmembrane protein (Figure 8.4, middle panel). This compromise would give the organosilicon molecules more fluidity, while overall still resulting in an energetically favorable coordination. To study the actual conformation (which may also depend non-linearly on concentration),⁴⁰ computational modeling is required, or the use of characterization tools with higher resolution. Although the precise conformation of organosilicon compounds in biological membranes is thus not clear, the results presented here demonstrate that interactions occur passively and for multiple types of compounds and membranes.

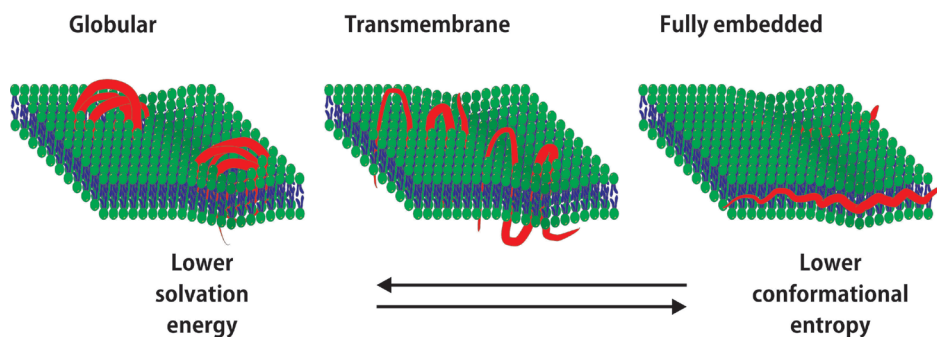


Figure 8.4. Different possible conformations for silicone oligomers and polymers in lipid membranes. Embedding of the polymer within the membrane decreases the solvation energy but is balanced by the entropic cost of deforming the molecule.

In conclusion, the results presented here reveal the incorporation of organosilicon compounds by cellular membranes. From this, it can be inferred that the impact of organosilicon compounds on sample preparation, experimental outcome and perhaps even human health should not be underestimated. Knowing that interactions with biological membranes are relatively stable, the notion that silicones are not systemically absorbed needs to be reconsidered.

Acknowledgments

The authors thank prof. Frans Leermakers for his valuable insights. This work has been conducted as part of the Perspectief Program Cancer ID with project numbers 14193 and 14196, which is funded by the Netherlands Organization for Scientific Research (NWO) and co-financed by JEOL Europe B.V., Hybriscan Technologies B.V., Aquamarijn Micro Filtration B.V. and Lionix International B.V.

References

1. Linti, G. *Organosilicon Chemistry V. From Molecules to Materials*. By Norbert Auner and Johann Weis. *Angew. Chemie Int. Ed.* 43, 2744 (2004).
2. Code of Federal Regulations. Title 21, Volume 3, section 173.340. (2018).
3. Code of Federal Regulations. Title 21, Volume 5, section 347.10. (2018).
4. Code of Federal Regulations. Title 21, Volume 8, section 878.3530. (2018).
5. Joint FAO/WHO Expert Committee on Food Additives (JECFA). WHO Technical Report Series 966 EVALUATION OF CERTAIN FOOD ADDITIVES AND CONTAMINANTS. *World Heal. Organ.* 27–32 (2011). doi:10.1016/S0140-6736(02)11326-2
6. Berthier, E., Young, E. W. K. & Beebe, D. Engineers are from PDMS-land, biologists are from polystyrenia. *Lab on a Chip* 12, 1224–1237 (2012).
7. Metcalf, T. J., Irons, T. G., Sher, L. D. & Young, P. C. Simethicone in the Treatment of Infant Colic: A Randomized, Placebo-Controlled, Multicenter Trial. *Pediatrics* 94, 29 LP – 34 (1994).
8. PART 332-ANTIFLATULENT PRODUCTS FOR OVER-THE-COUNTER HUMAN USE. *Fed. Regist.* 39, 19877 (1974).
9. Regehr, K. J. et al. Biological implications of polydimethylsiloxane-based microfluidic cell culture. *Lab Chip* 9, 2132–2139 (2009).
10. Duffy, D. C., McDonald, J. C., Schueller, O. J. A. & Whitesides, G. M. Rapid prototyping of microfluidic systems in poly(dimethylsiloxane). *Anal. Chem.* 70, 4974–4984 (1998).
11. Delamarche, E., Schmid, H., Michel, B. & Biebuyck, H. Stability of molded polydimethylsiloxane microstructures. *Adv. Mater.* 9, 741–746 (1997).
12. Esteves, T. C. et al. A microfluidic system supports single mouse embryo culture leading to full-term development. *RSC Adv.* 3, 26451–26458 (2013).
13. Kieslinger, D. C. et al. In vitro development of donated frozen-thawed human embryos in a prototype static microfluidic device: A randomized controlled trial. *Fertil. Steril.* 103, 680–686.e2 (2015).
14. de Almeida Monteiro Melo Ferraz, M., Nagashima, J. B., Venzac, B., Le Gac, S. & Songsasen, N. 3D printed mold leachates in PDMS microfluidic devices. *Sci. Rep.* 10, 1–9 (2020).
15. Ryan, J. W. Prevention of anal leakage of polyorganosiloxane fluids used as fat substitutes in foods. 1–4 (1988).
16. H.M. Lee, J. Baines, R. Walker, P. M. K. Safety evaluation of certain food additives. (2009).
17. Futrega, K. et al. Polydimethylsiloxane (PDMS) modulates CD38 expression, absorbs retinoic acid and may perturb retinoid signalling. *Lab Chip* 16, 1473–1483 (2016).
18. Łopacińska, J. M., Emnéus, J. & Dufva, M. Poly(Dimethylsiloxane) (PDMS) Affects Gene Expression in PC12 Cells Differentiating into Neuronal-Like Cells. *PLoS One* 8, 1–11 (2013).
19. Gusnard, D. & Kirschner, R. H. Cell and organelle shrinkage during preparation for scanning electron microscopy: effects of fixation, dehydration and critical point drying. *J. Microsc.* 110, 51–57 (1977).
20. Lytton, D. G., Yuen, E. & Rickard, K. A. Scanning electron and light microscope correlation of individual human bone marrow cells before and after culture in nutrient agar. *J. Microsc.* 115, 35–49 (1979).

21. Boyde, A. & Maconnachie, E. Histochemistry Treatment with Lithium Salts Reduces Ethanol Dehydration Shrinkage of Glutaraldehyde Fixed Tissue. *Histochemistry* 66, (1980).
22. Katsen-Globa, A., Puetz, N., Gepp, M. M., Neubauer, J. C. & Zimmermann, H. Study of SEM preparation artefacts with correlative microscopy: Cell shrinkage of adherent cells by HMDS-drying. *Scanning* 38, 625–633 (2016).
23. Boyde, A. & Maconnachie, E. Morphological correlations with dimensional change during SEM specimen preparation. *Scan. Electron Microsc.* 1981, 27–34 (1981).
24. Brunk, U., Collins, V. P. & Arro, E. The fixation, dehydration, drying and coating of cultured cells for SEM. *J. Microsc.* 123, 121–131 (1981).
25. Braet, F., De Zanger, R. & Wisse, E. Drying cells for SEM, AFM and TEM by hexamethyldisilazane: A study on hepatic endothelial cells. *J. Microsc.* 186, 84–87 (1997).
26. Nation, J. L. A new method using hexamethyldisilazane for preparation of soft insect tissues for scanning electron microscopy. *Biotech. Histochem.* 58, 347–351 (1983).
27. Nicholson, J. D. Derivative formation in the quantitative gas-chromatographic analysis of pharmaceuticals. Part II: A review. *Analyst* 103, 193–222 (1978).
28. Essaid, D. et al. Artificial plasma membrane models based on lipidomic profiling. *Biochim. Biophys. Acta - Biomembr.* 1858, 2725–2736 (2016).
29. Sackmann, E. Supported Membranes: Scientific and Practical Applications. *Science* 271, 43–48 (1996).
30. Milbrat, A. et al. Integration of Molybdenum-Doped, Hydrogen-Annealed BiVO₄ with Silicon Microwires for Photoelectrochemical Applications. *ACS Sustain. Chem. Eng.* 7, 5034–5044 (2019).
31. Beekman, P. et al. Immuno-capture of extracellular vesicles for individual multi-modal characterization using AFM, SEM and Raman spectroscopy. *Lab Chip* 19, 2526–2536 (2019).
32. Desai, G. et al. Oral Pharmaceutical Compositions of Simethicone. 28 (2008).
33. Enciso-Martinez, A., Timmermans, F. J., Nanou, A., Terstappen, L. W. M. M. & Otto, C. SEM–Raman image cytometry of cells. *Analyst* 143, 4495–4502 (2018).
34. Tsao, M. W. et al. Formation and characterization of self-assembled films of thiol-derivatized poly(dimethylsiloxane) on gold. *Macromolecules* 30, 5913–5919 (1997).
35. Soga, I. & Granick, S. Backbone orientation of adsorbed polydimethylsiloxane. in *Studies in Surface Science and Catalysis* 132, 817–820 (2001).
36. Halldorsson, S., Lucumi, E., Gómez-Sjöberg, R. & Fleming, R. M. T. Advantages and challenges of microfluidic cell culture in polydimethylsiloxane devices. *Biosens. Bioelectron.* 63, 218–231 (2015).

Supporting Information

SI8.1 structures

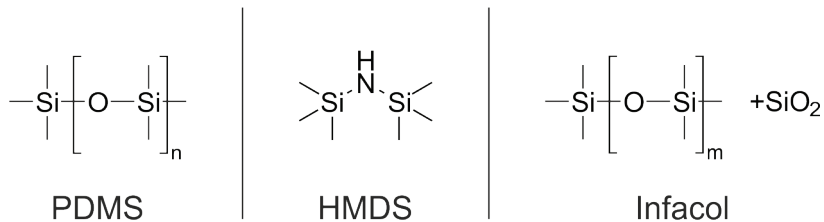


Figure SI8.1. Structures of the molecules used in this study. For uncrosslinked PDMS oligomers, $n = 20-90$. $m = 190-280$.

SI8.2 AES

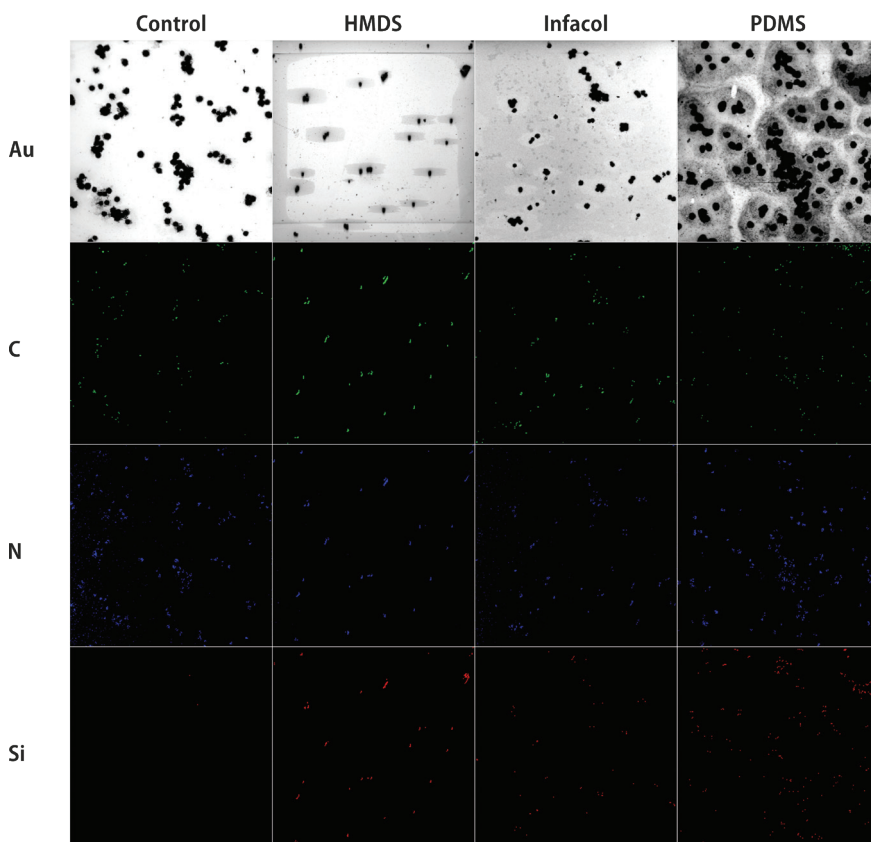


Figure SI8.2. AES data (C and Si data also shown in main article after image dilution) showing nitrogen species in all cells and the intense gold signal coming from the substrate, for comparison.

S18.3 IR

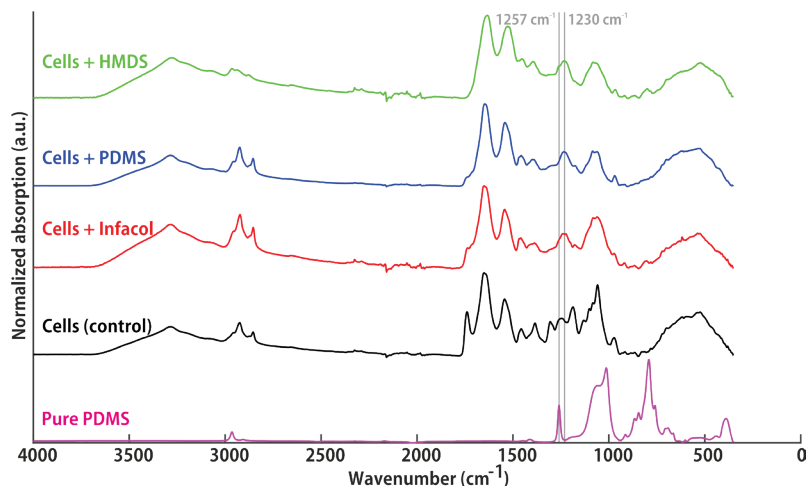


Figure S18.3. Full IR spectra. The region of interest, 1180 – 1300 cm^{-1} , is shown in the main text.

S18.4 Raman Spectroscopy

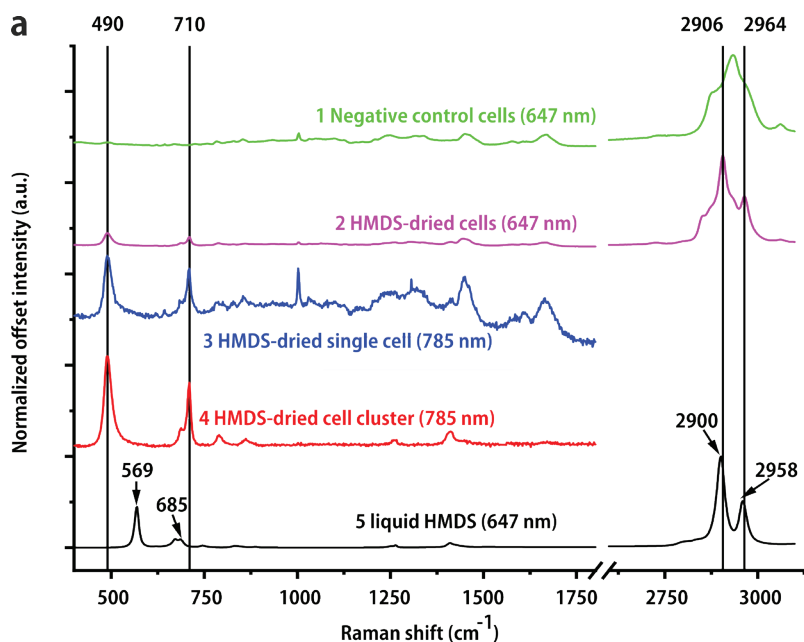


Figure S18.4. Additional Raman spectra obtained from other samples. Spectra (3) and (4) in Figure S14 correspond to a cell dried with HMDS (3) and to a cluster of dried cells with excess HMDS (4). Both, (3) and (4) display peaks at 490 and 710 cm^{-1} . The cell contribution to the Raman spectrum in (4) is not significant compared to the peaks at 490 and 710 cm^{-1} , indicating that the reaction with HMDS and biological matter is very efficient and can dominate the outcome of chemical probing.



Chapter 9

Conclusions and outlook



The aim of this thesis was to detect and characterize biological nanoparticles in blood, specifically tdEVs for their further utilization as cancer biomarkers. The complexity of body fluids, such as blood, required a technique able to (1) detect biological nanoparticles at the single particle level and (2) disclose physical and chemical features that can be used to distinguish tdEVs from other particles in blood and gain a better understanding about them. Hence, we sought to explore various methods that enabled the detection and characterization of individual particles and the discrimination of tdEVs from other EVs and non-EV particles in a label-free manner.

The first approach we used was correlative SEM-Raman micro-spectroscopy. We aimed to visualize submicrometer particles with high resolution SEM images while obtaining spatially correlated chemical information by means of Raman imaging. Because this approach was never applied neither to EVs nor to cells, we first needed to develop a sample preparation protocol and workflow to measure biological samples with correlative SEM-Raman. Cells are much bigger than EVs and easier to isolate, which made them a suitable sample to test our approach. Hence, we started by developing a sample preparation protocol and workflow for SEM-Raman on cells (*chapter 3*). This approach required a SEM-Raman compatible substrate and because samples were imaged in the SEM vacuum chamber, they needed to be dried. We acquired SEM-Raman images of cancer and non-cancer cells and, by using principal component analysis (PCA) and hierarchical cluster analysis on Raman data, we discriminated cells of different origin. We proceeded to downscale the SEM-Raman approach to EVs (*chapter 4*), but various problems needed to be solved first. For example, cells can easily be fixed, washed and pelleted by centrifugation. However, EVs require much greater centrifugation forces which may result in damage. Instead, we functionalized SEM-Raman compatible substrates with antibodies to specifically capture tdEVs. This further enriched tdEVs by flowing the sample through a microfluidic device. Alignment markers enabled the measurement of tdEVs by different instruments, namely SEM, Raman and AFM. SEM and AFM images revealed the presence of single particles of various sizes and morphologies, and PCA analysis of Raman images distinguished tdEVs from contaminant glue particles.

At this point it was clear that Raman micro-spectroscopy had the potential to distinguish and characterize tdEVs and to do so in a label-free manner. Inspired by Arthur Ashkin's technique of optical trapping, we developed a method in which a single laser beam optically trapped nanoparticles directly in suspension (*chapter 5*). The illumination of the sample by the laser resulted in Rayleigh and Raman light being scattered. By rapidly measuring sequences of Rayleigh scattering we were able to detect the moment when an individual particle was trapped and synchronously acquired Raman spectra labelled every timepoint with chemical information. The automation of this method enabled the trapping and release of particles and the continuous

acquisition of Rayleigh and Raman scattering. Our method was first validated with polystyrene and silica beads and then applied to tdEVs. Thus, our method fulfilled the requirements of single particle detection and chemical characterization. tdEVs overlap in size and density with EVs of different tissue of origin as well as lipoprotein particles (LPs) in blood plasma. Hence, it was important to know whether the global biomolecular composition, as measured by Raman, could be used as a fingerprint to identify tdEVs from other particles. We proved that this was possible by optically trapping, detecting and distinguishing single tdEVs from red blood cell-derived EVs and LPs (*chapter 6*). This is important because (1) this method relies on the intrinsic biomolecular composition of particles without the need of labelling and (2) it measures particles directly in suspension. Furthermore, based on Raman scattering, EVs showed a larger protein contribution compared to LPs and, based on Rayleigh scattering, we estimated the lowest size range of trapped particles to be between 80 and 320 nm. At this point, we had analyzed tdEVs from cultured cell lines (LNCaP and PC-3) and the plasma fraction of healthy donors, so we proceeded to analyze the plasma fraction of metastatic castration-resistant prostate cancer patients in search of tdEVs (*chapter 7*). Although it was expected most of the trapped particles to be LPs, the pilot study showed more particle types in both patients and healthy controls. Among all particles, we identified LPs, but not tdEVs as the ones we used as model (LNCaP EVs). Interestingly, the particles from the patient with the highest PSA level contained nucleic acids, as measured by our optical trapping and synchronized Rayleigh and Raman scattering method (OT-sRRs). In the future, however, a larger cohort of sample donors with well described clinical details should be included.

In *Chapters 3 and 4* we found some evidence indicating the incorporation of organosilicon compounds in cell membranes that impacts sample preparation, experimental outcome and perhaps human health. Some initial results are presented in *chapter 8*.

In our OT-sRRs method, the rapid acquisition of Rayleigh scattering intensities was instrumental to detect single particles, as described in *chapter 5*. Such an approach improved the current state of the field, where the use of the weaker Raman scattering accompanied with long acquisition times confounded the distinction of single versus multiple trapping events. Our method will, however, benefit from even shorter acquisition times and signal analysis tools to automatically segment time traces and reduce the analysis time. This may further discriminate aggregated particles that are trapped simultaneously. Even so, by only using the Raman spectra of trapped particles, we observed a possible aggregation of EVs and LPs when mixing plasma and PC-3 EVs. **Figure 9.1A** shows three types of samples: PC-3 EVs (green), particles from plasma (blue) and a 1:4 mixture of the previous two (gray). As expected, the majority of the particles from the mixed sample appeared to be LPs and few PC-3 EVs, as shown by their respective overlap with the reference PC-3 and plasma samples

and their mean Raman spectra in [Figure 9.1B](#) (see *chapter 6* for comparison). Interestingly, some particles from the mixed sample appeared between the PC-3 and plasma clusters, suggesting a Raman contribution from both particle types. Because each of the particles in between the two clusters corresponds to single trapping events, this suggests that PC-3 EVs and LPs aggregate and are trapped as a single particle. The association of LPs and EVs needs further investigation, but if proven *in vivo*, and given the fact that LPs outnumber EVs in plasma, the implications would go from co-isolation of particles and blocking of potential binding sites of EVs to data misinterpretation.

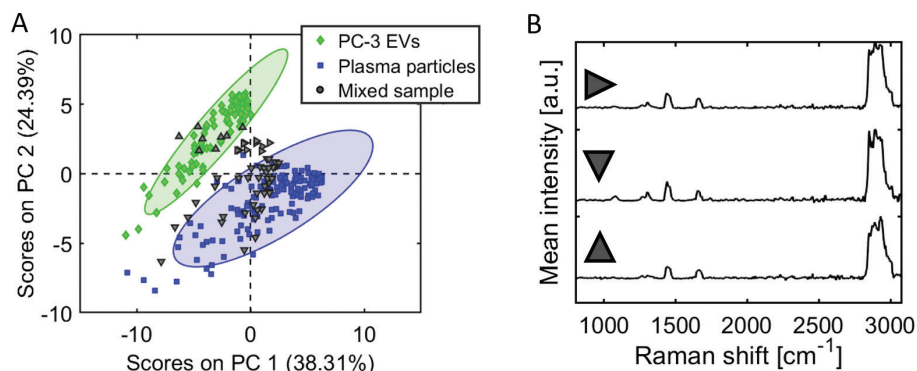


Figure 9.1. (A) Scores plot showing PC-3 EVs (green), particles from plasma (blue) and a mixture of PC-3 EVs and particles from plasma (gray). Based on NTA concentrations, 80% of the particles in the mixed sample are from plasma and 20% PC-3 EVs. (B) Mean Raman spectra corresponding to three subgroups of the mixed sample: PC-3 EVs, LPs and possible associated LPs and PC-3 EVs.

As explorative and characterization methods, SEM-Raman and OT-sRRs fulfill two important requirements for the utilization of tdEVs as cancer biomarkers: (1) the discrimination of tdEVs from other EVs and non-EV particles and (2) identification of their cellular origin. In terms of throughput and simplicity of sample preparation, OT-sRRs outperforms SEM-Raman. Nevertheless, for a clinical setting, OT-sRRs has still a very low throughput, especially when compared to flow cytometry (FCM), which can also detect submicrometer particles. [Table 9.1](#) shows an estimate of the throughput for the methods used in this thesis as well as other techniques for single EV analysis, which have been described in *chapter 1*.

Table 9.1. Overview of techniques for single EV analysis

Method	Reference	Information obtained	DL* (nm)	Thr* (prt/hr)
Surface				
TEM	[1]	Morphology, size	30	9×10^3
SEM	[2]	Topography, size	50	50
AFM	[2]	Morphology, bending modulus	30	3×10^3
Raman	[2]	Chemical composition	80	100
Suspension				
NTA	[3]	Particle size distribution	30	400
OT-sRRs	[4]	Chemical composition	80-320	$\sim 1.5 \times 10^4$ ^a
FCM	[5]	Antigen expression, refractive index	200	6×10^6
FM	[6]	Antigen expression	1000	4×10^6

*DL=Detection limit; Thr= Throughput in total number of particles per hour; ^aCalculated based on polystyrene beads ($\varnothing=100$ nm). Table adapted from [7].

High throughput becomes especially important for the identification of rare populations of EVs, such as tdEVs in blood. This is because tdEVs are outnumbered by the presence of other EVs and non-EV particles such as LPs. It is estimated that blood contains up to 10^{16} LPs, up to 10^{11} other EVs and, for mCRPC patients, only up to 10^4 tdEVs in one mL (Figure 9.2).^{6,8-12} Although fasting may help to decrease the amount of circulating LPs, it may still be difficult to detect the much less frequent tdEVs. Therefore, there is an obvious need of enriching blood for tdEVs or depleting it from LPs. Such an enrichment/depletion step becomes more important for techniques with a low detection limit. As it is shown in Figure 9.2, the concentration of LPs increases significantly with a decrease in particle diameter, suggesting the importance of such steps. Therefore, more non-EV particles need to be probed before finding a tdEV. Alternatively, for some diseases such as prostate cancer, urine might be a more suitable sample to use instead of blood plasma, as the EV to LP concentration ratio is higher in urine. However, it has to be taken into account that the total concentration of EVs in urine appears to be lower than in plasma.¹³

Approaches to increase the Raman throughput may include the development of on-chip Raman particle analysis or the integration of a Raman spectrometer to a flow cytometer. Higher throughput, however, will decrease the illumination time per particle, thereby lowering the signal-to-noise ratio. Hence, two approaches may be used to increase the Raman signal. The first approach involves the use of Raman labels, for example metal nanoparticles functionalized with both molecules that give rise to a unique Raman spectrum and proteins that specifically target antigens in the EV membrane. Hence, the metal nanoparticles may bind to EVs and illumination by a laser results in a strong ($\times 10^8$) Raman enhancement. Preliminary results on cells show the feasibility of such an approach to distinguish cellular origin (Figure 9.3). A second approach to

increase the Raman signal can be the use of coherent anti-Stokes Raman scattering (CARS). However, prior knowledge of the sample Raman spectra, as obtained in spontaneous Raman spectroscopy, is needed before CARS enables the discrimination of various EV types and non-EV particles. Since CARS has not been used for EV analysis, further research needs to address its feasibility, which might be specially challenging for submicrometer particles, but perhaps not for micrometer-sized particles.

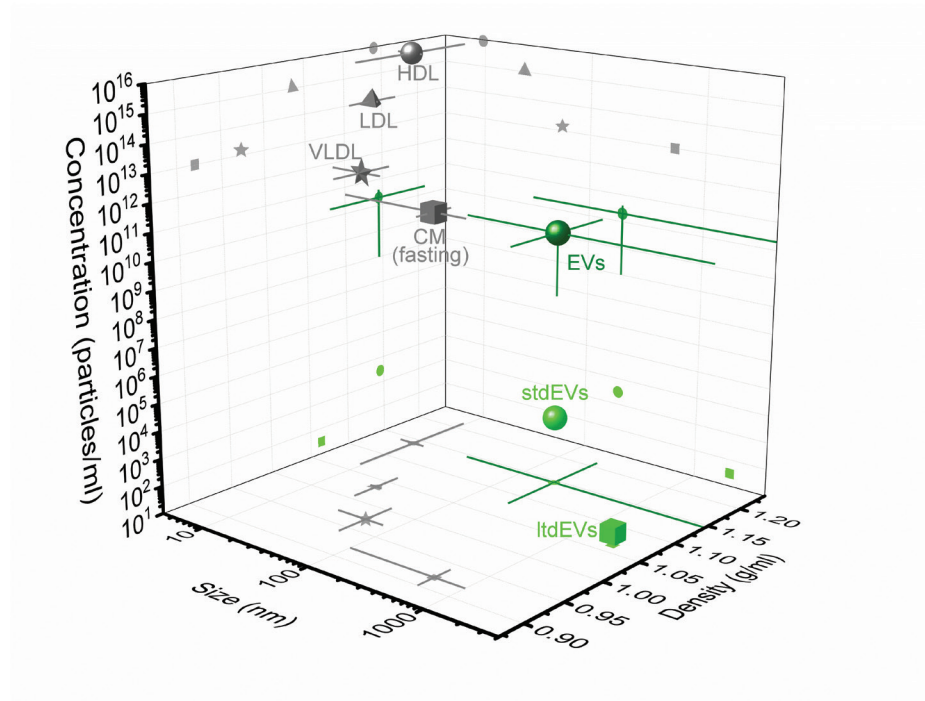


Figure 9.2. Concentration, size (diameter) and density of particles in blood plasma. 3D representation of concentration, size and density of extracellular vesicles (dark green circle), and the High-Density Lipoproteins (HDL, grey circle), Low-density Lipoproteins (LDL, grey triangle), Very Low-Density Lipoproteins (VLDL, grey star) and Chylomicrons (CM, grey square) during fasting in blood. The average and range (lines) of the three parameters are indicated in the figure. Values are derived from literature.^{9,10,12} The frequency of the large tumor derived extracellular vesicles (ltdEVs, light green circle) is determined in the *Cancer-ID* program and the small tdEVs (stdEVs, light green square) estimated using the frequency of ltdEVs.^{6,8,11} Figure adapted from [7].

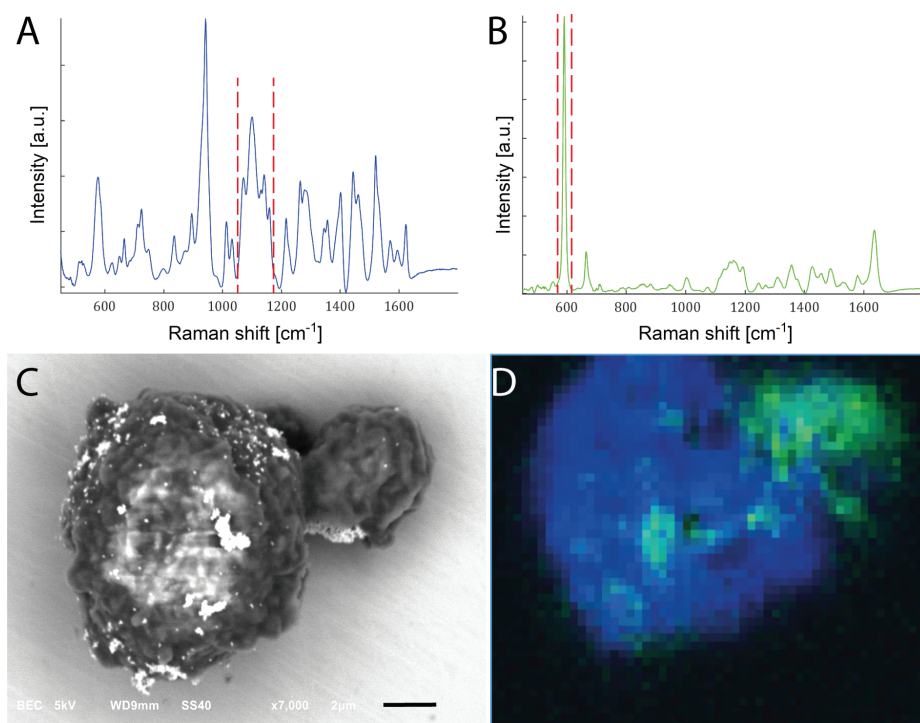


Figure 9.3. (A) and (B) show the Raman spectrum of two types of Raman labels consisting both of gold nanorods (Nanopartz™) functionalized with streptavidin and a molecule that is different for each type of Raman label. The Raman label in (A) is used to label LNCaP cells by a biotinylated anti-EpCAM linker and the Raman label in (B) is used to label leukocytes by a biotinylated anti-CD45 linker. (C) Backscatter electron image of two cells from a mixed sample of leukocytes and LNCaP cells. Gold nanorods are specially visible as bright dots, sometimes clustered. (D) False-color Raman image corresponding to cells in (C). The intensity of the blue and green pixels results from the integration of the Raman bands between the red-dotted lines in (A) and (B), respectively. Hence, the cell in the left is an LNCaP cell and the cell in the right a leukocyte, because blue pixels indicate the presence of Raman label (A) and green pixels of Raman label (B).

Chapters 5 to 7 focused on extracting information from single optically trapped particles. Nevertheless, the label-free analysis of the medium in which the particles are suspended, whether cell culture supernatant or plasma, can be probed by our OT-sRRs approach. In this case, the time intervals when no particle is trapped can be segmented and the corresponding Raman spectra revealed. This approach would enable the chemical characterization of particle-free media. A potential application is the analysis of particle-free blood plasma for the detection of for example enzymes, whose concentration increases under pathological conditions such as in cancer.

In chapter 7, we analyzed the particles in plasma of mCRPC patients and healthy controls. The difference in chemical composition among particles from different donors clearly reflects

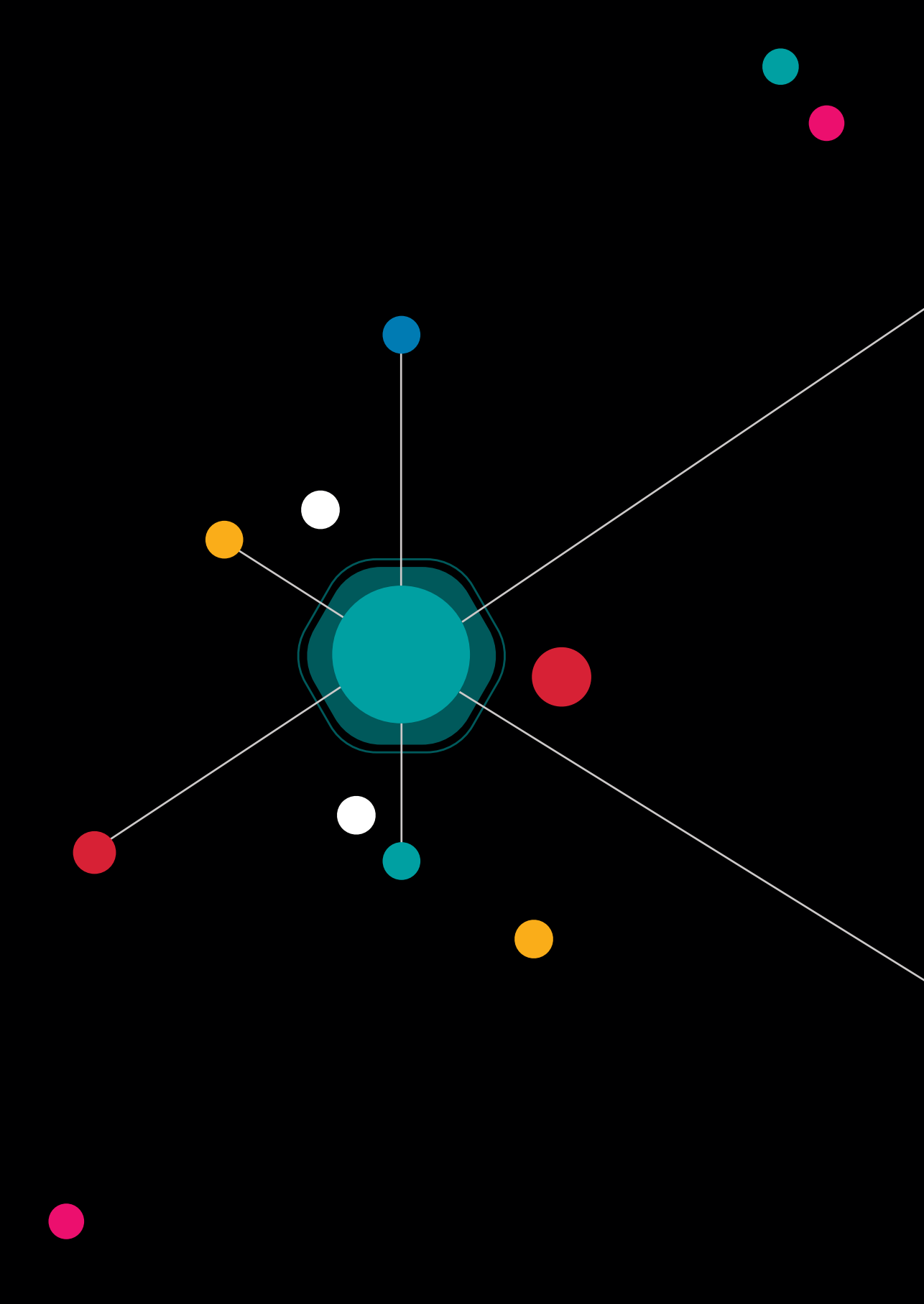
differences among them. However, at this moment it is difficult to conclude about the nature of the particles, except for the lipoproteins. Moreover, besides cancer itself, other factors such as age, diet, medication, may contribute to the presence of different particles among donors. For this reason, further studies require a larger cohort of patients and healthy donors, and detailed clinical data must be available to help interpret the data. In this thesis we used different LPs, EVs from cultured tumor cells and from red blood cells as reference material. Raman measurements of a library of reference particles will also help in explaining the origin of the unknown particles in blood plasma. Yet, the detection of nucleic acids in the particles from the patient with the highest PSA level gives rise to an interesting question about the differences in prognostic value, if at all, for nucleic acids associated to particles and circulating particle-free nucleic acids.

From *chapter 7*, we can comment that even though LPs interfere with the analysis of tdEVs, LPs may reflect an altered lipid metabolism as a result of many factors, among them cancer. Therefore, the utilization of LPs as cancer biomarkers should not be underestimated, but their systematic characterization with a larger cohort of cancer patients is necessary.

Whether specifically enriched for tdEVs or LP-depleted samples, the developments presented in this thesis can be used to characterize single particles, disclose their biomolecular composition and identify their cells of origin. This information can then be complemented by the measurement of more parameters with other techniques. A multivariate data analysis and the use of machine learning can then disclose relevant information that can be used for instance to find an optimal treatment or monitor the treatment response. The detection and characterization of nanoparticles is relevant to many other diseases and even fields such as nanoplastic pollution and its impact on global health.

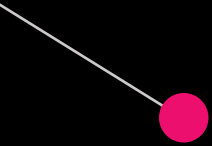
References

1. Rikkert, L. G., Nieuwland, R., Terstappen, L. W. M. M. & Coumans, F. A. W. Quality of extracellular vesicle images by transmission electron microscopy is operator and protocol dependent. *J Extracell Vesicles* 8, 1555419 (2019).
2. Beekman, P. et al. Immuno-capture of extracellular vesicles for individual multi-modal characterization using AFM, SEM and Raman spectroscopy. *Lab Chip* 19, 2526–2536 (2019).
3. Van Der Pol, E. et al. Optical and non-optical methods for detection and characterization of microparticles and exosomes. *J. Thromb. Haemost.* 8, 2596–2607 (2010).
4. Enciso-Martinez, A. et al. Synchronized Rayleigh and Raman scattering for the characterization of single optically trapped extracellular vesicles. *Nanomedicine Nanotechnology, Biol. Med.* 24, 102109 (2020).
5. de Rond, L. et al. Refractive index to evaluate staining specificity of extracellular vesicles by flow cytometry. *J. Extracell. Vesicles* 8, 1643671 (2019).
6. Nanou, A. et al. Circulating tumor cells, tumor-derived extracellular vesicles and plasma cytokeratins in castration-resistant prostate cancer patients. *Oncotarget* 9, 19283–19293 (2018).
7. Rikkert, L. G. et al. Cancer-ID: towards identification of cancer by tumor-derived extracellular vesicles in blood. *Front. Oncol.* 10, 608 (2020).
8. Nanou, A. et al. Tumour-derived extracellular vesicles in blood of metastatic cancer patients associate with overall survival. *Br. J. Cancer* 122, 801–811 (2020).
9. Kuchinskiene, Z. & Carlson, L. A. Composition, concentration, and size of low density lipoproteins and of subfractions of very low density lipoproteins from serum of normal men and women. *J Lipid Res* 23, 762–769 (1982).
10. Simonsen, J. B. What Are We Looking At? Extracellular Vesicles, Lipoproteins, or Both? *Circ. Res.* 121, 920–922 (2017).
11. Coumans, F., van Dalum, G. & Terstappen, L. L. W. M. M. L. W. M. M. CTC Technologies and Tools. *Cytom. A* 93, 1197–1201 (2018).
12. Johnsen, K. B., Gudbergsson, J. M., Andresen, T. L. & Simonsen, J. B. What is the blood concentration of extracellular vesicles? Implications for the use of extracellular vesicles as blood-borne biomarkers of cancer. *Biochim. Biophys. Acta - Rev. Cancer* 1871, 109–116 (2019).
13. van der Pol, E. et al. Particle size distribution of exosomes and microvesicles determined by transmission electron microscopy, flow cytometry, nanoparticle tracking analysis, and resistive pulse sensing. *J. Thromb. Haemost.* 12, 1182–1192 (2014).





Appendices



Summary

Cancer is one of the leading causes of mortality and morbidity around the world, second only to cardiovascular disease. Early detection, effective monitoring of the disease and optimal treatments may bring cancer from a deadly to a chronic controllable disease. Liquid biopsies may effectively detect and monitor cancer through the analysis of body fluids such as blood. Both under pathological and normal physiological conditions, cells release extracellular vesicles (EVs) for communication and waste removal purposes. EVs are particles enclosed by a lipid membrane that enable cellular communication by transferring messages encoded in the biomolecules that make up the EVs, such as lipids, proteins, nucleic acids and sugars. Because cancer cells release EVs that can enter the blood stream, a fraction of the particles in blood will be of tumor origin. Such tumor-derived EVs (tdEVs) may contain specific information about their parental cancer cells and may reflect the state of the patient. Thus, identifying and characterizing tdEVs can provide relevant information for cancer diagnosis, selection of optimal treatment and monitoring treatment response.

The detection and characterization of tdEVs in blood has been, however, challenging due to (1) their small size, which may be as small as 30 nm in diameter, (2) their size and density overlap with other more abundant EVs and non-EV particles in blood, such as lipoprotein particles and (3) the limited knowledge on their chemical composition. Therefore, the utilization of tdEVs as cancer biomarkers will largely benefit from techniques that are able to detect single biological nanoparticles and disclose their physical and chemical features, which can be used to distinguish tdEVs from other particles and gain a better understanding about them.

The aim of this work is to detect and characterize biological nanoparticles in blood, specifically tdEVs, at the single particle level. Hence, this thesis explores various methods that enable, in a novel way, the detection and chemical characterization of individual particles and the discrimination of tdEVs from other EVs and non-EV particles, such as lipoprotein particles, in a label-free manner.

One method explored is the correlation of scanning electron microscopy (SEM) and Raman spectroscopy data that enables the acquisition of high-resolution SEM images and the spatial correlation with chemical information as obtained from Raman micro-spectroscopic imaging. We developed a sample preparation protocol and workflow to study biological samples with correlative SEM-Raman. As a starting point, SEM-Raman characterization was performed on cancer and non-cancer cells (*chapter 3*). High resolution SEM images of non-labelled and non-

metal coated cells as well as Raman images were acquired. Cell morphology is then correlated with chemical information and, by performing multivariate analysis on the Raman spectra, cells of different origins are identified. Next, we downscaled the SEM-Raman approach to EVs (*chapter 4*) and developed a multi-modal platform for the specific capture of tdEVs on antibody-functionalized stainless-steel substrates. We performed a multi-modal analysis that correlates size, morphology and chemical information of single tdEVs by combining SEM, Raman and atomic force microscopy (AFM) imaging. The correlation of SEM and Raman images enabled to distinguish tdEVs from contaminant particles.

Another method is the development of optical trapping and synchronized Rayleigh and Raman scattering (OT-sRRs) for the detection and characterization of single biological nanoparticles, such as tdEVs, directly in suspension and in a label-free manner. Using a single laser beam, single EVs in suspension are trapped in the laser focal spot. The scattered Rayleigh signal is used to detect when an individual particle is trapped and the synchronously acquired Raman signal enables to assign a Raman spectrum to each trapped particle, thereby, disclosing global chemical composition of each individual particle. The automated continuous trapping and release of single particles enables to probe multiple single particles in the sample fluid. The OT-sRRs method was first validated with monodisperse beads and then applied to EVs (*chapter 5*). Next, the method was applied to EVs of different origins, including tdEVs, as well as to lipoprotein particles, which are a major component of blood plasma (*chapter 6*). We showed the Raman fingerprint of each particle type and associated it with relevant biomolecules. By performing principal component analysis (PCA) on a dataset consisting of Raman spectra of all the particles measured, we were able to distinguish tdEVs from red blood cell-derived EVs and lipoprotein particles in a label-free manner and directly in suspension. Additionally, based on the Rayleigh scattering, we estimated the size range of particles measured by our OT-sRRs method.

After having analyzed tdEVs from prostate cancer cell lines and plasma of healthy donors, we analyzed plasma of metastatic castration-resistant prostate cancer (mCRPC) patients and compared it to healthy controls at the individual particle level by means of OT-sRRs (*chapter 7*). PCA and hierarchical cluster analysis showed that the particles of some patients had nucleic acids that contributed significantly to their Raman fingerprint. Although this pilot study aimed at detecting and characterizing single tdEVs in mCRPC patients, significant differences were observed in terms of the general particle profile in the plasma fraction of some patients compared to healthy controls.

An interesting finding derived from studying cells and EVs with correlative SEM-Raman was the interaction of organosilicon compounds with biological membranes (*chapter 8*). We show some results that indicate the incorporation of organosilicon compounds in lipid membranes, which may affect sample preparation, experimental outcome and perhaps human health.

In conclusion, this thesis describes the implementation of various novel methods to study biological nanoparticles in blood, from cancer cells to tdEVs and from model nanoparticles to nanoparticles in the plasma of cancer patients. These developments open an avenue not only to exploit the potential of tdEVs as cancer biomarkers, but also to study other particles in body fluids and, with that, the general nanoparticle profile, which may be affected under pathological conditions such as cancer.

Samenvatting

Kanker is wereldwijd, na cardiovasculaire aandoeningen, de belangrijkste oorzaak van overlijden en ziekte. Vroegtijdige herkenning, effectieve controle en een optimale behandeling kan mogelijk van kanker een chronische in plaats van dodelijke ziekte maken. Met behulp van het afnemen en analyseren van lichaamsvloeistoffen, zoals bloed, kan kanker op een effectieve manier gedetecteerd worden. Zowel in pathologische en normale fysiologische laten cellen extracellulaire blaasjes (afgekort als EVs in het Engels) los voor communicatie en het verwijderen van afvalstoffen. EVs zijn kleine deeltjes bestaande uit een lipidemembraan met daarbinnen eiwitten, nucleïnezuren en suikers en kunnen door deze biomoleculen cellulaire communicatie verzorgen. Gezien het feit dat ook kankercellen EVs produceren, welke in de bloedbaan komen, zal een deel van alle deeltjes in bloed van een tumor afkomstig zijn. Deze tumor-afgeleide EVs (afgekort als tdEVs in het Engels) bevatten mogelijk specifieke informatie over de tumor waarvan deze afkomstig zijn en kunnen hierdoor een beeld geven over de status van een kankerpatiënt. De tdEVs kunnen een belangrijke bron van informatie zijn om kanker vast te stellen, het bepalen van een zo optimaal mogelijke behandeling en het toezicht houden op het effect van de behandeling.

Het is echter een uitdaging tdEVs op te sporen en te analyseren. Allereerst zijn de deeltjes erg klein, tot wel 30 nm. Daarnaast bevinden ze zich temidden van niet-tumor-afgeleide EVs en andere EVs deeltjes zoals lipoproteïnen. Tot slot is er weinig bekend over de chemische samenstelling van de tdEVs. Om tdEVs als marker te gebruiken in kankerdiagnostiek zijn technieken nodig die het mogelijk maken om tdEVs te onderscheiden van andere deeltjes door hun fysieke en chemische eigenschappen in beeld te brengen.

Het doel van dit onderzoek is het detecteren en karakteriseren van biologische nanodeeltjes in bloed en in het bijzonder tdEVs. In dit proefschrift worden verscheidene methoden onderzocht om, op een niet eerder uitgevoerde manier, tdEVs te detecteren en chemisch te karakteriseren op individueel deeltjesniveau en te onderscheiden van andere EVs en niet-EVs, zonder het gebruik van specifieke labels.

Een onderzochte methode is de correlatie tussen data verkregen met rasterelektronenmicroscopie (SEM) en met Raman spectroscopie om zodoende de hoge resolutie SEM afbeeldingen en ruimtelijke correlatie met chemische informatie van Raman spectroscopie mogelijk te maken. We ontwikkelden een protocol voor monstervoorbereiding en een methode om biologische monsters te onderzoeken met zowel SEM als Raman. Als startpunt is SEM-Raman

karacterisering uitgevoerd op kankercellen en niet-kankercellen (*hoofdstuk 3*). Zowel hoge resolutie SEM afbeeldingen als Raman afbeeldingen zijn verkregen van cellen zonder gebruik van label en metaallaagje. De celmorfologie is vervolgens gecorreleerd aan de chemische informatie en door het uitvoeren van multivariate analyse van de Raman spectra zijn cellen van verschillende oorsprong geïdentificeerd. Vervolgens hebben we de SEM-Raman methode toegepast op EVs (*hoofdstuk 4*). Een multimodaal platform voor het specifiek vangen van tdEVs op antilichaam gefunctionaliseerde roestvrijstalen substraten werd hier ontwikkeld. Een multimodale analyse werd uitgevoerd die grootte, morfologie en chemische informatie van individuele tdEVs correleert door het combineren van SEM, Raman en atoomkrachtmicroscopie (AFM). Het correleren van SEM en Raman afbeeldingen maakt het mogelijk om onderscheid te maken tussen tdEVs en andere nanodeeltjes.

Een andere gebruikte methode is de combinatie van het optisch vangen gevolgd door het detecteren en karakteriseren van individueel biologische nanodeeltjes, zoals tdEVs, met behulp van Rayleigh en Raman verstrooiing (OT-sRRs). Deze methode kan gebruikt worden zonder specifieke labels, direct in een oplossing van nanodeeltjes. Door het gebruik van een enkele laserbundel, kunnen individuele EVs in een oplossing worden gevangen in het focuspunt van de laser. Het verstrooide Rayleigh signaal wordt gebruikt om het vangen van individuele deeltjes te detecteren. Tegelijkertijd wordt een Raman signaal verkregen om aan elk individueel deeltje een Raman spectrum toe te kunnen wijzen waarbij de chemische samenstelling van elk deeltje wordt blootgelegd. Het automatisch continu vangen en weer vrijlaten van individuele deeltjes zorgt ervoor dat er meerdere individuele deeltjes uit een en hetzelfde monster onderzocht kunnen worden. De OT-sRRs werd eerst gevalideerd met monodisperse kraaltjes en vervolgens toegepast op EVs (*hoofdstuk 5*). Vervolgens werd de methode toegepast op EVs van verschillende afkomst waaronder tdEVs, maar ook lipoproteïne deeltjes welke een belangrijk bestanddeel uit het bloed zijn (*hoofdstuk 6*). We hebben de Raman vingerafdruk van elke type deeltje laten zien en deze geassocieerd met de relevante biomoleculen. Door het uitvoeren van een *principal component analysis* (PCA) op een dataset bestaande uit Ramanspectra van alle gemeten deeltjes zijn we in staat gebleken om tdEVs te onderscheiden van rode bloedcel-EVs en lipoproteïne deeltjes. Bovendien is er met behulp van Rayleigh verstrooiing het meetbereik bepaald van deeltjes gemeten met de OT-sRRs methode.

Nadat we tdEVs afkomstig van prostaatkanker cellijnen en uit plasma van gezonde donoren analyseerden, hebben we plasma van metastatische castratie-resistente prostaatkanker (mCRPC) patiënten vergeleken met het plasma van gezonde donoren als controle. Deze beide tdEVs zijn op individueel niveau vergeleken doormiddel van OT-sRRs (*hoofdstuk 7*). PCA en

hiërarchische cluster analyse lieten zien dat de deeltjes van sommige patiënten nucleïnezuren bevatten die significant bijdragen aan hun Raman vingerafdruk. Hoewel deze pilotstudie zich richtte op de detectie en karakterisering van individuele tdEVs in mCRPC patiënten werden significante verschillen zichtbaar in de generieke deeltjesprofielen tussen het plasma van patiënten enerzijds, en het plasma van gezonde controle donoren anderzijds.

Een interessante ontdekking tijdens het onderzoeken van cellen en EVs met correlerende SEM-Raman was de interactie van siliconen met biologische membranen (*hoofdstuk 8*). We laten resultaten zien die een indicatie zijn voor het integreren van siliconen in lipide membranen. Dit kan een effect hebben op monstervoorbereiding, experimentele uitkomsten en mogelijke menselijke gezondheid.

Concluderend beschrijft dit proefschrift de implementatie van verschillende nieuwe methoden om biologische nanodeeltjes in bloed te bestuderen, van kankercellen tot tdEVs en van model nanodeeltjes tot nanodeeltjes in het plasma van kankerpatiënten. Deze ontwikkelingen zetten de deur open voor zowel het gebruiken van tdEVs als kankermarker als ook het bestuderen van ander deeltjes in lichaamsvloeistoffen. Door het vaststellen van het normale profiel van nanodeeltjes, kunnen verandering onder pathologische omstandigheden zoals in kanker beter bestudeerd worden.

Scientific Output

Peer reviewed papers

1. **A. Enciso-Martinez**,* F.J. Timmermans,* A. Nanou, L.W.M.M. Terstappen, C. Otto, SEM–Raman image cytometry of cells, *Analyst*. 143 (2018) 4495–4502. DOI: 10.1039/C8AN00955D. *Authors contributed equally.
2. P. Beekman,* **A. Enciso-Martinez**,* H.S. Rho, S.P. Pujari, A. Lenferink, H. Zuilhof, L.W.M.M. Terstappen, C. Otto, S. Le Gac, Immuno-capture of extracellular vesicles for individual multi-modal characterization using AFM, SEM and Raman spectroscopy, *Lab Chip*. 19 (2019) 2526–2536. DOI: 10.1039/C9LC00081J. *Authors contributed equally.
3. **A. Enciso-Martinez**, E. van der Pol, A.T.M. Lenferink, L.W.M.M. Terstappen, T.G. van Leeuwen, C. Otto, Synchronized Rayleigh and Raman scattering for the characterization of single optically trapped extracellular vesicles, *Nanomedicine Nanotechnology, Biol. Med.* 24 (2020) 102109. DOI: 10.1016/j.nano.2019.102109.
4. **A. Enciso-Martinez**, E. Van Der Pol, C.M. Hau, R. Nieuwland, T.G. Van Leeuwen, L.W.M.M. Terstappen, C. Otto, Label-free identification and chemical characterisation of single extracellular vesicles and lipoproteins by synchronous Rayleigh and Raman scattering, *J. Extracell. Vesicles*. 9 (2020) 1730134. DOI: 10.1080/20013078.2020.1730134.
5. **A. Enciso-Martinez**, E. van der Pol, C.M. Hau, T.M. de Reijke, R. Nieuwland, L.W.M.M. Terstappen and C. Otto, Label-free detection and characterization of single submicrometer particles in plasma of prostate cancer patients. (2020) Manuscript in preparation.
6. P. Beekman,* **A. Enciso-Martinez**,* S.P. Pujari, L.W.M.M. Terstappen, H.T. Zuilhof, S. Le Gac, C. Otto. Organosilicon uptake by biological membranes. (2020) Submitted. *Authors contributed equally.
7. L.G. Rikkert, P. Beekman, J. Caro, F.A.W. Coumans, **A. Enciso-Martinez**, G. Jenster, S. Le Gac, W. Lee, T.G. Van Leeuwen, G.B. Loozen, A. Nanou, R. Nieuwland, H.L. Offerhaus, C. Otto, D.M. Pegtel, M.C. Piontek, E. Van Der Pol, L. De Rond, W.H. Roos, R.B.M. Schasfoort, M. Wauben, H. Zuilhof, L.W.M.M. Terstappen, Cancer-ID: towards identification of cancer by tumor-derived extracellular vesicles in blood. *Front. Oncol.* 10, 608 (2020). DOI: 10.3389/fonc.2020.00608
8. E.R.M. Heremans, A.S. Chen, X. Wang, J. Cheng, F. Xu, **A. Enciso-Martinez**, G. Lazaridis, S. Van Huffel, J.D.Z. Chen, Artificial Neural Network-Based Automatic Detection of Food Intake for Neuromodulation in Treating Obesity and Diabetes, *Obes. Surg.* (2020) 1–11. DOI: 10.1007/s11695-020-04511-6.

Abstracts accepted for oral presentations (presenter)

1. A. Enciso-Martinez , E. van der Pol , A.T.M. Lenferink, L.W.M.M. Terstappen and C. Otto. Optical tweezers and Raman spectroscopy of single extracellular vesicles, 17th European Conference on the Spectroscopy of Biological Molecules (ECSBM) – Amsterdam, September 2017.
2. A. Enciso-Martinez, F.J. Timmermans, P. Beekman, A. Nanou, H.S. Rho, L.W.M.M. Terstappen and C. Otto. Correlative SEM-Raman for cell and extracellular vesicle characterization, Dutch Biophysics meeting – Veldhoven, October 2017.
3. A. Enciso-Martinez, Identification and characterization of single Extracellular Vesicles (EVs) by means of optical tweezers and SEM-Raman spectroscopy. Invited speaker at CINVESTAV – Mexico, April 2018.
4. A. Enciso-Martinez, P. Beekman, A. Nanou, H.S. Rho, L.W.M.M. Terstappen and C. Otto. Characterization of cells and extracellular vesicles with correlative SEM-Raman, International Conference on Raman Spectroscopy (ICORS) - South Korea, August 2018.
5. A. Enciso-Martinez, E. van der Pol, A.T.M. Lenferink, L.W.M.M. Terstappen, T.G. van Leeuwen and C. Otto. Identification of single tumor-derived extracellular vesicles by means of optical tweezers and Raman spectroscopy, International Conference of Extracellular Vesicles (ISEV) – Kyoto, Japan, April 2019.

Abstracts accepted for poster presentation

1. A. Enciso-Martinez, A. Nanou, F.J. Timmermans, A.T.M. Lenferink, E. van der Pol, L.W.M.M. Terstappen and C. Otto. Identification and characterization of cells and extracellular vesicles (EVs) by SEM-Raman, Dutch Biophysics meeting – Veldhoven, October 2016.
2. A. Nanou, A. Enciso-Martinez, P. Beekman, W. Lee, H.S. Rho, S. Le Gac, C. van Rijn, H. Offerhaus, C. Otto and L.W.M.M. Terstappen. Cancer-ID: Isolation and characterization of tumor-derived extracellular vesicles, MIRA day – Twente, November 2016.
3. A. Enciso-Martinez A, E. van der Pol, A.T.M. Lenferink, L.W.M.M. Terstappen and C. Otto. Optical tweezers and Raman spectroscopy of single extracellular vesicles (EVs), International Conference on Raman Spectroscopy (ICORS) - South Korea, August 2018.
4. A. Enciso-Martinez, E. van der Pol, A.T.M. Lenferink, L.W.M.M. Terstappen and C. Otto. Optical tweezers and Raman spectroscopy of single extracellular vesicles (EVs), NLSEV – Amsterdam UMC, Amsterdam, November 2018.
5. A. Enciso-Martinez, E. van der Pol, A.T.M. Lenferink, L.W.M.M. Terstappen, T.G. van Leeuwen and C. Otto. Label-free identification of single EVs and lipoproteins, Dutch Biophysics meeting – Veldhoven, October 2019.

6. P. Beekman, A. Enciso-Martinez, L.W.M.M. Terstappen, C. Otto and S. Le Gac. Immunocapturing of extracellular vesicles on stainless steel for multi-modal individual characterization with correlative light, electron and probe microscopy, MicroTAS - Kaohsiung, Taiwan, 2018.
7. L.L. Zeune, S. de Wit, G. van Dalum, K. Andree, J. Swennenhuis, A. Enciso Martinez, A. Nanou, A. Mentink-Leusink, L.W.M.M. Terstappen, L. Majunke, B. Zill, M. Alunni-Fabroni, R. Lampignano, L. Yang, H. Neubauer, T. Fehm, M. Manicone, E. Rossi, R. Zamarchi, F. Farace, J.S. De Bono, C. Brune, Evaluating the consensus in circulating tumor cell scoring, ACTC Advances in Circulating Tumor Cells Liquid Biopsy in Clinical Practice Congress (ACTC 2017), Rhodes, Greece, October 2017.

Awards

2016: First prize winner for the best poster at the Dutch Biophysics meeting, Velhoven, The Netherlands

2016: First prize winner for the best poster at the MIRA day - University of Twente, Enschede, The Netherlands

2017: First prize winner of the Academic Publishing Bootcamp - University of Twente, Enschede, The Netherlands

2019: "Immuno-capture of extracellular vesicles for individual multi-modal characterization using AFM, SEM and Raman spectroscopy" featured on the cover of Lab on a Chip journal

Acknowledgments

Few pages are not enough to thank everyone that, in one way or another, accompanied and supported me through this challenging and amazing journey of four years. Without all of you, this accomplishment would not have been possible.

Leon, you have not only been a supervisor for me, but a life mentor since I first met you more than eight years ago. After that internship, I went back to Mexico all fascinated about your work and the kind of leader you are. Since then, I wanted everyone from my former university in Mexico to get to know you and learn from you. You came to Mexico and you left everyone fascinated and I was very glad you could also see a bit of my country together with Jessy. You not only supported me when applying for a scholarship to be able to pursue a master, but also during the world cup when Mexico lost against The NL. All that time I really wanted to work with you in such an exciting field and, after almost four years, I got the opportunity to go back to MCBP and work with you. During these four years you have been an inspiring person to me. Thank you for teaching me how to think out of the box, to be creative and pragmatic and, most importantly I think, find simple solutions to complex problems. I am very thankful that I can continue working with you as a team. Muchas gracias!

Cees, thank you very much for your amazing daily supervision, all your teachings and guidance. It was literally daily. Thank you for all those “five minutes” that became hours. No matter how busy you were, you always made time for me. I enjoyed very much our meetings and every meeting with you was very motivating and inspiring. Thank you for challenging me to dive deeper into the research. Thank you very much because the extra push needed in stressful times came from those motivating meetings with you. I am very thankful for having you as a my supervisor and co-promotor and I look forward to keep on collaborating with you. Dankjewel!

Dear committee members, prof. Ton van Leeuwen, prof. Guido Jenster, prof. Wouter Roos, prof. Srirang Manohar and prof. Frieder Mugele, thank you for accepting being part of my committee and thank you for your time reviewing my thesis.

Kiki and Niels: my Paranympths, my colleagues, mis amigos and part of my Dutch family. Thank you for welcoming me in The Netherlands with open arms, for all your support, advice, kindness and gezelligheid.

AMC team, thank you very much for the great collaboration we had and all the input you gave, which added a lot of value to my research. Edwin, I am very thankful for the level of detail of your feedback and, although it took quite some time to process, it added significant value to the papers and I learned a lot from it. Thank you also for the fun moments and gezelligheid together with Aleksandra. Ton, thank you very much for your constructive feedback and your very good and important questions, which were key to proceed. I was always looking forward to hearing your questions and comments after presenting my results. Rienk, thank you for your kindness and willingness to collaborate and support. Thank you also for the time you took to discuss with me. Every talk with you was an opportunity for me to learn crucial information about biological nanoparticles. Chi, thank you very much for all your support with FCM measurements and management of samples. Leonie and Linda, thank you very much for helping when needed, for your openness to discuss, share and compare methods and results and for your gezelligheid. Frank, thank you for the very interesting discussions and ideas. Onto more collaborations and gezelligheid with the AMC team.

My dear MCBP/BioEE/VyCAP colleagues: Afroditi, Ana, Andrea, Anouk, Arjan, Armagan, Aufried, Barbara, Cees, Christian, Dodo, Edwin, Fikri, Frank C, Frank T, Guus, Hoon, Ingrid, Ivan, Joost S, Joost vD, Joris, Joska, Kiki, Leon, Leonie, Lisa, Markus, Michiel, Narges, Peng, Pepijn, Richard, Ruchi, Sanne, Xichen, Yoon, Yvonne. You all make MCBP an ideal place to work and enjoy. All of you, each with a unique personality, have something in common: your eagerness to help, your constant support and your gezelligheid at work and outside work. Working from home is not the same. Bedankt voor alles en tot snel in de koffie pauze (vergeet niet jullie pasjes mee te nemen voor de koffie). Armagan, thank you for your support at the final stage of my thesis. Frank T, thank you for all what you taught me at the beginning of my PhD, thereby giving me a great start in the field. Ivan and Xichen, thank you for your friendship. Joost van D., thank you for teaching me all sorts of facts and bouldering techniques. Leonie, thank you for your very nice ideas and for the very enjoyable coffee breaks to catch up. Li, thank you for your great vibe, sincerity and gezelligheid. Going to work is a lot more fun when you are around. Thanks also to all the students that passed by MCBP, specially the students that I had the pleasure to supervise: Émeline, Xiang, Martine, Sven, Pascal, Sara, Lucinda and Bas. Thank you for your dedication and contributions. You all did a very nice job.

Pepi (the rockstar), amigo and teammate, always in to collaborate, for a chat, beer or doing karaoke. Thank you for being an essential part of my thesis and my PhD life in general. I enjoyed so much sharing with you moments in the lab. Our heated discussions and even the frustrating experiments make me nostalgic. I'm thankful for having you as a companion during trips, fiestas and conferences.

Ingrid, thank you very much for being so welcoming. When I arrived in The Netherlands with only two suitcases you provided me with a starting package with things to cook and eat. Thank you very much for being so caring, for being there when needed and for making me feel so welcome.

Anouk and Christian, thank you for all your support, kindness and gezelligheid at work and outside work. Besides being a solid foundation for MCBP, you bring a positive team spirit. I appreciate very much your sincere interest in everyone's wellbeing. Aufried, thank you for all your support, for taking care of one of the most beautiful setups at MCBP and for always bringing the good news that the Raman setup was working again.

Guus, thank you for choosing me as your student eight years ago because the story begins there. When I needed advice you were always there to help. Thank you for making me feel very welcome not only at MCBP, but also outside work with dinners, parties, drinks, Christmas markets and bouldering.

Officemates, thank you for being the coolest officemates. Special thanks to my long term "Roomies": Kiki, Sanne and Yoon. Thanks for being such great advisors and for making the office a place to look forward to go to.

Dear Cancer-ID team, it was a great pleasure collaborating with you all (>40 members). Every Cancer-ID meeting was an opportunity to learn and have fun. I would like to especially thank Afroditi, Edwin, Elmar, Gyllion, Hoon, Leonie, Linda, Melissa, Pepijn and Sven for your contributions, ideas and fun times that we all enjoyed together.

"Mexico crew", I enjoyed so much showing you Mexico at the rhythm of "Despacito". You all made this trip such a great experience. I am also very glad that you enjoyed my stories and thank you also for not falling asleep when I was driving, you always kept me company while driving.

My dear Dutch, Mexican and Belgian friends, and all of my other friends spread over the world. Thank you for sharing wonderful moments with me. Thank you for your company, support, advice, the laughs, the jokes, the trips, your hospitality, the fiestas, your messages, calls and visits. You all made these four years a lot more fun, I am truly thankful for having you as my friends and I wish to keep cultivating our friendship. My friends from the latest five generations of LA Voz, thank you for the unforgettable moments, for reminding me of my Latin roots and for your Latin spark which infected me with happiness.

Appendices

My family van Gorp, thank you very much for the big heart you all have and opening the doors of your home to me.

Mi querida familia muchas gracias por todo el apoyo que me han dado, por sus enseñanzas, las inolvidables visitas y por todo su cariño. Hermana y hermano, muchas gracias por estar siempre presente, por su apoyo y todos los momentos divertidos que paso con ustedes. Mamá y papá, muchas gracias por la educación que me han dado, por sus enseñanzas y apoyo incondicional. Mamá, gracias por ser mi ejemplo de dedicación. Papá, gracias por ser mi ejemplo de esfuerzo. Los quiero tanto!

Finally, mijn lieverd Chris, thank you for being the beautiful person you are, for being such a great listener, for your assertiveness and for all your support. Thank you because with you, life is so much beautiful, bright and fun. We keep growing together and looking forward to our next adventures. Love you!

To everyone: gracias, gracias, gracias!

Curriculum Vitae

Agustin Enciso Martinez was born in Zacatecas, Mexico the 25th of December of 1990. He finished high school summa cum laude at Tec de Monterrey – Campus Zacatecas and was awarded a scholarship to continue with his bachelor at Tec de Monterrey – Campus Monterrey. There, he started studying Biomedical Engineering in 2009 and during his bachelor studies he participated in various research activities. He was selected to do an internship at the University of Texas MD Anderson Cancer Center, Houston, USA, where he started working on cancer research. He continued with a research internship at the Medical Cell Biophysics department of the University of Twente (UT), Enschede, The NL, where he worked on the detection of tumor-derived extracellular vesicles (tdEVs) and cell fragments on functional surfaces. He went back to Mexico and did an internship at the CINVESTAV Monterrey on the viscoelastic properties of blood. In 2013, he graduated summa cum laude as Biomedical Engineer and was awarded a full-ride scholarship to continue with his master studies in Biomedical Engineering at KU Leuven, Belgium. He did an internship at IMEC, Belgium, on the electrical properties of cancer cells. He was selected to do an internship at Johns Hopkins School of Medicine, Baltimore, USA, which resulted in the publication of his work on artificial neural networks to automatically detect food intake for neuromodulation in treating obesity and diabetes. In 2016, he completed his master thesis titled *Electrical Impedance Based Cellular Assay for Cancer Cells* at IMEC and obtained the degree of Master of Science magna cum laude from KU Leuven. In 2016, he started his PhD at the Medical Cell Biophysics department of the UT. His research focused on the detection and characterization of single tumor-derived extracellular vesicles using various methods such as Raman spectroscopy, optical trapping and scanning electron microscopy, of which results are presented in this thesis. Throughout his PhD, Agustin contributed to the international relations of the UT during his 2-year presidency of the Latin American association of the UT, as an editor of the science and technology section of the magazine issued by the Mexican Embassy in The Netherlands and as a representative of the UT on a business trip to Mexico.

